Characterization of Growth and Real Structure of Nitride Based Semiconductor Devices by Use of Synchrotron Radiation

.....

.....

Zur Erlangung des akademischen Grades eines
DOKTORS DER NATURWISSENSCHAFTEN
von der Fakultät für Physik des
Karlsruher Instituts für Technologie (KIT)

genehmigte

DISSERTATION

von

Dipl.-Phys. Bojan Miljević
aus Serbien

Tag der mündlichen Prüfung: 20.04.2012

Referent: Prof. Dr. Gerd Tilo Baumbach

Korreferentin: Prof. Dr. Dagmar Gerthsen

ACKNOWLEDGMENTS

...dedicated to my wife Ana, for all her love and patience.

Thanks to all our children and to our Lord, who has saved us and who all impossible makes possible.

Contents

List of Figures

Chapter 1

Introduction

1.1 Nitride Based Semiconductors

In the past 20 years it was shown that nitride-based semiconductor devices are not just promising but very applicable in many of modern technology fields. The III-V nitride based compound semiconductors are recognized as advanced materials because of the wide range of their very interesting properties such as a direct bandgap tunable from 6.2 eV (AlN) down to 0.7 eV (InN), piezoelectricity, polarization, large breakdown voltage, bio-compatibility, high chemical and thermal stability, etc. Depending on the composition and structure, combined with nanotechnology group(III)-nitrides became ideal for many applications, including light emitting diodes (LED) and lasers, photodetectors, high electron mobility transistors, radio-frequency power transistors, piezoelectric filters, bio-sensors, pressure and temperature sensors and power convertors. One of the most common application is in high-brightness light-emitting and laser diodes with high efficiency, high reliability, quick response time and much longer lifetime compared to II-VI compounds operating in the short wavelength spectral region. Today, research on group(III)-nitrides is mainly focused on developing of current-injection laser diode which operates at room temperature by continuous wave [1].

According to the strong demand of the LED industry, one of today's most prominent material for producing photonic devices operating in green-blue-UV region is indium gallium nitride (InGaN). Beside it's great ability of operating in the short wavelength spectral region, the application fields of InGaN are the large area displays, efficient and long-lasting solid-state lightening (LED, photodetectors, laser waveguides) up to the high-density memory storage and high definition printing (laser diodes) [2].

1.2 Thin Films and Nanostructures as an Active Part of Photonic Devices

In the core of each opto-electronic device is an active part which is emitting light. The active parts are specially designed in order to fulfill the space confinement of the charge carriers to reach the quantized energy levels. The solid-state lightening is produced from low-dimensional systems such as thin films and nanostructures: quantum wells, quantum wires and quantum dots.

Thin GaN films and nanostructures of the related ternary compounds with indium or aluminium are mostly epitaxially grown on freestanding GaN (homoepitaxy) or on different substrates like sapphire or silicon-carbide (heteroepitaxy).

Metal-organic vapour phase epitaxy (MOVPE) is a widely used technique for the growth of group(III)-nitrides. This method can be described as a epitaxial deposition from gases on the hot substrate surface. The growth of thin GaN films and nanostructures is still under development in order to improve their properties. The connection between the growth process and desired structure on a nanometer-scale is often not obvious. Therefore, the characterization of the growth and structure of nitride-based semiconductors is a topic of many research groups worldwide.

1.3 Material Research by Use of Synchrotron Radiation

The X-ray scattering is in many ways an ideal probe for recent classes of device electronic systems since it allows in-situ, non-invasive investigation of structural properties of materials with nanoscale or even atomic resolution. The ability for X-radiation to deeply penetrate material structures makes it a useful tool for probing bulk properties of device materials. This is an advantage over surface sensitive techniques such as electron scattering and microscopy, or scanning tunneling microscopy. The fundamental diffraction-limited resolution of X-ray scattering based techniques is well below 1 Ångström.

High degree of X-ray energy tunability at synchrotron facilities makes it possible to perform measurements that are element-specific to certain chemical constituents, or use core-level sensitivity at the resonant edges to study magnetism with resonant magnetic scattering.

The rather weak signal of X-ray diffraction from thin films and nanostructures usually requires a very bright and collimated X-ray beam. Both of these requirements, namely high collimation along with a high photon flux, are intrinsically satisfied by highly brilliant third-generation synchrotron radiation. Nowadays, synchrotron radiation is widely used in many fields of physics, chemistry, and biology as well as in medicine, arts and archeology. The main interest of this thesis is in the material research of structure and surface morphology. Therefore, considering the use of

synchrotron radiation, the focus will be on the X-ray scattering methods.

1.4 Aim of the PhD Thesis

In order to characterize one complete nitride-based semiconductor device, one can benefit from systematical study of the growth and of the structure of every step building it from the substrate through the nucleation and buffer layer up to the nanostructures as an active part and the capping layer at the end. For such device with an excellent optical luminescence and quantum efficiency one needs a high quality GaN buffer layer with as low as possible threading dislocation density, since these crystal imperfections negatively affect the electrical and optical properties of GaN-based devices as they work as very effective non-radiative recombination centers [1]. One proposed method for reduction of threading dislocation density is an *in-situ* deposition of SiN_x interlayer which acts as a nano-mask partially stopping the propagation of dislocations. A series of thin GaN films with different dislocation densities were systematically grown at Institute of Optoelectronics, University of Ulm. The threading dislocation density was changed by tuning of the SiN_x deposition time. It was a task to develop a robust X-ray scattering method to characterize them without destruction of the future device. The series of thin GaN films was characterized by X-ray scattering methods to study the influence of SiN on the crystalline quality, surface and interface roughness of thin films. The results of this investigation will be presented and discussed (chap. 6) in order to substantiate a model system for the simulations of diffuse scattering. The reciprocal space maps in both coplanar and grazing incidence geometries were measured to support the development of a new non-destructive method for determination of the threading dislocation densities.

Thin GaN films, epitaxially grown on the sapphire substrate, are commonly used template for growth of nanostructures such as quantum dots or quantum wells. It is difficult to grow the InGaN quantum dots with the high indium content and to have them stable after the capping. The composition, the growth mechanism, the strain inside them and the interdiffusion are still not known and a detailed characterization is still pending. Therefore, the main topic of this thesis is the evolution of InGaN quantum dots during capping. The sample series of freestanding and overgrown InGaN quantum dots (grown at Institute of Solid State Physics, University of Bremen) have been characterized by X-ray scattering methods in several geometries (grazing incidence diffraction, asymmetrical X-ray diffraction) to answer on structure, composition and strain. Beside the characterization by use of synchrotron radiation, the InGaN islands were studied by atomic force microscopy in order to gain the information in a real space about the morphology of dots and overgrowing material. The results will be presented and discussed (chap. 7) with a special aspect on the theoretically predicted phase separation in InGaN resulting in two types of islands, indium rich and with less indium content.

The structure of the thesis is organized as follows. After the introduction, in the

chapter 2 will be described the structure and the physical properties of InGaN with the actual status of the common knowledge and theoretical basics in the field. In the chapter 3, the short introduction to the theory of X-ray scattering from thin films and nanostructures will be introduced. The chapter 4 and the chapter 5 will describe the experimental setups and technical details of the X-ray scattering experiments and of the scanning probe microscopy experiments, respectively. As mentioned above, the results of the study on thin GaN films with different dislocation densities will be presented and discussed in the chapter 6 as well as the results of the study on evolution of the InGaN quantum dots in the chapter 7. Further comes the chapter 8 with the conclusions of the thesis and at the end there is an outlook with the future perspectives (chapter 9).

This work is a part of the Helmholtz Association Virtual Institute *PINCH Photonics*. The VI PINCH (Process Integrated Characterization of Wide Band Gap) Photonics project has the aim to build up the in-situ MOVPE growth reactor dedicated to non-destructive characterization of GaN-based epi-layers and their structures by in-situ (during MOVPE growth) synchrotron methods and in-situ optical methods. This project is a broad collaboration between some of the most prominent crystal growth groups (University of Bremen, University of Ulm, UNIPRESS(Polish Academy of Sciences)) from one side and the X-ray characterization and theory experts on another side (Karlsruhe Institute of Technology (ISS/ANKA and LAS, Faculty of Physics), Charles University of Prague).

The research on GaN, InGaN and related nitride-based semiconductor devices in recent years has shown advantage of their solid-state lightening by means of efficiency, high output power and tunable wavelength, but their real structure has not been fully characterized and understood. This PhD thesis should bring us one step further towards better understanding of relation between the growth and the real structure of modern nitride-based semiconductors and towards determining the origin of luminescence which is still not known.

Chapter 2

Structure and physical properties of InGaN

InGaN is a direct wide band gap semiconductor material consisting of a mixture of gallium nitride (GaN) and indium nitride (InN). The lateral crystal lattice parameter and corresponding band-gap depend on composition, i.e. on the indium incorporation x in the $In_xGa_{1-x}N$ ternary compound. Fig. 2.1 shows the band gap and the corresponding wavelength of several semiconductor materials as a function of the lateral lattice (a) constant which is directly related to the composition. It can be seen that group(III)-nitrides covers a wide spectral range from deep ultraviolet (AlN) to infrared (InN). One could tune the photoluminescence wavelength (band gap) by varying the amount of indium incorporated in the InGaN ternary compound. But, it is not possible to choose exactly any wavelength in the range between UV (belonging to 3.4eV - the room temperature band gap of GaN) and near infrared (0.7eV - the room temperature band gap of InN) [3]. The main reason is the solid phase miscibility gap in mixing of GaN and InN due to large difference in interatomic spacing. This will be discussed further in the sec. 2.5.2.

In this chapter, the structure and material properties of group(III)-nitrides will be summarized. It will be used as a background needed for this PhD thesis. Some heterostructures which consist of epitaxially grown group(III)-nitrides will be described. These materials are mostly grown by metal organic vapour phase epitaxy (MOVPE) (sec. 2.2) and have to be grown on foreign substrates as GaN wafers are still rare and expensive. Sapphire (Al_2O_3) is a widely used material as a substrate (sec. 2.3) in spite of the large lateral lattice mismatch between GaN and sapphire substrate of 16.1% when grown in the [0001] direction [5]. The epitaxy of thin GaN films on the sapphire substrate will be described. Finally, there will be an introduction to the thin GaN films and to the InGaN ternary compounds, especially InGaN quantum dots, which will be the main topic of this PhD thesis. For thin GaN films the focus will be on threading dislocations as the strain relaxation mechanism and for InGaN quantum dots focus will be on the strain in InGaN ternary compounds and on the phase separation due to a solid phase miscibility gap.

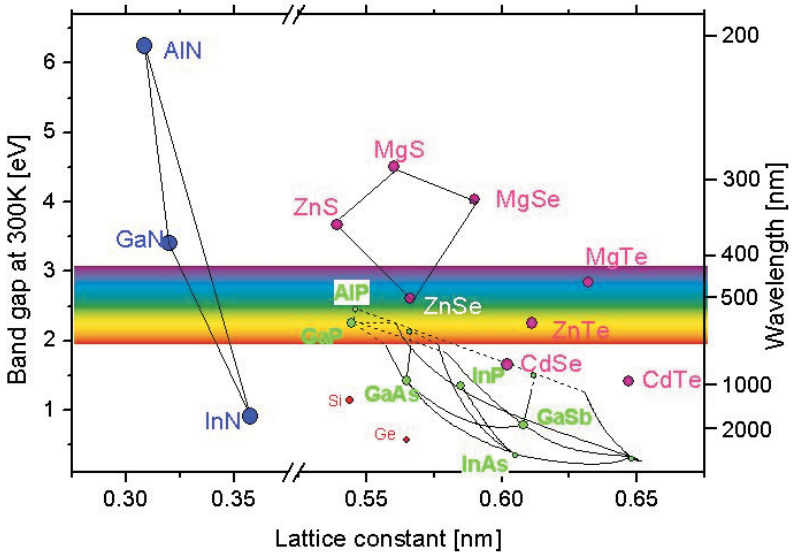

Figure 2.1 Band gap and the corresponding wavelength as a function of the lattice constant [4].

2.1 Group(III)-nitrides

GaN and the group(III)-nitrides can crystallize in hexagonal (wurtzite) and in cubic (zincblende) structure. However, the hexagonal structure is more common. The GaN wurtzite structure is shown in (Fig. 2.2).

In the case of the wurtzite structure (space group $P6_3mc$), the primitive GaN unit cell contains 4 atoms, 2 of gallium and 2 of nitrogen. The positions of the atoms in the unit cell (fig. 2.2 (a)) are as follows: Ga (0,0,0), Ga(2/3,1/3,1/2), N(0,0,0+u), N(2/3,1/3,1/2+u), where u depends on material: u(GaN)=0.377Å, u(AlN)=0.382Å, u(InN)=0.379Å [1]. Figure. 2.2 (b) shows the hexagonal structure of GaN and related materials. The shape of the wurtzite cell is a vertically oriented prism. Vector **c** in direction [0001] is defining the unit cell height (vertical lattice parameter) and it is perpendicular to the hexagonal base, defined by two vectors **a** forming the angle of 120°.

There are no consistent reference values of the lattice parameters of group(III)-nitrides, even for nominally undoped samples grown by the same methods, as it is discussed recently by Moram and Vickers in [6]. Nevertheless, lattice parameters of the three most used materials, GaN, InN and AlN, are given in the table 2.1. The values are given for nominally strain-free materials evaluated from the data published in [6] and the references therein.

As shown in figure 2.3, there are three mostly used stable crystallographic planes for the growth of nitride-based structures. Growth of the c-plane{0001}(fig. 2.3 (a))

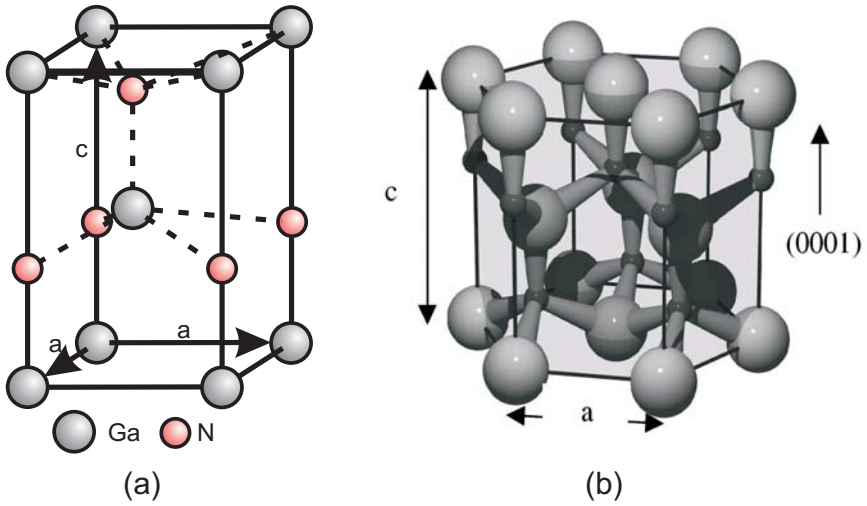

Figure 2.2 Wurtzite structure of GaN: (a) hexagonal unit cell and (b) molecular view of the formed hexagonal prism.

material	a [**Å**]	c [**Å**]
GaN	3.1889±0.0015	5.1855±0.0015
InN	3.5377±0.0005	5.7038±0.0007
AlN	3.1112±0.0015	4.9796±0.0015

Table 2.1 Lattice parameters of nominally strain-free GaN, InN and AlN.

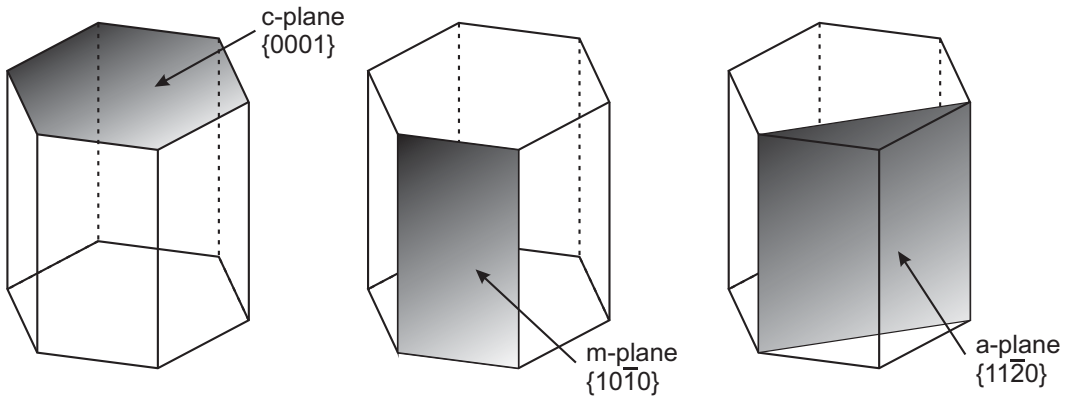

Figure 2.3 GaN crystallographic planes of interest: (a) c-plane, (b) m-plane, (c) a-plane.

(on the c-plane oriented sapphire), which is up to now mostly used, leads to a spontaneous piezoelectric polarization within the heterostructure [7] which reduces the efficiency of charge carrier radiative recombination. Therefore, in the recent years, research on the GaN epitaxial growth is more and more focused on the growth of non-polar m-plane $\{10\bar{1}0\}$ (fig. 2.3 (b)) [8] and a-plane $\{11\bar{2}0\}$ [9] as well as of semi-polar surfaces $\{11\bar{2}2\}$ and $\{20\bar{2}1\}$ [10].

Depending on the characteristic of group(III)-nitrides which is to be exploited, there is a variety of their applications.

2.2 MOVPE growth of group(III)-nitrides

Among all available techniques for epitaxial growth of GaN and related materials, currently metal-organic vapour phase epitaxy (MOVPE), hydride vapour phase epitaxy (HVPE) and molecular beam epitaxy (MBE) are mainly used. HVPE is well developed for large scale crystallization, but it is difficult to control it to sufficiently produce abrupt interfaces of the grown structures. However, today high temperature, high pressure HVPE is used for production of bulk GaN single crystals. Growth of III-V nitrides by MBE is a process capable for producing uniform epitaxy of diverse structures with abrupt interfaces and allows *in situ* monitoring. The main disadvantage of MBE is a high cost and the limiting throughput of the process itself has the low growth rate which is not acceptable for the industrial production. Most flexible epitaxial growth technique is MOVPE which strengths are: uniform growth of abrupt interfaces, high purity, simple growth reactor, large scale production, high growth rates, possibility of selective growth, *in situ* monitoring [11]. There are also disadvantages like expensive reactants and hazardous precursors, but above all MOVPE of nitride-based semiconductor devices is a robust technique suitable for the mass production and is currently the most widely used technology. To illustrate that, all nitride-based optoelectronic commercial device structures are fabricated by

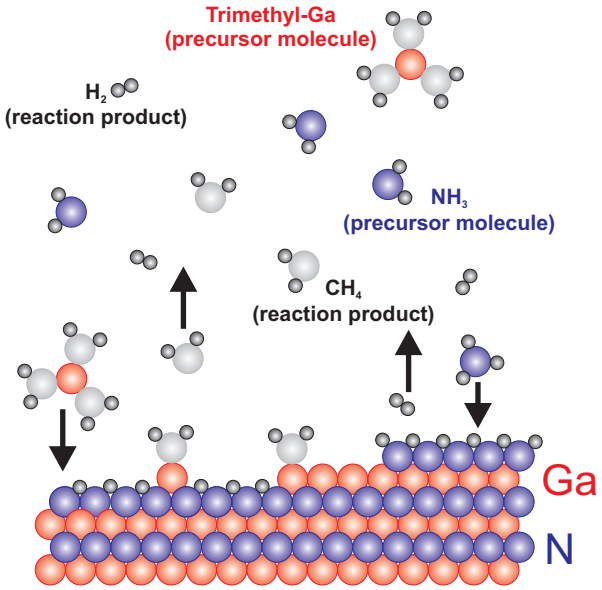

Figure 2.4 A schematic view of the MOVPE processes (courtesy of Dr. B. Krause).

MOVPE [12]. The samples studied in this PhD thesis are grown with MOVPE, therefore this growth method will be described in detail.

MOVPE or organometallic vapour-phase epitaxy (OMVPE) or metal-organic chemical vapour deposition (MOCVD) are different names of the same process which can be described as an epitaxial deposition from gases on a hot substrate surface. This process involves simultaneous heat, mass and momentum transfer together with gas and surface reactions. A models which completely describes the MOVPE must consider fluid dynamics, thermodynamics and kinetics of gas-phase and surface reactions [12]. Taking into account the high GaN melting point of 2500° [13] and the high vapour pressure of nitrogen of $45 \cdot 10^3$ bar at this temperature, the growth temperature for good crystalline quality GaN layer has to be above 1000°C with the optimized pressure (gas flow) of the nitrogen source. NH_3 seems to be the best nitrogen precursor for the MOVPE of GaN due to very high partial pressure ratio of NH_3 over trimethylgallium (TMG) required for deposition of GaN [12].

A number of processes are happening during the MOVPE deposition (fig. 2.4) at the sample surface and above it: absorbtion, desorption, surface diffusion, pre-reactions etc. Figure 2.5 shows the gallium nitride chemical reaction pathway which consist of decomposition and adduct [14]. The fundamental models of MOVPE gas phase kinetics are described in the works of Pawlowski et al. [15], Teles et al. [16], Parikh and Adomaitis [14]. Surface reactions have been studied in [17].

In principle, there is variety of chemical processes with certain probability, but nevertheless one of them is as follows: $(CH_3)_3Ga + NH_3 \rightarrow GaN_{(s)} + 3CH_{4(g)}$.

The group(III) precursors used in the MOVPE growth are: trimethyl-gallium, -indium, -aluminium (TMG, TMI, TMA) or triethyl-gallium, -indium, -aluminium

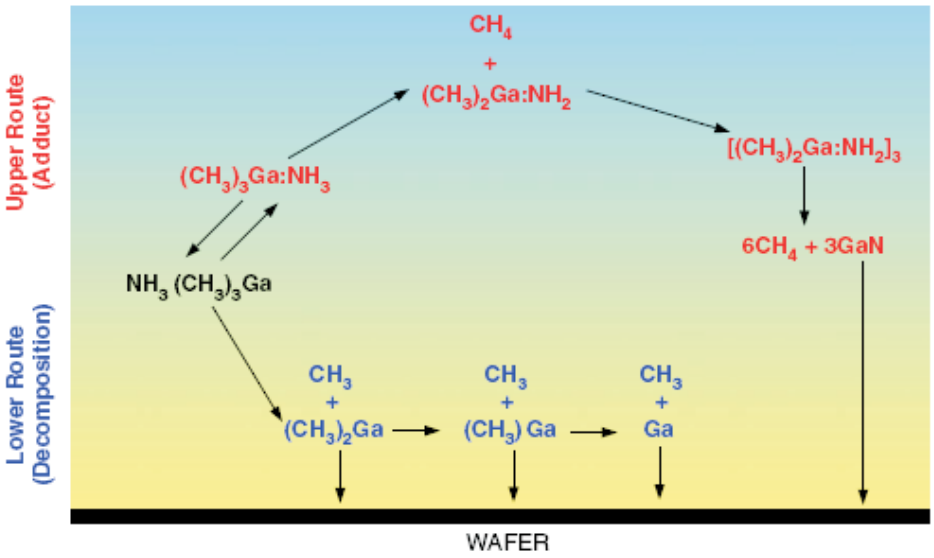

Figure 2.5 The GaN chemical reaction pathway in the MOVPE growth process [14].

(TEG, TEI, TEA). Carrier gas can be either N_2 or H_2. For the semiconductor electronics the p- or the n-type of III-nitride material is achieved by extrinsic doping, with Mg for producing of p-type, and by doping with Si for n-type.

With the development of MOVPE technology up today, there exist several types of reactors for epitaxial growth: horizontal, vertical close-coupled shower head, oblique and the custom-built reactor designs. Whatever the reactor, it needs to have a main flow consisting of TMG+NH_3+H_2, a subflow of N_2+H_2 mixture and the heating of the substrate. More on this topic can be found in [11, 12, 18].

2.3 Epitaxy of GaN grown on Sapphire

Epitaxy can be translated "to arrange upon" from the Greek roots *epi*, meaning "above" and *taxis*, meaning "in ordered manner". As homoepitaxy is still rare and expensive due to lack of "good" commercial freestanding GaN substrates, almost all the development of nitride based devices has been made by heteroepitaxy, growing on foreign substrates. A widely used substrate is sapphire (Al_2O_3), beside alternative substrates as 6H-SiC, spinel ($MgAl_2O_4$), LGO ($LiGaO_2$) etc.

As it was already mentioned in the section 2.1, hexagonal GaN and related ternary alloys are mostly epitaxially grown in three crystallographic orientations, c-, m- and a-direction. In the case of sapphire substrate, the most easily grown stable surfaces are as follows: c-plane GaN which grows on the c-sapphire, m-GaN on the a-sapphire and a-GaN on the r-sapphire. We will be focused on the most important for this thesis, c-GaN grown on the c-sapphire. Vertically, the GaN growth direction [0001] follows

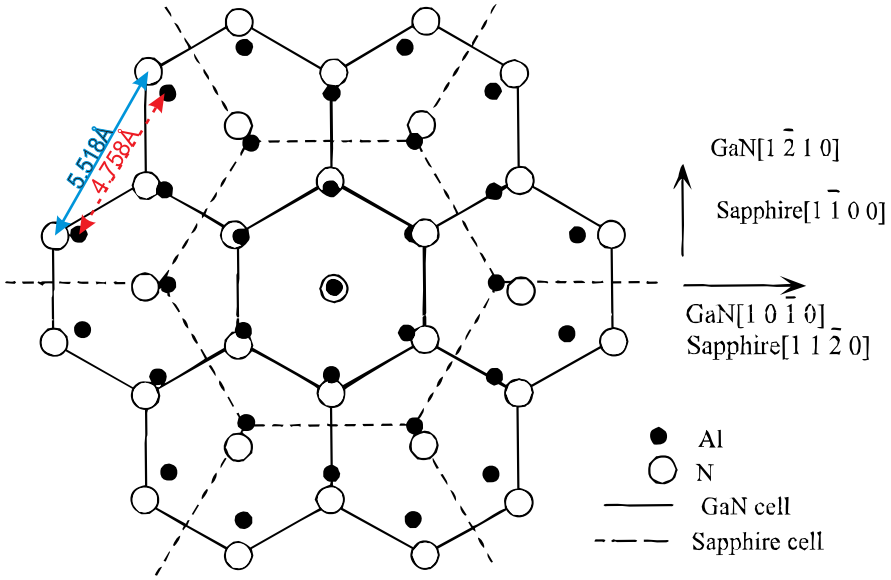

Figure 2.6 Planview of GaN and sapphire basal planes {0001}. Reproduced after [1, 18]

the same orientation [0001] of the sapphire unit cell. The in-plane orientation of the GaN epitaxial layer unit cell with respect to the sapphire substrate unit cell is turned by 30° (see fig. 2.6). It can be seen how the N atoms (white circles) form hexagons of the GaN unit cell over sapphire (Al_2O_3) represented by Al atoms (black circles). It is shown how the lateral unit cell parameters of the sapphire substrate a_S and of GaN epitaxial layer a_L are related. To one sapphire lateral constant correspond $\sqrt{3}$ times lateral constant of GaN producing the lattice mismatch of approximately 16%: $\frac{(a_L\sqrt{3}-a_S)}{a_S} \approx 16\%$ where $a_L = 3.186$Å belongs to the layer (GaN) and $a_S = 4.758$Å to the substrate (sapphire).

The substrate miscut means an angular deviation of the growth direction from [0001]. The growth on slightly miscut sapphire substrate was found to be the solutions for compensating the mismatch of the GaN epitaxial layer [19]. It was shown that substrate miscut enhances the electrical, optical and morphological properties of thin film [19–22]. Miscut of the sapphire substrate for growth of GaN epitaxial layers was investigated and optimized in the works of Brückner et al. [23], Perlin et al. [24] and Lu et al. [19]. The best film quality was related to the substrate miscut of about 0.3°. This result is today in common use of many groups [25–29]. Improvement of the optical and morphological qualities of thin films grown on the miscut sapphire substrate might be explained by better providing of nucleation sites and effectively accommodating the lattice mismatch. This will be discussed further in the section 6.5.

Several steps are required in every heteroepitaxy, starting with the nitridation of the substrate and with or without heating, then depositing of a low temperature buffer layer and its annealing, all in order to suppress the generation of threading

dislocations [12]. Threading dislocations are defects in the crystal which drastically reduce the efficiency of devices (see 2.4.1). The low-temperature deposition is usually followed by long-term epitaxy at higher temperatures to achieve suitable crystalline and surface quality. To overcome large difference in thermal expansion coefficient and mismatch between epi-layer and the substrate, the growth of thin film usually begins with deposition of a low temperature (LT) AlN nucleation layer [30, 31] or GaN [32]. In this way one can obtain much better wetting and more stabile growth of thin film which is to be grown above.

Improving of both surface morphology and crystallinity was obtained by nitridation of the sapphire substrate [33, 34].

Initially, when the deposition starts, small clusters nucleate and further grow forming either two-dimensional (2D) or three-dimensional (3D) isolated islands, depending on the adatoms binding energy and their density [35]. The islands coalesce until the surface is fully covered, then the layer is complete. 2D and 3D growth modes are widely documented. Si is often used as a surfactant [12].

Further technological improvement of the GaN and related material epitaxial layers grown on the sapphire by MOVPE is masking by SiN which stop threading dislocations propagating to the thin film surface. This is used in the growth of thin GaN films with different dislocation densities studied in this PhD thesis. Masking by SiO_2 leads to the epitaxial lateral overgrowth (ELO). ELO can result in the threading dislocation density below 10^6 cm^{-2}.

2.4 Thin GaN films

Thin GaN films are mostly used as a buffer layer for growing advanced nanometer-size heterostructures, namely quantum dots (QD) and quantum wells (QW). A term *thin film* is used to describe a layer of certain material with the thickness of sub-nanometer range (atomic monolayer) up to several micrometers, depending on further application. The effect which should be emphasized, when speaking on optical and electrical properties of thin films, is the space confinement of charge carriers in a two-dimensional object causing the quantum phenomena. Quantum effect is expressed by existing the discrete energy levels which charge carriers may have:

$$E_n = \frac{n^2\pi^2\hbar^2}{2mL^2}, \tag{2.1}$$

where L is the film thickness and m is an effective mass of the charge carriers. How the density of states depends on the energy of low-dimensional systems is in the best way shown in the figure 2.7. In the thin film, interfaces act as the potential barriers with abrupt change of the energy level. Exactly this is used for making of active part of opto-electronic devices. This figure will be further discussed with the quantum size effects of the low-dimensional systems in the section 2.5.3.

The epitaxial growth of a thin GaN film on the sapphire due to the lattice mismatch produces a micro-strain inside the film. The strain must be partially relaxed

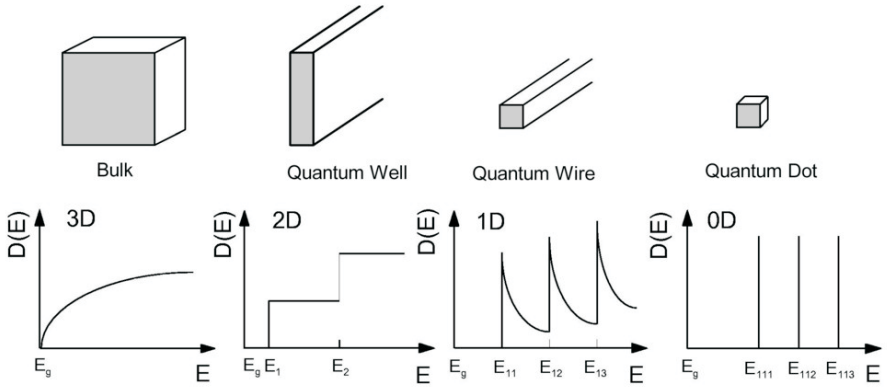

Figure 2.7 Density of states as a function of dimension [36].

because of the large mismatch. Cracks and other defects can be formed. Thin film consists of mosaic blocks. The mosaic blocks in the film may be misoriented from the mean in-plane orientation and they may have a broad size distribution. When InGaN is grown on a GaN buffer, then the structure becomes even more complicated due to different composition, elastic strain and possible interdiffusion between the layers. All these crystall imperfections can negatively affect the opto-electrical properties of the future device. Therefore, the proper characterization of the thin GaN film structural properties as composition, strain, misorientation and the size of the mosaic blocks, etc. is of very high importance.

2.4.1 Strain relaxation mechanisms: Threading Dislocations

When the epitaxial layer is growing on the foreign substrate, the strain in the crystal occurs due to the lattice mismatch between the substrate and the layer. The epitaxially grown crystal lattice tends to relax what may cause producing of many different, elastic or inelastic, defects: interfacial misfit dislocations, threading dislocations, stacking faults (basal, prismatic), grain boundaries, etc. Extended defects in hexagonal GaN epitaxial layers are documented in the works of Ruterana and Nouet [37] and of Dimitrakopulos et al. [38, 39].

Threading dislocations act as non-radiative recombination centers effecting negatively the electrical and optical properties of epitaxial layers [40–42]. Type of threading dislocation can be screw, edge and mixed [43–45]. The screw threading dislocations follow c-direction (fig. 2.8) $\mathbf{b}_s = [0001]$, edge type propagates in the a-direction $\mathbf{b}_e = 1/3\langle 11\bar{2}0\rangle$, while mixed type is a combination of screw and edge, which can be described by Burgers vector $\mathbf{b}_m = 1/3\langle 11\bar{2}3\rangle$. Figure 2.9 shows how the edge and the screw type are correlated in the crystal.

Threading dislocations are typically characterized by transmission electron microscopy (TEM), etch pit density (EPD), by cathodoluminescence (CL) combined with scanning electron microscopy (SEM) and by atomic force microscopy (AFM).

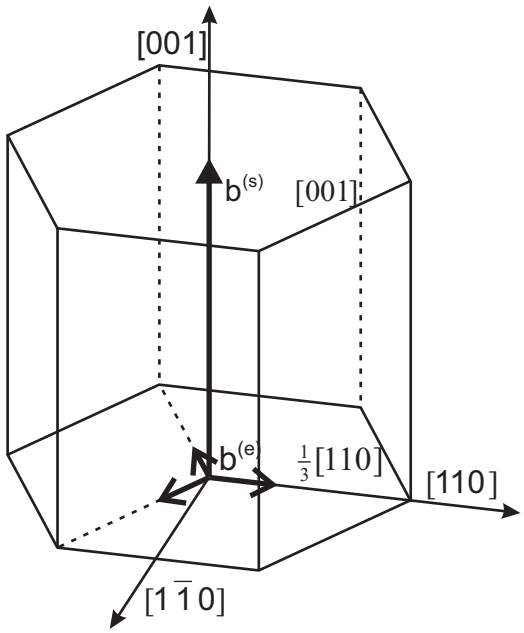

Figure 2.8 Threading dislocations in GaN crystal: screw type follows the c-direction and edge type propagates in a-direction.

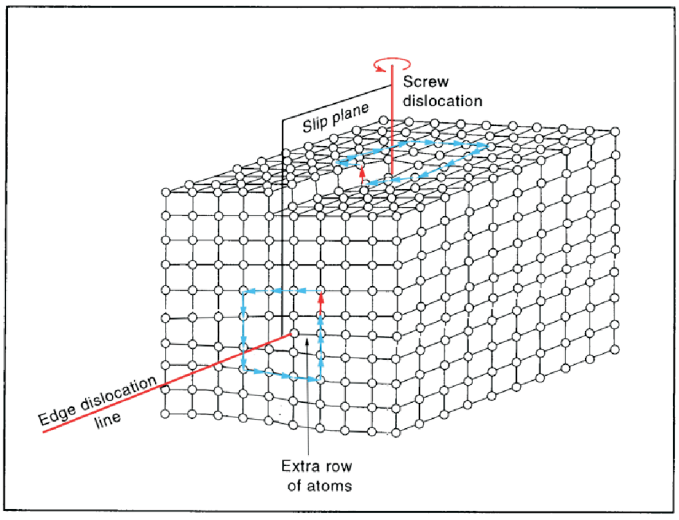

Figure 2.9 Threading dislocations in GaN crystal [46].

TEM gives a cross-sectional view of dislocations in the film propagating to the surface (fig. 2.10 (a), but the method itself is destructive. The result might be not

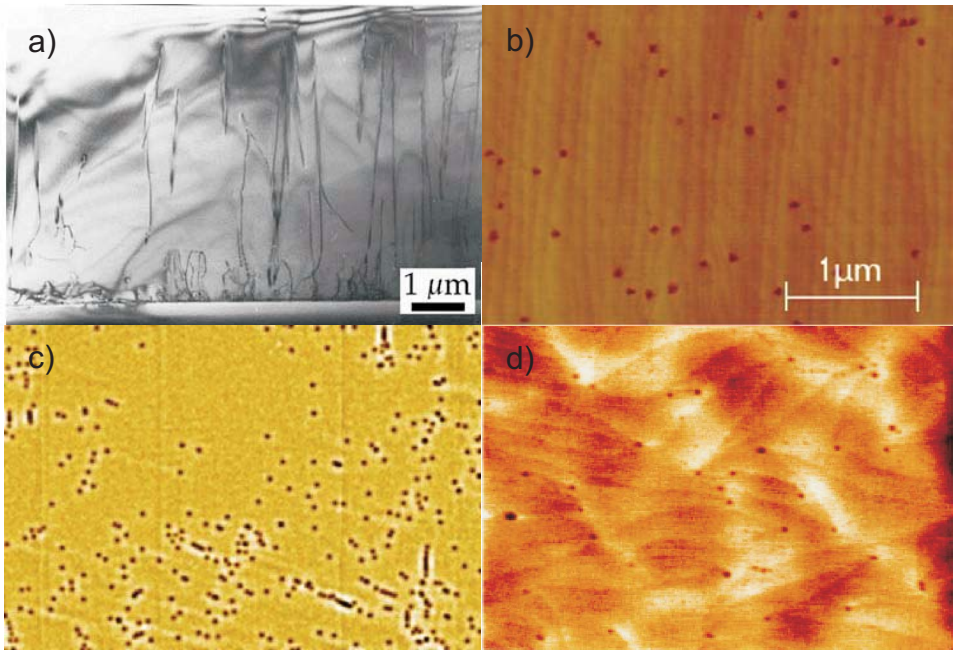

Figure 2.10 Threading dislocations in GaN crystal characterized by a) cross-sectional transmission electron microscopy [47], b) etch pit density [26], c) combined cathodoluminescence and scanning electron microscopy [48] and by d) atomic force microscopy with contrast enhanced by scanning capacitance microscopy [49].

representative because of the local probing of TEM. EPD is a measure of the semiconductor wafer quality which uses the etching of the sample surface. The etching rate is increased at dislocations of the crystal, resulting in pits (fig. 2.10 (b)). Their density can be determined by optical microscopy. CL can enhance the visibility of dislocations and the surface then can be scanned by SEM (fig. 2.10 (c)) or AFM. Figure 2.10 (d) shows the AFM which contrast was enhanced by capacitance. The EPD method does not distinguish the different types of dislocations, while this can be done with the X-ray method. Diffuse X-ray scattering is a non-destructive method to characterize threading dislocations. It was shown that dislocations influence the broadening of the X-ray diffraction peaks [50, 51]. The density of dislocations can be determined from the slope of the angular scan trough the diffraction peak (rocking curve) [52]. Ratnikov at al. has evaluated the contribution of particular dislocation types to the shape of diffraction peaks in different geometries of reciprocal space [44]. More deep discussion on diffuse X-ray scattering from dislocations will be presented together with the results of our experiments on X-ray diffuse scattering from threading dislocations in epitaxial GaN layers in the sec. 6.6.

Quality of thin film crystallinity, and by that quality of the device made of it,

strongly depends on the dislocation density. Therefore, structure of threading dislocations, their networking and methods of suppressing either their generation or propagation through the film is interest of many groups which research is focused on the group(III)-nitrides thin films. One of the methods which partially stop propagating of threading dislocations is *in situ* depositing of SiN_x during the growth process proposed by [26,53]. This method was used in research on thin GaN film investigated in this thesis and it will be discussed further in the sec. 6.1.

2.5 InGaN ternary alloys

The InGaN quantum wells and quantum dots play a huge role acting as an active part of many opto-electronical devices. The InGaN has a great advantage of having the operating wavelength which can be tuned by changing the composition. However, there is a certain limitation of mixing manifested by having the stable and unstable ternary alloy phases depending on the growth temperature and composition of intentional gas phase. Composition and strain can influence the gap bowing [54] and by that change the optical properties of the alloy [55]. Since the effects of the composition and of the strain inside InGaN compound are overlapping and this is further complicated by interdiffusion and phase separation, there is still no clear interpretation of its real structure and the origin of luminescence is an open question [56–59]. Understanding of the nature of InGaN nanostructures is emerging, but is still the challenging topic.

2.5.1 Strain in InGaN ternary alloys

One of the main topics of this thesis is a study of the InGaN quantum dots evolution during capping. The strain plays a huge role in the formation of the InGaN islands as well as in the capping by different materials. Determination of the strain inside the islands can lead to the answer on their composition, depending on how the signals are superposed. Due to relatively large difference in the lattice parameters of GaN and InN hexagonal unite cells, InGaN films epitaxially grown on a GaN buffer layer are strained. By growth of $In_xGa_{(1-x)}N$ in c-direction [0001] on the c-GaN, the in-plane lattice parameter a_{InGaN} is compressed trying to adapt to the buffer lattice parameter a_{GaN} as shown in the figure 2.11, while the out-of-plane lattice parameter c_{InGaN} is expanded. The absolute values of the strain components and change of the lattice parameters depend on the indium content x. The stress tensor of the hexagonal unit cell can be described by Hooke's Law:

$$\sigma_i = \sum_j C_{ij}\epsilon_j, \quad i,j = \{1,\ldots,6\}, \tag{2.2}$$

where C_ij are the elastic constants and ϵ_j are the strain components. The elastic constants again depend on the indium content x [61]. For isotropic biaxial strain ($\epsilon_1 = \epsilon_2$) perpendicular to the c-axis, as expected due to the fact that the wurtzite

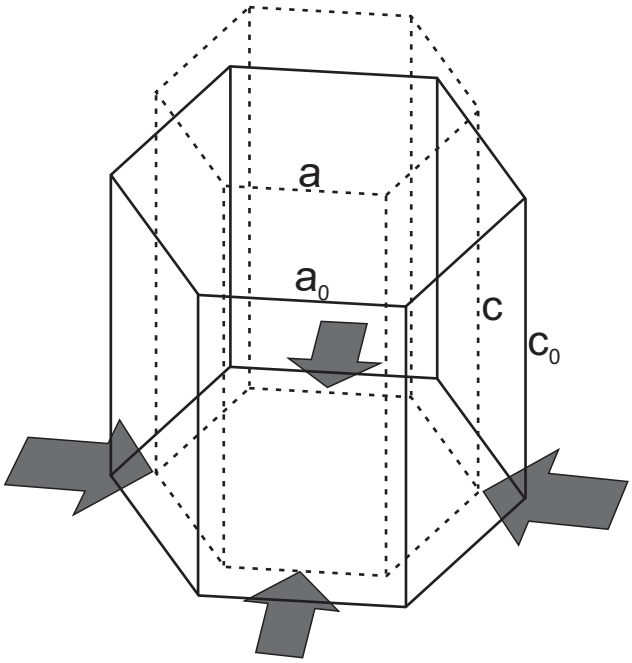

Figure 2.11 InGaN unit cell under biaxial strain which acts in the basal plane (after [60]). a and c denote strained unit cell parameters, while a_0 and c_0 are bulk (relaxed) values.

basal plane is isotropic [35], relation between the strain component in the growth direction ϵ_3 and components in the basal plane (ϵ_1 and ϵ_2)can be written as [35, 60]:

$$\epsilon_3 = -\frac{C_{13}}{C_{33}}(\epsilon_1 + \epsilon_2) = -2\frac{C_{13}}{C_{33}}\epsilon_1. \tag{2.3}$$

The out-of-plane strain ($\epsilon_3 \equiv \epsilon_\perp$) and in-plane strain ($\epsilon_1 \equiv \epsilon_\parallel$) are defined through [62]

$$\epsilon_\perp = \frac{c - c_0}{c_0} \quad \epsilon_\parallel = \frac{a - a_0}{a_0}, \tag{2.4}$$

with a and c denoting the strained lattice parameters and a_0, c_0 the relaxed ones. Inserting the eq. 2.4 in the eq. 2.3 results in:

$$\frac{c - c_0}{c_0} = -\frac{2C_{13}}{C_{33}}\frac{a - a_0}{a_0} = -D(x)\frac{a - a_0}{a_0}, \tag{2.5}$$

where $D(x)$ is the distortion factor [6, 62]

$$D(x) = -\frac{\epsilon_\perp}{\epsilon_\parallel} = \frac{2\nu}{1 - \nu}. \tag{2.6}$$

ν is the Poisson's ratio along [0001] for a hexagonal system related to the elastic constants by

$$\nu = \frac{C_{13}}{C_{13} + C_{33}}. \tag{2.7}$$

For determination of the chemical composition, the Vegard's Rule [63] is used. It describes how the lattice parameters (a_0, c_0) change with the chemical composition x. Neglecting the deviations, it is generally assumed to be linear for the semiconductor alloy systems:

$$a_0(x) = x a_{\mathrm{InN}} + (1-x) a_{\mathrm{GaN}}, \tag{2.8}$$

$$c_0(x) = x c_{\mathrm{InN}} + (1-x) c_{\mathrm{GaN}}, \tag{2.9}$$

where $a_0(x)$ and $c_0(x)$ are the relaxed (or bulk) in-plane and out-of-plane lattice parameters of the $In_xGa_{(1-x)}N$ compound. Similarly, the Poisson's ratio dependence on the chemical composition in a first-order approximation is [60]:

$$\nu(x) = x\nu_{\mathrm{InN}} + (1-x)\nu_{\mathrm{GaN}}. \tag{2.10}$$

The substitution of equations 2.8, 2.9 and 2.10 in the expression 2.5 results in the following function of the indium content x [60]:

$$Ax^3 + Bx^2 + Cx + D = 0, \tag{2.11}$$

where the terms A, B, C and D are as follows:

$$A = (\nu_{\mathrm{InN}} - \nu_{\mathrm{GaN}})(a_{\mathrm{InN}} - a_{\mathrm{GaN}})(c_{\mathrm{InN}} - c_{\mathrm{GaN}}), \tag{2.12}$$

$$\begin{aligned} B &= (1+\nu_{\mathrm{GaN}})(a_{\mathrm{InN}} - a_{\mathrm{GaN}})(c_{\mathrm{InN}} - c_{\mathrm{GaN}}) \\ &+ (\nu_{\mathrm{InN}} - \nu_{\mathrm{GaN}})\left[(a_{\mathrm{InN}} - a_{\mathrm{GaN}})c_{\mathrm{GaN}} + (a_{\mathrm{GaN}} - a(x))(c_{\mathrm{InN}} - c_{\mathrm{GaN}})\right], \end{aligned} \tag{2.13}$$

$$\begin{aligned} C &= (a_{\mathrm{InN}} - a_{\mathrm{GaN}})\left[(1+\nu_{\mathrm{GaN}})c_{\mathrm{GaN}} - c(x)\right] \\ &+ (c_{\mathrm{InN}} - c_{\mathrm{GaN}})\left[(1+\nu_{\mathrm{GaN}})a_{\mathrm{GaN}} - \nu_{\mathrm{GaN}}a(x)\right] \\ &+ (\nu_{\mathrm{InN}} - \nu_{\mathrm{GaN}})(a_{\mathrm{GaN}} - a(x))c_{\mathrm{GaN}}, \end{aligned} \tag{2.14}$$

$$D = (1+\nu_{\mathrm{GaN}})a_{\mathrm{GaN}}c_{\mathrm{GaN}} - \nu_{\mathrm{GaN}}a(x)c_{\mathrm{GaN}} - a_{\mathrm{GaN}}c(x), \tag{2.15}$$

where $a(x)$ and $c(x)$ are the lattice parameters of the $In_xGa_{(1-x)}N$ compound which can be measured by XRD. The analytical solution of equation 2.11 gives three different indium content x, but only one with a physical meaning, i.e. a value $0 \leq x \leq 1$ [60]. Once the indium content is determined, the lattice parameters of the relaxed InGaN, the strain components and Poisson's ratio can be calculated.

The in-plane lattice parameter of an InGaN layer or island grown on a GaN buffer layer is constrained to the in-plane lattice parameter of GaN, but relaxes partially during further growth. The in-plane strain relaxation degree R is defined as [6, 60]:

$$R = \frac{a(x) - a_{\mathrm{GaN}}}{a_0(x) - a_{\mathrm{GaN}}} \cdot 100[\%], \tag{2.16}$$

where $a(x)$ and $a_0(x)$ are measured and fully relaxed in-plane lattice parameters of $In_xGa_{(1-x)}N$.

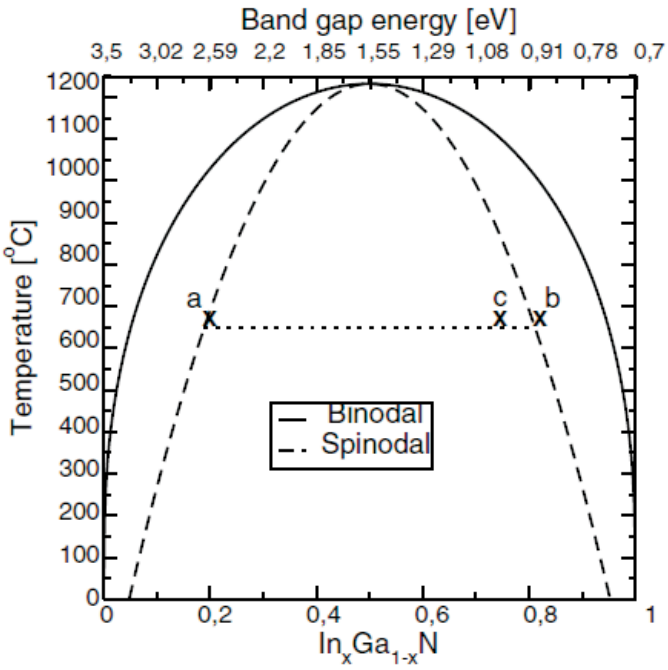

Figure 2.12 Phase diagram of InGaN. Below the spinodal line there is an unstable growth regime for $In_cGa_{1-c}N$ which leads to phase separation to a low In content $In_aGa_{1-a}N$ and a high In content $In_bGa_{1-b}N$ [68].

2.5.2 Phase separation

The difficulty to grow a high In content InGaN alloy is due to the significantly higher vapour pressure of nitrogen compared to the indium and gallium precursors [64]. The phase separation of InGaN alloy was observed by Osamura et al. in 1975 by annealing [65]. In InGaN films, the phase separation has been evidenced in the works of Singh et al. [66] and of El-Masry et al. [67]. Before these works, several authors reported on the MOVPE growth of InGaN thin films at 700°-800°C, but all with the maximum 30% of indium. Singh and co-workers have reported on phase separation in InGaN films with the presence of low and high indium concentration. In the same study it was shown that it is possible to grow InGaN with the maximum indium concentration of 81% by growing the GaN/InGaN/GaN heterostructure. El-Masry et al. observed phase separation in samples with composition $\geq$ 28% InN. Intentionally grown layer of 49% indium result in phases of 14% and 95%. This means that phase separation can be used as advantage to grow the indium-rich alloys.

The large difference of 11% in the interatomic spacing between InN and GaN gives a rise to a solid phase miscibility gap. Solid phase miscibility gap of InGaN alloys bulk crystal was modeled by Ho and Stringfellow using the thermodynamical consideration of InGaN stability by theoretical calculation of the enthalpy and the molar free energy of mixing for $In_xGa_{1-x}N$ [68]. In figure 2.12 the temperature de-

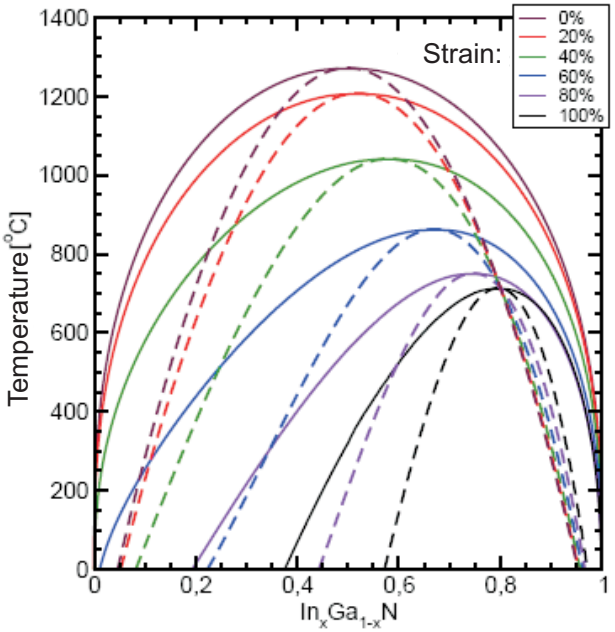

Figure 2.13 Phase diagram of InGaN for different strain states proposed by Tessarek et al [70]. The shift of the unstable region towards higher x with increasing of strain is visible.

pendence of the indium content x is presented. The binodal line (solid) represents the equilibrium InN solubility in GaN which is calculated as the composition at given temperature where $\partial G/\partial x = 0$, where G is the molar free energy. The condition for the spinodal composition (dashed) is $\partial^2 G/\partial^2 x = 0$. Above the binodal line there is a completely stable region for miscibility. Between binodal and spinodal lines is a region of metastable solubility and mixing of InGaN. Below the spinodal line is an unstable region of growth regime where phase separation occurs.

The large difference in the equilibrium lattice constants of InN and GaN result in an internal strain. The strain can strongly influence the InGaN alloy properties. Theoretical models for strained InGaN films show the suppression of the phase separation in $In_xGa_{1-x}N$ [16, 55, 69]. Due to elastic strain energy, the internal energy of mixing is remarkably reduced [16]. The effect of phase separation suppression is more pronounced for more In-rich films. This is again confirmed for zinc-blende ternary group(III)-nitride alloys [69]. Recent studies have shown that the unstable region shifts toward higher indium content with increasing strain [70]. Figure 2.13 shows the pairs of binodal and spinodal curves for different strain states of the InGaN. For a fully strained InGaN layer, the unstable region is significantly reduced.

Energy gap and optical properties are also influenced by spontaneous spinodal decomposition [55]. O'Donnell and co-workers report on complete insolubility of InN in GaN and argue on existing of almost pure InN nanocrystalline inclusions in which the quantum confinement leads to a dominant emission band in the blue or green

spectral region [56].

Studies by XRD reciprocal space mapping confirmed multi-phase InGaN with different In content and different strain relaxation [62, 71, 72], but up to now there is no XRD study confirming the multi-phase in InGaN islands.

2.5.3 InGaN Quantum Dots

Basically, the name "quantum dots" is used for the 3D island-like nanostructures of the sizes that shows a quantum confinement effect of the charge carriers leading to a narrow bandwith of the output light close to form a discrete line in the energy spectrum. This phenomenon is widely used in other semiconductor systems such as group(III)-arsenides (InGaAs QDs), group(III)-phosphides, SiGe/Si and group(II)-group(IV) materials. Research on nitride based quantum dots is, up to now, focused on AlGaN/GaN QDs, on buried GaN in AlN capping layer [73] and on InGaN quantum dots grown on GaN. It was found that the strain driven forming of the islands is not always the case for nitrides [74].

In this thesis, the focus will be on the freestanding and overgrown InGaN quantum dots. There are several methods to grow InGaN QDs, by Stranski-Krastanow, by segregation method, by nano-droplet technique etc. The chosen method strongly influences structure properties of the quantum dots. The mechanism of the islands formation is not yet understood as well as influence of the structure on the optical properties.

The deeper investigation of the relationship between the shape and morphology of InGaN quantum dots and the growth conditions will be presented in the discussion of the AFM results in the section 7.2.9. The results of the X-ray scattering study on the real structure, the indium content, the strain relaxation and strain distribution in InGaN quantum dots will be discussed in sec. 7.5 with respect to the proposed phase separation model.

Quantum Dots

A history of quantum mechanical effects in epitaxial semiconductor low-dimensional systems is closely related to the development of growth techniques and technologies to fabricate thin epitaxial films having the nanostructures of dimensions that can cause space confinement of the charge carriers (electrons and holes) showing the quantum effect in its electrical and optical properties. In the beginning of 1970's, molecular beam epitaxy was developed to the state of producing thin layers with hight of the order of 1 nm having the abrupt interfaces. This enable the research on the quantum states of confined carriers in very thin heterostructure quasi-2D layers [75, 76]. This pioneer work of Dingle and co-workers on 2D systems is followed by Arakawa, Kayanuma, Wang among the others. Research on one-dimensional (1D) systems such as chain-like structures and nanowires become important after [77]. Theoretical and

experimental work on quasi zero-dimensional (0D) systems such as colloids, clusters and quantum dots came in the focus of scientific interest because the possibility of the space confinement in all three directions [78].

The quantum confinement is characterized by several consequences: (i) the fundamental gap exhibits a blue shift, (ii) in nanocrystallites the filled and the empty states become quantized, (iii) optical dipole transitions across the fundamental gap become allowed. All three effects increase with decreasing size of the crystallites [79].

When the motion of electron is confined in all three directions, we have zero-dimensional system (0D) where the energy spectrum is discrete and the DOS is a series of δ-function peaks (fig. 2.7 0D):

$$E = {E_x}^i + {E_y}^j + {E_z}^k \tag{2.17}$$

with i is an integer. Dimensions of the quantum dot are about De Broglie wavelength expressed as:

$$\lambda_{deBroglie} = \frac{2\pi\hbar}{\sqrt{3m^* k_B T}} \tag{2.18}$$

where the product of Boltzmann constant k_B and the temperature T represents the thermal energy of the system. Density of electronic states depending on the energy changes with the space confinement, as motion of the electrons are restricted, and for the quantum dot it can be expressed as:

$$D_{0D}(E) = \frac{2}{L_z L_y L_x} \sum_{l,m,n} \delta(E - E_{l,m,n}). \tag{2.19}$$

The energy spectra of the quantum dots is represented by atomic-lines-like delta-functions. More on theoretical consideration of the quantum effects in low-dimensional systems is given in the appendix B.

More detailed description of the electrical and optical properties of quantum dots will not be considered here and can be found elsewhere [80]. We will focus on the growth and structural properties of quantum dots hopping that research in this field could help to answer on how does the structure of quantum dot affect its opto-electrical properties.

The Growth of Quantum Dots

Fabrication of the quantum dots often employs a self-assembling using different growth modes. The growth modes of epitaxy in conditions close to the thermodynamic equilibrium are as follows: Frank-van der Merwe-growth, Stranski-Krastanow-growth and Volmer-Weber-growth. Difference between the growth modes is in the relation between the adsorbate surface and interface tension and the substrate surface tension. If the sum of the adsorbate surface tension σ_{a} and the adsorbate-substrate interface tension σ_{as} is smaller than a substrate surface tension σ_{s}, then the growth is two-dimensional (2D-growth) or so-called "layer-by-layer" (Frank-van der Merwe)

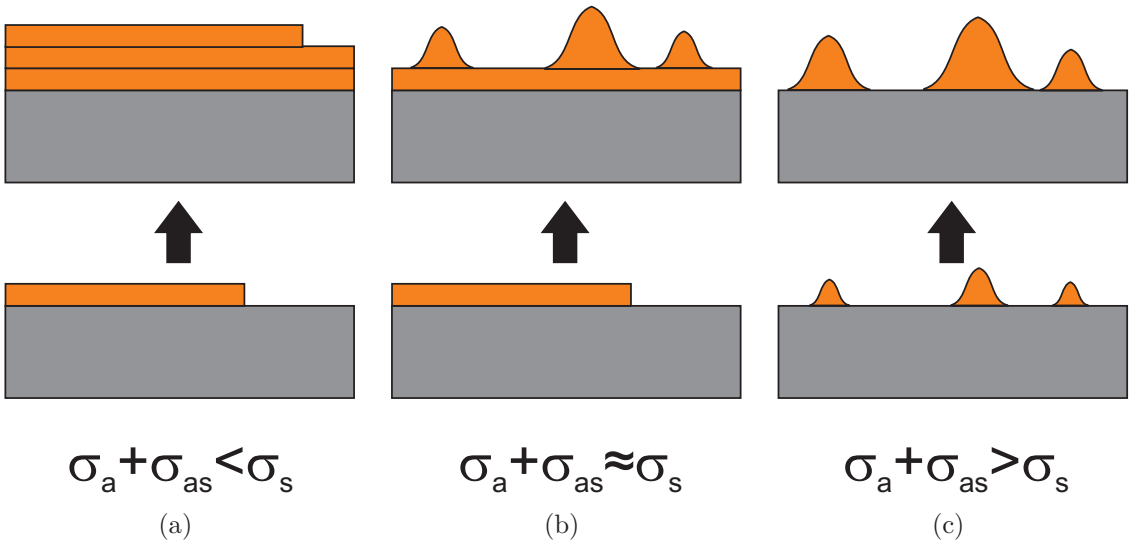

Figure 2.14 Growth modes of epitaxy in thermodynamic equilibrium: (a) Frank-van der Merwe (b) Stranski-Krastanow and (c) Volmer-Weber.

(fig. 2.14 (a)). In Stranski-Krastanow growth mode (fig. 2.14 (b)), the sum of the tensions related to the adsorbate is approximately equal to the substrate surface tension. After the critical thickness of the wetting layer, the growth continues with the islands formation (3D-growth). Fig. 2.14 (c) shows the Volmer-Weber growth where 3D-growth starts from the very beginning of deposition, with the nucleation of islands, due to the sum of the adsorbate surface and interface tension being bigger than the substrate surface tension. Only Stranski-Krastanow and Volmer-Weber growth modes can result in dots.

In the growth of quantum dots might be that the thermodynamic equilibrium is not satisfied but limited by the surface kinetics. For the growth of InGaN quantum dots, a transition from 2D to 3D growth has been identified, at high growth rates, which does not involve a standard Stranski-Krastanow growth mode [74].

The growth of InGaN quantum dots studied in this thesis does not fit to any of these models. Clearly, the islands are formed from the deposited material with the thickness lower than a critical (Stranski-Krastanow excluded). The islands are formed from the transition from 2D-growth to 3D-growth, i.e. the nucleation layer transforms itself into two type of islands (Volmer-Weber excluded). Therefore, their growth will be discussed (sec. 7.5) from the aspect of the phase separation with binodal and spinodal decomposition.

Chapter 3

X-ray Scattering From Thin Films and Nanostructures

The X-ray scattering is one of the most important methods for characterization of thin films and nanostructures such as quantum dots, quantum wires and quantum wells. By using the X-ray scattering, the structure of thin films, morphology, strain in the material, electron density and many other properties can be determined. The X-rays can interact differently with matter, can be absorbed and can be elastically or inelastically scattered. In this chapter we will focus on the principles of elastic X-ray scattering. First of all, interaction of X-rays with matter will be described. Then, X-ray reflectivity, a robust method which use a total external reflection of X-rays will be described. Further, the elements of kinematical diffraction theory will be summarized. The calculus will be, later in this thesis, used for theoretical explanations and simulations of measured diffraction profiles. At last, the scattering geometries will be considered as a preparation for the X-ray scattering experiments which will be performed on thin films and InGaN quantum dots.

3.1 Interaction of X-rays with Matter

X-rays are electromagnetic waves with the wavelength in the region of Ångström (10^{-10}m) [81]. This wavelength corresponds to dimensions of an atom, atomic plane interspacing in the crystals and dimensions of the nanostructures what gives a rise to investigate them by use of X-rays. The electric field of a monochromatic plane wave of X-rays with photon energy $\hbar\omega$ can be written as

$$\mathbf{E}(\mathbf{r}, t) = \mathbf{E}_0 e^{\mathrm{i}(\mathbf{K}\cdot\mathbf{r}-\omega t)}. \tag{3.1}$$

The length of the wave vector $|\mathbf{K}|$ in vacuum is given by $|\mathbf{K}| = \frac{\omega}{c} = \frac{2\pi}{\lambda}$ where c is the velocity of light. Inside a material this length changes to $|\mathbf{k}| = n|\mathbf{K}|$, where n is refraction index. X-rays (or Röntgen radiation) can interact with matter in different ways.

Incident beam of X-rays can be **absorbed** by material resulting with the weaker outgoing beam. This process is described by exponential reduction of incident intensity I_0 while propagating through the sample: $I(z) = I_0 e^{-\mu z}$ where $I(z)$ is intensity of X-rays depending on the sample thickness z and μ is absorbtion coefficient of the sample material at certain energy of X-rays. X-ray absorption can undergo several different processes: photoelectric absorption, fluorescent X-ray emission and Auger electron emission.

Incoming beam can also be **refracted** or **reflected**. Every media has its own refractive index, which is equal to one for vacuum by definition. For X-rays, refractive index is expressed as follows: $n = 1 - \delta + \mathrm{i}\beta$ where δ is related to the electron density and is in the order of 10^{-5} and β is even much smaller and this coefficient is related to the absorption of material. From previous one can see that refractive index for X-rays is close to unity but little bit less than one. Therefore, X-rays can undergo *total external reflection* if the incident angle is smaller than the critical one ($\alpha_c = \sqrt{2\delta}$) (fig. 3.1). That means that the incident X-ray beam is reflected by material surface. More words about X-ray reflectivity will be in the next section.

Incident X-ray beam can be **diffracted**. Elementary, diffraction of X-rays from a crystal lattice is given by Bragg's Law: $n\lambda = 2dsin\theta$ where n is an integer, λ is the X-rays wavelength, d is atomic net plane spacing and θ is an angle between the incident X-ray beam and the plane of diffraction, so called *Bragg angle*. More on this will be in the sec. 3.3.

By elastic scattering we consider the event of interaction of electric field of X-rays with the electrons in the material which emit scattered wave where the wavelength of the incident and of the scattered wave is essentially the same in the classical description. In quantum mechanical description, the incident X-ray photon has a momentum of $\hbar\mathbf{K}$ and an energy of $\hbar\omega$. Momentum transferred in the elastic scattering event is $\hbar\mathbf{Q} = \hbar\mathbf{K}' - \hbar\mathbf{K}$ where $\hbar\mathbf{K}'$ and $\hbar\mathbf{K}$ are final and initial photon momenta, respectively. $\mathbf{Q}$ is called *wavevector transfer* or *scattering vector* and it describes elastic scattering process. $\mathbf{Q}$ is usually in units of $\mathrm{\AA}^{-1}$.

To describe interaction of X-rays with matter, one should consider combination of Maxwell equations of propagating the electromagnetic wave together with the material equations. Maxwell equations are as follows [82]:

$$\mathbf{rotE} = -\frac{\partial \mathbf{B}}{\partial t} \qquad \mathbf{rotH} = \frac{\partial \mathbf{D}}{\partial t} + \mathbf{j} \qquad \mathbf{divD} = \rho \qquad \mathbf{divB} = 0. \tag{3.2}$$

Material equations describe the magnetic and electric field in the medium:
$\mathbf{B} = \mu_0\mu_r\mathbf{H}$, $\mathbf{D} = \epsilon_0\epsilon_r\mathbf{E}$ and $\mathbf{j} = \hat{\sigma}\mathbf{E}$. Combining the first two of Maxwell equations (3.2) and the first of material ones, the result for the wavefield inside material ($\mathbf{j} = 0$) is as follows:

$$\mathbf{rot}\,\mathbf{rotE}\,(\mathbf{r}, t) = -\mu_0\mu_r \frac{\partial^2 \mathbf{D}(\mathbf{r}, t)}{\partial t^2}. \tag{3.3}$$

Electric field $\mathbf{E}$ and electric displacement $\mathbf{D}$ can be expressed as product of components dependent just on the position (radius-vector) and just on time:

$$\mathbf{E}\left(\mathbf{r},t\right)=\mathbf{E}(\mathbf{r})e^{-\mathrm{i}\omega t}\qquad\mathbf{D}\left(\mathbf{r},t\right)=\mathbf{D}(\mathbf{r})e^{-\mathrm{i}\omega t}\tag{3.4}$$

and after simple calculus using the fact that $\epsilon_0\mu_0=\frac{1}{c^2}$, equation (3.3) becomes:

$$\mathbf{rot}\,\mathbf{rot}\mathbf{E}\left(\mathbf{r}\right)=\mathbf{K}^2\mu_r(\mathbf{r})\epsilon_r(\mathbf{r})\mathbf{E}(\mathbf{r}).\tag{3.5}$$

If ϵ_r is varying slowly over the wavelength λ and $\mathbf{Q}\ll\mathbf{k}$ from previous we got wave equation for the medium, so-called *Helmholtz equation*:

$$\left(\triangle+\mathbf{K}^2\right)\mathbf{E}\left(\mathbf{r}\right)=\hat{\mathbf{V}}(\mathbf{r})\mathbf{E}(\mathbf{r})\tag{3.6}$$

where $\hat{\mathbf{V}}$ is an operator of scattering potential [82]. The Helmholtz equation (eq. 3.6) can be separated into the vacuum wave equation:

$$\left(\triangle+\mathbf{K}^2\right)\mathbf{E}\left(\mathbf{r}\right)=0\tag{3.7}$$

and the contribution by a scattering potential in the medium:

$$\hat{\mathbf{V}}=\mathbf{K}^2(1-\epsilon_r(\mathbf{r}))=-\mathbf{K}^2\chi(\mathbf{r})\tag{3.8}$$

where $\chi(\mathbf{r})=\epsilon_r(\mathbf{r})-1$ is electrical susceptibility (polarizability) of the medium which is directly proportional to the electron density. One of the exact solutions of Helmholtz equation, using *Green function* $G(\mathbf{r},\mathbf{r}')=-\frac{1}{4\pi}\frac{e^{\mathrm{i}|r-r'|K}}{|\mathbf{r}-\mathbf{r}'|}$ is:

$$\mathbf{E}\left(\mathbf{r}\right)=\mathbf{E}_{\mathrm{inc}}(\mathbf{r})+\int d\mathbf{r}'G(\mathbf{r},\mathbf{r}')\mathbf{V}(\mathbf{r}')\mathbf{E}(\mathbf{r}')\tag{3.9}$$

which is representing the outgoing spherical wave in vacuum, while incident wave is a plane wave $\mathbf{E}_{\mathrm{inc}}=\mathbf{E}_0e^{\mathbf{iKr}}$. This can be solved further by iterations. If it stops after the first iteration, this is called Born approximation of the first order by replacing the true wavefield with the incident one: $\mathbf{E}(\mathbf{r}')\approx\mathbf{E}_{\mathrm{inc}}(\mathbf{r}')$. Then, the equation (3.9) becomes:

$$\mathbf{E}\left(\mathbf{r}\right)=\int d\mathbf{r}'\left(\frac{\mathbf{K}^2\chi(\mathbf{r}')}{4\pi}\right)e^{\frac{\mathrm{i}|r-r'|K}{|\mathbf{r}-\mathbf{r}'|}}\mathbf{E}_{\mathrm{inc}}(\mathbf{r}').\tag{3.10}$$

Using the connection between susceptibility and electron density :

$$1-\epsilon_r=-\chi=\frac{4\pi r_0}{\mathbf{K}^2}\rho\tag{3.11}$$

finally we have the wave equation so-called "diffraction integral":

$$\mathbf{E}\left(\mathbf{r}\right)=\int d\mathbf{r}'\left(-r_0\rho(\mathbf{r})\right)e^{\frac{\mathrm{i}|r-r'|K}{|\mathbf{r}-\mathbf{r}'|}}\mathbf{E}_{\mathrm{inc}}(\mathbf{r}').\tag{3.12}$$

where r_0 is the scattering length of each electron and ρ is the electron density. Previous equation is valid just in the Fraunhofer approximation or far-field diffraction where the square of the size D of scattering object is much smaller then product of the X-rays wavelength λ and distance object detector R ($D\ll\sqrt{\lambda R}$).

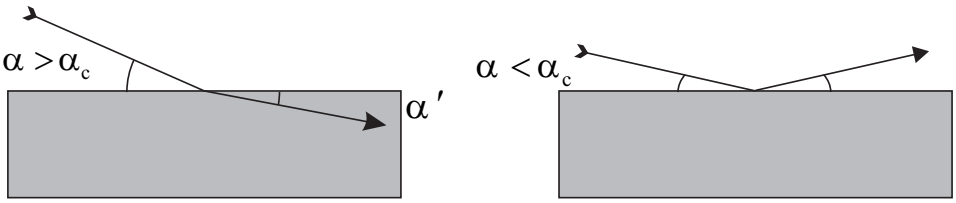

Figure 3.1 Total external reflection of X-rays from the material surface.

3.2 X-ray Reflectivity

If X-rays come with small incident angle, than, due to the fact that the refractive index of materials for X-rays is smaller then one, they can be almost completely reflected from the sample surface. This phenomena is called *total external reflection*. Angle which define when X-rays start to penetrate into material is named a critical angle of total external reflection and depends on the material and on the X-rays wavelength. X-ray reflectivity (XRR) is a method to measure the scattering intensity close to the origin of the reciprocal space (000). With other words it is insensitive to crystal structure, but is very sensitive to the surface morphology. Also, XRR has ability to probe the buried interfaces of multilayered film as well as to study correlation between them.

The expression of refractive index is as follows:

$$n = 1 - \delta + i\beta. \tag{3.13}$$

δ is related to the electron density through the expression:

$$\delta = \frac{2\pi\rho r_0}{k^2} \tag{3.14}$$

where ρ is the electron density (in [el./Å^3]), $r_0 = 2.82 \times 10^{-5}$Å is the scattering length for each electron and $k = 2\pi/\lambda$ is the wavevector of the X-ray radiation which has the wavelength λ. Imaginary part of the refractive index is dependent on the material absorption coefficient:

$$\beta = \frac{\mu}{2k}. \tag{3.15}$$

In the terms of atomic density and atomic scattering length, δ becomes:

$$\delta = \frac{2\pi\rho_a f^0(0) r_0}{k^2}. \tag{3.16}$$

Dispersion corrections to atomic scattering length $f(\mathbf{Q})$ are neglected and $\mathbf{Q} = 0$. A critical angle depends on the electron density and on the energy of the X-rays:

$$\alpha_c = \frac{\sqrt{4\pi\rho r_0}}{k}. \tag{3.17}$$

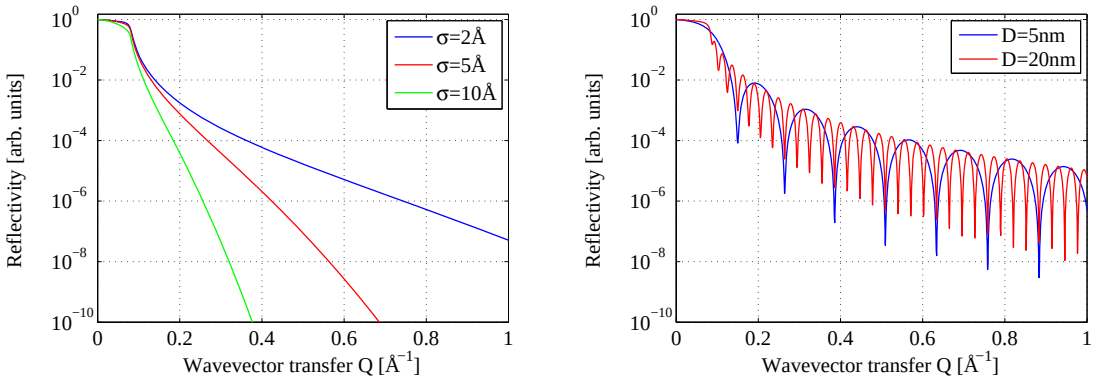

(a) (b)

Figure 3.2 The X-ray reflectivity curves of thin film with (a) different surface roughness σ and (b) different top layer thickness D.

For the rough surface, the intensity of the X-ray reflectivity is reduced by a factor of

$$\exp^{-\sigma^2 q_z^2}, \tag{3.18}$$

with σ being the root mean square (r.m.s.) roughness. Therefore, the surface roughness influences the slope of the X-ray reflectivity curve. Figure 3.2 (a) shows the reflectivity curves of the same material with different surface roughness of 2Å(blue), 5Å(red) and 10Å(green). The intensity drops faster with increasing the roughness. Reflectivity curves with different top layer thickness are shown in figure 3.2 (b). The thickness oscillations, so-called "Kiessig fringes", are well pronounced. A period of oscillations is directly related to a film thickness D through:

$$t = \frac{2\pi}{D}. \tag{3.19}$$

Correction of measured intensity due to the larger beam spot ("footprint") than the sample size

In the X-ray reflectivity measurements, due to the grazing incidence of X-rays, the footprint of the beam f is often larger than the longitudinal dimension l of the sample and only a part of the incident beam is reflected. Therefore, the experimental data need to be corrected. The footprint f is:

$$f = \frac{d}{\sin\theta}, \tag{3.20}$$

where d is the vertical size of the X-ray beam (fig. 3.3). For $\theta < \theta_L$, the measured

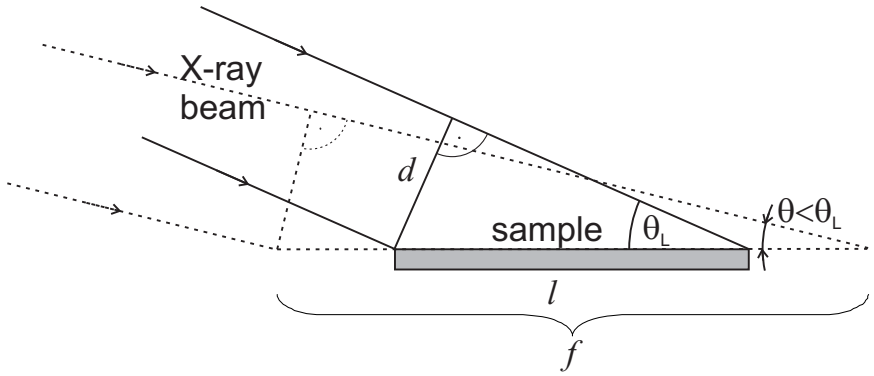

Figure 3.3 The footprint of the incident beam on the sample in the X-ray reflectivity measurements. The dashed line represents the case of the footprint being larger than the sample size for incident angles smaller than θ_{L}. The limit case is shown by solid line.

intensity, I_{exp}, is lower than the incident intensity I_0:

$$I_{\mathrm{exp}} = I_0 \cdot \frac{l \sin\theta}{d}. \tag{3.21}$$

The corrected intensity is then:

$$I_{\mathrm{corr}} = I_{\mathrm{exp}} \cdot \frac{f}{l} = I_{\mathrm{exp}} \cdot \frac{d}{l \sin\theta}. \tag{3.22}$$

The experimental data must be corrected up to the angle when the footprint equals the size of the sample:

$$\theta_{\mathrm{L}} = \arcsin\frac{d}{l}. \tag{3.23}$$

The case of the limit is shown in the figure 3.3 (solid line).

3.3 Kinematical Diffraction

Diffraction of X-rays from crystals, thin films, crystalline and polycristalline nano-objects is one of the most used methods in characterization of their structure. As was mentioned before, the wavelength of X-ray radiation corresponds to the dimensions of crystal unite cell parameters and distances between atomic planes investigated.

In the processes described by kinematical diffraction, scattering is considered to be weak what implies that multiple scattering effects can be neglected. For the sample structures investigated in this thesis by X-ray diffraction kinematical approximation is satisfactory: thin GaN films with different but huge dislocation densities (6.1) and InGaN quantum dots with quite nonuniform size and orientation (7.1.1) are far from perfect crystals, therefore the dynamical diffraction approach is not needed.

In the case of X-ray diffraction, scattering vector $\mathbf{Q}$ has nonzero value and must be close to the reciprocal lattice point $\mathbf{G}$ to fulfill the Bragg condition. The magnitude of the scattering vector is related to the scattering angle θ of X-rays with the wavelength λ by:

$$|\mathbf{Q}| = \left(\frac{4\pi}{\lambda}\right) \sin\theta. \tag{3.24}$$

Reciprocal lattice point is determined by Miller indices (hkl) and by reciprocal lattice parameters.

Scattering Amplitude

The intensity of diffracted X-ray beam is the result of the scattering from many electrons in the sample material. Let us summarize the facts about the scattering amplitude and intensity from the simplest possible system to more complex. For this we recall total scattering length of the scattering from an atom to express the atomic form factor in units of Thomson scattering length $(-r_0)$:

$$f^0(\mathbf{Q}) = \int \rho(\mathbf{r}) \mathbf{e}^{\mathrm{i}\mathbf{Q}\cdot\mathbf{r}} \mathrm{d}\mathbf{r} \tag{3.25}$$

which is equal to atomic number Z for $\mathbf{Q} \to 0$ and equal 0 for $\mathbf{Q} \to \infty$. The X-ray diffraction is an averaging method which intensity is statistically averaged from the contribution of all electrons acting in the scattering process. With other words, the phase information is lost. The orientational average of the phase factor is [81]:

$$\langle e^{\mathrm{i}\mathbf{Q}\cdot\mathbf{r}} \rangle_{\text{orient.av.}} = \frac{\sin(Qr)}{Qr} \tag{3.26}$$

If the absorption and inelastic scattering due to atomic excitations is taken into account, the atomic form factor is:

$$f(\mathbf{Q}, E) = f^0(\mathbf{Q}) + f'(E) + \mathrm{i}f''(E) \tag{3.27}$$

where f' and f'' are real and imaginary parts of dispersion corrections to f^0.

The scattering amplitude from a molecule can be written as:

$$S^{mol}(\mathbf{Q}) = \sum_{\mathbf{r}_j} f_j(\mathbf{Q}) e^{\mathrm{i}\mathbf{Q}\cdot\mathbf{r}_j} \tag{3.28}$$

where f_j is the form factor of the j^{th} atom in the molecule.

Most complex is the scattering from a crystal lattice. The crystal lattice in three dimensions is given by a set of vectors of the form [81, 83, 84]:

$$\mathbf{R}_\mathbf{n} = u\mathbf{a}_1 + v\mathbf{a}_2 + w\mathbf{a}_3. \tag{3.29}$$

$\mathbf{R_n}$ is a *direct lattice vector* with $\mathbf{a}_1, \mathbf{a}_2, \mathbf{a}_3$ being the crystal lattice constants and u, v, w integers. The vectors of crystal lattice constants define the *unite cell* of the crystal. The *reciprocal lattice vector* is defined as:

$$\mathbf{G} = h\mathbf{a}_1^* + k\mathbf{a}_2^* + l\mathbf{a}_3^* \tag{3.30}$$

where the integers h, k, l are the *Miller indices* which are used to notify the family of scattering atomic planes in the crystal, that closest to the origin has intercepts $(a_1/h, a_2/k, a_3/l)$ on the axes $\mathbf{a}_1, \mathbf{a}_2, \mathbf{a}_3$ [81]. End of the reciprocal lattice vector is called *reciprocal lattice point*. Relation between the unit cell and the reciprocal space is given by:

$$\begin{aligned} \mathbf{a}_1^* &= \frac{2\pi}{V_{\mathrm{uc}}}\mathbf{a}_2 \times \mathbf{a}_3, \\ \mathbf{a}_2^* &= \frac{2\pi}{V_{\mathrm{uc}}}\mathbf{a}_3 \times \mathbf{a}_1, \\ \mathbf{a}_3^* &= \frac{2\pi}{V_{\mathrm{uc}}}\mathbf{a}_1 \times \mathbf{a}_2, \end{aligned} \tag{3.31}$$

where V_{uc} is the volume of the unit cell. Reciprocal space (wavevector space) is spanned by reciprocal vectors which fulfill $\mathbf{a}_i \cdot \mathbf{a}_j^* = 2\pi\delta_{ij}$ whit δ_{ij} being the Kronecker delta ($\delta_{ij} = 1$ if $i = j$ and equal zero otherwise). The scalar product of the reciprocal and direct lattice vector is an integer and equal to:

$$\mathbf{G} \cdot \mathbf{R_n} = 2\pi\left(hu + kv + lw\right). \tag{3.32}$$

The length of the reciprocal lattice vector is equal to:

$$|\mathbf{G}_{hkl}| = \frac{2\pi}{d_{hkl}} \tag{3.33}$$

where d_{hkl} is a distance between diffraction planes. $\mathbf{G}_{hkl}$ is perpendicular to the planes $\{h\ k\ i\ l\}$ in the direct lattice [81]. The Miller index notation of hexagonal crystals is usually in the form $(h\ k\ i\ l)$ with $i = -(h + k)$. For example, (110) is denoted as $(11\bar{2}0)$. X-ray diffraction requires that scattering vector is equal to the reciprocal lattice vector (Laue condition):

$$\mathbf{Q} = \mathbf{G} \tag{3.34}$$

which is equal to the Bragg's Law:

$$\lambda = 2d\sin\theta \tag{3.35}$$

having in mind dependence of the scattering vector on the radiation wavelength and on the incidence angle of X-ray beam (eq. 3.24).

Scattering amplitude for the crystal consists of two terms:

$$S^{crystal}(\mathbf{Q}) = \overbrace{\sum_{\mathbf{r}_j} S_j(\mathbf{Q}) e^{i\mathbf{Q}\cdot\mathbf{r}_j}}^{\text{unit cell structure factor}} \overbrace{\sum_{\mathbf{R_n}} e^{i\mathbf{Q}\cdot\mathbf{R_n}}}^{\text{lattice sum}} \tag{3.36}$$

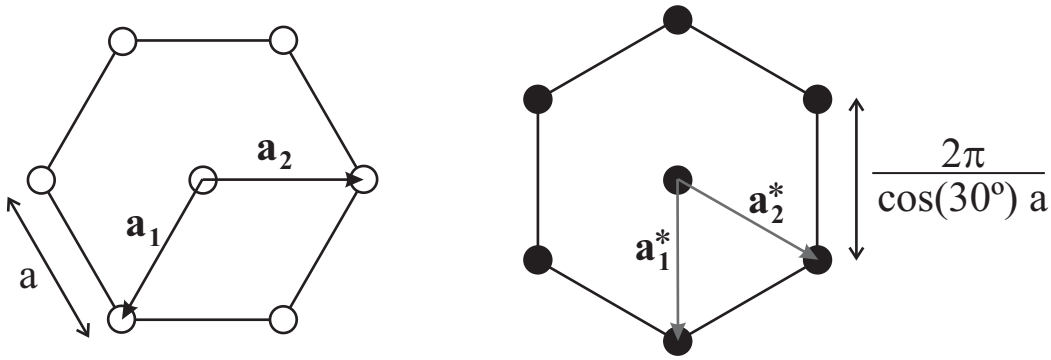

Figure 3.4 The basis of hexagonal unit cell in real space (left) and corresponding reciprocal unit cell in wavevector space (after [81]).

The *unit cell structure factor* is the scattering amplitude from molecules or atoms which form the unit cell of a crystal and the *lattice sum* comes from the phases of huge number of the unit cell in the sample of crystalline material which makes scattering amplitude non-vanishing only if Laue condition 3.34 is fulfilled. Lattice sum is in the literature also named a *shape function*.

Since GaN thin films are mostly grown as a wurtzite crystal, and used in this thesis, the basis of hexagonal unit cell in real space and corresponding reciprocal unit cell are shown in figure 3.4. Specific of the hexagonal unit cell is that lateral basis constants are of the same length $|a|$ forming an angle of 120°, while vertical unit cell constant c is perpendicular to both of them. For a hexagonal crystal, the distance d_{hkl} between the diffraction planes defined by Miller indices is related to lattice parameters by:

$$\frac{1}{d_{hkl}^2} = \frac{4(h^2+k^2+hk)}{3a^2} + \frac{l^2}{c^2}. \tag{3.37}$$

Inserting the eq. 3.37 in eq. 3.35 results in relation between the Bragg angle θ of a certain reflection (hkl) and the lattice parameters:

$$\sin\theta = \frac{\lambda}{2d} \quad \Rightarrow \quad \theta = \arcsin\left(\frac{\lambda}{2}\sqrt{\frac{4\,(h^2+k^2+hk)}{3a^2} + \frac{l^2}{c^2}}\right) \tag{3.38}$$

The structure factor of a hexagonal GaN unit cell is according to the positions of atoms in the unit cell (sec. 2.1):

$$S_{\mathrm{GaN}}^{\mathrm{u.c.}} = f_{\mathrm{Ga}}\left(1 + e^{-2\pi\mathrm{i}\left(\frac{2h}{3}+\frac{k}{3}+\frac{l}{2}\right)}\right) + f_{\mathrm{N}}\left(e^{-2\pi\mathrm{i}\cdot\frac{3l}{8}} + e^{-2\pi\mathrm{i}\left(\frac{2h}{3}+\frac{k}{3}+\frac{7l}{8}\right)}\right) \tag{3.39}$$

where f_{Ga} and f_{N} are the atomic form factors of Ga and N atoms. Combination of Miller indices defines the intensity of reflection. The allowed reflections of diffraction from hexagonal crystal systems are for any even l and $h + 2k \neq 3n$, while forbidden are with $h + 2k = 3n$ and any with odd l, where n is an integer. Figure 3.5 shows

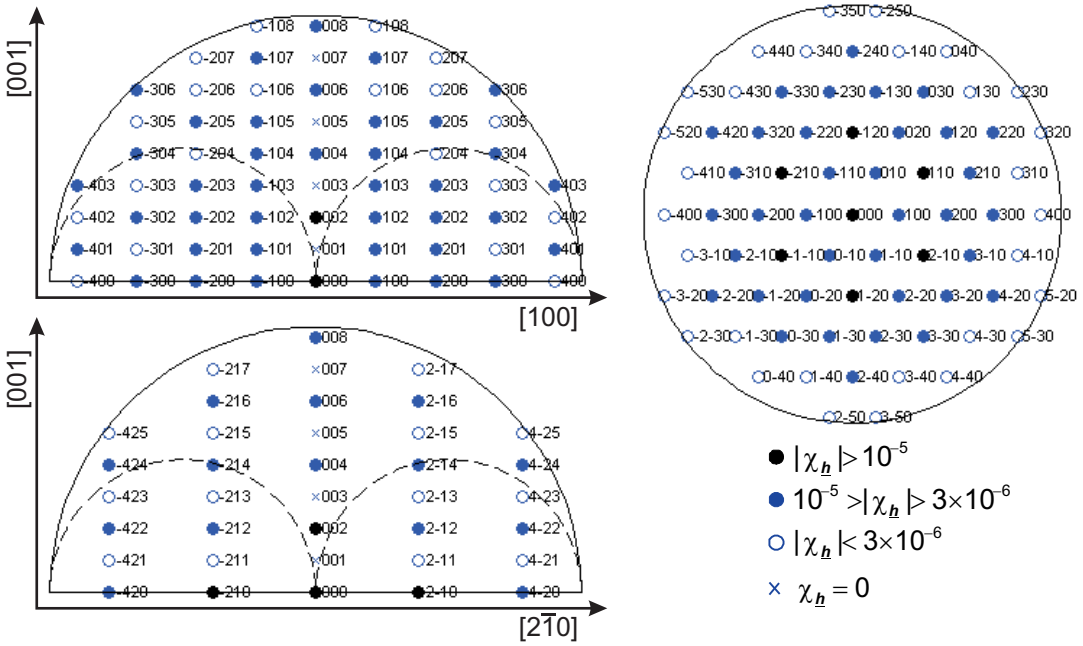

Figure 3.5 Reflections from c-plane GaN crystal for the synchrotron radiation energy of 10keV. Reciprocal space plane spanned by [100] and [001] (left-top) and the plane spanned by [2$\bar{1}$0] and [001] (left-bottom). Right: the in-plane reflections in the plane perpendicular to [001] [85].

the reflections from c-GaN crystal for the synchrotron radiation energy of 10keV. For the calculation of scattering intensities, the electric susceptibility was used. Electric susceptibility is directly proportional to the electron density by (using the eq. 3.11):

$$\chi(\mathbf{r}) = -\frac{\lambda^2 \mathbf{r_0}}{\pi}\rho(\mathbf{r}). \tag{3.40}$$

The intensity of the reflections are marked differently. Very intense reflections are marked black, coming from the atomic planes with the biggest scattering potential, medium intense are marked gray, weak reflections with the open circles and forbidden by the crosses. The dimension of the circles is directly proportional to the used X-rays energy. The reflections accessible for the Bragg diffraction are inside the circle (solid) with the radius of $\frac{4\pi}{\lambda}$ and outside of the circles (dashed) with the radius of $\frac{2\pi}{\lambda}$, where λ is the wavelength (see sec. 3.3.3).

Scattering Intensity

Intensity of the scattering is directly proportional to the squared absolute value of the scattering amplitude:

$$I \propto |S(\mathbf{Q})|^2 \tag{3.41}$$

X-ray scattering from thin films and nanostructures is a result of diffraction on many incoherent parts of the crystal which usually have volume defects and imperfections due to epitaxial growth. X-ray scattering is an averaging characterization method. For epitaxially grown thin films, there is a sharp peak component coming from the substrate and a broad intensity distribution as a result of the superposed scattering intensities coming from different parts of the film (fig. 3.6). Peak width is related to the film crystalline quality, the narrower is the peak, better is the crystalline quality. Kinematical description of the scattering intensity from the "substrate plus film" system for incoherent superposition is expressed as:

$$I(\mathbf{q}) \propto \left| S^{\text{u.c.}}_{\text{substrate}}(\mathbf{q}) \cdot \frac{1}{1 - e^{\mathrm{i}\mathbf{q}c_1}} \right|^2 + \left| S^{\text{u.c.}}_{\text{film}}(\mathbf{q}) \cdot \frac{1 - e^{\mathrm{i}\mathbf{q}D}}{1 - e^{\mathrm{i}\mathbf{q}c_2}} \cdot e^{-\frac{(\mathbf{q}\sigma)^2}{2}} \right|^2 \tag{3.42}$$

where q is the *reduced scattering vector* defined as a difference between the scattering vector and the reciprocal lattice vector:

$$\mathbf{q} = \mathbf{Q} - \mathbf{G} \tag{3.43}$$

Since substrate and film may have different lattice constants, the reciprocal lattice vectors with an amplitude of $\mathbf{G} = 2\pi\sqrt{4\left(h^2 + k^2 + hk\right)/3a^2 + (l/c)^2}$ are different and therefore we may have two different reduced scattering vectors. In the previous equation, a smooth substrate with a lattice constant c_1 and a thin film of a thickness D having a lattice constant c_2 are considered. The damping factor $e^{-\frac{(\mathbf{q}\sigma)^2}{2}}$ is due to the roughness. The signals from the substrate and the film can be also coherently

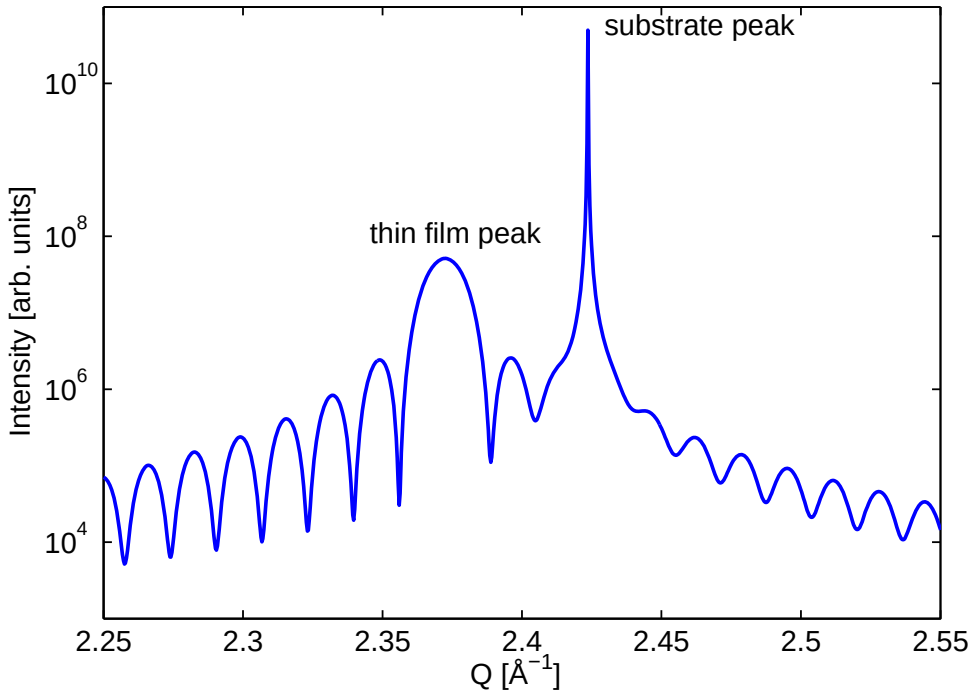

Figure 3.6 Calculated diffraction (0002) peaks of thin $In_{0.22}Ga_{0.78}N$ film with thickness of 38.3nm and r.m.s. roughness of 0.5nm grown on the GaN substrate (assumed to be smooth).

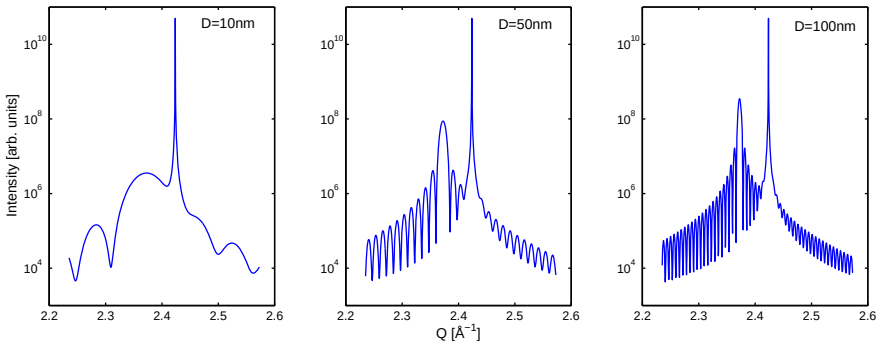

Figure 3.7 The effect of the film thickness on the diffraction intensity profile. Calculated diffraction profile of the same sample structure as in the fig. 3.6, just with different thin film thickness, D: 10nm (left), 50nm (middle) and 100nm (right).

superposed if there is a phase correlation between two different scattered waves. As an example of kinematical diffraction, figure 3.6 shows the plot of theoretically calculated scattering intensity (eq. 3.42) from InGaN thin film grown on a GaN substrate for the (0002) reflection. The concentration of In in the film is 22%, film thickness is 38.3nm and root mean square roughness is 0.5nm, while roughness of the substrate was assumed to be smooth. Oscillations on the diffraction curve are coming from the thin film thickness. Diffraction peaks are well separated due to different lattice constant in the scattering direction.

The effect of thin film thickness is shown on the figure 3.7. The finite film thickness gives rise to intensity oscillations with the period:

$$T = \frac{2\pi}{D} \tag{3.44}$$

The bigger is the film thickness, shorter is the oscillation period in reciprocal space as shown for film with the thickness 10nm (3.7 left), 50nm (3.7 middle) and 100nm (3.7 right). All other parameters of the film and of the substrate were kept the same.

The effect of the interface roughness on diffraction intensity is shown in the figure 3.8. The root mean square interface roughness was tuned from being completely smooth, $\sigma = 0$ (left), through $\sigma = 10nm$ (middle) to the $\sigma = 50nm$ (right). The intensity of the thickness oscillations on both sides of the central maximum is reduced by the damping factor mentioned above, the maximum intensity from thin film remains unchanged. The bigger the roughness is, the more are thickness oscillations damped.

The simulation assumes the scattering from differently oriented mosaic blocks as coherently scattering domains in the crystal [86, 87]. The structure of many relaxed layers can be represented by a composition of mosaic blocks. The boundaries are created by network of threading dislocations. The scattering intensity is averaged over all possible mosaic block orientations.

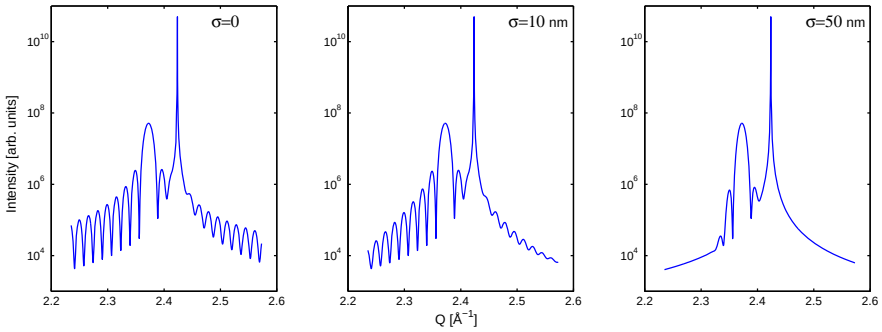

Figure 3.8 The effect of the film interface roughness on the diffraction intensity profile. The root mean square interface roughness was tuned from being completely smooth, $\sigma = 0$ (left), through $\sigma = 10nm$ (middle) to the $\sigma = 50nm$ (right).

When thin film consists of several layers, the interfaces between the layers plays a big role. Interfaces have a certain roughness which might be repeatable in the layers grown above with partial or full correlation between them. The separate contributions of different layers to the total scattering intensity can be, therefore, coherently or incoherently superposed depending on how the interfaces are correlated [86]. Exact description of the scattering intensity reciprocal space distribution can be found for statistically homogeneous crystal with correlation between crystal deformation [86,88,89] and for correlated interfaces of multilayers [51,90–93]. Mosaic structure of GaN epitaxial layers were studied by X-ray scattering in [44,52,88,94–96].

Approximations and Limits

The kinematical approximation of X-ray scattering is based on the weak scattering limit. When the scattering is weak, then the multiple scattering processes can be neglected. Therefore, kinematical approximation can be applied to the imperfect crystal systems, formed from microscopic mosaic blocks. The size of these blocks is taken to be small enough, that the magnitude of the X-ray wavefield does not change much over the depth of the mosaic block [81].

Another phenomenon which is neglected when kinematical approximation has been derived is the absorption effect. In practice, some approximations must be applied to correct the measured intensities. One of these is analytical method of diffraction from a crystal with an extended, flat face where it is assumed that the crystal is large enough to intercept the whole beam, what is usually the case by experiments using collimated beam.

When the crystal is perfect, both the multiple scattering effects and the absorption effects have to be taken into account. The theory which goes beyond the kinematical approximation is known as *dynamical diffraction theory*.

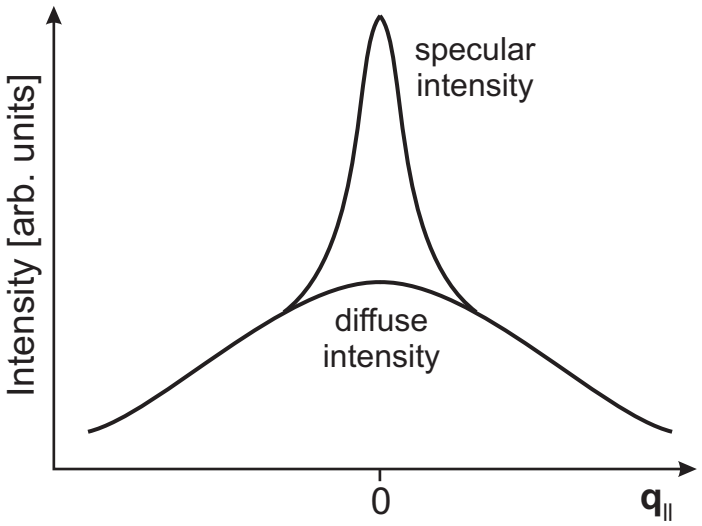

Figure 3.9 Diffraction intensity peak composed by two components: specular scattering intensity (sharp) and diffuse scattering intensity (broad).

3.3.1 Specular and Diffuse Scattering

The scattered intensity is the sum of the Bragg diffraction intensity and the intensity of diffuse scattering :

$$\begin{aligned} I(\mathbf{q}) &= |\langle S(\mathbf{q})\rangle|^2 + \left(\langle |S(\mathbf{q})|^2\rangle - |\langle S(\mathbf{q})\rangle|^2\right) \\ &= I_{\text{Bragg}}(\mathbf{q}) + \mathbf{I}_{\text{diffuse}}(\mathbf{q}). \end{aligned} \tag{3.45}$$

The Bragg intensity is the part of the scattered intensity which is a δ-function at $\mathbf{Q}_{\|} = \mathbf{G}_{\|}$, having the angular distribution as narrow as possible. $\mathbf{q}_{\|}$ is the lateral component of the $\mathbf{q}$ and $\mathbf{G}_{\|}$ corresponding component of the reciprocal lattice vector. Figure 3.9 depicts a diffraction intensity peak composed by two components. The sharp *specular* scattering is the Bragg scattering at $\mathbf{q}_{\|} = \mathbf{0}$ and contains the information about the average sample structure. The broad intensity distribution underneath is attributed to the diffuse scattering. Diffuse scattering is caused by the surface and interface roughness and by crystal defects.

The characterization of threading dislocations in thin Gan films by X-ray scattering is one of the main topics of this PhD thesis. Therefore, we will focus on a diffuse scattering from threading dislocations. The threading dislocation density is directly proportional to the square of FWHM of the rocking curve (ω-scan diffraction peak) [97]:

$$\rho_{\text{s}} = \frac{\Delta\omega_{\text{s}}^2}{2\pi \ln 2 \cdot |\mathbf{b}_{\text{s}}|^2}, \quad \rho_{\text{e}} = \frac{\Delta\omega_{\text{e}}^2}{2\pi \ln 2 \cdot |\mathbf{b}_{\text{e}}|^2}, \tag{3.46}$$

where $\Delta\omega_{\text{s}}$ and $\Delta\omega_{\text{e}}$ are the rocking curve widths of the reflections sensitive to a threading dislocation type, screw or edge and $|\mathbf{b}_{\text{s,e}}|$ is the Burgers vector absolute value for each type. The reflections sensitive almost completely to the screw type

dislocations are in the direction of the screw dislocation Burgers vector (sec. 2.4.1) $\mathbf{b}_s = [0001]$, therefore $(000l)$ measurable by symmetrical coplanar XRD. Similarly, the reflections for edge type follow edge dislocation Burgers vector $\mathbf{b}_e = 1/3\langle 11\bar{2}0\rangle$, namely $(11\bar{2}0)$, $(1\bar{2}10)$ and $(\bar{2}110)$ or their higher order reflections, accessible by grazing incidence diffraction. For GaN, the absolute values of Burgers vectors are $|\mathbf{b}_s| = c(\mathrm{GaN}) = 5.185$ Å and $|\mathbf{b}_e| = a(\mathrm{GaN}) = 3.189$ Å. This model gives just a rough estimation, because it assumes only a Gaussian diffraction peak profile and does not take the correlation between dislocations into account.

In the approach developed in [52] which consider threading dislocations propagating perpendicular to the sample surface including the spatial correlation, it was found that type of threading dislocations follows from the asymptotic behavior of the rocking curve in $\log I - \log Q$ representation. The central part of the profile is Gaussian and the tails of the peak follow the power laws. The rocking curves follow a q^{-3} if measured with a wide open detector, while the rocking curves measured with an analyzer crystal obey a q^{-4} behavior. Here, only the symmetrical reflection have been considered, but not just the screw type contributes to the broadening of symmetrical diffraction peak. Also, the stress relaxation at the sample surface is not included.

3.3.2 Measured Diffraction Intensity

In a real measurement, the total scattering intensity must be considered. The integrated intensity is found to be [81] :

$$I\left(\frac{\text{photons}}{\text{s}}\right) = \Phi_0\left(\frac{\text{photons}}{\text{unit area}\times\text{s}}\right) r_0^2 P N \frac{\lambda^3}{V_{\text{uc}}}\frac{1}{\sin 2\theta}\,|S(\mathbf{Q})|^2 \tag{3.47}$$

where Φ_0 is an incident flux of the photons with the wavelength λ scattered from the electrons having a differential cross section of $r_0^2 P$ each (P is a polarization factor). The total scattering intensity is proportional to the squared absolute value of the unit cell scattering amplitude, as mentioned before, and to the number of unit cells, N. 2θ is the angle between the incident and the scattered photon beam.

Synchrotron light is polarized and due to this fact the intensity is different depending on the scattering plane chosen for the experiment. The electrons in a synchrotron cycle in the horizontal plane. Their acceleration is, therefore, also in the horizontal plane in which the emitted X-rays are linearly polarized. The polarization factor P is equal to unity if the scattering plane is vertical (perpendicular to the polarization plane) and equal to $\cos^2 2\theta$ if the wavevector transfer is in the horizontal plane:

$$P = \begin{cases} 1 & \text{vertical scattering plane} \\ \cos^2 2\theta & \text{horizontal scattering plane} \end{cases} \tag{3.48}$$

Let us consider the factors which affect the uncertainty of the measured scattering intensity. The sources of X-rays at the synchrotron storage rings produce a white

light, which usually need to be monochromatic in order to be used for the scattering experiments. Monochromatization is usually done by use of monochromator with a certain energy resolution, $\frac{\Delta E}{E}$. This limit is caused by divergence of the beam coming from the X-ray source and by optical characteristics of the monochromator.

Secondly, there is a geometric aspect of the scattering. The incident flux of the photons with the cross-sectional area A_0 is coming by the angle α_i to the sample surface and effective illuminated area is $A = A_0/\sin\alpha_\mathrm{i}$. The calculated intensity must be multiplied by the factor of $\frac{1}{\sin\alpha_\mathrm{i}}$.

Now, we are coming to the resolution of the experiment caused by the divergence of the incident and diffracted beam. This will be discussed separately in the next subsection.

Detailed calculation of the corrections to theoretically calculated intensity in order to fit measured scattering intensity can be found elsewhere [81, 86, 87].

Resolution Element

Using the synchrotron radiation for the scattering experiments, the incident beam is usually collimated before being scattered in the interaction with the sample. Both the incidence and the scattered beam are divergent what produces uncertainty due to the overlapping of different scattering signals.

The resolution element is an area in reciprocal space that is illuminated by the incident beam and at the same moment accepted by the detector under geometrical and spectral conditions of the scattering experiment. The scattering intensity is averaged over the resolution element. Resolution element of the X-ray scattering in coplanar geometry ($Q_z - Q_x$ plane) can be approximately calculated by [86]:

$$A_\mathrm{coplanar} = \Delta Q_x \cdot \Delta Q_z \tag{3.49}$$

where ΔQ_x and ΔQ_z are dependent on the wavevector amplitude K (by this on the energy), on the incoming and outgoing angles $\alpha_\mathrm{i,f}$, and on the divergence of the incident and the scattered beam $\Delta\alpha_\mathrm{i,f}$:

$$\Delta Q_x = K\sqrt{\sin^2\alpha_\mathrm{f}\left(\Delta\alpha_\mathrm{f}\right)^2 + \sin^2\alpha_\mathrm{i}\left(\Delta\alpha_\mathrm{i}\right)^2} \tag{3.50}$$

$$\Delta Q_z = K\sqrt{\cos^2\alpha_\mathrm{f}\left(\Delta\alpha_\mathrm{f}\right)^2 + \cos^2\alpha_\mathrm{i}\left(\Delta\alpha_\mathrm{i}\right)^2} \tag{3.51}$$

This is valid neglecting the change of K and assuming statistical independence of the parameters used [86].

If the scattering process is in the plane of surface as *grazing incidence diffraction* (sec. 3.3.3), then the resolution element can be expressed as [86, 98]:

$$A_\mathrm{GID} = \Delta Q_\parallel \cdot \Delta Q_z \tag{3.52}$$

$$\Delta Q_\parallel = K\sqrt{\sin^2\theta_{B\parallel}\left[\alpha_\mathrm{f}^2\left(\Delta\alpha_\mathrm{f}\right)^2 + \alpha_\mathrm{i}^2\left(\Delta\alpha_\mathrm{i}\right)^2\right] + \cos^2\theta_{B\parallel}\left[\left(\Delta\theta_\mathrm{f}\right)^2 + \left(\Delta\theta_\mathrm{i}\right)^2\right]} \tag{3.53}$$

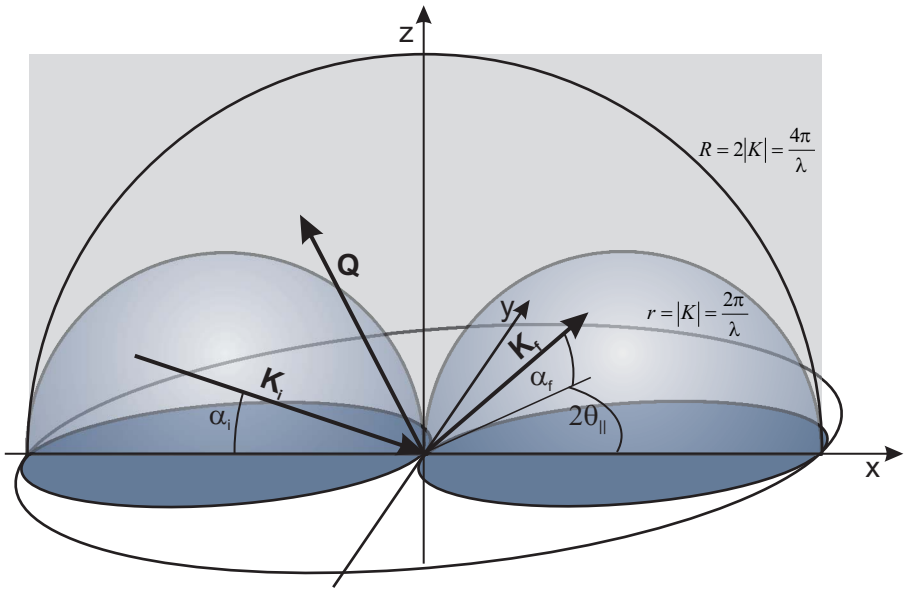

Figure 3.10 For fixed incident wavevector, the reciprocal space is for the diffraction accessible in the region outside of the small half-spheres (r) with the radius equal to the wavevector absolute value and inside of the big half-sphere (R). For coplanar scattering, the vector Q and both incident and exit wavevectors lay in the $x - z$ plane (gray-marked rectangle). After [86].

$$\Delta Q_z = K\sqrt{(\Delta\alpha_\mathrm{f})^2 + (\Delta\alpha_\mathrm{i})^2} \tag{3.54}$$

That means that the resolution element depends on the certain choice of four different angles: incoming and outgoing angles $\alpha_{\mathrm{i,f}}$ and the in-plane Bragg angles between the lateral projection of the incident and the scattered beam and the diffraction plane $\theta_{\mathrm{i,f}}$.

3.3.3 Scattering Geometries

Let us set the coordinate system as follows: x is oriented along the propagating X-ray beam direction, y also laying laterally, but perpendicular to the beam propagation and z to follow the sample surface normal, that means perpendicular to the $x - y$ plane. Figure 3.10 shows the accessible region for the Bragg diffraction which is in between half-spheres with the radius of $r = |\mathbf{K}| = \frac{2\pi}{\lambda}$ and half-sphere with the radius of $R = 2\,|\mathbf{K}| = \frac{4\pi}{\lambda}$ for fixed incident wavevector. Usually, scattering geometries can be divided into coplanar and non-coplanar X-ray diffraction. Coplanar case is when the scattering vector is in $x - z$ plane (marked by rectangle) same as incident wavevector and the surface normal. The choice of the scattering geometry depends on the reflection from the scattering crystal plane which is to be measured and on the specific structure information which is to be investigated.

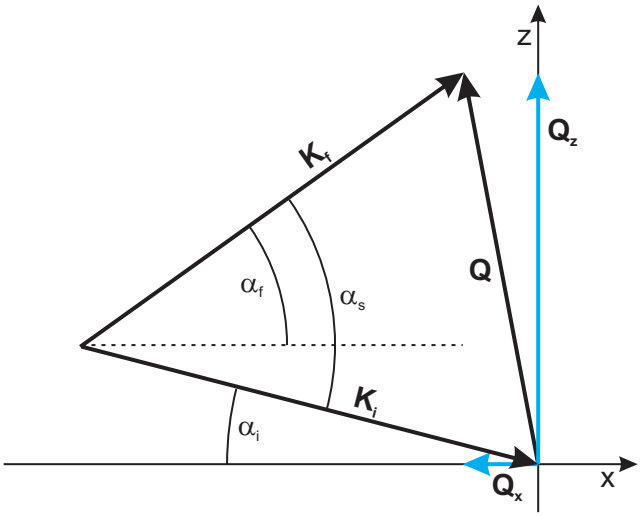

Figure 3.11 Coplanar geometry: components of the scattering vector in the $Q_x - Q_z$ plane.

Coplanar X-ray Diffraction

In the coplanar scattering geometry, all vectors, $\mathbf{K}_i$, $\mathbf{K}_f$ and $\mathbf{Q}$ are in the same plane, perpendicular to the sample surface. Figure 3.11 shows the scattering vector $\mathbf{Q} = \mathbf{K}_f - \mathbf{K}_i$ in the coplanar scattering geometry with:

$$\begin{aligned} Q_z &= K\left(\sin\alpha_\mathrm{f} + \sin\alpha_\mathrm{i}\right) \\ Q_x &= K\left(\cos\alpha_\mathrm{f} - \cos\alpha_\mathrm{i}\right) \end{aligned} \tag{3.55}$$

where the angle between the scattered wavevector and the surface is $\alpha_\mathrm{f} = \alpha_\mathrm{s} - \alpha_\mathrm{i}$. Incidence angle, α_i is usually named ω denoted from the rotation of the sample circle of the goniometer. The scattering angle, α_s, kept by detector is equal to 2θ.

Coplanar geometry can be symmetrical and asymmetrical. Symmetrical or specular X-ray diffraction is the particular case where scattering vector Q is parallel to the Q_z direction and $\alpha_\mathrm{f} = \alpha_\mathrm{i}$ (ω is equal θ). In asymmetrical X-ray diffraction, scattering vector does not follow Q_z, but is still in the Q_x-Q_z plane, same as the surface normal. In asymmetrical case, the diffraction crystal planes are inclined with respect to the surface.

Non-coplanar X-ray Diffraction

Figure 3.12 shows the scattering vector in non-coplanar scattering geometry with components:

$$\begin{aligned} Q_x &= K\left(\cos\alpha_\mathrm{f}\cos 2\theta_\parallel - \cos\alpha_\mathrm{i}\right) \\ Q_y &= K\cos\alpha_\mathrm{f}\sin 2\theta_\parallel \\ Q_z &= K\left(\sin\alpha_\mathrm{f} + \sin\alpha_\mathrm{i}\right) \end{aligned} \tag{3.56}$$

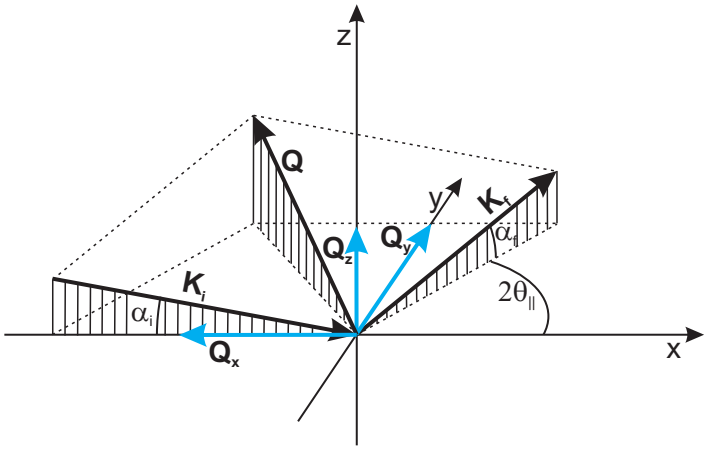

Figure 3.12 Non-coplanar geometry.

where $2\theta_{||}$ is the in-plane component of the scattered beam.

There are many examples of use of the non-coplanar scattering geometry in the material structure characterization as methods grazing incidence small angle X-ray scattering (GISAXS) and grazing incidence diffraction (GID). GISAXS is a surface technique which does not employ diffraction from the crystal planes but scattering of the surface objects shape and their distribution and possible space correlation. GID will be discussed in the next section since it has been used in this thesis for the research on both thin GaN films and InGaN quantum dots.

Grazing Incidence Diffraction

Grazing incidence X-ray diffraction is a non-coplanar X-ray scattering from the planes sitting perpendicular to the surface, employing the evanescent wave which exists when X-rays angle of incidence to the sample is smaller the the critical angle for total external reflection. GID is surface sensitive technique and therefore used for investigation of small objects which are on the surface or buried below it or for research on the surface changes even during the growth or postgrowth process.

A common way to describe the scattering vector in grazing incidence geometry is to define its radial and angular component:

$$\begin{aligned} Q_{\mathrm{r}} &= K\left(\cos\alpha_{\mathrm{f}}\sin\theta_{\mathrm{f}} + \cos\alpha_{\mathrm{i}}\sin\theta_{\mathrm{i}}\right) \\ Q_{\mathrm{a}} &= K\left(\cos\alpha_{\mathrm{f}}\cos\theta_{\mathrm{f}} - \cos\alpha_{\mathrm{i}}\cos\theta_{\mathrm{i}}\right) \\ Q_z &= K\left(\sin\alpha_{\mathrm{f}} + \sin\alpha_{\mathrm{i}}\right) \end{aligned} \tag{3.57}$$

Q_{r} is following the radial direction of the measured in-plane reflection, Q_{a} is in-plane deviation from the radial direction following the angular scan (rocking curve through the radial point). Q_z is parallel to the surface normal. If the incident and the exit angles are small and deviation from the radial axis in angular scan is small as well

($Q_\mathrm{a} \ll Q\mathrm{r}$), then the equation 3.58 can be approximated by:

$$\begin{aligned} Q_\mathrm{r} &\approx 2K \sin\theta_\mathrm{B} \\ Q_\mathrm{a} &\approx 2K \sin\theta_\mathrm{B} \sin\Delta\phi = Q_\mathrm{r} \sin\Delta\phi \\ Q_z &\approx K\left(\alpha_\mathrm{f} + \alpha_\mathrm{i}\right) \end{aligned} \tag{3.58}$$

where Bragg angle θ_B is equal to the in plane angle $\theta_\parallel$ (fig. 3.12). The penetration depth of the evanescent wave can be tuned with the incident angle. Therefore, GID is a method very sensitive to the surface structure. How the penetration depth depends on the angle of incidence and on material properties, is given assuming very small angles by [99]:

$$\Lambda(\alpha_\mathrm{i}) = \frac{\lambda}{4\pi}\left\{\frac{1}{2}\left[\sqrt{\left(\alpha_\mathrm{i}^2 - \alpha_\mathrm{c}^2\right)^2 + \chi''^2} - \left(\alpha_\mathrm{i}^2 - \alpha_\mathrm{c}^2\right)\right]\right\}^{-\frac{1}{2}} \tag{3.59}$$

where α_i is the incident angle, $\alpha_\mathrm{c} = \sqrt{2\delta}$ is the critical angle related to the electron density of the sample material (eq. 3.14) and $\chi'' = 2\beta$ is double imaginary part of the refraction index connected to absorbtion properties of material (eq. 3.15). The critical angle and the imaginary part of the refraction index depend on energy. Figure 3.13 shows the penetration depth dependence on the incidence angle for three different nitride-based materials using the X-rays with energy of 8keV. Even at the incidence angle equal to zero, there is a certain penetration of the evanescent wave of X-rays in the sample. With increasing incident angle, the penetration depth increases. The critical angle of total external reflection is where penetration depth start to increase rapidly (AlN: 0.26177°,GaN: 0.33696°,InN: 0.35679°). After the critical angle is approached, the X-rays penetrate, according to the previous equation, more deep by increasing of incident angle. Differences between penetration depth curves for different materials are in the critical angle due to different electron densities and in maximum penetration depth reached because of different absorbtion properties.

From the shape of performed rod grazing incidence $\alpha_i - \alpha_f$ scans it can be determined whether the intensity is coming from the "bulk" or "surface" part of the structured thin film [100, 101]. This fact is then used for the clear attributing of the measured diffraction peaks to the specific structure.

Because of rather weak scattering from the small volume surface objects, there is a need of the synchrotron light.

Mostly used theoretical model to describe the scattering process of grazing incidence diffraction is *distorted wave Born approximation (DWBA)* [102]. DWBA is in principal a semi-kinematical approach which consider several typical processes to describe multiple scattering effects of in-plane diffraction from the small objects placed either on the surface or buried below it.

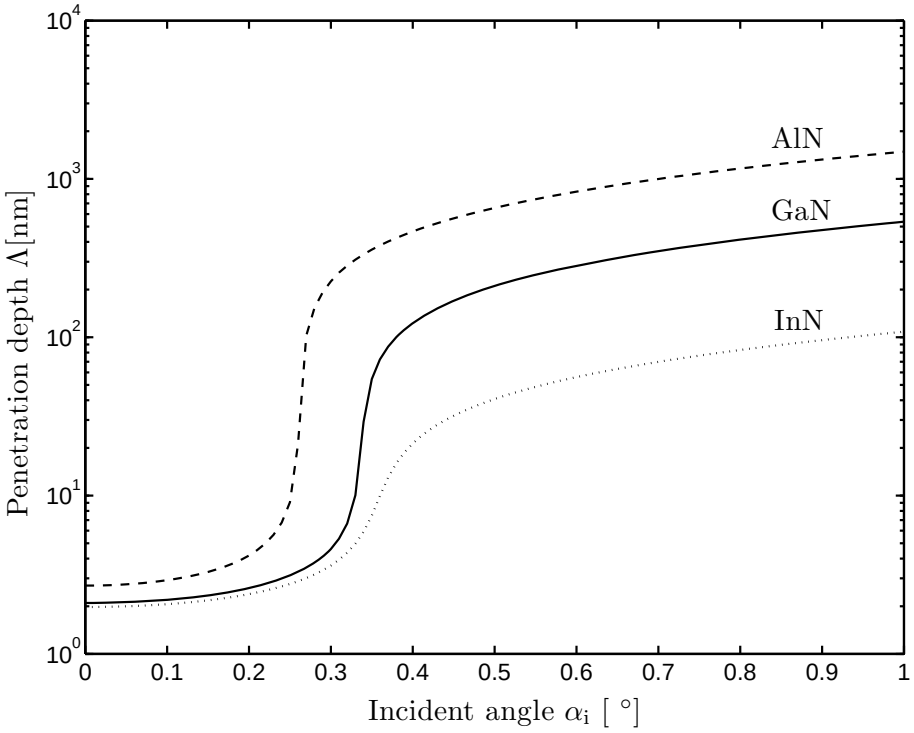

Figure 3.13 Dependence of the penetration depth Λ of X-rays at 8keV on the grazing incident angle α_i for different group(III)-nitride materials: AlN(dashed line), GaN (solid) and InN (dots).

Chapter 4

X-Ray Scattering Experiments

Interaction between accelerated electrons with the electrons of the target results in two types of radiation. The inelastic interaction with outer electrons gives so-called *Bremsstrahlung* due to deceleration which is a continuous radiation. Second type is *characteristic radiation* with high peaks according to spectral atomic lines as a result of energy transfer of the electron coming from outer shell populating some of the inner shells.

Synchrotron has three big components: first, the injector which can be either microtron booster or linear accelerator, second is the storage ring which keeps the electrons cycling on the same orbit by electromagnetic field and third part are the sources of X-rays: banding magnets or insertion devices (ID). Insertion devices (wigglers and undulators) are straight sections of many pairs of magnets oriented in the opposite direction making the electron beam wiggling and by this multiplying the photon intensity at the ends. This ends with the optical components between the X-ray source and finally diffractometer are so-called *beam lines*. Many of the parameters like electron energy and current in the storage ring, stability and lifetime, type of X-ray source, combination of the optical components influence the quality of the photon beam at the experimental station. Figure 4.1 shows panorama and schematical view of the storage ring with microtron booster and the beam lines of Ångströmquelle Karlsruhe synchrotron (ANKA).

One of the most important properties of X-ray sources is their brilliance B [81]:

$$B = \frac{\text{number of photons per second}}{(\text{mrad})^2\,(\text{mm}^2\text{source area})\,(0.1\%\text{bandwidth})}. \tag{4.1}$$

The beam intensity (in units of photons per second) after the monochromator can be further calculated as the a product of the brilliance, angular divergences set by the horizontal and vertical apertures (in milliradian), the source area (in mm^2) and the bandwidth of the monochromator relative to 0.1%. The source flux is given as the number of photons per second per unit surface area.

Synchrotron radiation is produced when relativistic electrons travel along curved trajectories. In a synchrotron, the electrons cycle in a storage ring being kept on their

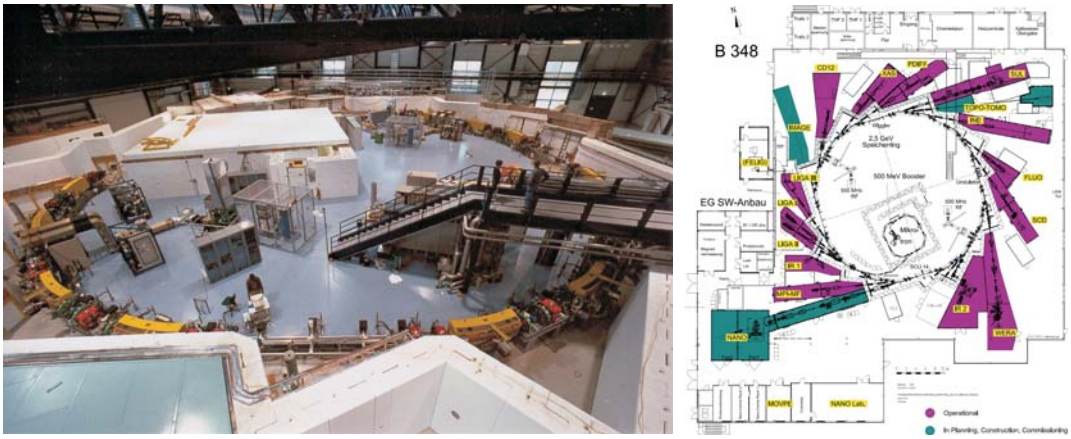

Figure 4.1 Ångströmquelle Karlsruhe (ANKA) Synchrotron Light Source: A view on the electron storage ring (left) and schematical view from the top (right). [103]

orbits by bending magnets. The relativistic electron emits the radiation in a cone with the opening angle:

$$\gamma^{-1} = \frac{m_0 c^2}{E_0}, \tag{4.2}$$

where the electron rest mass is given by m_0 and the speed of light given by c. The axis of this cone is parallel to the velocity of the electron. Typical values of γ are $\gamma^{-1} = 0.85 \times 10^{-4}$ for the ESRF, and for ANKA it is

$$\gamma \; = \frac{2.5 \; \cdot 10^3 MeV}{0.511 \; MeV} \quad = \; 4892 \approx 5000 \Rightarrow \gamma^{-1} = 0.2 \times 10^{-3}. \tag{4.3}$$

Full calculation gives a dependence of γ^3 for the boost in frequency. This means a shift from the radio waves to the X-ray regime. In the horizontal plane, synchrotron radiation from a bending magnet exhibits a fan-like angular distribution which can be reduced geometrically by inserting aperture slits in front of the sample. When the wiggler radiation is used, the horizontal divergence (full width at the half maximum, FWHM) is

$$\Delta\theta_h = K\gamma^{-1}, \tag{4.4}$$

while the vertical divergence is still given by γ^{-1}. The deflection parameter K is a measure of the maximum horizontal deflection of an electron when passing through a wiggler or undulator. In order to optimize the flux at the sample, many beam lines use the optical elements (monochromators or mirrors) that horizontally focus the X-ray beam onto the sample position. The horizontal divergence is then of the order of several milliradians. If one is aiming to perform 3D reciprocal space mapping, this value is often too high. A reduction of the divergence can be achieved by placing aperture slits in front of the focusing element. This is, however, only possible at the

expense of photon flux. When undulator radiation ($K \approx 1$) is used, the divergence is further reduced. The vertical and the horizontal divergences are given by:

$$\Delta\theta_v = \Delta\theta_h = \gamma^{-1}\sqrt{\frac{1 + K^2/2}{nN}}, \tag{4.5}$$

where n is the order of harmonic and N is the number of magnetic pair periods [81].

4.1 Experimental Setup: Synchrotron Diffraction Beam Line

Beam line, as a combination of optical components, slits, filters, absorbers and monitors, defines whether photon beam will be monochromatic or not, energy of the X-rays, focusing, dimensions and the beam profile. Coming from the X-ray source, the light is firstly collimated and focused by horizontally collimating and vertically collimating mirrors. For diffraction purpose, monochromatic X-ray beam is used. Energy of monochromatic beam is selected by monochromator which can be either double-crystal monochromator (DCM) (typically Si(111)) or multilayer monochromator (MM). The energy resolution $\frac{\Delta E}{E}$ is usually 10^{-3} to 10^{-4}. After monochromator, there are number of slits which serve as the apertures defining the beam with and hight and to suppress the scattering from the edges. Ionization chamber is used to monitor the intensity of the primary beam and set of attenuators are used to absorb part of the beam when detector is measuring direct beam or diffractometer is in the Bragg condition.

An Example: NANO - beam line at ANKA synchrotron light source

NANO - beam line at ANKA synchrotron light source is used as an example of modern diffraction beam line. Figure 4.2 shows the design of NANO - beam line with main optical components from the X-ray source (superconducting undulator) up to the multipurpose heavy-duty diffractometer. Beside tunable energy with good resolution in the range between 3keV and 25keV, high flux of photons, small beam spot size, possibility of having collimated (parallel) and focused beam, choice to switch between monochromatic and white or pink beam, there is a particular characteristic of the NANO - beam line: possibility to characterize thin films and nanostructure surfaces and interfaces by X-rays *in-situ* and real time during the growth or postgrowth process. Specially designed growth chambers (with Cp or Be windows) can be positioned at diffractometer and connected to the gas, vacuum or heating environment. The NANO beam line is dedicated to high-resolution X-ray diffraction and scattering from surfaces and interfaces, but other methods as anomalous X-ray scattering (AXS) or coherent diffraction imaging (CDI) are also available.

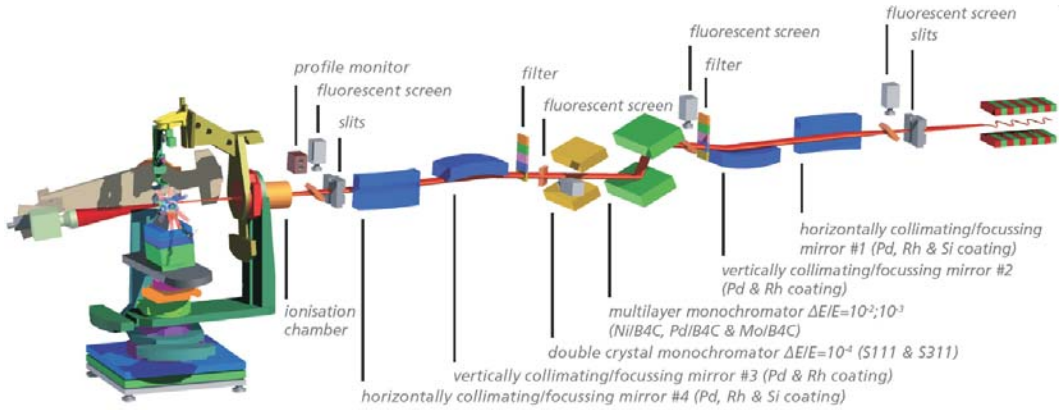

Figure 4.2 A modern diffraction beam-line: Design of NANO beamline optics and the multi purpose diffractometer of the experimental station NANO1 at ANKA synchrotron. [103] (by courtesy of Dr. S. Bauer)

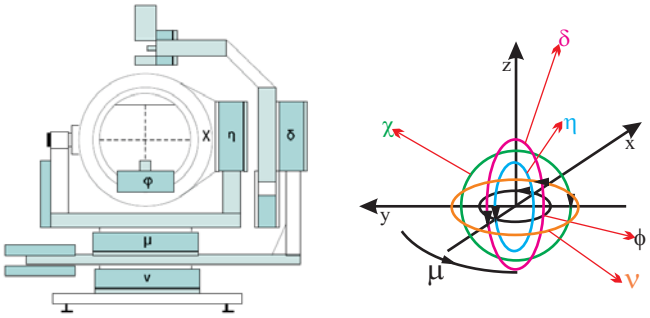

Figure 4.3 Six-circle (4+2) diffractometer. 4 motors are used for the sample positioning (η, μ, ϕ, χ) and 2 for the detector (δ and ν).

Diffractometer

Diffractometer is an instrument with a number of motors which places the sample with respect to the incoming beam to fulfill a Bragg condition and to perform scans in the reciprocal space. Scattered beam is kept by detector. Usually there is a motorized goniometer head to position the sample in the center of rotation of aligned diffractometer. Center of rotation should coincide with the spot of direct beam on the sample to be measured. Principle scheme of the six-circle (4+2) diffractometer is shown in the figure 4.3

4.2 Diffraction Geometries

Depending on the material research specific interest, it is possible to focus on the certain part of the reciprocal space to answer on the structural properties of investigated samples.

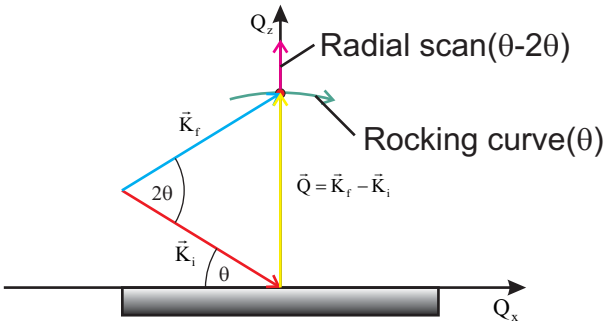

Figure 4.4 Scans in coplanar geometry.

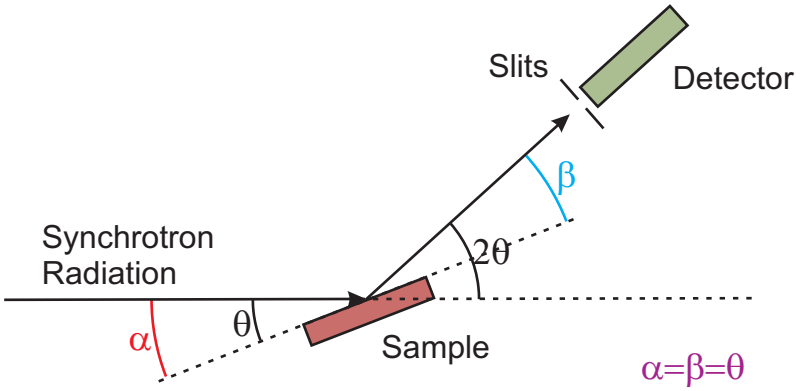

Figure 4.5 Symmetrical coplanar XRD.

Most common is to divide scanning through the reciprocal space by diffraction geometries, as already introduced in sec. 3.3.3. One geometry is *coplanar diffraction geometry* with the scattering vector laying mostly in the $Q_z - Q_x$ plane. Another one is *non-coplanar* geometry when the incident and the scattered wavevectors are not in the same plane. The special case of non-coplanar geometry is a *grazing incidence geometry* where the scattering vector is almost completely in-plane as a result of diffraction from the atomic planes sitting perpendicular to the sample surface.

Synchrotron light is polarized and depending on the geometry used in the experiment, intensity is not the same. Therefore, in order to use most of the intensity from the synchrotron radiation to have the best possible conditions for the strong diffraction response, it is better to use a vertical scattering plane, especially for weak scattering from the material with the low scattering potential. This is used in the GID studies on thin GaN films and on InGaN quantum dots measured in this thesis, as samples were placed vertically and the reflections were measured in-plane, therefore in the vertical polarization plane.

Figure 4.4 shows schematically how two of the most used scans, radial scan and rocking curve look in the reciprocal space spanned in $Q_x - Q_z$ plane (coplanar geometry). Figures 4.5 and 4.6 show the coplanar XRD experiments are performed for symmetrical and asymmetrical case, respectively. In the figures, θ is a Bragg angle

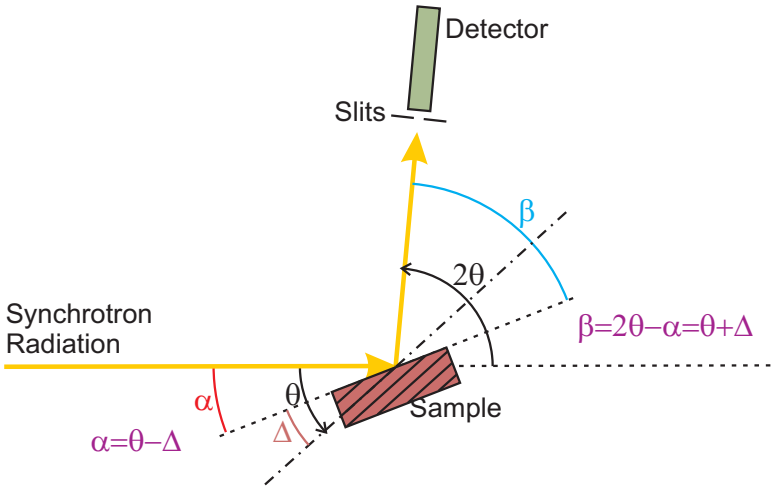

Figure 4.6 Asymmetrical coplanar XRD.

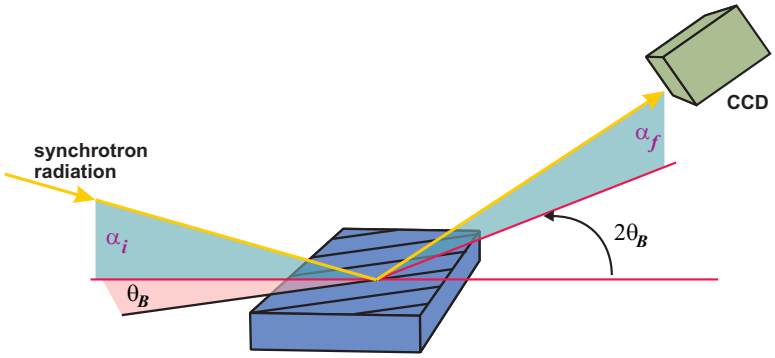

Figure 4.7 Schematic view of grazing incidence diffraction geometry. Note that the incidence and the exit angles are very small, close to the value of the material critical angle of total external reflection of photons with the certain energy.

and α and β are angles of the incoming and the scattered beam to the sample surface. Δ is an inclination angle between the scattering planes and the surface (fig. 4.6).

Non-coplanar scattering experiment is more complicated to perform. Figure 4.7 shows grazing incidence diffraction where scattering planes are perpendicular to the surface. First, the reflectivity condition with the incident angle close to the critical angle of total external reflection need to be satisfied. The detector should be placed at the position of double Bragg angle and then, the sample should be rotated around its surface normal to find the diffraction signal.

4.3 Experimental and Technical Details of the X-ray Study of InGaN QDs

Part of measurements have been performed at European Synchrotron Radiation Facility (ESRF) in Grenoble, France, at beam line ID01 (fig. 4.8). A synchrotron radiation energy of 7.75 keV was used, corresponding to the wavelength $\lambda = 1.56$ Å. The beam size before the sample was 0.1 μm×0.1 μm. We have used a MaxiPix 2D detector with evacuated flight tube and slits. The detector characteristics are as follows: the number of pixels is 256×256, with the pixel size of 55 μm covering the area of 14.08×14.08 mm^2. The distance between sample and detector was 1 m. The resolution in reciprocal space was below $5 \cdot 10^{-4}$nm^{-1} for one pixel and $8.6 \cdot 10^{-3}$nm^{-1} for the region of interest of 20 pixels (Q_{r}-direction) The angular opening in the Q_z direction was 0.8° and the intensity in this direction was integrated. To avoid air scattering and damage of the samples due to reactions with ozone, the samples were measured under helium atmosphere. The sample was oriented vertically and, according to the PSIC configuration of the diffractometer [104], the ϕ was used as a scanning motor θ, δ as detector motor 2θ, while μ and ν were arranged to fulfill the grazing incidence specular condition.

The GID reciprocal space maps were measured at ANKA, Karlsruhe Institute of Technology, SCD beam line (fig. 4.9) using the synchrotron radiation energy of 8 keV. The scattered intensity was detected with a YaP scintillation detector and integrated over an α_{f}-range of 2° and $\Delta 2\theta = 0.1°$. The collimated X-ray beam was attenuated by absorber set (no. 3 at same fig.) before coming to the sample (1) protected under He atmosphere (2). The diffracted beam was first going through the flight tube (6) with two pairs of slits in front (4) and at the end (5) of it, finally being detected at the position (7). The resolution in reciprocal space was $4 \cdot 10^{-2}$nm^{-1}. All maps were measured with the same resolution and in the same manner, meaning same steps in radial and angular directions.

In the radial GID scans, the intensity at each point was plotted as counts collected in the region of interest normalized to the monitor counts. The region of interest is the area of CCD defined by 20 pixels in Q_{r}-direction and integrated over 256 pixels in the Q_{z}-direction. The effect of the resolution was checked and it was found that there is no influence on the GID results except at the buffer GaN layer peak. The resolution

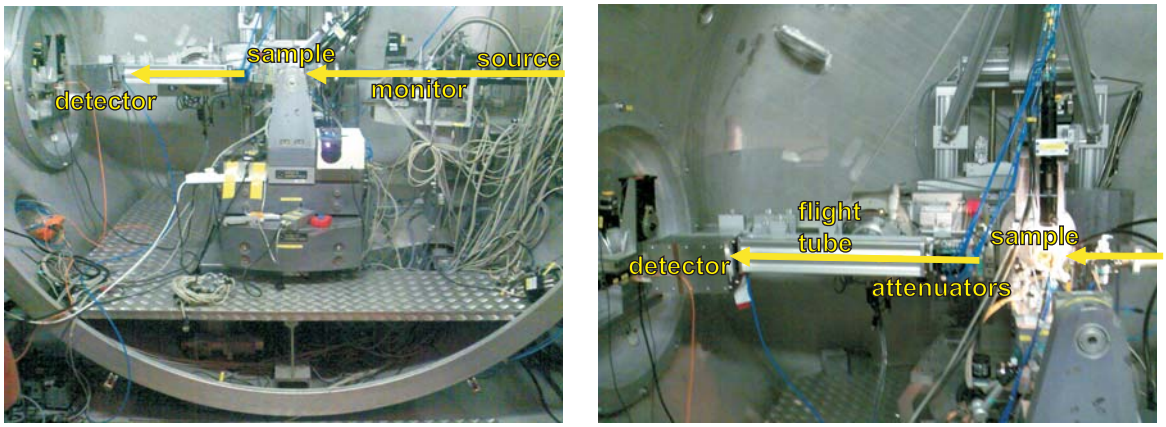

Figure 4.8 Experimental X-ray scattering setup of ID01 beam line, ESRF (Grenoble).

element of the GID experiment is calculated using the formulation 3.52 considering the properties of the ID01 beam-line optics and the geometrical configuration of the setup. It is determined to be $A_{\mathrm{GID}} = 2.59 \cdot 10^{-4}\text{Å}^{-2}$. The GID radial scan in the vicinity of $(10\bar{1}0)$ was repeated in four different azimuthal directions and the results show no visible difference. Therefore, in the section 7.3 is presented only one scan on each sample per reflection.

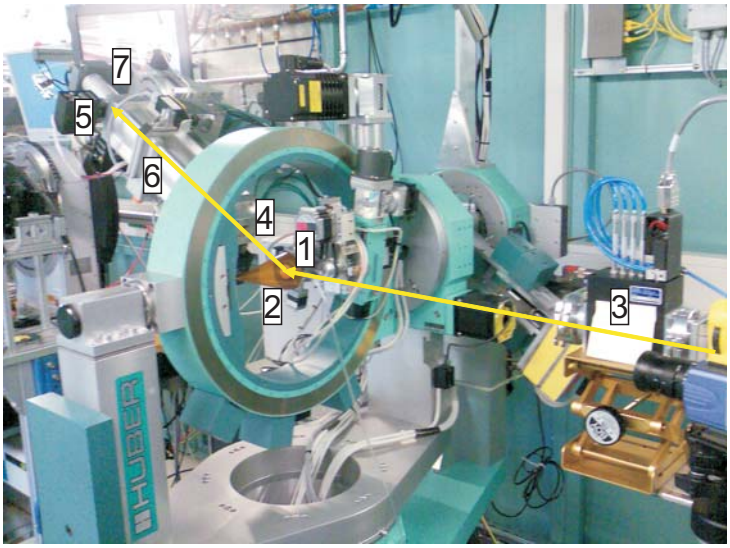

Figure 4.9 Experimental X-ray scattering setup of SCD beam line, ANKA (Karlsruhe).

Chapter 5

Scanning Probe Microscopy Experiments

Complementary method to the X-ray scattering methods, used in this thesis for investigation of the surface objects and surface morphology, is atomic force microscopy (AFM). Atomic force microscopy allows local probing of the sample surface and provide information about the size, shape and distribution of quantum dots which support the interpretation of the X-ray data. X-ray scattering methods give information in the reciprocal space where these effects are superposed and they result from the averaging over the illuminated part of the sample.

All of the AFM measurements shown in this thesis, have been performed in the large sample ultra-high vacuum (UHV) scanning probe microscopy (SPM) system connected to the analysis cluster of the UHV Analysis Laboratory at ANKA. The experiments were done under UHV conditions although it was not necessary as InGaN quantum dots samples have already been air exposed prior measurements. The SPM system was used for the first time. By these experiments the complete operational status was confirmed.

5.1 Atomic Force Microscopy: Principle

Principle of the atomic force microscopy is rather simple and employs elastic changes of the cantilever with the tip at the end, scanning the surface hight and by this changing the optical response in the position sensitive detector, due to different spatial position of the laser spot reflected from the cantilever. The pioneer work of Ernst Ruska in electron optics and electron microscopy become very actual after the invention of scanning tunneling microscopy (STM) by Binnig and Rohrer [106–108] for which they got a Nobel prize, in the year 1986. The AFM was invented [109] to enable the scanning of insulators what was not possible by STM. In the years after that AFM and STM become one of the standard methods in surface analysis and nanoscience.

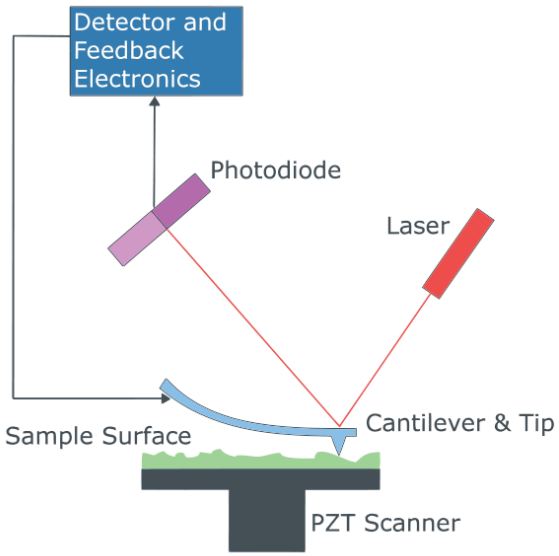

Figure 5.1 Principle scheme of the atomic force microscopy [105].

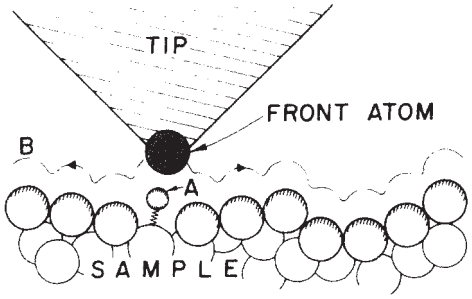

Figure 5.2 Principle of the atomic force microscopy [110].

Figure 5.1 shows a schematic of the atomic force microscopy. A focused laser beam is falling on the tip of the cantilever which is deflected by the force from touching the sample surface. The laser beam is reflected from the cantilever to the position sensitive detector which is connected to the feed-back electronic system controlling the applied force. In our case, the scanner is mounted on a piezoelectric tube which again is mounted on a motorized xyz-stage. X- and y-motors serve for positioning of the tip and for selecting the area of interest for scanning. An AFM system detects the z-displacement keeping the force being constant. By this AFM scans the surface topography.

The choice of cantilever tip by means of its material and curvature (sharpness) depends on the sample which is to be scanned and on the scanning mode used.

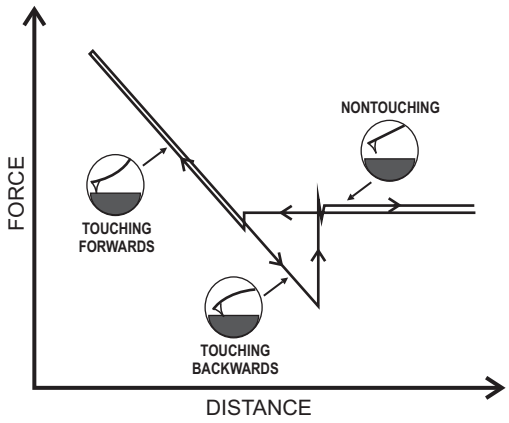

Figure 5.3 Typical force-distance curve measured in AFM experiment (after [110]).

5.1.1 Scanning AFM Modes

Scanning of surfaces in nanometer range can be done in several modes. Typically, the modes are divided by criteria of touching. In contact AFM mode, the AFM tip touch the surface during scanning, while in non-contact AFM mode it does not touch. There is, however, new developed methods which employs rather both like the tapping AFM mode where scans are done by resonant oscillating of the tip and touching of the sample surface.

Contact AFM

By contact or force-modulation mode the AFM tip of cantilever drags on the surface using the repulsive force. When measuring rather small surface objects like quantum dots, very important is to properly measure the force-distance curve for the pair tip-sample material. By this the AFM system is optimized to be sensitive for the dots and in the same time not to destroy them. When the tip comes close to the sample, the cantilever is deflected from its equilibrium position to the atomic force experienced by the tip [110]. The attracting van der Waals force becomes bigger as the cantilever approaches the surface. The cantilever bends toward the sample (see fig. 5.3 touching forwards). Due to piezo-motors creep, the force-distance curve, when moving away from the surface, is not identical to the one moving towards the surface. The tip is attracted to the surface, but the cantilever bends away from surface (see fig. 5.3 touching backwards) because the z-motion increases the distance between surface and cantilever while the tip wants to stick to the surface. When the tip is retracting from the sample, there is still a contact between them as long as the adhesive and capillary forces non-touching regime. Next peculiarity in scanning quantum dot surface is to optimize the speed of scans, because after approaching the dot comes a valley which might look not resolved in the AFM scan due to fast moving of the tip up and down. Finally, the shape of the quantum dots might be not the true one due to artifacts.

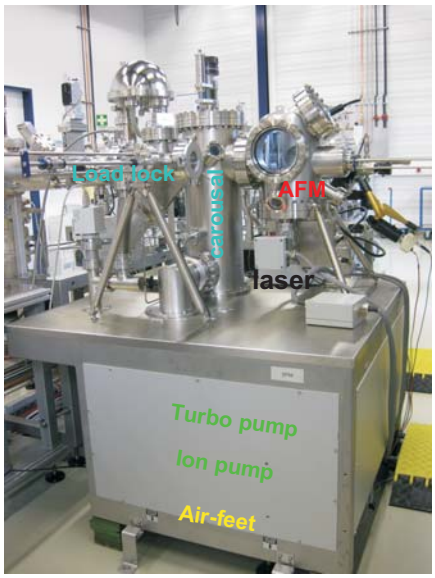

Figure 5.4 Large sample ultra-high vacuum AFM connected to the UHV analysis cluster at ANKA.

Also, scans should be repeated in the several directions of the scanner and on different places of the sample to have more accurate AFM results.

5.2 Large Sample UHV SPM at ANKA

The large sample ultra high vacuum scanning probe microscope (fig. 5.4) installed at UHV Analysis Laboratory, ANKA, KIT is the *Omicron* factory designed system. The Large Sample Beam Deflection AFM (LS AFM) is designed for applications on semiconductor wafers from 1 inch to 4 inches in diameter. Due to the our SPM system specifics, only samples up to 1 inch can be mounted. The microscope offers a wide scan range as well as atomic resolution capability. Precision tip coarse positioning within an area of 10 mm×10 mm is accomplished via remote controlled piezoelectric stepper drives with variable step sizes ranging from 20 nm to 200 nm. This feature is also used for the safe, remote controlled tip exchange. The LS AFM employs the spring suspension with eddy current damping for effective vibration isolation [111]. The SPM system is mounted on the air-feet which accommodate the outer vibrations from the ground. With the same aim of vibration damping, the SPM is connected to the analysis cluster through the double bellow. Technical details and description could be found in [112].

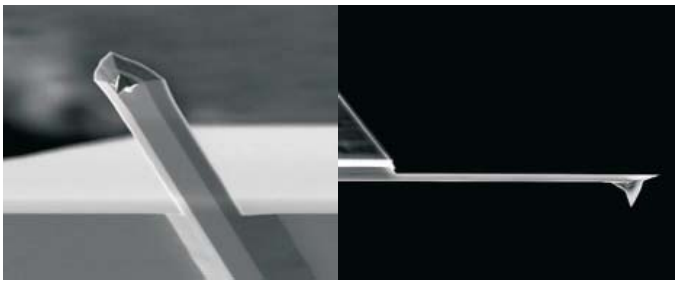

Figure 5.5 A tip for the contact mode atomic force microscopy used in the measurements [113].

5.3 Experimental and Technical Details of the AFM study

Prior the scanning process the samples were heated to 130 °C to remove the water from the sample surface and sample holders. The pressure in the SPM system was 10^{-10} to 10^{-9} mbar.

The samples were measured in contact mode using a single-crystalline silicon tip, type "CONTR" made by *Nanoworld* manufactory. The tip (fig. 5.5) is shaped like a pyramid with a height of 10-15 μm, with the curvature radius less then 8nm, the force constant of 0.2 N/m and the resonance frequency of 13 kHz. The reflecting side of the cantilever is coated by highly reflex aluminum film. Further details can be found in [113].

The samples were measured several times as scans were repeated at several different positions on the sample to have a better statistics of results. The representative images are shown. It was found that the shape of the islands and their distribution are well visible at the measured sample area of 1 μm $\times$ 1 μm. Therefore, most of the AFM images presented here have this size. The optimized speed of scanning was 500 nm/s. The optimization criterium was the shape of the islands. Scanning with higher speed results with the shape with an artifact that after highest point was reached, tip did not succeed to follow the slope to the bottom. The scanning direction was changed to study the influence of the sample drift on the measurements (see next section). The force which is used in the AFM experiment is 3nN (not calibrated). All AFM results have been evaluated by the *WSxM* scanning probe microscopy software developed by "Nanotec Electronica" (see ref. [114]).

5.3.1 Scanning Artifacts

The general results show some features which might be under suspect. For some of the samples, the type B islands have the elongated shape which might be due to too much force applied during the sample drift over the tip. The same might happen for the type A dots which might be formed by scanning procedure. The question is how

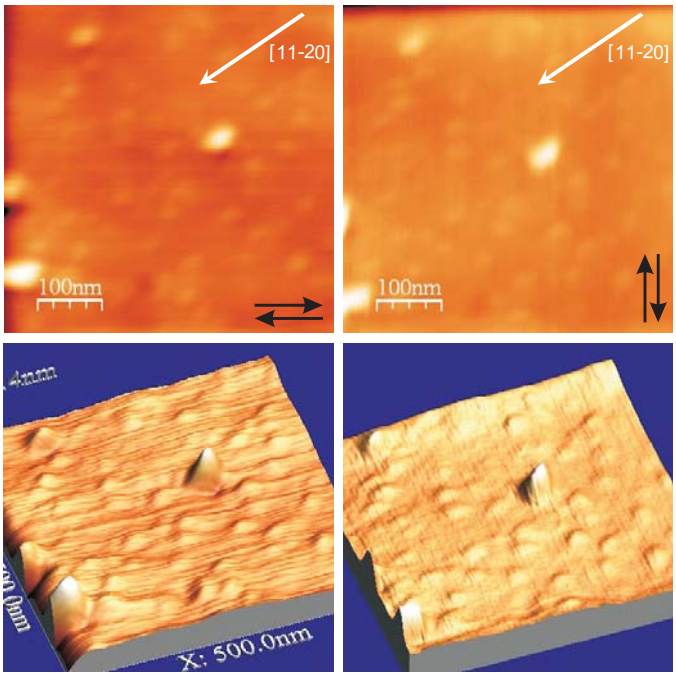

Figure 5.6 AFM (500nm × 500nm) on InGaN quantum dots proving no influence of the scanning direction drift to the elongation of the islands. Left: scanner position of 0° - scanning left and right. Right: scanner position of 90° - scanning up and down.

reliable are the results of the AFM experiments, are they influenced by the scanning process?

The influence of the scanning drift on the islands elongation was investigated by verification performing the following measurements: scanning the same area of the example sample surface, just in a different directions perpendicular one to another. Sample where the asymmetrical shape is most pronounced (FT2) is used here. Figure 5.6 shows the result of verification. Left-hand side depicts the AFM of the surface area with size of 500nm × 500nm scanned in the directions left-right (scanner in the position 0°). On the right-hand side of the figure, the AFM image of the same surface is shown, just it was scanned in the up-down directions (scanner position of 90°). Bottom images are 3D visualizations of the AFM results to enhance the lines which are scanning artifacts. Both scans show the scanning lines (ripples) due to the tip dragging on the surface (horizontal lines on the left-side scan and vertical lines on the right-side scan). This feature, coming from the different tip-sample contact area, can be clearly distinguished from the small and big islands shape. Both images show the same islands and cover the same area. The drift exists but it is much smaller than the height of the islands. Comparing the elongated shape of the higher island and its direction on the different scans, it was proved that they are not influenced by the scanning procedure.

Chapter 6

Results: GaN Thin Films with Different Dislocation Densities

Using c-plane oriented sapphire (Al_2O_3) as a substrate for the epitaxial growth of GaN, the large lattice mismatch between substrate and film typically results in a high dislocation density. The dislocation density can be reduced by in-situ deposition of a SiN_x intermediate layer (see chap. 2). Here, the results of the systematic X-ray diffraction study of the influence of the SiN_x interlayer on the GaN thin film crystalline structure and dislocation density is presented. The diffuse scattering intensity increases with increasing dislocation density. Due to this fact, it was possible to design a non-destructive experimental method for determination of threading dislocations density. The method, based on the Monte-Carlo simulations of the diffuse scattering is done by M. Barchuk and Prof. V. Holý from Charles University in Prague. X-ray scattering experiments have been performed using synchrotron radiation needed to enhance the low diffuse scattering intensity. They were performed in both, coplanar and GID geometry, because of the propagation direction of dislocations (sec. 2.4.1). The results of this study was published in [115]. One of the possible applications (published in [116]) show that the method can be used to determine the threading dislocations density of different types, independently.

Up to now it was not investigated whether in-situ deposited SiN_x interlayer influences the crystalline quality, surface and interface roughness. It is a topic of the next sections to study whether is possible to tune the dislocation density of the thin GaN film without significantly changing its average crystalline quality that this sample series can be used as a model system for studying the correlation of dislocation by the simulations of diffuse scattering.

6.1 GaN thin films: Samples

It was shown that the dislocation density can be reduced by in-situ deposition of a SiN_x intermediate layer with a sub-monolayer coverage [26, 53] (see section 2.4).

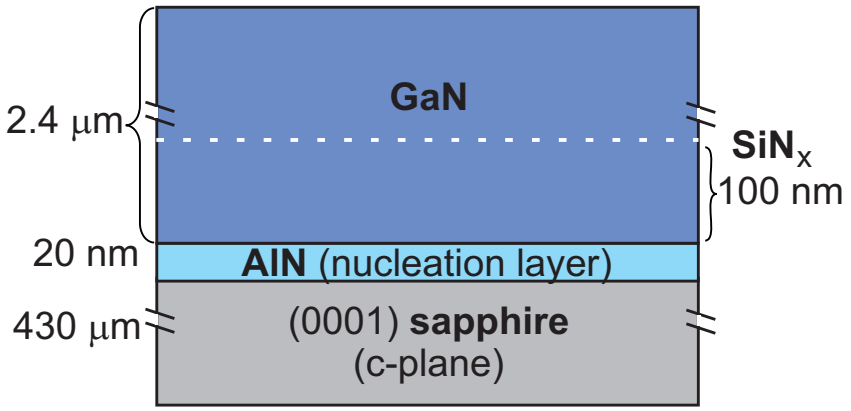

Figure 6.1 Structure of the thin GaN films with different dislocation densities. The deposition time of SiN_x is tuned. An exception is the sample S1 without SiN_x with total GaN thickness of 1.8 μm.

The sample series was grown with the aim that samples have a different dislocation densities. This is done by tuning of the SiN_x deposition time.

A series of GaN thin films with different dislocation densities was grown by metal-organic vapor phase epitaxy in an AIXTRON 200/RF-S horizontal flow reactor [117]. All layers were grown on 2" c-plane (0001) epi-ready sapphire wafers slightly miscut by about 0.3 towards the a-plane. This miscut has been shown to improve the optical properties of the layer [23, 118].

On top of the substrate, an oxygen doped AlN nucleation layer (20 nm) was deposited, followed by a 100nm thick GaN layer (Fig. 6.1). The GaN growth was then interrupted by in-situ deposition of a SiN_x mask, followed by GaN overgrowth. The total thickness of the GaN film is 2.4 μm with an exception for the sample S1 without SiN_x with 1.8 μm thickness. Oxygen doping was done using a mixture of 0.3% oxygen in nitrogen. Before deposition, the substrates went through in situ annealing [25] at 1200 1C for 10 min in a hydrogen atmosphere. A reduced reactor pressure between 70 and 200mbar and the standard precursors trimethyl-aluminum (TMAl), trimethyl-gallium (TMGa) and high-purity ammonia were used to deposit the NL and the nominally undoped GaN layer, respectively. The optimized growth conditions for the oxygen doped AlN nucleation layer and the GaN thin film are described in [26]. The SiN_x intermediate layer has been deposited at a distance to the GaN/AlN interface where the best crystalline quality of the GaN film is expected [119]. The defect density has been systematically varied by tuning the SiN_x interlayer deposition time between 0 and 180 seconds. The dislocation density has been determined from the etch pit density. The values decrease with increasing SiN_x interlayer deposition time and vary between $2.6 \cdot 10^8$ cm^{-2} and $20 \cdot 10^8$ cm^{-2}. Description of the samples is given

in the table 6.1.

sample	t (s)	ρ ($10^8 cm^{-2}$)
S1	0	20
S2	120	7.6
S3	150	4.8
S4	180	2.6

Table 6.1 The thin GaN films with different dislocation densities. First column: sample name, second column: SiN_x deposition time, third column: dislocation densities measured by EPD.

The cross-sectional TEM image (fig. 6.2) clearly shows the reduction of the threading dislocations after propagating through the in-situ deposited SiN_x mask. The deposition times used for in the growth of investigated samples are far below full coverage of the sample surface with one monolayer, i.e. SiN_x interlayer acts as a nano-mask which partially blocks threading dislocations to propagate further to the surface.

6.2 Technical Details of the X-ray Scattering Experiments

Scattering experiments have been performed using synchrotron radiation with the radiation energies of 8 and 10 keV at the SCD-beamline (Angströmquelle Karlsruhe, ANKA) using a 4+2 circle diffractometer with NaI point detector. The samples have been studied by X-ray reflectivity and diffraction in both coplanar and grazing incidence diffraction (GID) geometry. For all reflections, rocking curves and radial scans have been measured.

For the rocking curves, the detector is kept at a fixed position 2θ where θ is the Bragg angle, while the sample angle ω is varied. The momentum transfer q is kept constant. The measurement is sensitive to the angular orientation of the lattice planes. For radial scans, both the detector and the sample angle are varied during the scan with $\Delta(2\theta) = 2 \cdot \Delta(\omega)$. The size of q is varied, but its direction is kept constant. This measurement is sensitive to the distance between the lattice planes.

For the radial coplanar measurements, q is perpendicular to the sample surface and the lattice planes parallel to the surface are probed. In GID geometry, the incident

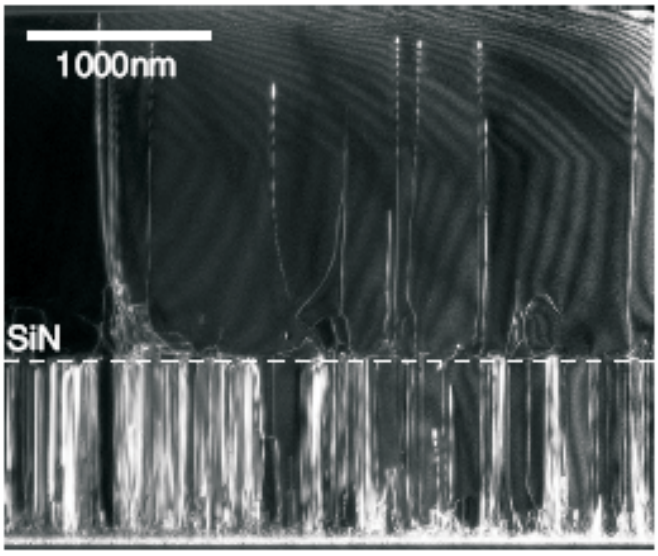

Figure 6.2 Cross-sectional TEM [115, 120] of thin GaN film with an in-situ deposited SiN_x interlayer (dashed line). SiN_x acts as a mask which partially stop threading dislocations propagating to the surface.

and the scattered beam have a very small angle with respect to the sample surface (external total reflection). The Bragg angle is in the plane of the sample, and q is parallel to the sample surface, probing lattice planes perpendicular to the surface.

The radial scans and the rocking curves of the coplanar (0002) and (0004) reflections and the in-plane $(11\bar{2}0)$ and $(10\bar{1}0)$ reflections, as well as equivalent reflections at different azimuth angles have been measured.

6.3 Influence of the SiN_x on the Crystalline Quality of Thin GaN Films

Figure 6.3 show a complete region of the reciprocal space in symmetrical coplanar geometry measured in this study. It could be divided into two parts. First is a part with the q_z between 2 Å^{-1} and 3 Å^{-1} containing the reflections GaN(0002) and AlN(0002). Second part is the higher order diffraction of the first one following the same crystallographic orientation, GaN(0004) and AlN(0004) around the position of q_z=5 Å^{-1}. In between these regions there is a sharp peak of the sapphire substrate Al_2O_3(0006) at q_z=2.9 Å^{-1}. The FWHM of the substrate peak is $6{\cdot}10^{-4}$ Å^{-1}.

The results of the angular scans (rocking curves) widths are presented in the figure 6.4 (a) and figure 6.4 (b) shows the widths of radial scans measured on (0002) and (0004) reflections for both, GaN and AlN layers. Comparing the different peaks, generally, both GaN peaks are sharper than corresponding AlN peaks due to fact that GaN is a signal diffracted from the 1.8-2.4 μm thick film and AlN is coming from the

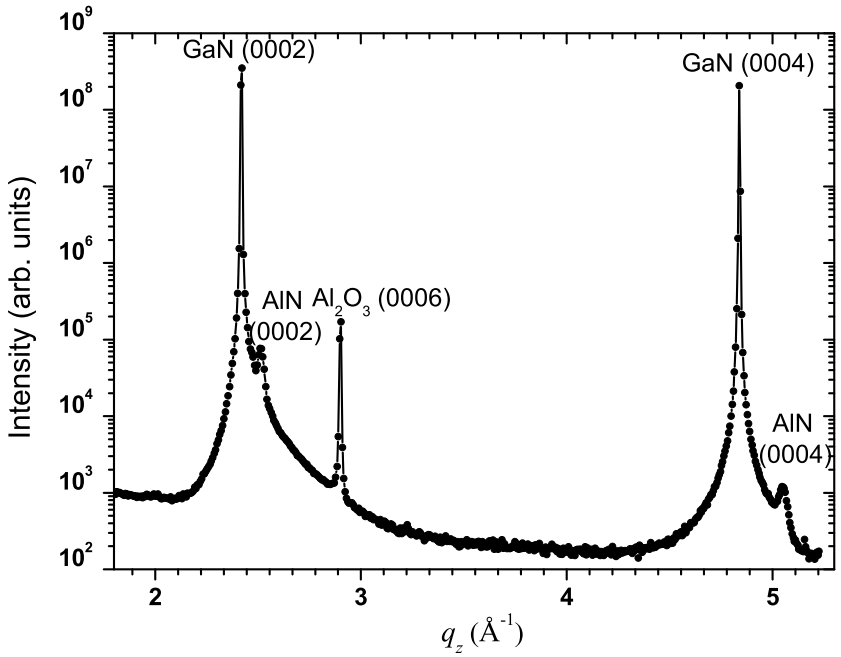

Figure 6.3 Complete region in the radial direction measured in coplanar scattering geometry performed on thin GaN film without SiN (S1). The reflection belonging to GaN, AlN and sapphire are labeled.

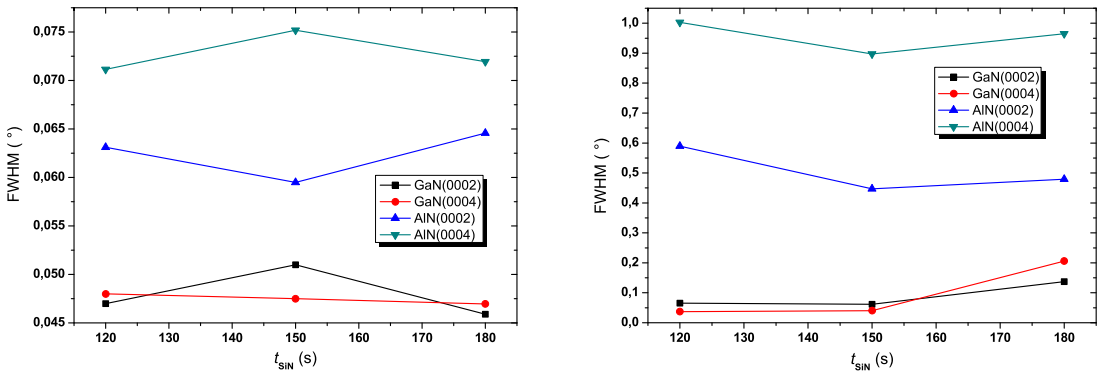

(a) (b)

Figure 6.4 The full widths at the half maximum of the angular (a) and radial (b) scans measured in the coplanar geometry.

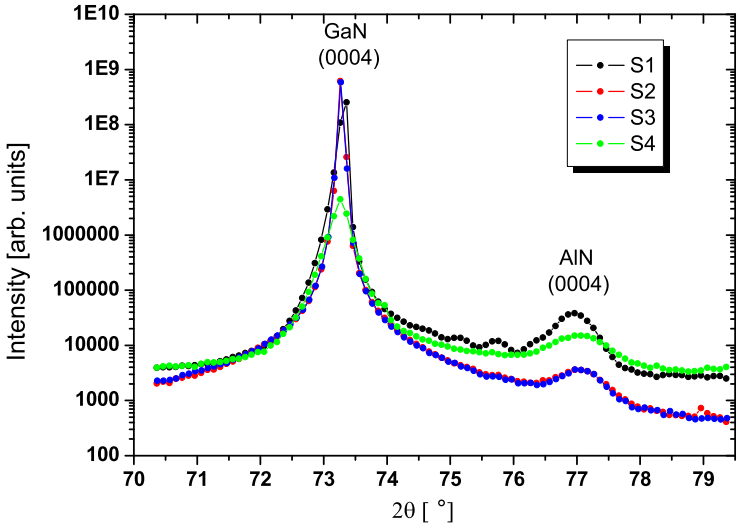

Figure 6.5 The radial scans of the GaN (0004) reflection. The measured data on the sample S1 (solid circles, black) show pronounced oscillations coming from the AlN nucleation layer thickness, while they are not visible on the scans measured on other samples.

nucleation layer with the thickness of about 20 nm. Important is that the width of each peak is similar comparing through samples. This indicates that change of the SiN_x interlayer deposition time does not affect significantly the diffraction response of GaN film in the [0001] crystallographic direction.

Looking to the radial scan of (0004) measured on different samples one can conclude on the interface quality between the AlN nucleation layer and the GaN thin film. Figure 6.5 shows the (0004) radial scans for all of the samples. Two main differences are visible. One is the slope of the diffraction peaks which goes differently for various samples. The slope of the sample S4 with most od SiN_x follows the slope of the sample S1 without SiN_x, while the intensity of GaN Bragg peak for two intermediate samples S2 and S3 drops more rapidly. Another difference is in the oscillations close to AlN Bragg peak, which are well pronounced just for the sample without SiN_x. For the samples with SiN_x, the thickness oscillations are smeared out. The period of the oscillations corresponds to a thickness of 22 nm and the first maximum is at the position of AlN nucleation layer. The result of thickness is in a good agreement with the expected value for AlN nucleation layer. The miscut was not taken into account when measuring, therefore the peak intensities are not correct. The X-ray beam penetrates the entire film under the measurement angle, but the coherence length is smaller than the film thickness. Therefore, no conclusion about the influence of SiN on the coherence can be made (even if some influence might be possible). However, the diffraction profiles of the samples with in-situ deposited SiN_x interlayer are very

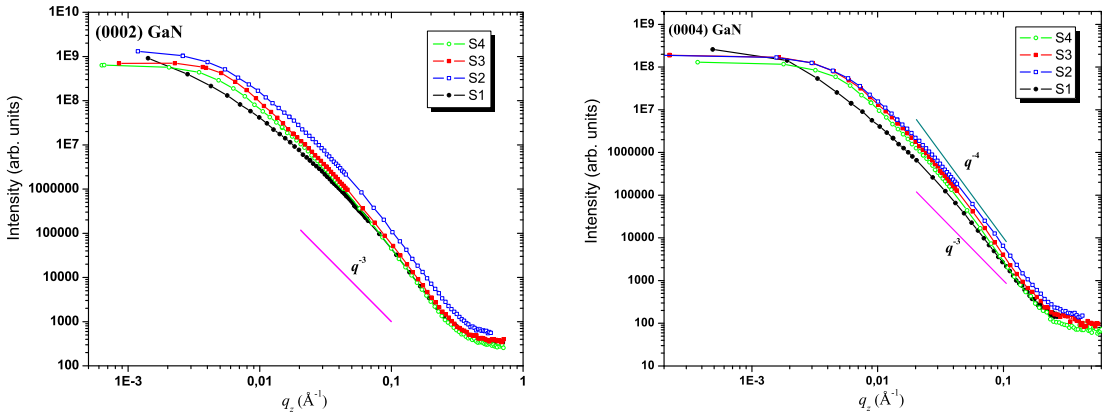

Figure 6.6 The angular scans measured on thin GaN films plotted in the $\log I - \log q$ representation: the rocking curves of (a) GaN(0002) and (b) GaN(0004) reflection. The slopes of the power lows q^{-3} and q^{-4} are shown as reference.

similar from the the Bragg peak width and diffuse part point of view.

Figure 6.6 shows the rocking curves measured on thin GaN films of (a) GaN(0002) and (b) GaN(0004) reflections plotted in the $\log I - \log q$ representation as was proposed in the literature [52] to check whether the tails of the intensity distributions follow the asymptotic power laws expected for scattering from dislocations. For measurements with the open detector, the $I \propto q^{-3}$ law is observed. In the case of a collimated diffracted beam, there is one integration less in reciprocal space which gives rise to the $I \propto q^{-4}$ law. Therefore, the slopes of the power lows q^{-3} and q^{-4} are shown in the plots as a reference. This is a starting point for the study of diffuse scattering from threading dislocations which will be the main topic in the section 6.6. In order to characterize the in-plane properties of epitaxially grown thin GaN films with different dislocation densities, the grazing incidence diffraction were performed and for each sample two different reflections were measured, $(10\bar{1}0)$ and $(11\bar{2}0)$. The equal GID rocking curves $(10\bar{1}0)$ in four different azimuthal directions (fig. 6.7 (a)) show that there is no preferential orientation in thin GaN film confirming perfect in-plane hexagonal symmetry. This is as well shown by radial GID scans of the same reflection measured in various orientations (fig. 6.7 (b)). For comparison, the figure shows the radial scans measured on the samples S1 and S4, without and with most of SiN. The radial Bragg peak position stay the same being independent of azimuthal angle and of SiN_x deposition time as well. Generally, the widths of the rocking curves of the in-plane reflections (fig. 6.8) are about ten times bigger than the rocking curves widths of the reflections measured in coplanar geometry. This might be due to the fact that edge type dislocation density is expected to be approximately an order of magnitude higher than the density of screw type of threading dislocations. Since in-plane reflec-

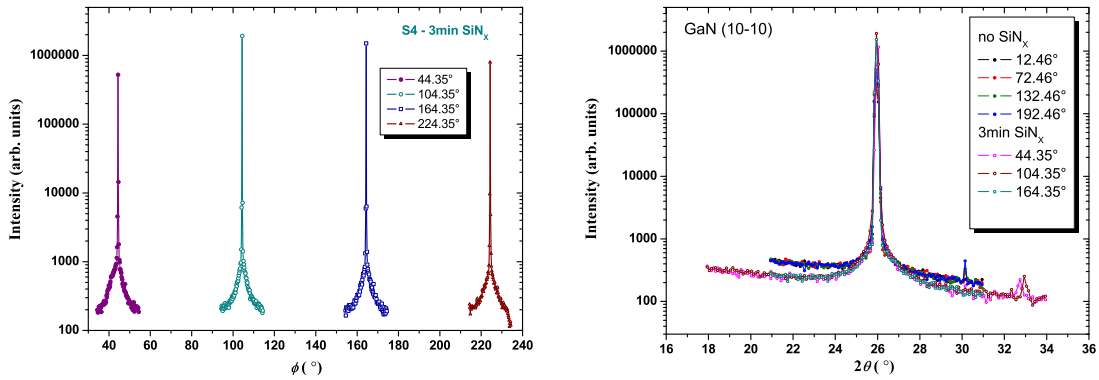

(a) (b)

Figure 6.7 GID angular and radial scans in different azimuthal orientation measured on thin GaN films. (a) the rocking curves of GaN($10\bar{1}0$) in 4 directions measured on the sample S4 and (b) radial scans of the same reflection in various directions measured on the samples S1 and S4 for comparison.

tions are mostly sensitive to the edge type and coplanar mainly to the screw type of dislocations, the difference in the rocking curves widths is directly evidenced.

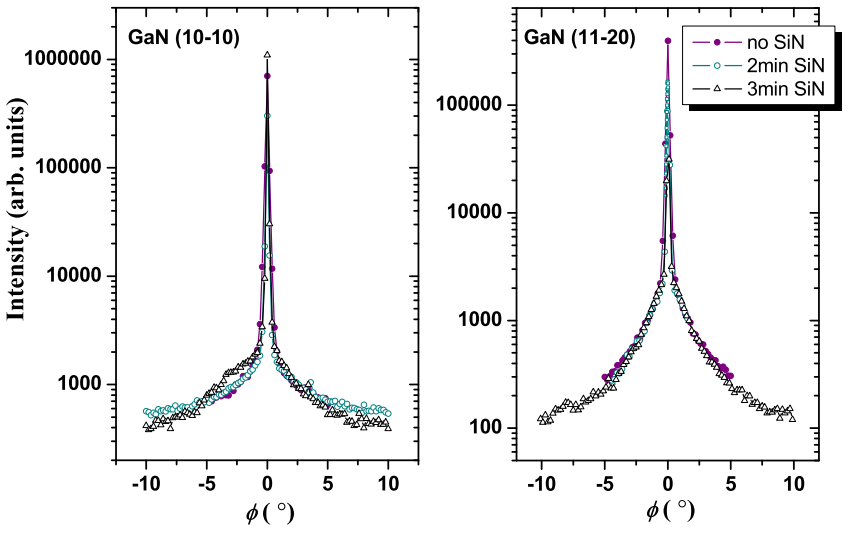

Figure 6.8 GID rocking curves of the ($10\bar{1}0$) and ($11\bar{2}0$) reflections measured on thin GaN films with different dislocation densities depending on the SiN_x deposition time.

6.4 Influence of SiN_x on the X-ray Reflectivity of Thin GaN Films

The aim of this section is to study whether the in-situ deposited SiN_x interlayer influences the surface roughness of the GaN. For this purpose X-ray reflectivity measurements have been performed. The scans were done using the synchrotron radiation energy of 8keV in the symmetrical coplanar geometry (incident angle = exit angle) with the detector position (2θ) in the range between 0.3 and 10 degrees. The scanning step was 0.005° and 0.01° for the sample motor (ω=θ) and detector motor (2θ), respectively. The critical angle for total external reflection of GaN at 8keV is $\theta_c = 0.337°$.

The data measured in the X-ray reflectivity experiments were corrected because of the beam footprint being larger than the sample size as explained in the section 3.2. Than, it was corrected for the background intensity.

After the corrections have been done the maximum of intensity was normalized to one.

Simulations of the experimental X-ray reflectivity curves were performed using the commercial software "Leptos" [121]. For the fitting model used in simulations the relatively thick GaN film with a thin oxide layer on the top was assumed. The roughness of the sapphire substrate can be neglected due to the thickness of GaN. The fitting parameters were the GaN film roughness, the oxide roughness and the oxide thickness. Firstly, the density of the oxide was allowed to vary, than it was fixed to be $3 g/cm^3$. Figure 6.9 shows the results of X-ray reflectivity measurements (open circles) together with the corresponding fit to the proposed model (solid lines), for each sample separately. For better visibility, the simulated curves are offset by the factor of 10. All X-ray reflectivity curves exhibit drop of intensity after exceeding the critical angle ($2\theta_c$) as expected. The slopes of the X-ray reflectivity curves are similar but not the same, comparing the different samples, as can be seen on the figure 6.10. This indicates a variation of the surface roughness, since the slope of reflectivity curve strongly depends on it (sec. 3.2).

The results of the fits are summarized in the table 6.2. The r.m.s. surface roughness of the thin GaN film decreases with increasing SiN_x deposition time and, therefore, with decreasing of the threading dislocation density. The nominal values of the surface roughness vary from 0.4 nm to 0.8 nm. It is shown that the thickness of the oxide stays almost the same independently on the SiN_x deposition time varying between 0.61 nm and 0.83 nm. The r.m.s. roughness of the oxide layer is found to be between 0.15 nm and 0.3 nm with the tendency to decrease with increasing of the SiN_x deposition time.

Figure 6.11 shows the density profiles corresponding to the fitting values. The density is plotted as a function of the sample depth normalized to the GaN film surface. The region where the density changes take place is in the vicinity of the surface, therefore the plot covers the region from 2 nm below up to 2 nm above the

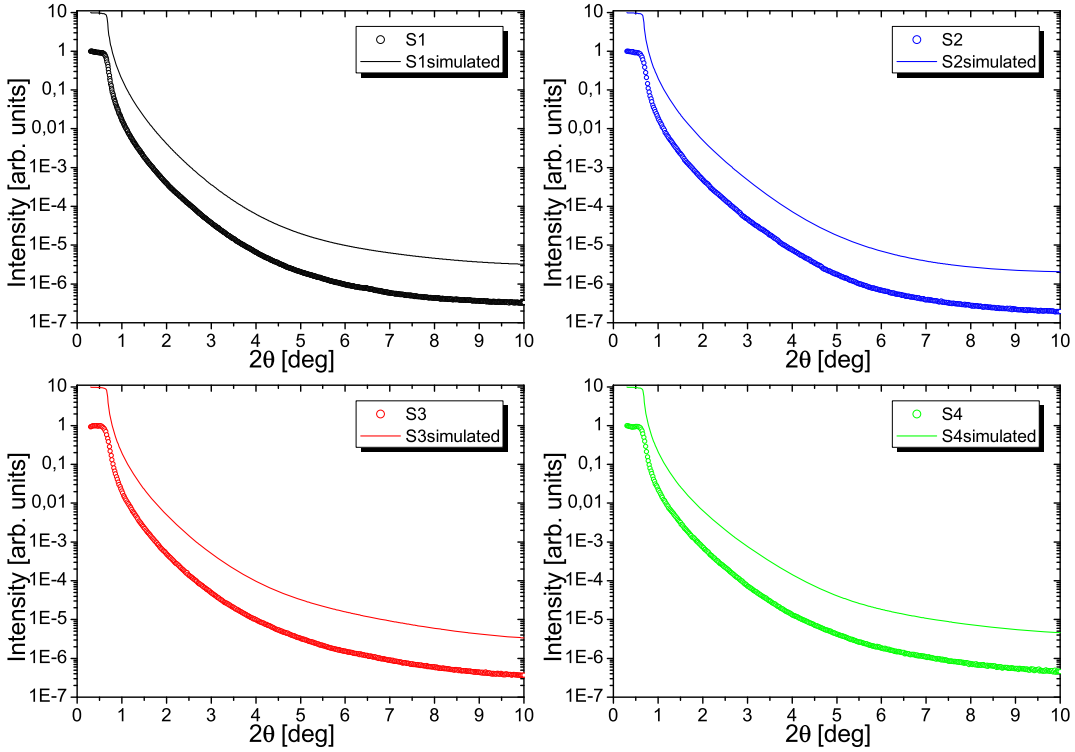

Figure 6.9 The reflectivity curves measured on all samples (marked on the graphs). Experimental data is plotted as scatter (open circles). The corresponding fits of measured data done by *Leptos* software are presented by solid lines. The intensities of the fits shown here are multiplied by the factor of 10 in order to be better visible (otherwise it overlaps with the measured data).

surface. The density drops more steep with decreasing of the surface roughness. This can be seen comparing the samples having the different roughness. The contribution of the oxide layer is highlighted on the inset graph (fig 6.11). Here, the depth is normalized to the oxide surface. The slopes of the density profile follow the oxide roughness (tab. 6.2). The density profile of the model is a result of the contribution of both, GaN film density and oxide density profiles.

In order to discuss the influence of the oxide parameters on the density profile, the density profiles of the oxide (dot+line) together with the oxide thickness (line) are plotted in figure 6.12. This show only the contribution of the oxide. The density profile is a broad Gaussian-like distribution with the maximum lower than the value assumed in the fitting. The maximum value increases with thickness while drops with increasing of the roughness. The oxide thickness does not change much comparing the samples and there would be no significant change of the total density profiles if

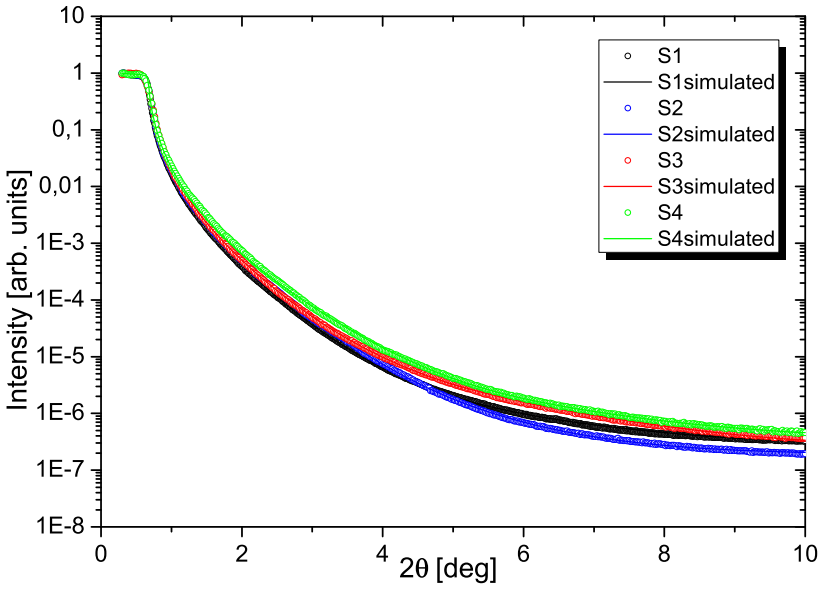

Figure 6.10 The X-ray reflectivity curves compared for all samples.

the average value of 0.71 nm is used. Both, the thickness and the roughness of the oxide have values with the error estimated to be as 10%. In the simulation overlap the several effects which together change the density profile. However, significant is the trend of decreasing of the GaN surface roughness with increasing of the SiN_x deposition time.

Summarizing the results, it is shown that the surface of the GaN film is getting smoother with increasing the SiN_x deposition time. The fitting model contains an overlayer of thin oxide since the samples were exposed on the air. Now, let us compare the results to the literature. It was reported [122] that the native oxide, which is predominantly in the β-Ga_2O_3 form, covers the surface of the GaN film grown on the sapphire substrate. This modification has a density of 5.88g/cm^3 and its crystal structure was determined to be the monoclinic [123]. This density is a twice higher than the oxide density used in the fitting. Beside the Ga_2O_3, the presence of Ga_xO_y with the lower binding energy than of the Ga_2O_3 has been reported [124]. Here, the chemical structure of the oxide was not investigated. However, the oxidation of GaN is kinetically limited process restricted to the surface [125], the GaN film is not strongly perturbed and affected by morphology of the oxide layer.

Let us discuss how the X-rays coherence length compare to the typical features on the GaN surface. The longitudinal coherence length of the X-ray beam in this experiment was determined to be $L_\mathrm{L} = 220$ nm from the definition given in [81]:

$$L_\mathrm{L} = \frac{1}{2} \cdot \frac{\lambda^2}{\Delta\lambda} = \frac{1}{2} \cdot \left(\frac{E}{\Delta E}\right) \cdot \lambda, \tag{6.1}$$

sample	$\sigma_{\text{GaN}}^{\text{r.m.s.}}$ (nm)	t_{oxide} (nm)	$\sigma_{\text{oxide}}^{\text{r.m.s.}}$ (nm)
S1	0.774	0.825	0.285
S2	0.671	0.662	0.304
S3	0.648	0.761	0.188
S4	0.448	0.614	0.166

Table 6.2 The roughness of thin GaN films revealed from the X-ray reflectivity. The third and the fourth columns show a thin oxide thickness and roughness, respectively.

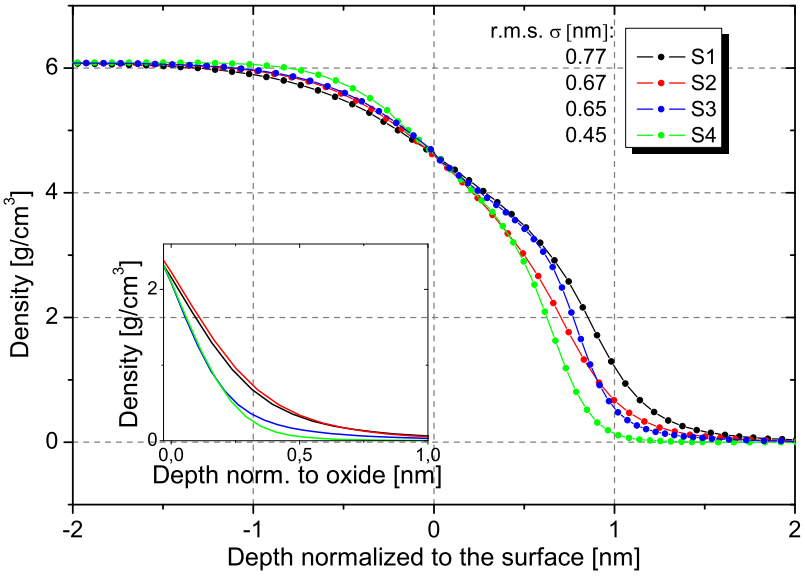

Figure 6.11 The density profiles of the sample models used in the fit of X-ray reflectivity curves. Density is plotted in the function of the sample depth normalized to the surface. Only the region close to the sample surface (±2 nm) is shown.

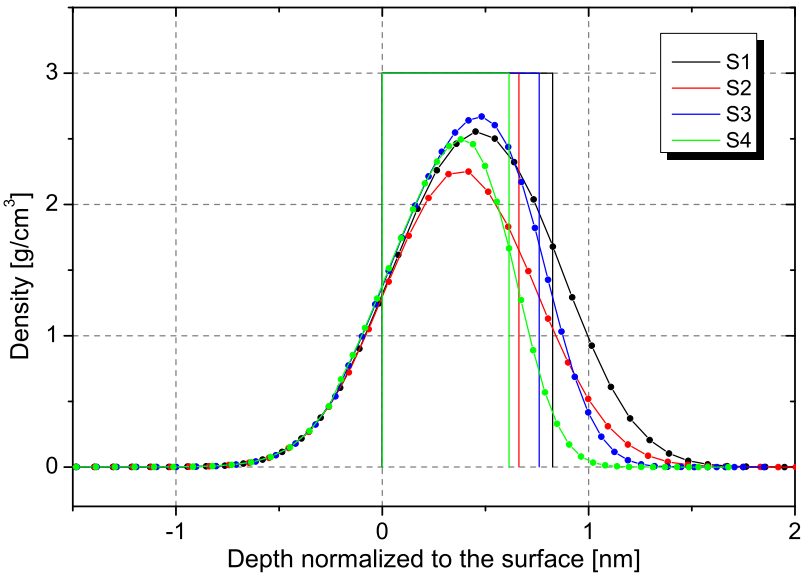

Figure 6.12 The discussion on the influence of the oxide parameters (thickness and roughness) on the density profile compared for all of the samples.

where $\frac{\Delta E}{E}$ is the spectral resolution ($3.5 \cdot 10^{-4}$ for the SCD beam line, ANKA) and λ is the wavelength of X-rays used in measurements (1.5498 Å). The spatial coherence length is determined by [86]:

$$L_{\mathrm{S}} = \lambda \frac{R}{2r_{\mathrm{s}}} \approx \frac{\lambda}{2\Delta\alpha_{\mathrm{i}}}, \tag{6.2}$$

where R is the distance between the source and the sample, r_{s} the size of the source and $\Delta\alpha_{\mathrm{i}}$ is the divergence of the incident angle. L_{S} was estimated to be close to 1 μm. The main features responsible for the surface roughness of GaN films are pits of the threading dislocations and surface steps [41]. For the threading dislocation density of typically 10^8 cm^{-2} (same as 1 μm^{-2}), the average distance between the pits is 870 nm. A typical distance between the surface steps is about 100 nm (as verified by AFM). Comparing the value of coherence length with the typical distances of the surface morphology, the values obtained by this X-ray reflectivity study are describing the local roughness of the surface with the diffuse contribution of the several features outside on the larger scale than the coherence length as results of the averaging over the complete area of the film illuminated by the X-ray beam ($\sim$ 10mm^2).

6.5 Substrate miscut and the tilt of the layers in GaN thin films

The miscut of Al_2O_3 substrate, and the tilt of AlN and GaN layers have been determined by measuring the maximum position of the rocking scans of the specular reflections Al_2O_3(0006), AlN(002) and GaN(002) as a function of the azimuth ϕ. The schematic of the measurements is shown in the figure 6.13. The tilt δ of the lattice planes with respect to the surface causes the the deviation of the scattering vector from the q_z direction. The samples was turned around the surface normal with the azimuthal angle step of 20° and at each position the angular scan was performed. This precession results in the maximum intensities laying on the circle shown in figure 6.13. The peak position of the measured scattering intensity is a projection on the q_z axis.

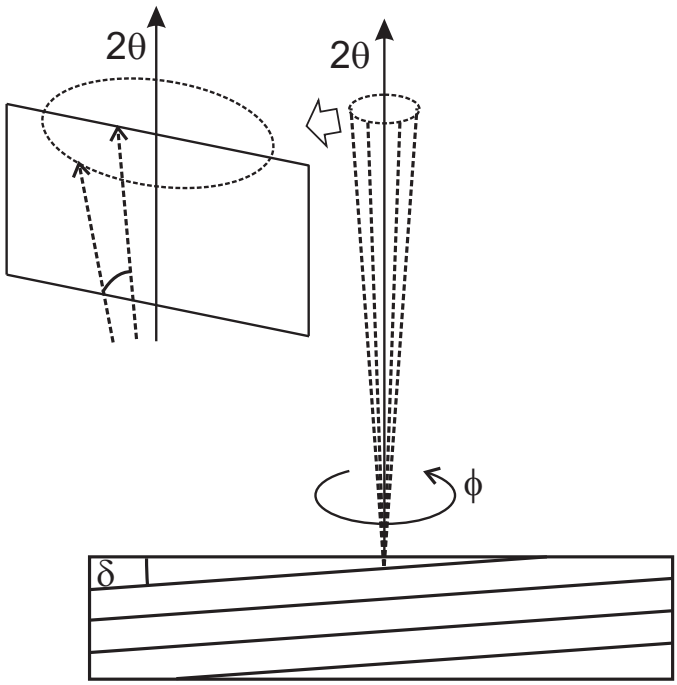

Figure 6.13 Miscut δ influences the tilt of the RLP around the q_z.

Fig. 6.14 (a)) shows the rocking curves of GaN(0002) measured at various azimuthal orientations (the sample being rotated in-plane, around the surface normal). The position of the peak is then plotted as a function of ϕ (6.14 (b) dots). The range of azimuthal angle rotation was restricted to 240° due to the limitation of the experimental setup.

The obtained function follows a sinus. It was fitted to a mathematical description how the peak position θ changes around its central position θ_0 due to the tilt δ of the crystal planes:

$$\theta = \delta \sin(\phi - \phi_0) + \theta_0 \tag{6.3}$$

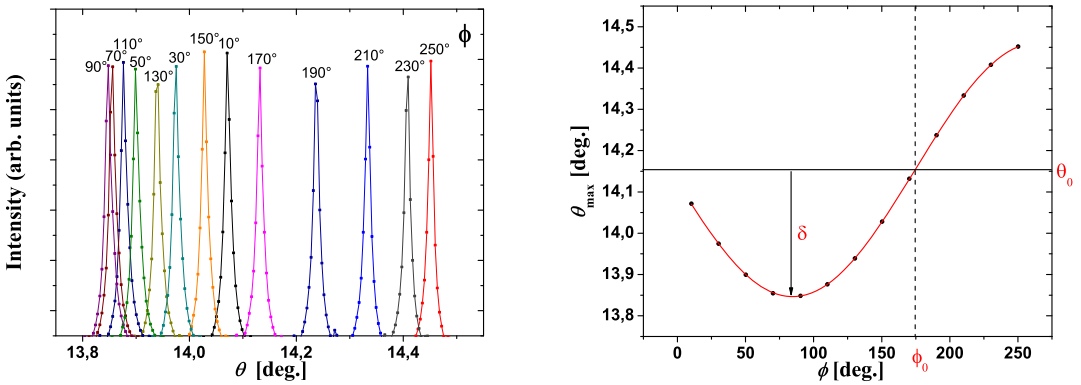

(a) (b)

Figure 6.14 Vertical tilt measured by change of the rocking curve peak position: (a) the rocking curves of GaN(0002) reflection measured at various azimuthal direction and (b) the peak maxima as a function of the azimuthal angle ϕ. (dots). A line represents the fit.

where ϕ_0 is the azimuthal angle corresponding to the peak central position θ_0 (fig. 6.14 (b)). The fit of experimental data to the equation 6.3 is presented by the curve in fig. 6.14 (b). The amplitude of the observed sinus function presents the tilt of the layer or the miscut, when the substrate peak is measured. For the example shown here the fit results are as follows, the central peak position, corresponding azimuth and the tilt of the GaN film are equal to $\theta_0 = 14.154°$, $\phi_0 = 174.542°$ and $\delta = 0.307°$, respectively.

Fig. 6.15 shows the results of the tilt of thin GaN film (dots), AlN buffer layer (squares) and the miscut of the sapphire substrate (triangles) measured for two extreme samples: (a) without SiN_x (maximum dislocation density) and (b) with 180s deposition time of SiN_x (minimum dislocation density). The experimental data are presented as dots and the fit curves by lines. Both graphs exhibit a good agreement between fit and experimental data for all layers in the film. Vertical lines mark the crystallographic orientation of the $[11\bar{2}0]$ plane and the equivalent direction of the planes from the same crystallographic family. Their positions are known from the grazing incidence diffraction performed on the samples before the study of the tilt and miscut. For all layers, the tilt (absolute maximum of the fit) is oriented along the GaN$[11\bar{2}0]$ direction (see fig. 6.15 dashed line).

The sapphire substrate has a miscut of $(0.257 \pm 0.002)°$, slightly deviating from the optimum 0.3° reported in the literature [19,23,24]. The vertical tilt $(0.295 \pm 0.002)°$ of the AlN layer and the tilt $(0.308 \pm 0.002)°$ of the GaN layer are close to the optimum value. They have not exactly the same value, indicating that the lattice mismatch between GaN and AlN is partially compensated by a tilt of the unit cell. The observed values have been found to be independent of the SiN_x deposition time.

A model of the thin GaN film grown above the AlN buffer layer on the c-plane

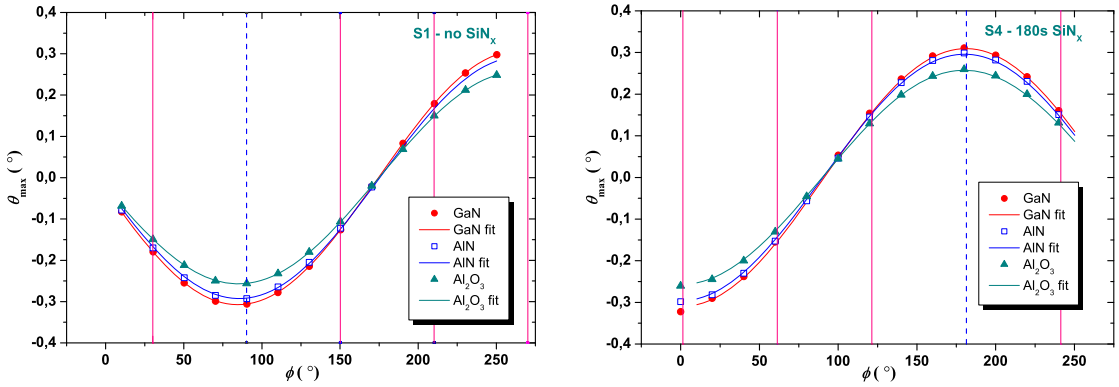

Figure 6.15 Results of the vertical tilt of thin GaN film (dots), AlN buffer layer (open squares) and the miscut of the sapphire substrate (triangles) for the samples (a) S1 without SiN_x and (b) S4 with most of SiN_x deposited. The curves represent the fits of the simulated data. Vertical lines show the orientation of $[11\bar{2}0]$ plane (dashed) and the planes from same crystallographic family (solid).

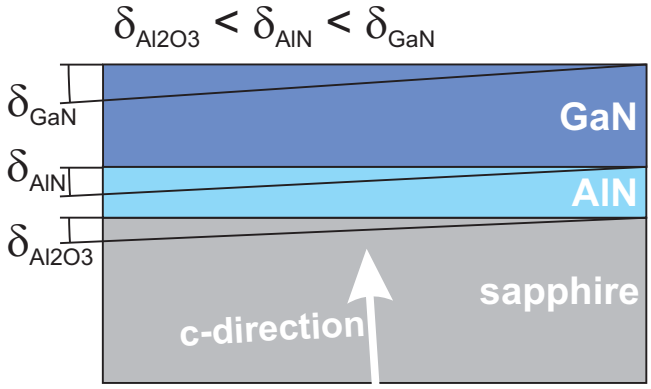

Figure 6.16 Miscut of the sapphire substrate and the vertical tilt of AlN and GaN epitaxial layers.

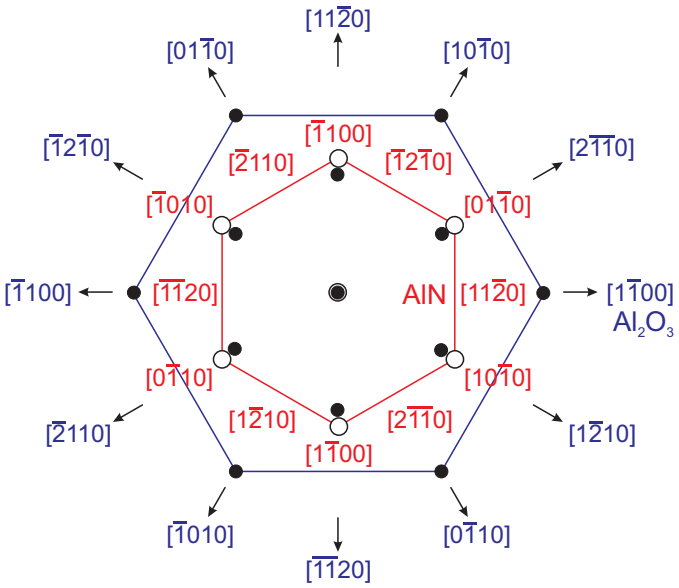

Figure 6.17 The crystallographic in-plane directions of a c-AlN epitaxially grown on the c-sapphire (top view). The in-plane directions of sapphire are marked after [128] and the epitaxial orientation relationship of single crystalline AlN with respect to the sapphire substrate is same as for GaN, AlN $[11\bar{2}0]$ ∥ Al_2O_3 $[1\bar{1}00]$ [127].

oriented sapphire is shown on the figure 6.16. The tilt of the layers follows the orientation of the substrate miscut with increasing value from the bottom to the top, $\delta_{Al_2O_3} < \delta_{AlN} < \delta_{GaN}$.

The reason for the benefits from the epitaxial growth on the sapphire substrates with a certain small miscut has generally only been speculated upon [126], but it is not explained yet up to my knowledge. It might be that the epitaxial growth on the miscut substrate is better related to a strain relaxation. There is a question, is it due to the compensation of the lattice mismatch or due to the strain relaxation at steps. Figure 6.17 shows the in-plane crystallographic orientation of AlN grown on the sapphire. The growth direction of both the film and the substrate is [0001]. AlN $[11\bar{2}0]$ is oriented parallel to the Al_2O_3 $[1\bar{1}00]$ defining the epitaxial relationship [127].

If we plot a c-plane interface between AlN and sapphire at the room temperature and consider two parallel networks of relaxed unit cells forming the crystal lattices trying to fit one on the top of another, than the resulting picture is as shown in the figure 6.18. The red hexagons represent AlN unit cells connecting the N sites. The big blue hexagons show the basis of the sapphire unit cell and smaller blue hexagons connect the Al sites intentionally suggesting the place where the AlN hexagons should sit. One AlN hexagon (circle 1) is fixed to be perfectly placed in the middle of the Al_2O_3 hexagon (arbitrary centered). Looking in direction of AlN$[11\bar{2}0]$, after the period of $15{\cdot}d_{11\bar{2}0} = 15\sqrt{3}\cdot a_{AlN}$, there is another AlN hexagon (circle 2) which approximately

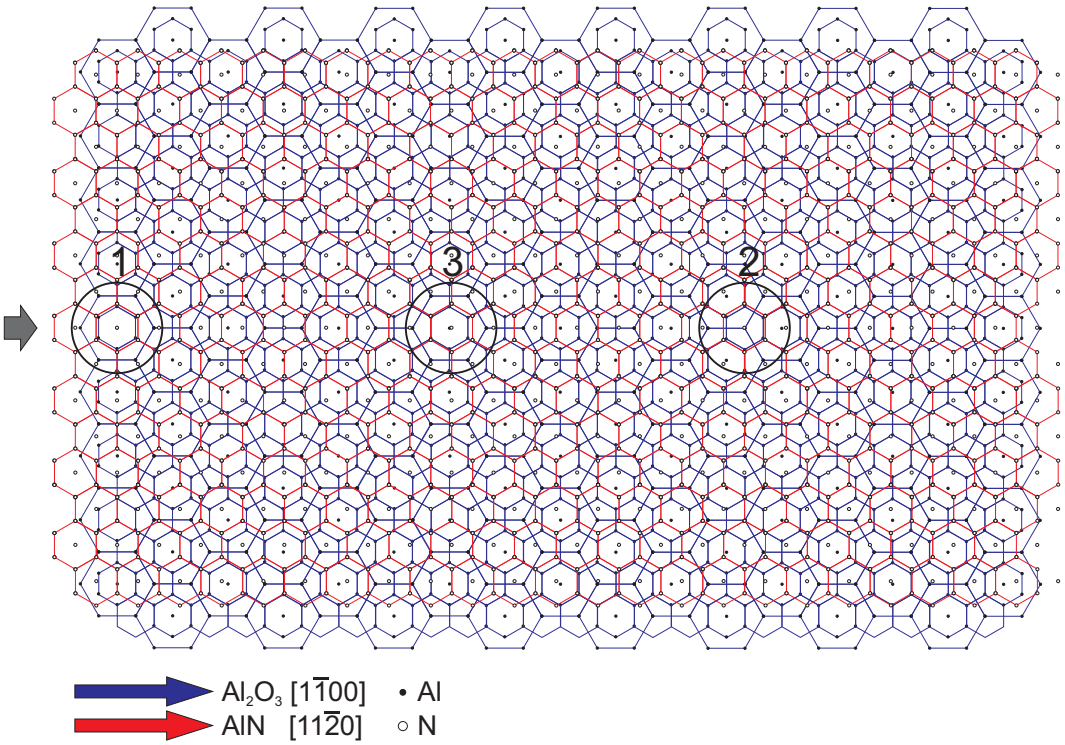

Figure 6.18 A top view of the in-plane arranging of the c-AlN epitaxially grown on the c-sapphire. The big blue hexagons represent the base of Al_2O_3 unit cell while the small blue hexagons connect the Al sites (black) which are to be fit with N atoms (white) from the AlN (red hexagons). The arrows show the direction of the miscut Al_2O_3 [1$\bar{1}$00] ∥ AlN [11$\bar{2}$0]. This image corresponds to the case of the room temperature.

matches on the sapphire. The lattice mismatch considered above is valid for the room temperature. The situation is a bit different at elevated temperatures. At the growth temperature of 950° C for growth of AlN buffer layer, the mismatch of AlN grown on the sapphire become smaller, because thermal expansion of the sapphire is stronger than of AlN as shown in the figure 6.19. The data used here is taken from the reference [129]. For AlN, the bulk value is used employing the analogy with GaN for which was reported that at temperatures higher than 800 K, the thermal expansion coefficients and the lattice parameters of thin film coincide with the bulk values [130]. The lateral lattice parameters at 950° C are $a_{\mathrm{AlN}} = 3.1259$ Å and $a_{\mathrm{Al_2O_3}} = 4.7941$ Å for AlN and sapphire, respectively. Calculating the length of repeating approximately matching hexagons in the same direction as above we found that it is reduced down to the $8{\cdot}d_{11\bar{2}0}$ (circle 3) what almost doubles the opportunity for epitaxy without the misfit dislocations.

Our theoretical consideration of the lattice mismatch confirms the results of HRTEM study of the GaN/sapphire interface in the work of Ning et al. [127]. But, it is hard to relate this result to the favorable 0.3° miscut of the sapphire substrate.

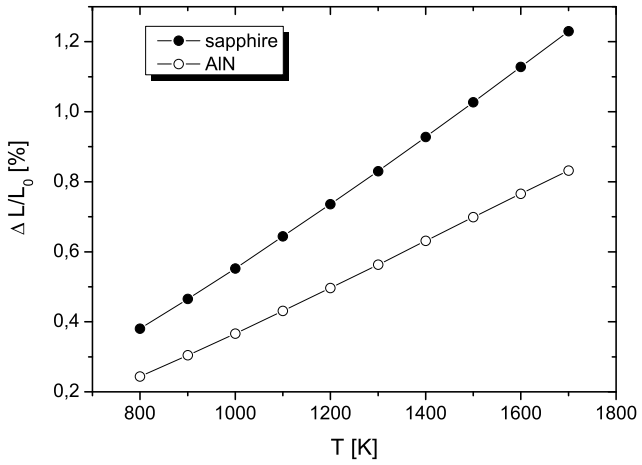

Figure 6.19 The linear thermal expansion of AlN and sapphire laterally.

Could it be that the preferable substrate miscut is better related to the partial strain relaxation at step edges? First, we should know what is expected for the sapphire surface steps. The AFM measurements of the annealed sapphire surface show regular steps and terraces [131–133]. The steps are self-organized in mainly two directions $[1\bar{1}00]$ and $[11\bar{2}0]$ [131]. The temperatures of annealing vary between 1000° C and 1400° C. The time of annealing procedure is different from article to article with the values of 1h up to 12h. Also, the steps and terraces structure appear on the sapphire substrate surface after the temperature ramp in the standard growth procedure of GaN at 1050° C grown at c-Al_2O_3 as shown by high resolution TEM study in [127]. For nominally non-miscut sapphire, the average width of the terraces is expected in the range of 40-65 nm [131, 132]. The steps height is determined to be mostly equal to the minimal distance between Al and O layers in the sapphire unit cell, 0.216 nm [131], what corresponds to the value of $\frac{1}{6}c_{Al_2O_3}$ reported in [127].

For the substrates with certain miscut of few degrees and for the substrates without miscut, but annealed at temperatures higher than 1400° C, the step bunching takes place. In our case of the sapphire substrates with relatively small miscut (0.257°) thermally cleaned at 1200° C for only 10 minutes, it is not likely for the step bunches to form.

Figure 6.20 a) shows the schematic of the surface with the steps and terraces of the sapphire crystal without any miscut. The growth direction [0001] (arrow) is perpendicular to the terraces, parallel to the surface normal (dashed line). Figure 6.20 b) represents the sapphire surface with the miscut which practically compensates the inclination of the stepped morphology. In this case, the c-direction is again perpendicular to the terraces but off the surface normal. Figures don't show the average surface, but the long range instability. The miscut angle δ can be derived from the

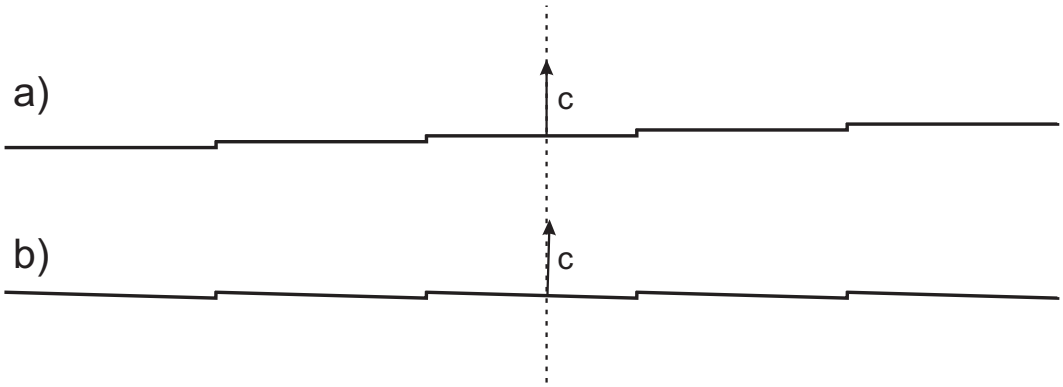

Figure 6.20 A schematic of the sapphire surface with the steps and terraces a) without any miscut and b) with the miscut which compensates the inclination of the stepped surface morphology. The hight of the steps are ten times bigger than in reality with respect to the step width.

ratio of the step hight and the terrace width:

$$\delta = \arctan\left(\frac{\text{step height}}{\text{av. terrace width}}\right). \tag{6.4}$$

For nominally non-miscut substrates, the step height is equal to $\frac{1}{6}c_{Al_2O_3} = 0.216$ nm as mentioned before. The terrace width depends more on annealing temperature than on the time of annealing. The higher is the annealing temperature, shorter is the terrace width. Typical values of the width are from 65.5 nm for the temperature of 1000° C [131] to the 43.6 nm for the annealing temperature of 1100° C [132]. Considering the thermal cleaning temperature of 1200° C applied on the sample series studied here [26,134], the terrace width is expected to be approximately 40 nm. The miscut angle compensating the inclination formed by steps is than equal to $\delta = \arctan 0.216/40 \approx 0.3°$. Assuming the regular steps without step bunching, the terrace width value which corresponds to the miscut of 0.257° measured on the sapphire substrate in this study is 48.4 nm.

The difference between miscut of the sapphire substrate and the vertical tilt of AlN buffer layer is 0.038°, and further between vertical tilts of AlN and GaN film is 0.013°. It could be explained by the fact that lateral lattice parameter of the GaN unit cell is bigger than for the AlN and, further the length of $\sqrt{3}a_{AlN}$ is bigger than the sapphire lateral lattice parameter. Therefore, tilt of the layers is getting bigger trying to compensate the mismatch. This difference is much larger between AlN and Al_2O_3 than between GaN and AlN. This might be the reason for the bigger difference between AlN tilt and the sapphire miscut than the difference between GaN and AlN tilts.

6.6 Diffuse Scattering from Threading Dislocations

In the previous sections, it was shown that it is possible to tune the dislocation density of the thin GaN film without significantly changing its average crystalline quality. The change of the in-situ deposition time of SiN_x does not affect the diffraction signal of both rocking curves and radial scans in coplanar scattering geometry, as well as in grazing incidence diffraction. Also, there is no preferable orientation indicating the in-plane isotropy of the GaN hexagonal unit cell. The X-ray reflectivity of thin GaN films shows the trend of decreasing of the GaN surface roughness with increasing of the SiN_x deposition time, but this changes do not affect the diffuse scattering around the Bragg peak far from the reflectivity conditions and from the reciprocal space origin. The tilt of GaN and AlN layers follow the miscut of the sapphire substrate and the values stay unchanged with increasing the SiN_x deposition time. The experimental results show the strong influence of the SiN_x interlayer deposition time on a defect density, while the GaN average unit cell is relaxed and perfectly hexagonal, independent of the deposition time. Therefore, the here studied sample type is a perfect model system for studying the correlation of dislocations by a new approach of kinetic Monte-Carlo simulations of the diffuse scattering caused by dislocations [115].

6.6.1 Theoretical Model of Diffuse Scattering from Dislocations

The problem of the determination of the dislocation density in GaN and related materials from X-ray diffraction data were investigated in [52, 97, 135–138]. Metzger et al. [97] determined the dislocation density from the broadening of diffraction curves using the equations 3.46. The dislocation type has been derived from a Williamson-Hall plot. The limits of this rather simple model was already discussed in sec. 3.3.1.

A direct connection between the tensor components of lattice microdistortion and major dislocation types was found by Ratnikov et al. [135]. They used two (Bragg and Laue) diffractions in order to determine stress tensor components from the width of the diffraction curves. To use this method, it is necessary to perform measurements with different setups, and to handle tensor quantities. In addition, only thick GaN epitaxial layers can be examined in such way.

It was already mentioned that Kaganer et al. [52] developed their approach for determining the density of threading dislocations perpendicular to the surface, including their spatial correlation. The density of dislocations is determined from the width of the calculated x-ray diffraction profiles. The type of threading dislocations follows from the asymptotic behavior of the rocking curve in $\log I$-$\log q$ representation. The stress relaxation at the sample surface was not included. Recently, Kaganer et al. [136] applied the Monte Carlo simulation method to determine the density of dislocations. This work was restricted to the symmetrical Bragg case diffraction. Only misfit and screw threading dislocations were taken into account in their calculations. This is not sufficient because due to the surface relaxation edge threading dislocations

give rise to diffuse scattering in symmetric diffractions as well. With increasing film thickness, threading dislocations, rather edge ones, play the main role in x-ray peak broadening, while the influence of misfit dislocation dramatically drops down.

Holý et al. [137] simulated diffraction curves of symmetrical diffractions for screw and edge types of threading dislocations in the frame of the microdiffraction imaging method. Daniš et al. [138] estimated the density of pure screw dislocations perpendicular to the surface including the correlation in their positions. These works can be considered as a background for our theoretical model.

In our study [115], a numerical Monte Carlo simulation of the dislocation positions and types was used. The reciprocal space intensity distribution was computed taking into account both screw and edge threading dislocation, perpendicular to sample surface. The surface relaxation was included in the displacement field. A comparison of simulated and measured reciprocal space maps allows us to determine the densities of particular threading dislocation types. For the simulation of the reciprocal-space distribution of scattered intensity we assume that (i) the measured intensity is averaged over a statistical ensemble of all configurations of the dislocations and (ii) the distance sample-detector is large so that the far-field limit can be used. The validity of assumption (i) depends on the density of dislocations, on the coherently irradiated sample surface S_{coh} of the primary radiation and on the total size of the irradiated sample surface S_{s}. The far-field approximation is valid if the diameter of S_{coh} is much smaller than the diameter of the first Fresnel zone, which can be approximated by $\sqrt{R\lambda}$, where R is the sample-detector distance and λ is the wavelength.

First of all, the random positions of a number of dislocations crossing the S_{coh} is generated for each type. The displacement field of all dislocations in S_{coh} are calculated assuming a linear superposition [139]:

$$\mathbf{u}(x,y,z) = \sum_{\alpha=1}^{5} \sum_{j=1}^{N_\alpha} \mathbf{u}^{(\alpha)}(x - x_j^{(\alpha)}, y - y_j^{(\alpha)}, z), \tag{6.5}$$

where $\mathbf{u}^{(\alpha)}(x,y,z)$ is the displacement vector in point (x,y,z) due to a dislocation type α ending at the sample surface. The scattering intensity depends only on the component of the total displacement field parallel to the diffraction vector $\mathbf{h}$. In symmetrical XRD this is just z component which is for the screw and edge type, respectively:

$$\begin{aligned} u_z^{(\mathrm{s})}(\mathbf{r}) &= \frac{b_z^{(\mathrm{s})}}{2\pi} \arctan\left(\frac{y}{x}\right), \\ u_z^{(\mathrm{e})}(\mathbf{r}) &= \frac{\nu}{1-\nu} \frac{\mathbf{r}\cdot\mathbf{b}^{(\mathrm{e})}}{2\pi} \frac{z + 2r(\nu-1)}{r(r-z)}, \end{aligned} \tag{6.6}$$

where ν is the Poisson ratio. The intensity of the X-ray wave scattered by this part of the sample was calculated using the far-field limit and kinematical approximation:

$$I(q) = \left| A \int_{S_{\mathrm{coh}}} \int \mathrm{d}x\mathrm{d}y \int_{-r}^{0} \mathrm{d}z \mathrm{e}^{-\mathrm{i}\mathbf{h}\cdot\mathbf{u}(\mathbf{r})} \mathrm{e}^{-\mathrm{i}\mathbf{q}\cdot\mathbf{r}} \right|^2, \tag{6.7}$$

where A is a constant containing among other parameters the amplitude of the primary wave and the susceptibility. The final step is the convolution of the simulated intensity distribution with the resolution function of the experimental setup.

6.6.2 Comparison of Measured and Simulated Reciprocal Space Maps

The diffuse scattering of the (0002), (0004), $(10\bar{1}4)$, $(10\bar{1}0)$ and $(11\bar{2}0)$ reflections has been studied. The diffuse scattering of the coplanar reflections is dominated by contribution of mainly the screw type dislocations propagating in [0001]. Similarly, the diffuse scattering of the in-plane reflections is mostly caused by pure edge type of dislocations going in the $[11\bar{2}0]$ direction (see sec. 2.4.1). That was a reason to measure exactly the chosen reflections.

We have measured reciprocal space maps on the sample series. Our collaborators from Charles University of Prague have developed and applied a Monte-Carlo simulation of the defect configuration and numerically computed the non-averaging amplitude of the scattered wave. From the set of experimental RSMs in symmetrical (0004) diffraction we could separate the contributions from pure screw and edge dislocations and compare them and their main cuts with the simulated maps.

The contributions of edge and screw dislocations follow different power laws. The tails of the experimental data are well described by the sum of these contributions. The results of our approach are consistent with the ones published in [52]. From the analysed RSMs and rocking curves the dislocation densities have been calculated for all measured samples and the results correspond well to the values determined from the etch pit density (tab. 6.1). It was confirmed that the dislocation density decrease with increasing SiN_x interlayer deposition time.

Figure 6.21 shows the reciprocal space maps of (0004) measured on two extreme samples (a) S4 - with most SiN and (b) S1 - without SiN. The shape of the peak tells that broader diffuse scattering must be from higher dislocation density. Similarly, the reciprocal space maps of $(10\bar{1}4)$ reflection is shown in the same figure, (c) measured on the sample S4 and (d) measured on the sample S1.

Figure 6.22 depicts the q_x- and q_z-cuts through the Bragg (0004) and $(10\bar{1}4)$ peak. On each graph the results of different samples are compared. The cuts are shown in the $logI - logq$ representation. The dots are measured data points and the lines belong to the simulations. The results of this new method for determination of the threading dislocation densities is given in the table 6.3. The accuracy of the resulting dislocation densities is between $\pm 12\%$ and $\pm 23\%$.

In order to apply a new developed method for determining the dislocation densities, we have measured the reciprocal space maps in grazing incidence geometry to study diffuse scattering from the edge type threading dislocations [116]. Figure 6.23

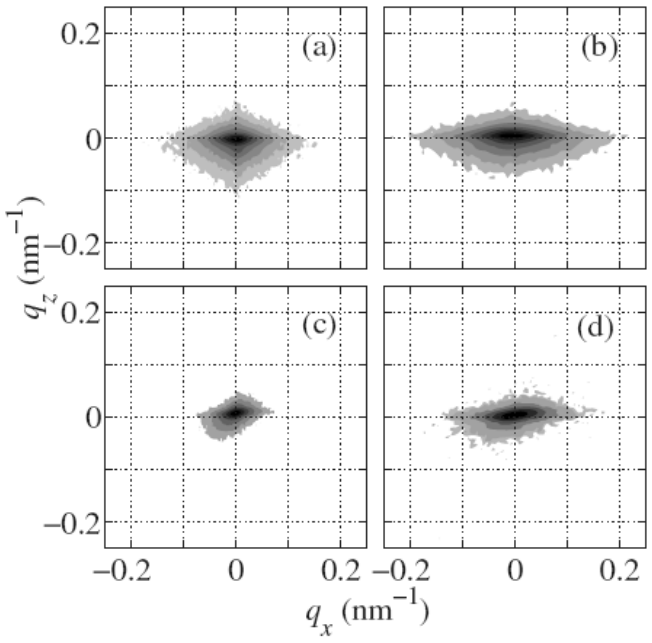

Figure 6.21 The diffuse scattering from threading dislocations - measured reciprocal space maps: a) sample S4 - (0004) reflection, b) sample S1 - (0004) reflection, c) sample S4 - $(10\bar{1}4)$ reflection, d) sample S1 - $(10\bar{1}4)$ reflection [115].

sample	**screw type** (10^8 **cm**$^{-2}$)	**edge type** (10^8 **cm**$^{-2}$)	**together** (10^8 **cm**$^{-2}$)
S1	2.1	20.6	22.7
S2	1.6	6.9	8.5
S3	1.3	4	5.3
S4	1.1	1.7	2.9

Table 6.3 Densities of screw and edge threading dislocations determined from the measured intensity distributions.

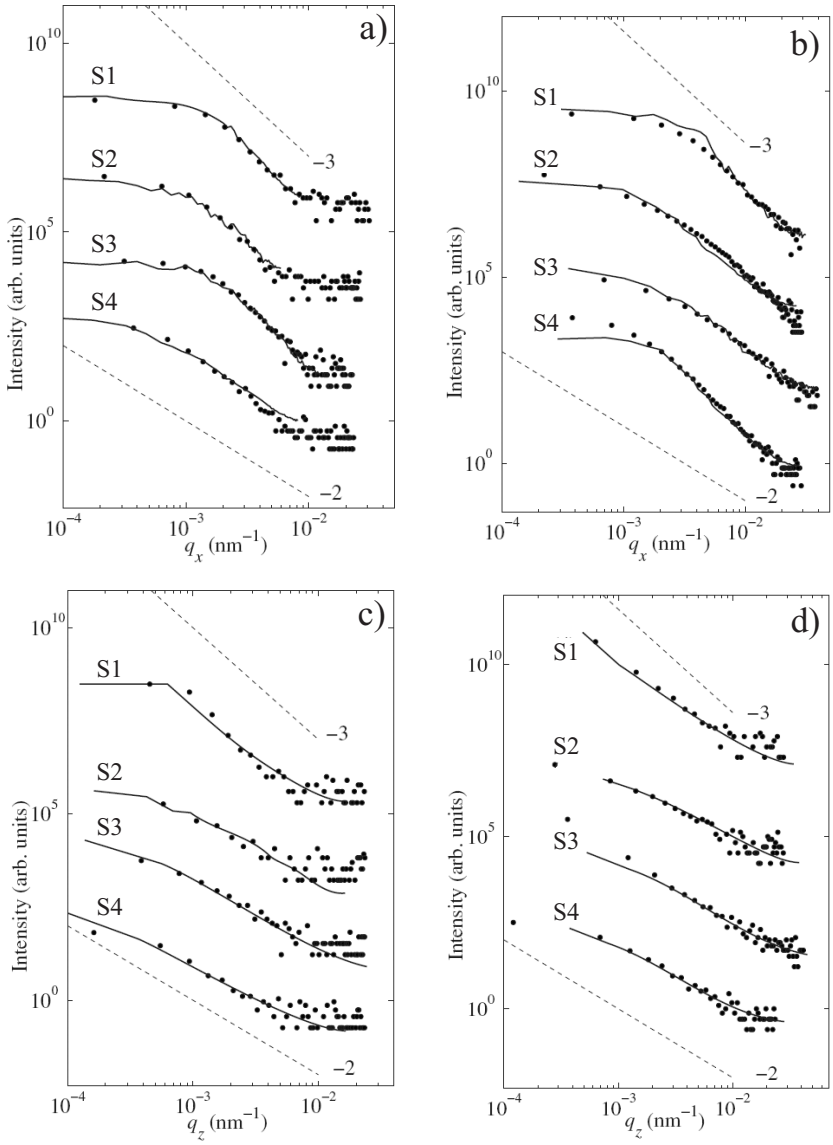

Figure 6.22 Upper row: The experimental (dots) and theoretical (solid lines) q_x scans of a) (0004) and b) $(10\bar{1}4)$. GaN diffraction compared for the samples S1 (the highest dislocation density) to S4 (the lowest dislocation density). Bottom row: Similar situation for the q_z scans of c) (0004) and d) $(10\bar{1}4)$ GaN diffraction [115].

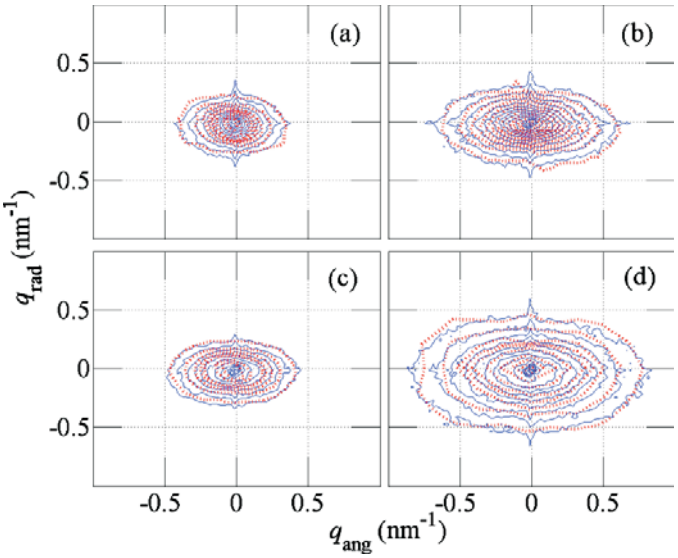

Figure 6.23 The measured (blue, solid) and simulated (red, dashed) reciprocal space maps of $(10\bar{1}0)$ (a) and (b) and $(11\bar{2}0)$ (c) and (d) for the sample S4 (left) and for the sample S1 (right) [116].

shows the measured (blue, solid) and simulated (red, dashed) reciprocal space maps of $(10\bar{1}0)$ (a) and (b) and $(11\bar{2}0)$ (c) and (d) for the sample S4 (left) and for the sample S1 (right). The intensity step is $10^{0.25}$ in the logarithmic scale. A good agreement between the measurements and fitting results can be observed. Since diffuse scattering in GID geometry depend almost completely on the edge dislocation density, it was possible to determine it with relatively high accuracy (error$\sim \pm 9\%$). The results of the edge threading dislocation densities are given in the table 6.4.

The main advantage of the GID application of the developed method for determination of the dislocation density is based on the absence of the screw type contribution to the scattered intensity. Therefore, a determination of the pure edge type dislocation density is possible and by this the result is more reliable. The optimum characterization of the epitaxial GaN film would be in combination of both the coplanar (to cover the surface relaxation by edge type dislocations) and GID approach(to cover the pure edge type dislocations) for the best accuracy.

sample	**edge type** (10^8 **cm**$^{-2}$)
S1	20.6±1.9
S2	7.0±0.6
S3	4.1±0.4
S4	2.1±0.2

Table 6.4 The edge threading dislocations densities determined from the measured intensity distributions in grazing incidence diffraction.

Chapter 7

Results: Evolution of InGaN Quantum Dots During Capping

7.1 Evolution of InGaN Quantum Dots During Capping

The GaN capping layer applied on the InGaN quantum dots (QDs) grown by Stranski-Krastanow (SK) mode dissolve them, while growth by segregation method, depositing the InGaN below the critical thickness of nucleation layer (wetting layer) for forming the islands in SK mode, results in more stabile and more In-rich quantum dots. In this chapter, the results of systematic X-ray diffraction study on a series of the samples with the various capping layers (GaN or InGaN) grown on two different temperatures are presented. The X-ray diffraction results are combined with the results of atomic force microscopy investigation of freestanding and overgrown QDs surface topographs. By obtaining the information in reciprocal space(XRD) and in real space (AFM) one may have a much better insight in the real structure, strain, shape and other properties of the InGaN nanometer-sized islands.

The large strain of 11% between GaN and InN, freestanding InGaN quantum dots tend to dissolve during GaN capping (fig. 7.1) [140]. Therefore, it is not clear which structures (the original quantum dots or microscopic inclusions of the segregated material due to the dissolution of the dots) are really responsible for the luminescence.

For the quantum dots grown by the Stranski-Krastanow method, the TEM studies on the capped InGaN samples indicate that the dissolution process is not a continuous shrinking of the islands but that the island density decreases with increasing cap thickness. One of the reasons of dissolving the islands grown by SK mode is due to fact that growth temperature of high crystalline quality GaN capping layer is at 1050°C and it is known that In dissolves after about 700°C. This is improved by recent growth studies [141, 142] in which the QDs are stabilized. The growth indicates a different mode than a Stranski-Krastanow. The segregation method by phase separation of InGaN have been suggested. A detailed characterization was

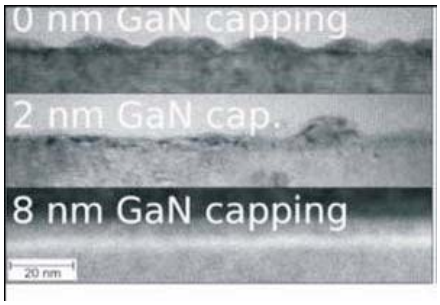

Figure 7.1 TEM of SK-grown quantum dots dissolving during capping.

pending.

7.1.1 Growth of the InGaN Quantum Dots

A novel method of the growth of InGaN quantum dots that are stabile during overgrowth has been developed by the group of Prof. Hommel IFP,Uni-Bremen [141,143]. It was shown that, by overgrowth of formation layer at same growth conditions, it is possible to have nanostructures stabilized and protected for further growing of high crystalline GaN capping layer at high temperature. The capping layer was improved in the work of Ch. Tessarek et al. [142].

Growth of the InGaN quantum dots can be described as follows. Thin GaN film of about 2μm was epitaxially deposited on the c-sapphire (Al_2O_3) substrate forming the template for growth of quantum dots (grown independently prior the growth of quantum dots). Additional thin GaN layer of 300 nm has been grown before dots deposition. The growth was in H_2 atmosphere at 1050°C. The general growth parameters for all samples are: NH_3-flux 3000 sccm, N_2 5000 sccm and reactor pressure of 700 torr. This is followed by deposition of the few monolayers of $In_xGa_{1-x}N$ with thickness of 1.5-2nm which is below the critical thickness for forming the wetting layer in SK-growth mode. It is predicted that the island formation is caused by phase separation (see 2.5.2) due to spinodal decomposition [142]. Following this model, $In_xGa_{1-x}N$ decomposes into regions with a low In and with a high In content. Then, desorption of the regions with high In content takes place since is not stable in the temperature range around 650°C. Just the regions with low In content should remain on the surface which form the island structures. The growth conditions for InGaN quantum dots are as follows: TMI-flow of 263 sccm, TMG-flow of 3 sccm, leading to In/(In+Ga)=0.82 (molar gas phase fraction), V/III-ratio=3827, the nominal layer thickness of 1.5 nm.

As capped structures are necessary for electrically driven devices, the goal is to have $In_xGa_{1-x}N$ quantum dots protected from dissolving, ready for subsequent GaN capping at high temperature. For that reason, the growth was continued by deposition of formation layer (FL) of $In_yGa_{1-y}N$, where $y < x$. Thickness of the formation layer was 7 nm and the growth conditions are kept unchanged as for growth of quantum

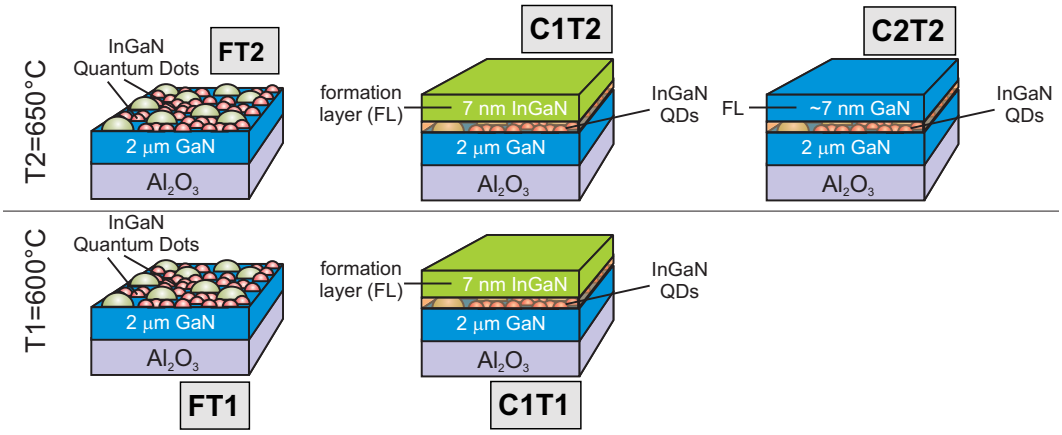

Figure 7.2 InGaN quantum dots samples. Growth temperatures T1 and T2 are marked. Left column: freestanding InGaN QDs, middle: overgrown with InGaN, right: overgrown with GaN.

dots.The growth conditions InGaN as formation (capping) layer are: TMI-flow of 23.4 sccm, TMG-flow of 4.5 sccm, leading to In/(In+Ga)=0.21, V/III-ratio=11070, SiH_4 flow of 0.1 sccm with the nominal layer thickness of 7 nm. For the capping with pure GaN, following growth parameters were used: TMG-flow of 6 sccm, leading to V/III-ratio=10516, SiH_4 of 0.1 sccm.

The systematically grown sample series is schematically shown in the figure 7.2. The growth temperature were plotted versus the sample structure.

7.1.2 Experiments on the InGaN QDs

The sample series was measured by atomic force microscopy (7.2). The aim was to investigate the surface morphology of both non-capped and capped quantum dots grown at different temperature. Surface morphology of the samples is described by quantities such as the quantum dots vertical and horizontal sizes, their shape, density and distribution. Information in direct space resulted from AFM will be used further to support the explanation of the X-ray diffraction data measured in grazing incidence and coplanar geometries on quantum dots together leading to a complete picture of their real structure.

The AFM does not provide the information about the chemical composition in the islands, strain between nanostructures and the buffer layer, interdiffusion of different material and misorientation of dots. Therefore, InGaN quantum dot samples were measured by X-ray scattering methods. First of all, grazing incidence diffraction has been performed to study their structure. Results of radial and angular scan and reciprocal space maps, as well, are presented in the section 7.3. In addition to the GID study, the asymmetrical X-ray diffraction in coplanar geometry was done (7.4). This should complement the results from AFM and GID and answer to the chemical composition and strain which effects are overlapped in the results of GID.

7.2 AFM of Freestanding and Overgrown InGaN Quantum Dots

Here, the study of both freestanding and overgrown InGaN quantum dots by atomic force microscopy is presented. First, the experimental and technical details are described. Then, the results of the AFM experiment are presented, first the general observations and after the specific details, separately. The features of AFM results are compared by the growth temperature and by different structure of the sample. Finally, a possible model of the overgrowth of InGaN quantum dots based on AFM results is proposed.

7.2.1 AFM of InGaN Quantum Dots: General Overview

An overview of the AFM results on the sample series of InGaN quantum dots is shown in figure 7.3. The AFM images are ordered in such a way that growth temperature is plotted versus complexity of the sample structure. The rows correspond to the growth temperatures T1= 600 °C (down) and T2= 650 °C (up). The structure of the samples is sorted in the columns (from left to right): freestanding (F) quantum dots, quantum dots overgrown by InGaN (C1) and quantum dots overgrown by GaN (C2)). The colour scale of the AFM images corresponds to the z-scale indicated.

Generally, the AFM images show two types of nanostructures: big islands of low density (type B) and small islands almost completely covering the sample surface (type A). These two different types of structure have been evidenced for all samples. The islands have a broad size spread and they are non-homogeneously grown. Their distribution is influenced by the steps on the buffer layer surface. For some of the samples it was difficult to find a plateau between the step bunches. Comparing the images of different sample, one can observe that surface morphology changes. The type B islands are elongated for the freestanding dots samples (see Fig.7.3 (a) and (d)), independent of the deposition temperature. When overgrown (Fig. 7.3 (b), (c) and (e)), they become more round and their lateral size is reduced. The type A islands at freestanding samples are much more pronounced when grown at temperature T2 (Fig. 7.3 (a)) than at T1 (Fig. 7.3 (d)). By overgrowing, their height increase and that more when grown at temperature T1 (same fig. e). Both type of islands are randomly distributed with an exception of the sample C2T2 where type B islands show the forming of chains (sec. 7.2.6). The detailed shape and size of the islands will be described separately in the following sections. The lateral size an the height of the islands have been determined from the line profiles of the AFM images. The profiles were taken at different positions of the image and following different directions. Densities of both type of islands have been estimated by counting them over the scanned area and then multiplying to have the density expressed in the units per cm^2.

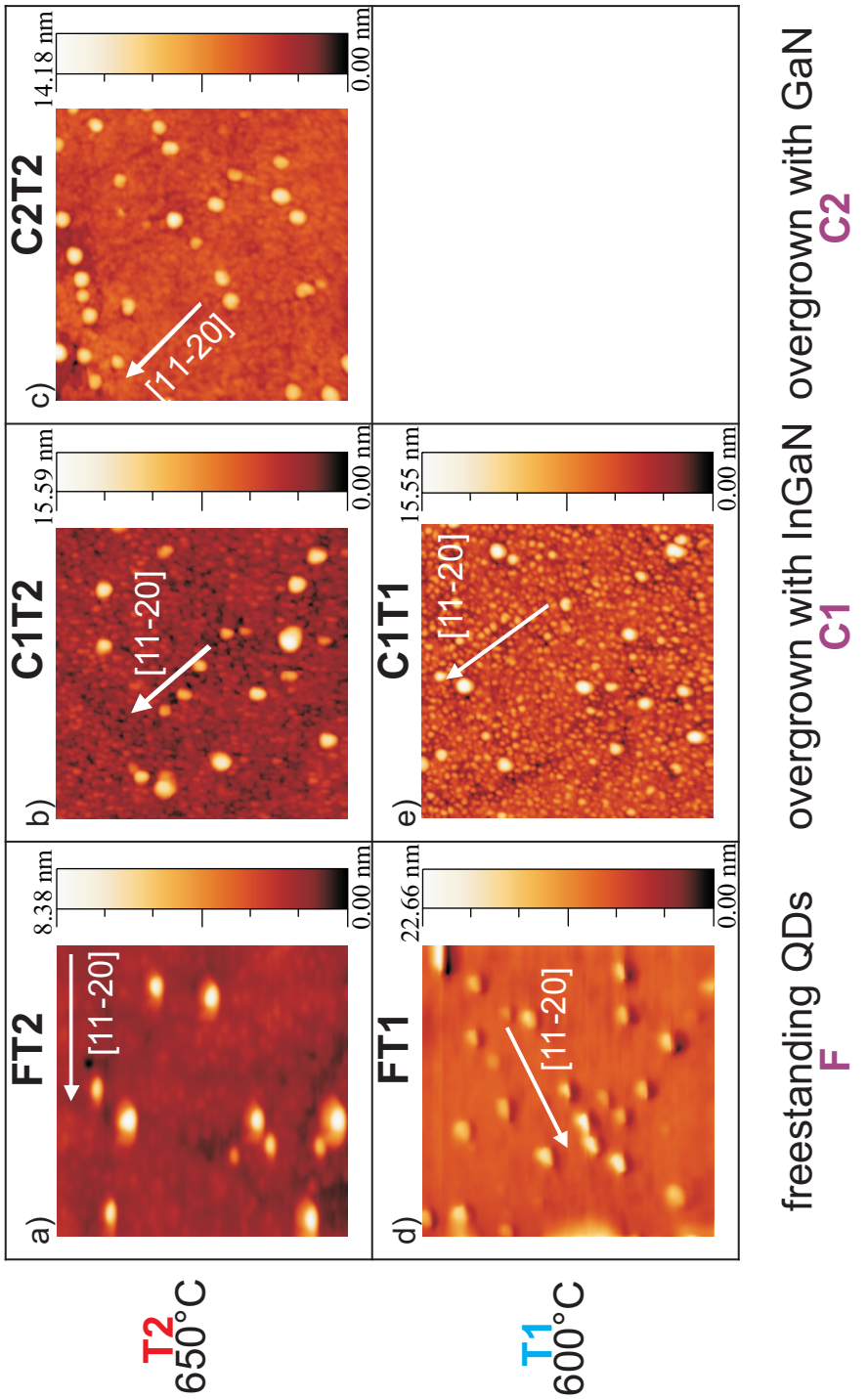

Figure 7.3 Overview of the atomic force microscopy results on InGaN quantum dots samples. The complexity of the sample structure is presented by columns: the freestanding (F) quantum dots and the overgrown quantum dots by InGaN layer (C1) and by GaN (C2). The rows correspond to the growth temperature of the quantum dots: 600°C (T1) and 650°C (T2).

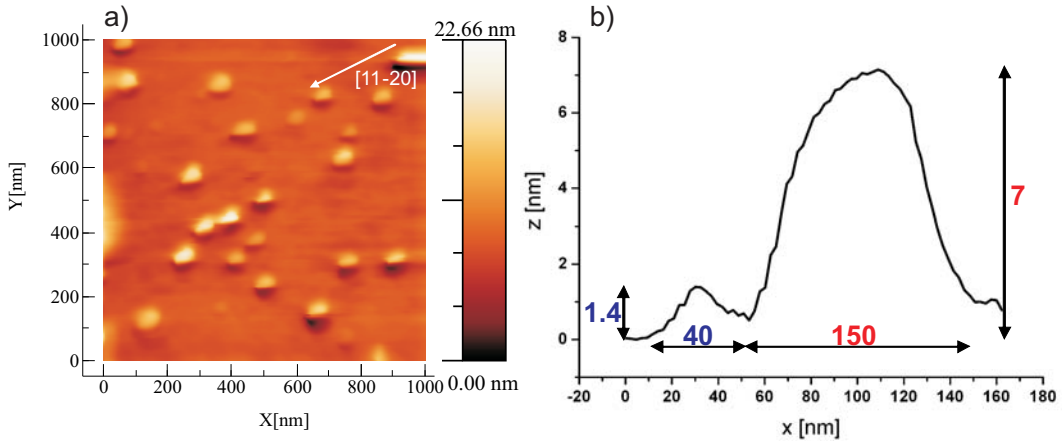

Figure 7.4 Atomic force microscopy on **freestanding** InGaN quantum dots grown at **600°C** (sample **FT1**): a) plan view with the colour scale and b) representative profile of the sample surface with islands size measures.

7.2.2 Freestanding InGaN Quantum Dots Grown at 600°C-FT1

The AFM image of the sample FT1 with the freestanding InGaN quantum dots is shown in figure 7.4 (a). The figure 7.4 (b) shows a representative line profile along the sample surface. The type A islands with the average height about 1.5nm are less well defined being superposed by the substrate surface morphology. There is a certain transition between the islands and surface waviness. Laterally, type A islands have the average diameter of 40nm. Pronounced type B islands with the average height of 7nm are randomly distributed on the surface. Density of type B islands is estimated to be $\approx 2 \cdot 10^9 \mathrm{cm}^{-2}$. The basis shape of type B islands is elongated in the direction of $[11\bar{2}0]$ forming an ellipse with the relation between major and minor diameter as follows $\frac{a}{b} = \frac{3}{2}$, where average a and b are 150nm and 100nm, respectively. Figure 7.5, showing a 3D AFM, is presented to enhance the visibility of the nanostructures placed on the sample surface.

7.2.3 Freestanding InGaN Quantum Dots Grown at 650°C-FT2

Figure 7.6 shows the plane view AFM and the representative line profile measured on the surface of another sample with the freestanding InGaN quantum dots, grown at the higher temperature, FT2. In comparison to the sample FT1, AFM on the sample FT2 shows that type A islands are much more pronounced covering the sample surface almost completely. Their average height is 1nm. Density of the dots is estimated to be $3 \cdot 10^{10} \mathrm{cm}^{-2}$. Lateral dimensions of type A islands stay the same, round shape with 40nm in diameter.

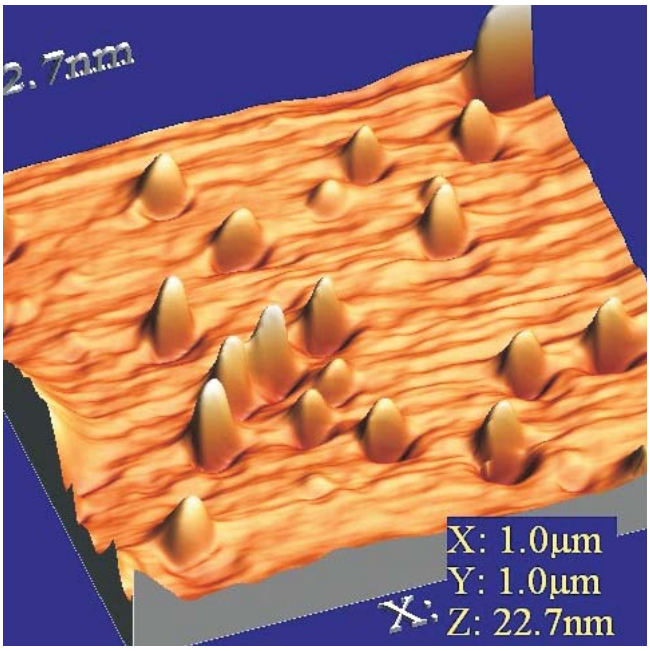

Figure 7.5 3D view of AFM on **freestanding** InGaN quantum dots grown at **600°C** (sample **FT1**).

The type B islands are elongated in a same manner as for the sample FT1, with the ratio between the major and minor axis being 3:2. Just, for the sample FT2, they have smaller dimensions laterally: average a and b are 110nm and 75nm, while the height remains practically the same, 7nm. The elongation is again following the direction of $[11\bar{2}0]$. Random distribution of the islands is kept, while density of $\approx 1 \cdot 10^9 \mathrm{cm}^{-2}$ is lower than for the sample FT1.

7.2.4 By InGaN Overgrown InGaN Quantum Dots (600°)-C1T1

Figure 7.8 shows the surface of the sample with $In_xGa_{1-x}N$ quantum dots overgrown by $In_yGa_{1-y}N$ layer. In contrast to the overgrowth of quantum dots grown by Stranski-Krastanow mode, instead of completely covering and surrounding the dots, formation layer, which is grown above the dots layer, might grow more on the top of the quantum dots following the surface morphology of the freestanding dots sample FT1.

Type A islands kept the round shape, laterally, just with the diameter of 25nm, which is smaller than for the type A islands of the freestanding sample grown at the same temperature, FT1. The average height of type A islands is 5nm. Their density is estimated to be $9 \cdot 10^{10} \mathrm{cm}^{-2}$.

Lateral shape of the type B islands is changed from elongated to the weakly elongated - more round (see fig. 7.8). Their lateral dimensions are reduced to the

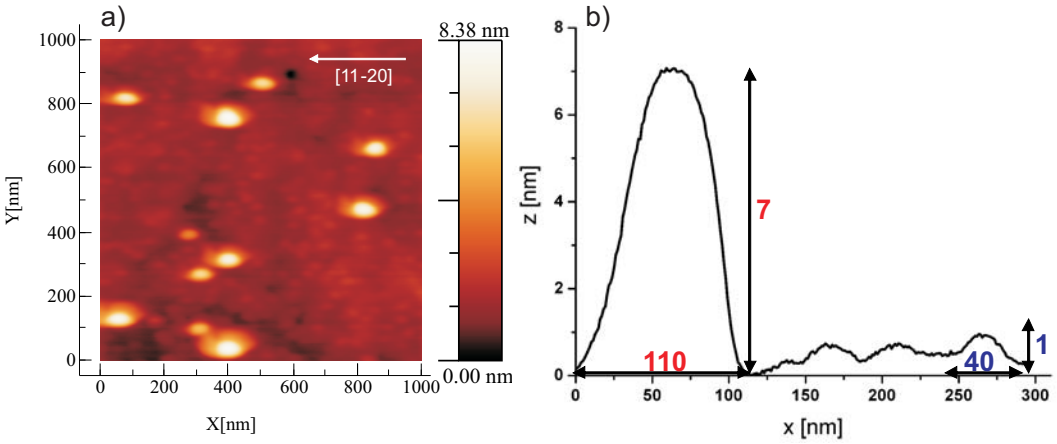

Figure 7.6 Atomic force microscopy on **freestanding** InGaN quantum dots grown at **650°C** (sample **FT2**): a) plan view with the colour scale and b) representative profile of the sample surface with islands size measures.

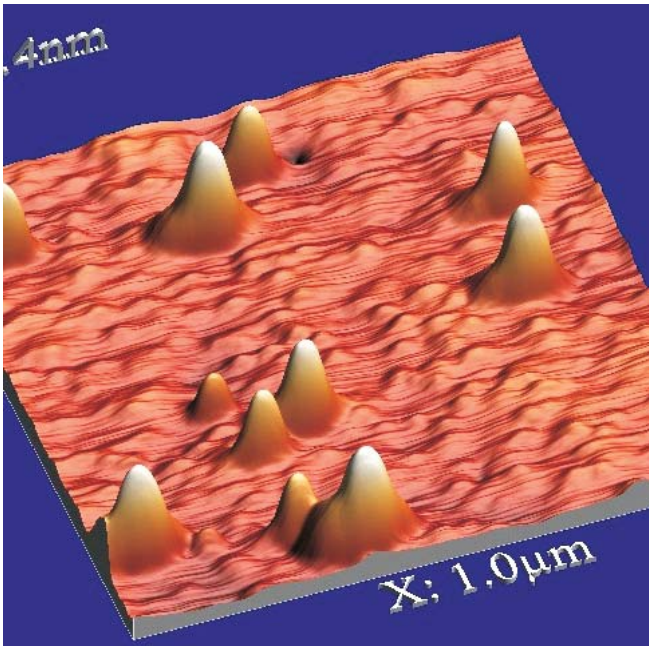

Figure 7.7 3D view of AFM on **freestanding** InGaN quantum dots grown at **650°C** (sample **FT2**).

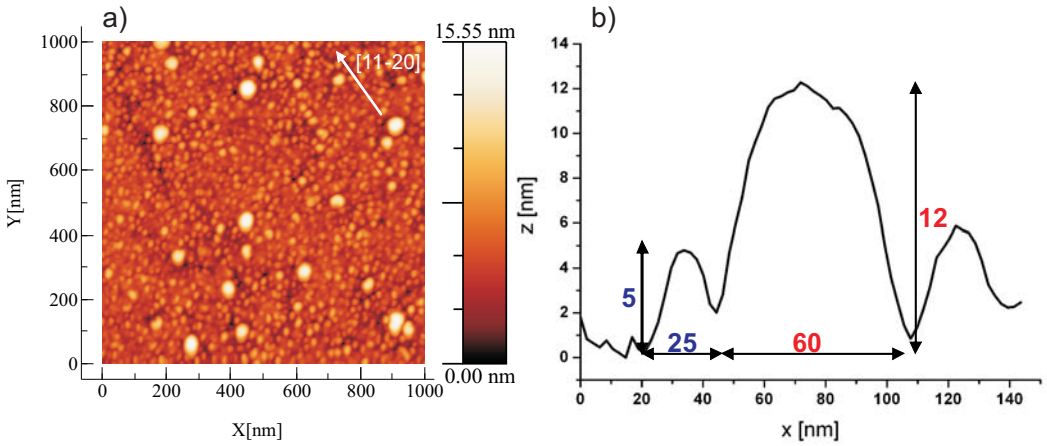

Figure 7.8 Atomic force microscopy on $In_xGa_{1-x}N$ quantum dots grown at **600°C overgrown by $In_yGa_{1-y}N$** (sample **C1T1**): a) plan view with the colour scale indicated and b) representative profile of the sample surface with islands size measures.

diameters of a =70nm and b =60nm, while average height is 12nm. Density of the randomly distributed overgrown type B islands remains the same as for the sample with freestanding quantum dots FT1.

7.2.5 By InGaN Overgrown InGaN Quantum Dots (650°)-C1T2

The AFM results on the sample C1T2, with by InGaN overgrown quantum dots, are shown on the figures (7.10a- the plane view and same fig. b-the line profile, 7.11- 3D view). Only difference to the sample C1T1 is the growth temperature. Similarly to the AFM results of the sample C1T1, it was observed that overgrowth take place more on the top of the islands, following the surface morphology of the FT2. The sample surface is in general smoother than for the sample grown at lower temperature. The root mean square roughness is 0.8nm.

The type A islands are higher than the freestanding ones but less high than overgrown at lower temperature. The average height is 2.7nm. Their lateral shape is round with the diameter of 30nm which is reduced comparing the freestanding case FT1 but less in respect to the overgrown by same material at lower temperature C1T1. Density of type A islands is $7.7 \cdot 10^{10}\text{cm}^{-2}$, what is comparable to the sample C1T1.

The type B islands are randomly distributed with the shape which elongation is not so pronounced. The average diameter is 75nm. Their height of 10nm is smaller than height of the same type of islands of C1T1. Density of higher islands is found to be $1.8 \cdot 10^{9}\text{cm}^{-2}$.

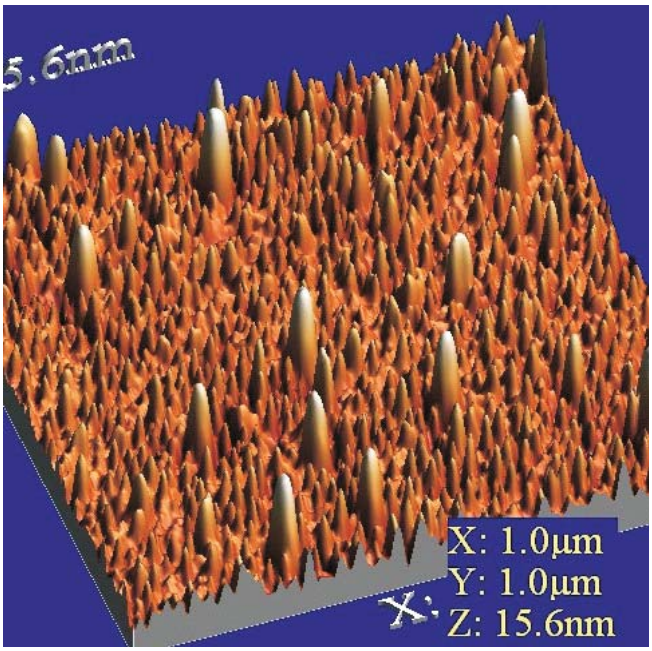

Figure 7.9 3D view of AFM on the $In_xGa_{1-x}N$ quantum dots grown at **600°C overgrown by $In_yGa_{1-y}N$** (sample **C1T1**).

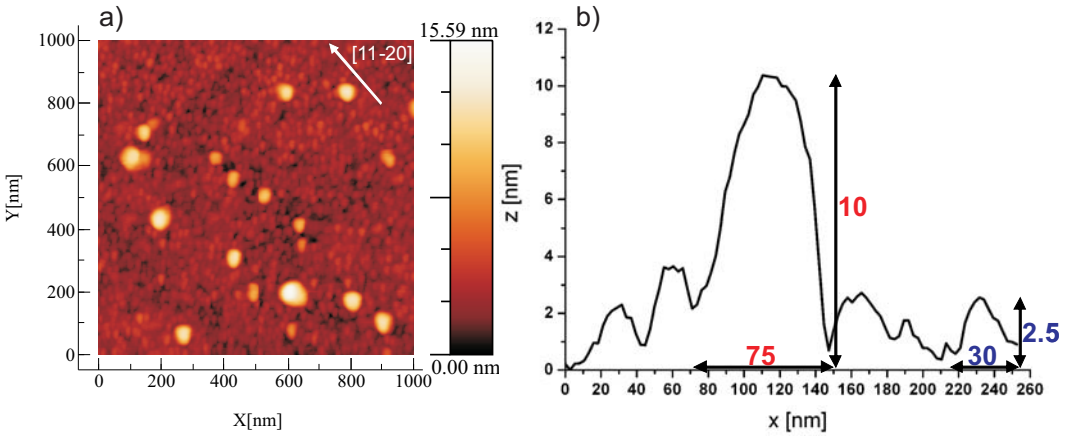

Figure 7.10 Atomic force microscopy on $In_xGa_{1-x}N$ quantum dots grown at **650°C overgrown by $In_yGa_{1-y}N$** (sample **C1T2**): a) plan view with the colour scale and b) representative profile of the sample surface with islands size measures.

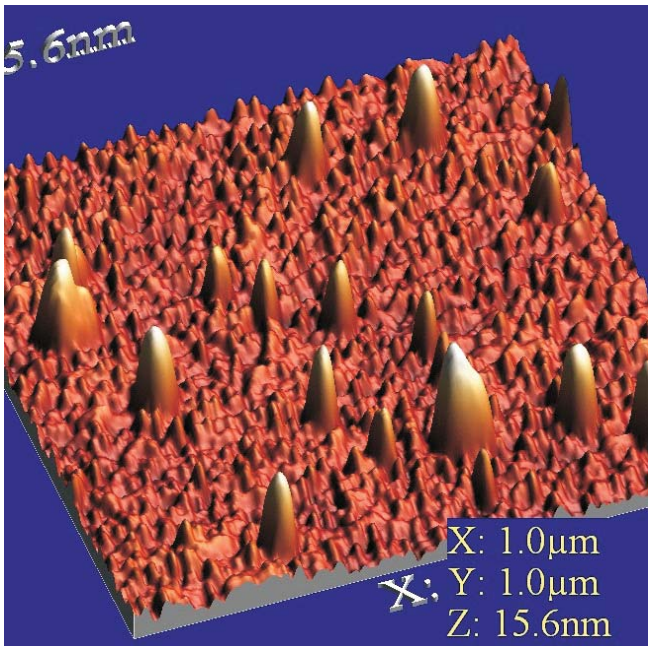

Figure 7.11 3D view of AFM on the $In_xGa_{1-x}N$ quantum dots grown at **650°C overgrown by $In_yGa_{1-y}N$** (sample **C1T2**).

7.2.6 By GaN Overgrown InGaN Quantum Dots (650°)- C2T2

Figure 7.12 shows the AFM results on the surface of the sample C2T2 with InGaN quantum dots, now overgrown by pure GaN. The plane view of the scanned surface area is shown at the 7.12a and the fig. 7.12b shows the representative lateral line profile. The round lateral shape and both, the later and vertical size of the type A dots are the same as for the sample grown at the same temperature but overgrown by InGaN, C1T2. The average diameter is 30nm and the mean height is 2.5nm. Seems that surface is in general a bit smoother, meaning that islands are more close to the surface corrugation with a mean of 0.75nm.

More shrinking of the islands of type B has been observed laterally. The average diameter is 60nm. The mean height is 8nm what is close to the height of the same type of islands at freestanding sample. Their density is estimated to be $2.9 \cdot 10^9 \mathrm{cm}^{-2}$ what is higher than for the other samples. No elongation at all has been evidenced.

The result which assign this sample from the others is that big islands of this sample show the spatial ordering in the direction of $[11\bar{2}0]$ and the directions of the same crystallographic family following hexagonal symmetry in 60° and 120°. To inspect this phenomenon more closely, the AFM of larger area has been performed. The left-hand side of figure 7.14 shows the ($2\mu\mathrm{m} \times 2\mu\mathrm{m}$) AFM image. The chains of type B islands are visible in the mentioned directions, just they do not so strictly follow that orientations, but may be curved or inclined. Two dimensional fast Fourier transform (FFT) of the AFM image doesn't show ordering correlation, but might be

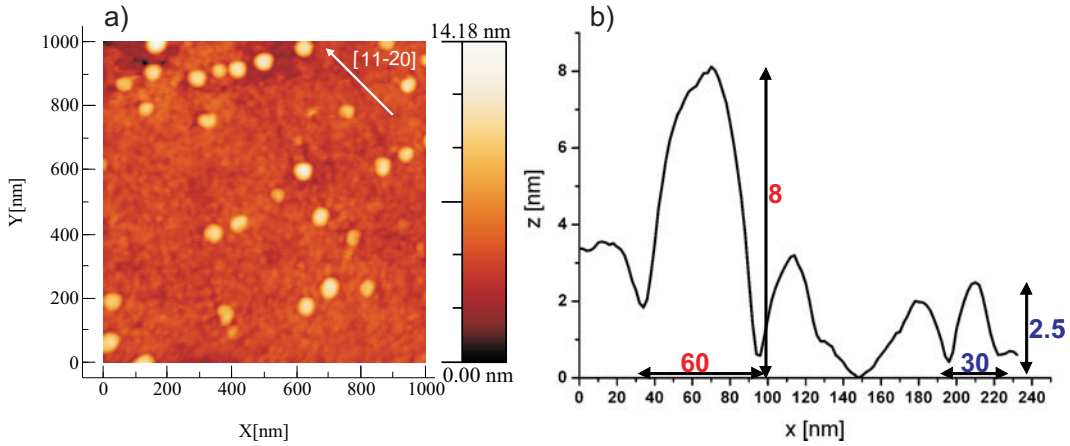

Figure 7.12 Atomic force microscopy on $In_xGa_{1-x}N$ quantum dots grown at **650°C overgrown by pure GaN** layer (sample **C2T2**): a) plan view with the colour scale and b) representative profile of the sample surface with islands size measures.

that scanned area of 2μm by 2μm is too small to reveal ordering correlation signals. The first intensity maximum in 2D FFT image has a diameter of 0.12nm^{-1} which correspond to the lateral dimension of $d_{\text{L}}^{\text{FFT}} = 49.1$nm in the real space (using the Bessel function for conversion). This result of FFT is comparable to the mean lateral distance between higher islands in the oriented row $d_{\text{L}}^{\text{AFM}} = 51 \pm 12$nm.

7.2.7 Comparison of the AFM Results by Structure

For the samples with the freestanding, not-overgrown, InGaN quantum dots, type A islands have a round lateral shape with the diameter of 40nm. The mean height is 1.4nm and 1nm for FT1 and FT2, respectively. The islands of the type B are randomly distributed and laterally elongated in the direction of $[11\bar{2}0]$ with sizes of (150nm by 100nm) for sample FT1 and (110nm by 75nm) for FT2.

Generally, AFM results on the samples with the $In_xGa_{1-x}N$ quantum dots overgrown by $In_yGa_{1-y}N$ ($y < x$) show three main features: (a) non-embedding overgrowth following the surface morphology of the samples with freestanding dots, (b) lateral shrinking of the both types of islands and (c) much weaker elongation of the type B islands than for the sample with freestanding quantum dots.

When freestanding InGaN quantum dots are overgrown by pure GaN (sample C2T2), the surface is more smooth. Shape and size of the type A islands remain the same as for the sample overgrown by InGaN at same temperature (C1T2), but the type B islands are laterally reduced to the diameter of 60nm and no elongation has been observed at all. An average height of 8nm is not much higher than of the same type of non-overgrown ones, but the density is higher. The ordering of islands of the type B has been observed. Their density behaves inhomogeneously forming the chains.

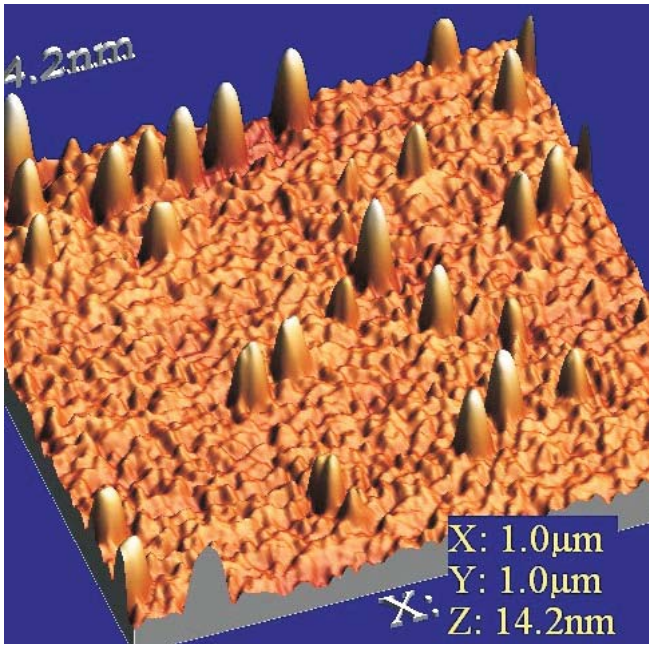

Figure 7.13 3D view of AFM on the $In_xGa_{1-x}N$ quantum dots grown at **650°C overgrown by GaN** (sample **C2T2**).

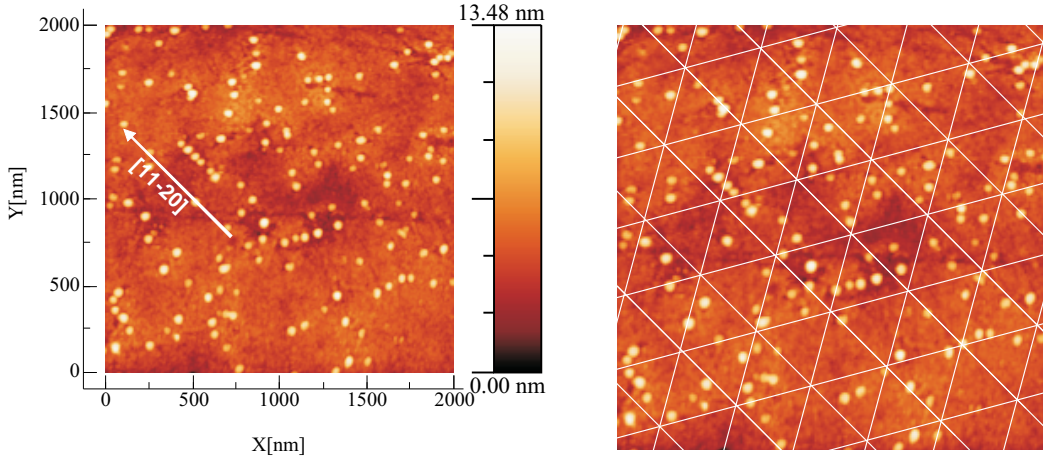

Figure 7.14 Spatial ordering of the higher InGaN islands in the $[11\bar{2}0]$ direction and in directions of the same crystallographic family: a) $2\mu m \times 2\mu m$ AFM image of the sample C2T2 and b) same, just with the lines following crystallographic directions.

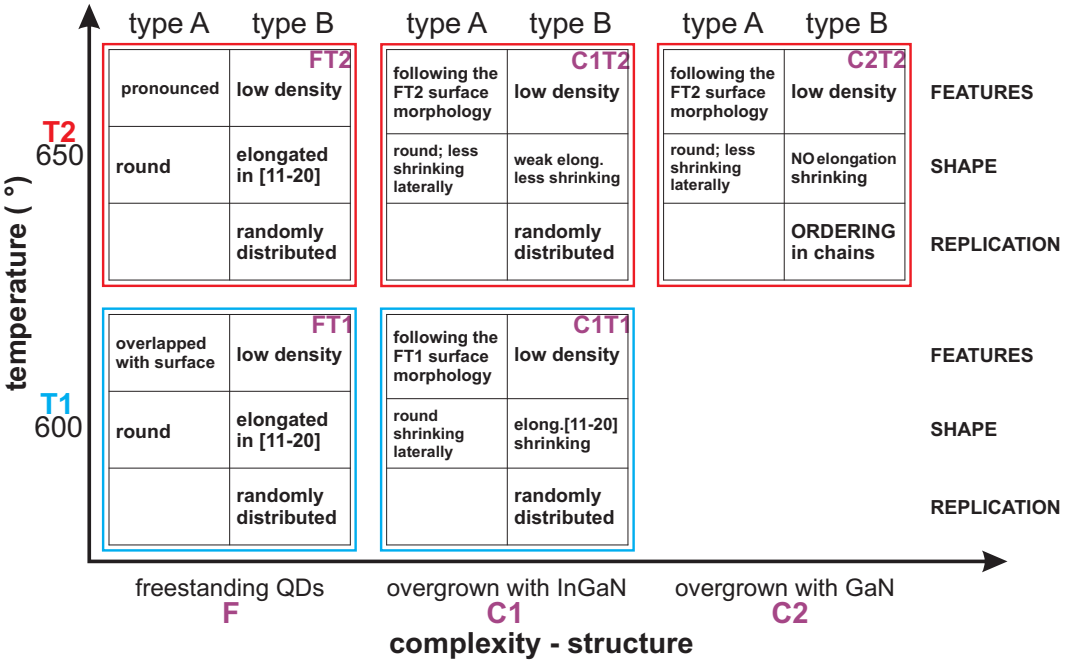

Figure 7.15 A summary of the atomic force microscopy results on the complete series of sample with the InGaN quantum dots. Abscise represents a sample structure complexity, while the growth temperature is on the ordinate.

Some of the chains are oriented in the certain directions of the family of $[11\bar{2}0]$. The chains might be curved and/or inclined to these directions. Encountered observations on high islands (shrinking laterally, not much overgrowth in height direction, higher density and ordering of the islands) might be explained by surface diffusion of the InGaN material compensating the strain induced by overgrowing GaN layer. This will be further discussed (sec. 7.2.9).

7.2.8 Comparison of the AFM Results by Growth Temperature

Comparing the results of AFM on samples grown at different temperature, the height of the islands of either type A or type B is generally reduced when the growth temperature is higher. Elongation of the type B islands does not change by growth temperature. The density of type B islands is a bit smaller when grown at higher temperature. The sample overgrown by pure GaN has no matching sample grown at lower temperature T1, therefore can not be compared.

The summary of the qualitative AFM results on the complete series of sample is shown in the figure 7.15.

Table 7.1 shows the quantitative AFM results on the InGaN quantum dots sample series. The density of type A islands for the samples FT1 and C2T2 was not possible

	type A			type B		
sample	diameter [nm]	height [nm]	density [10^9cm^{-2}]	a ; b* [nm]	height [nm]	density [10^9cm^{-2}]
FT1	40	1.5	—	150; 100	7	2.2
FT2	40	1	30	110; 75	7	1.1
C1T1	25	5	90	70; 60	12	2.1
C1T2	30	2.7	77	75	10	1.8
C2T2	30	2.5	—	60	8	2.9

Table 7.1 The AFM results on the InGaN quantum dots samples. For each type of islands (A and B), diameter, height and density are shown. *For type B islands whit pronounced elongation, the two values are given for major and minor diameter of the ellipse. When a and b are equal, just one value is given.

to determine.

7.2.9 Discussion on AFM: possible model of InGaN quantum dots

In this section, the size and the shape of our InGaN islands as well as their aspect ratio will be compared with other InGaN islands reported in the literature. This will be followed by discussion in order to study the influence of the growth conditions on the islands morphology.

Up to the segregation method used for the growth of our samples, InGaN islands have been grown either by MOVPE or MBE, mostly using the Stranski-Krastanow growth mode. The aspect ratio (height/width) of typically 0.5 [144] is always larger than for our islands which is between 0.03 and 0.08 for freestanding and 0.08-0.2 for the overgrown samples (see Tab. 7.2).

Nanostructures grown by segregation method are still not fully investigated and the mechanism how they are formed is not yet understood. Similar islands to our type B islands have been found by the group which established a segregation method

sample	type A	type B
FT1	0.04	0.06
FT2	0.03	0.08
C1T1	0.20	0.18
C1T2	0.09	0.13
C2T2	0.08	0.13

Table 7.2 Aspect ratio (height/width) of the InGaN islands investigated in this thesis.

of InGaN quantum dots growth [141, 143, 145] while similar to type A islands were reported just by depositing much more InGaN material (20 nm) [146] up to the recent study in [70]. Tessarek et al. [70] reported on two phases InGaN islands, In-poor QD-like structures (with the hight of 1-1.5 nm) and In-rich islands (with the hight of 20 nm).

The lateral sizes of both types of our InGaN islands are much different than grown by Stranski-Krastanow mode (typically in the range of 10 nm) reported in the literature [144, 147, 148]. Their aspect ratio corresponds more to the pure InN islands [149, 150]. The islands with a shape comparable to our type B islands have been reported in [151] where InGaN islands (with the width of 50 nm and the height of 13 nm) were grown by nano-alloyed droplet growth technique.

The In-rich InGaN quantum dots with the similar aspect ratio to our islands have been observed in [152, 153]. The uncapped islands are measured by AFM and capped by TEM. However, the AFM images look very much as the nucleation layer before coalescing and the estimation of 80% of indium in the islands (determined by coplanar XRD without taking the strain into account) is not confirmed by PL and their stability under GaN capping can not be clearly visible from TEM image.

In the following paragraph we will consider how the growth conditions influence the InGaN islands shape.

The shape of the InGaN islands strongly depends on the growth conditions and can be tuned by changing the V/III molar ratio, the ammonia flux and the growth temperature [74, 154–156]. Two typically observed island shapes are shown in the figure 7.16. Depending on the growth condition, the islands may have Gaussian shape (Fig. 7.16 (a)) or mesa shape (Fig. 7.16 (b)). Gaussian shape assumes the island outer line being similar to a Gaussian function with the characteristic slope of a bell-shaped curve. Mesa shape can be described as a broad column with the flat plateau on the top. For MBE grown InN islands, it was found that shape depends

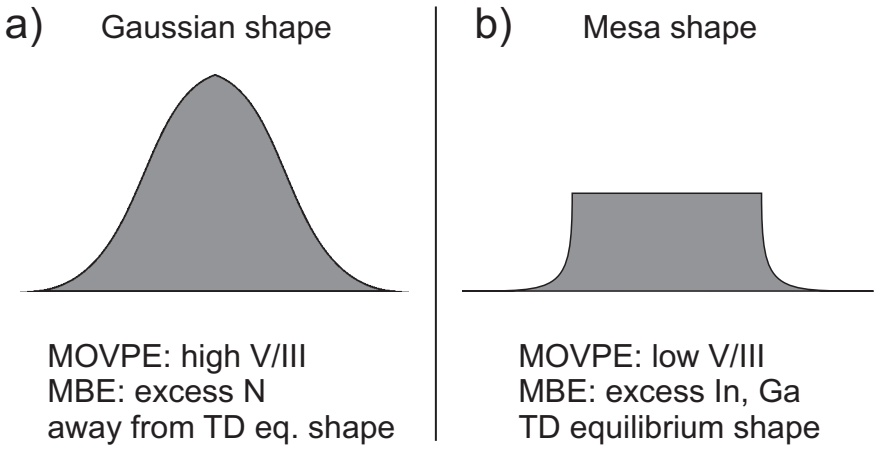

Figure 7.16 Different shape of InGaN islands as a function of the growth conditions: a) Gaussian shape away from the thermodynamical equilibrium, b) mesa shape due to thermodynamical equilibrium.

on the flux condition [149]: when an excess of nitrogen is used, Gaussian islands are grown, while islands with a mesa shape are observed when an excess of indium is used. By analogy, this result could be applied to the MOVPE growth with different V/III molar ratio, changing the metal/organic gas phase. If the V/III molar ratio is high, then islands are grown with the Gaussian shape, while the mesa shape is formed when the low V/III ratio is applied [155]. Study of the influence of ammonia, as nitrogen precursor in MOVPE, on the growth mode in InGaN grown on GaN [157] shows that increasing the partial pressure of NH_3 leads to 3D growth. High NH_3 flow rate leads to InGaN quantum dots with the large diameter, while at too low NH_3 flow rate the quantum dots disappear [156]. The islands density decreases and the average height increases with increasing growth temperature for constant material deposited [74]. That the islands density is inversely proportional to the growth temperature is well known from the literature and confirmed for the group(III)-nitrides in [155, 158].

The same two types of island shapes were found in the previous study on the InGaN islands grown by segregation method as our samples [145, 146]. The mesa shaped islands were found to be grown at early stage of nucleation (after average thickness of deposited material t =1.3 nm) preferentially at defect sites of the GaN templates. Islands have a low density. After deposition of t =26 nm, keeping all other growth parameters unchanged, the Gaussian shape of the InGaN islands is observed and their density increases.

Figure 7.17 schematically shows the shape of InGaN islands based on our AFM results. In contrast to the observation in [145, 146], we have just Gaussian islands shape. The V/III molar ratio used for the growth of our InGaN islands is $\approx$ 3900 and the temperature is varied between 600 and 650 °C. Our samples were prepared with the segregation method as in [142, 143, 146] but the mesa shaped islands were not found, just the Gaussian ones.

Now, we will focus on the driving force for having exactly observed island shapes. The question is whether the heteroepitaxially grown islands reach their equilibrium shape or they might be limited by surface kinetics. It is known from the literature that Gaussian shape is never an equilibrium one. Theoretical prediction of GaN nanostructure equilibrium shape calculated from Wulff's plot and its Legendre transformation [159, 160] is a complete hexagonal pyramid which can be truncated for the case when thermodynamical equilibrium is not fulfilled. This prediction is done for the selective area growth and the growth rates of different planes vary under different growth conditions. Recent investigation of the island shape by Cao et al. [149] confirmed that mesa shape with the flat top is more close to an equilibrium shape than the Gaussian one which is limited by surface kinetics. This discussion can be valid to our case and the argumentation can been used for the growth of InGaN islands. The fact, which goes in favor of kinetically limited islands shape, is that diffusion of nitrogen atoms on non-equilibrium surfaces in excess N significantly reduces the mobility of group-V atoms [161]. Therefore, they can not diffuse to form an energetically preferable mesa shape of islands. In our case, the reasons for keeping the InGaN islands away from reaching the thermodynamical equilibrium shape lay in alloying, strain, relatively high V/III molar ratio and relatively low growth temperature.

Overgrowth

The overgrowth of InGaN quantum dots grown in Stranski-Krastanow mode results in their complete dissolution after GaN capping layer of few nm [59] leading to a smooth surface [162]. In contrast to this, here we have the overgrowth which seems that surface atoms diffuse and place more on the top of the islands than in the valley (Fig. 7.17 (b)). Both, type A and type B InGaN islands are still there and well visible. The similar overgrowth of InGaN quantum dots was, up to my knowledge, not reported yet. A possible explanation for deposition of group-V atoms more on the island top might be in energetically preferable position from the aspect of thermodynamical equilibrium over positioning on the island slope which is energetically not stable under N-rich condition [163]. The AFM results show that height of the islands is increased while lateral sizes are decreased. Shrinking of the overgrown InGaN islands has been found. It seems to be more pronounced for the overgrowth with GaN at higher growth temperature and for the overgrowth with InGaN at lower one.

Different density of the same type islands at freestanding and overgrown samples is due to the fact that samples were not successively grown but following the same recipe which might result in the deviation of island density.

Ordering of the type B islands in chain form has been observed. Their orientation might be influenced by crystallographic orientation in the family of $[11\bar{2}0]$ (see Fig. 7.14 (b)), but much stronger influence comes from the preferable nucleation and positioning of the islands at the GaN surface steps typical for the MOVPE growth of group(III)-nitrides. That should be the reason for the chains being curved. Step edges act as a diffusion barrier and due to this islands are more distributed on the terraces between the edges oriented in a $[11\bar{2}0]$ direction.

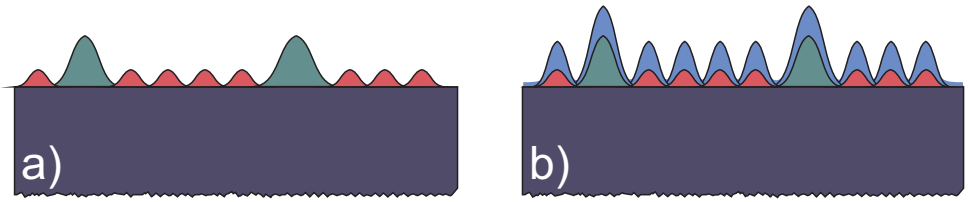

Figure 7.17 Schematic of the surface shape based on the atomic force microscopy results: a) surface of the freestanding $In_xGa_{1-x}N$ quantum dots and b) quantum dots overgrown by formation layer of either $In_yGa_{1-y}N$ ($x > y$) or GaN.

7.3 Grazing Incidence X-ray Diffraction Study on InGaN QDs

Grazing incidence diffraction experiments on freestanding and overgrown InGaN quantum dots have been performed in order to study their structural evolution during capping. The GID method itself was introduced in sec. 3.3.3. It was shown that GID is a surface sensitive technique which may resolve the scattering from the surface objects and the scattering from the bulk material, since the grazing incidence angle can be tuned and by this the penetration depth can be chosen (see fig. 3.13). Therefore, the depth controlled measurements have been performed to enhance the scattering signal coming from the surface nanostructures.

In order to investigate the structure of the samples, line radial and angular scans were performed. Reciprocal space map have been measured on the all of the samples to study relative strain, lateral size and misorientation of the InGaN freestanding and overgrown islands.

Incident angle was tuned to enhance the contribution of the surface structure. Therefore, GID radial and angular scans are performed at different incident angles. As an example, figure 7.18 (b) shows three radial scans in grazing incidence geometry of $(20\bar{2}0)$ on the sample C1T1 with overgrown InGaN quantum dots, performed at different angles of incidence: 0.25° (solid circles), 0.5° (open circles), 0.8° (crosses). First of the angles is below and others are above the critical angle for total external reflection of GaN. The calculated penetration depths are presented at the figure 7.18 (a) according to the theoretical consideration (eq. 3.59) described in the section 3.3.3. The penetration depth as a function of the incident angle is plotted for the X-ray energy of 7.75 keV used in our experiment. At an incident angle of $\alpha_i = 0.25°$, calculated penetration depth is 3 nm, while the penetration depth of 210 nm and 420 nm correspond to the incident angles of $\alpha_i = 0.5°$ and $\alpha_i = 0.8°$, respectively. A change of the diffracted signal is especially visible on the InGaN(1) peak (fig. 7.18 (b)). The peak increases with decreasing incident angle.

The incident angle scans at three different Bragg positions are presented in the figure 7.19. The α_i-scan on the $(20\bar{2}0)$ GaN Bragg peak is marked with the solid

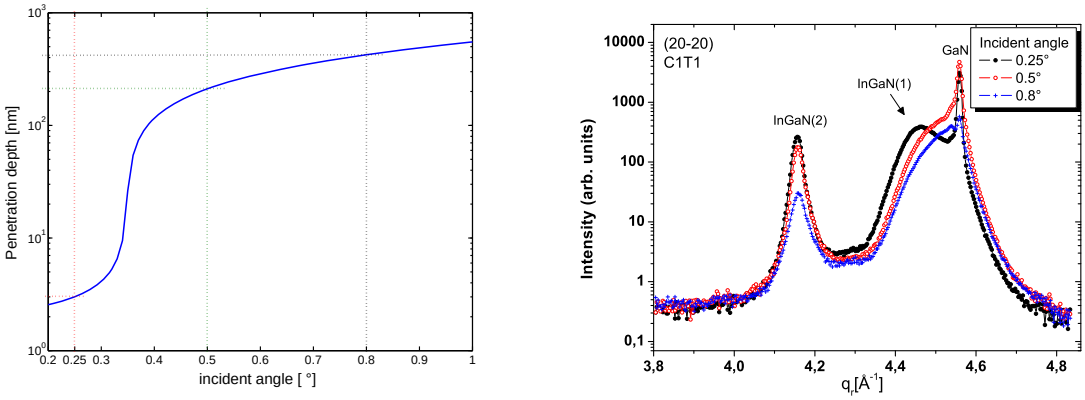

(a) (b)

Figure 7.18 (a) X-ray penetration depth in the function of the incident angle and (b) corresponding GID radial scans at different incident angles.

circles, the α_i-scan on the InGaN(1) peak with the open circles and the α_i-scan on the InGaN(2) peak with the crosses. All scans show, as expected, maximum intensity at incident angle being equal to the critical angle α_c and after that intensity decreases with penetrating more deep in the material. Incident angles used in the experiment are marked with the numbers (1-3). The slope of α_i-scan can give a sign to distinguish between the bulk and surface signals [100, 101, 164, 165]. For the scan at InGaN(1) peak, a different slope can be observed than for other two peaks. This indicate that InGaN(1) could be attributed to the scattering from the part most close to the surface and this might explain the change of the diffracted signal observed in the fig. 7.18 (b). It will be discussed further in the following sections.

7.3.1 Qualitative Observations

Grazing incidence X-ray diffraction radial and angular scans in the vicinity of $(10\bar{1}0)$ and $(20\bar{2}0)$ have been measured at incident angle of $\alpha_i = 0.25°$ for all of the samples. As an example, figure 7.20 shows the radial scans of $(20\bar{2}0)$ on both freestanding (solid circles) and overgrown (open circles) quantum dots. The features can be described as follows: sharp diffraction peak at the position of pure GaN, a shoulder at $q_r = 4.546$ Å^{-1} for the sample with freestanding quantum dots and a separate peak ($q_r = 4.467$ Å^{-1}) named InGaN(1) for the overgrown sample, and the last one is a diffraction peak at the position around $q_r = 4.15$ Å^{-1} marked as InGaN(2). We will focus on the phenomenological description of the surface structure of two different InGaN islands and their evolution due to capping. The peaks have different full width at the half maximum (FWHM). A shoulder is a broad component close to the narrow GaN Bragg peak. The InGaN(2) peak is broader than GaN. The most broad intensity distribution exhibits the InGaN(1) peak of the sample with capped quantum dots.

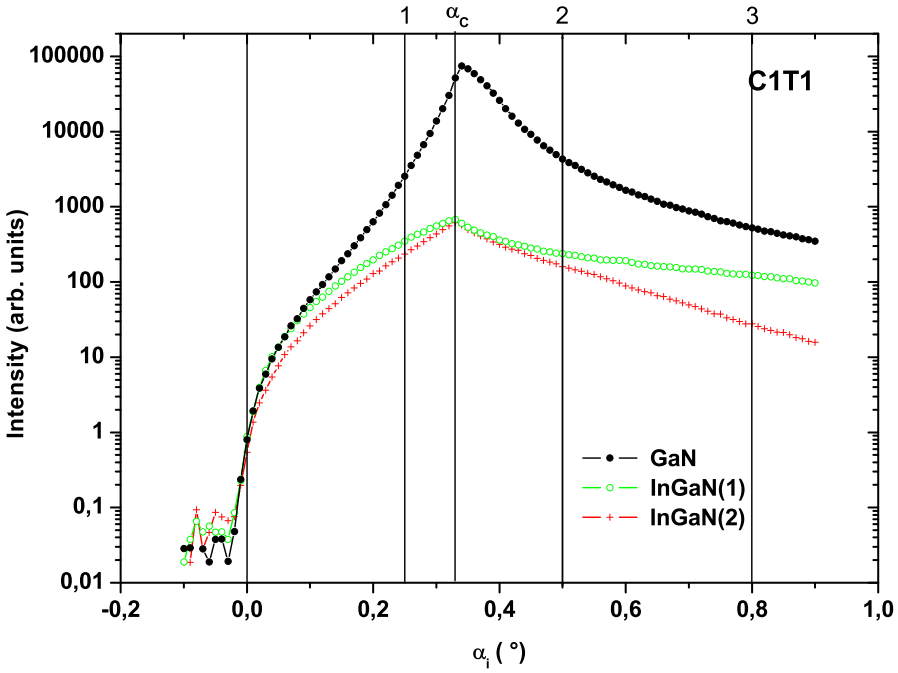

Figure 7.19 Grazing incidence diffraction scans of incident angle at three different Bragg positions: GaN peak (solid circles), InGaN(1) peak (open circles) and InGaN(2) peak (crosses). α_c marks the critical angle. The lines correspond to the incident angles used in our experiment: 1 - 0.25°, 2 - 0.5°, 3 - 0.8°.

The InGaN(2) peak is slightly asymmetric and thickness oscillations are visible close to it. There is a slight difference in the position of InGaN(2) peak for capped and uncapped sample visible for all samples. The radial GID scan on the freestanding quantum dots exhibiting two separate InGaN diffraction signals (InGaN(1) shoulder and InGaN(2) peak) is, up to my knowledge, the first time ever evidence of the phase separation in InGaN islands. Similar results of the phase separation confirmed by two InGaN peaks with different In content have been observed for InGaN films [71], but for InGaN islands not yet.

7.3.2 Same Growth Temperature - Effect of the Capping

In this section, the effect of the different capping material will be presented as well as comparison of the GID results obtained from the capped and uncapped (freestanding) InGaN quantum dots. Exact positions of the diffraction peaks and their widths will be given together with the other results as misorientation and size effects revealed from the reciprocal space maps (sec. 7.3.5).

Figure 7.21 shows GID radial scans of (a) the $(10\bar{1}0)$ and (b) the $(20\bar{2}0)$ reflection for the samples grown at the same temperature, T1=600°C. The scans corresponding

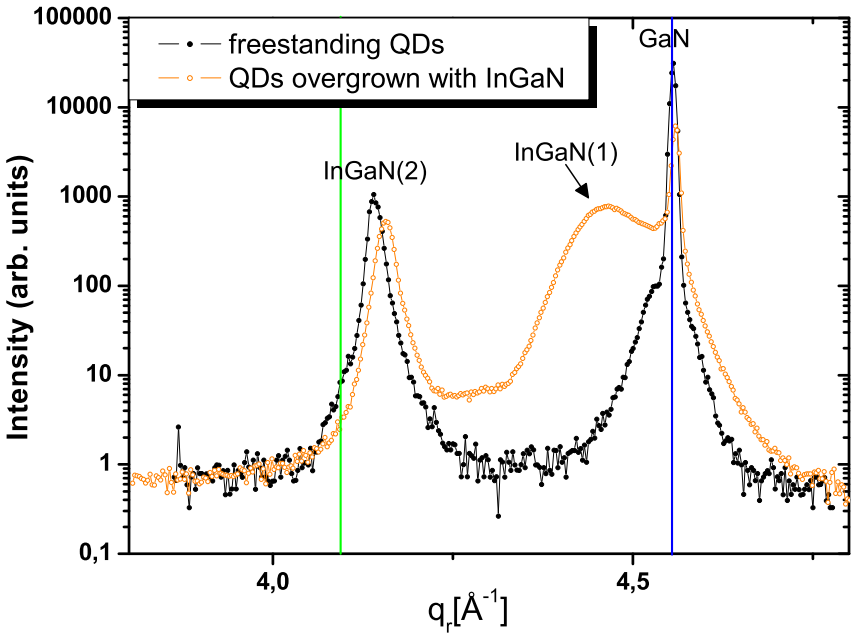

Figure 7.20 An example of the grazing incidence diffraction radial scans on the samples with InGaN quantum dots. Energy of 7.75keV is used. Here are presented two scans in the vicinity of the $(20\bar{2}0)$ reflection, one on the sample with freestanding quantum dots (black solid circles) and another one on the overgrown quantum dots (open circles). Position of the pure GaN ($q = 4.554$ Å^{-1}) and InN ($q = 4.094$ Å^{-1}) are marked by lines. For further explanation see text.

to the sample with freestanding InGaN quantum dots (FT1 - solid circles) and with InGaN overgrown InGaN quantum dots (C1T1 - open circles) are presented. The scans on both samples and in both reflections show a sharp GaN Bragg peak coming from the buffer layer and well separated InGaN(2) peak. The InGaN(2) corresponds to the In-rich islands which might be the type B islands observed in AFM. This thesis will be confirmed by AXRD reciprocal space maps study later on in the section 7.4.

There are two main differences. One is that InGaN(2) peak is shifted to higher values in direction of GaN Bragg peak for the overgrown sample C1T1. Another difference is in the peak InGaN(1). For the sample with freestanding InGaN quantum dots (FT1), one can observe a broad shoulder with the maximum of intensity close but not identical to the position of GaN Bragg peak. In contrast to this, for the capped sample (C1T1), InGaN(1) is much stronger, separate peak with even broader intensity distribution.

The separation is more visible for the higher reflection (fig. 7.21 (b)). The shoulder in the scans on FT1 could be attributed to the type A islands, partially strained to the GaN buffer layer. On the other hand, strong InGaN(1) peak might come from the InGaN formation layer whit about 10% of indium content. It was already discussed that InGaN(1) belongs to the most top region close to the surface of the sample. Such a broad intensity distribution tells about non-uniform lattice constant in the overgrown material.

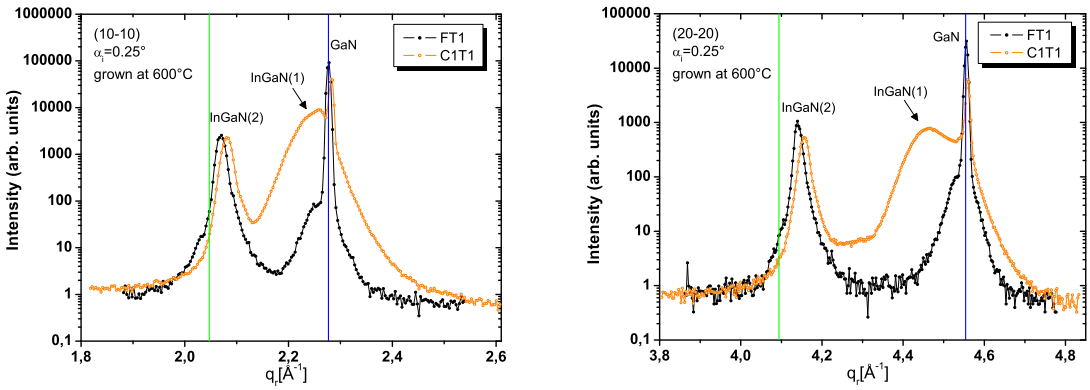

(a) (b)

Figure 7.21 GID radial scans of the samples grown at same temperature T1 in a vicinity of a) $(10\bar{1}0)$ and b) $(20\bar{2}0)$ reflections. Solid circles: the sample with freestanding InGaN QDs, open circles: the sample with InGaN QDs overgrown with InGaN.

Similarly to the previous figure, the GID radial scans on the samples grown at the temperature T2=650°C are shown in the figure 7.22. Beside the samples with freestanding quantum dots (solid circles) and with InGaN overgrown quantum dots (open circles), there is a sample with GaN overgrown InGaN quantum dots (crosses). All scans show a sharp GaN Bragg peak and well separated InGaN(2) peak.

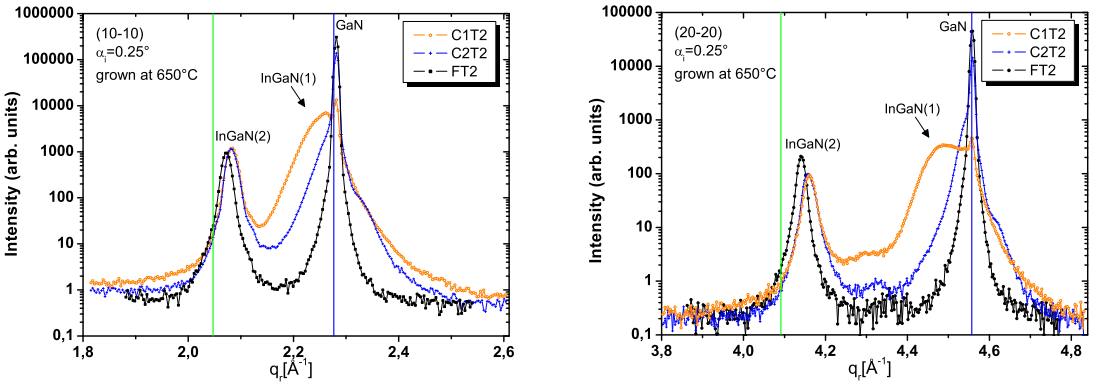

(a) (b)

Figure 7.22 GID radial scans of the samples grown at same temperature T2 in a vicinity of a) $(10\bar{1}0)$ and b) $(20\bar{2}0)$ reflections. Solid circles: the sample with freestanding InGaN QDs, open circles: the sample with InGaN QDs overgrown with InGaN, crosses: InGaN QDs overgrown with GaN.

The radial scan on the sample FT2 with the freestanding QDs, the shoulder close to GaN is not visible. In the contrast to what has been observed for the FT1, results on FT2 exhibit a broad second component below the narrow pure GaN peak. This broad component might belong to the type A islands, but in this case, completely strained to the GaN buffer layer lattice constant since the positions of GaN sharp and GaN broad components coincide.

The shape of the InGaN(1) peak stays almost the same for the sample C1T2 in comparison to C1T1 (both overgrown with InGaN). The situation is very much different for the sample C2T2 (overgrown with GaN), where GaN peak has asymmetrical shape and consists of: (a) a narrow peak from the GaN buffer layer, (b) one shoulder on the lower part and (c) another shoulder on the higher side of the GaN. The radial scans on both overgrown samples exhibit a shift of InGaN(2) peak to the higher values.

7.3.3 Same Layer Structure - Different Growth Temperature

Freestanding InGaN Quantum Dots

Figure 7.23 (a) shows radial scans of $(20\bar{2}0)$ reflection performed on the samples grown at different temperature but both of same structure, freestanding InGaN quantum dots. Comparing the scans on this figure, one can observe that the peaks GaN and InGaN(2) stay at the same position having the similar width.

The main difference is visible in the shoulder InGaN(1) close to the GaN Bragg peak. For the sample FT1 the peak is visible with the maximum of intensity at the position of $q_r = 4.546$ Å^{-1} and the peak width is $\Delta q_r = 0.056$ Å^{-1}. For the sample

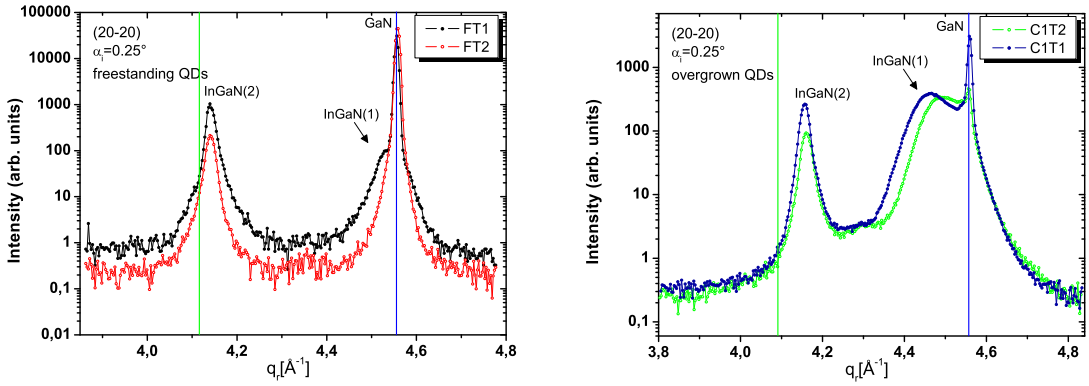

Figure 7.23 GID radial scans of the samples of the same structure, but grown at different temperature, T1=600°C (solid circles) and T2=650°C (open circles). (a) freestanding quantum dots, (b) quantum dots overgrown with InGaN.

grown at higher temperature FT2, the shoulder does not exist but there is a broad component with the position matched to a GaN peak exhibiting no asymmetry. Its width of $\Delta q_r = 0.029$ Å^{-1} is almost a twice smaller than for the sample FT1.

Overgrown InGaN Quantum Dots

The GID radial scans on the samples both with InGaN overgrown quantum dots, but grown at different temperatures, are shown in the figure 7.23 (b). One can observe a well pronounced shift of the InGaN(1) peak towards lower values when the sample is grown at lower temperature (C1T1). For the same sample, higher intensity of the InGaN(2) peak has been observed.

7.3.4 Reciprocal Space Maps on InGaN QDs

Measuring the radial and angular scans on sample series with freestanding and overgrown InGaN quantum dots, two types of islands have been confirmed and the change of the surface signal coming from the overgrown material has been studied. To obtain better insight in surface structure and to study the effects of size, shape and misorientation of the quantum dots GID reciprocal space maps (RSM) on the series has been measured. Here, the reciprocal space maps in GID geometry and their results will be presented and evaluated.

Please, note that q values in both, radial and angular directions, in the reciprocal space map of the higher reflection, $(20\bar{2}0)$ are twice larger than in the reciprocal space map of $(10\bar{1}0)$. The intensity of the plots has been normalized that plots of

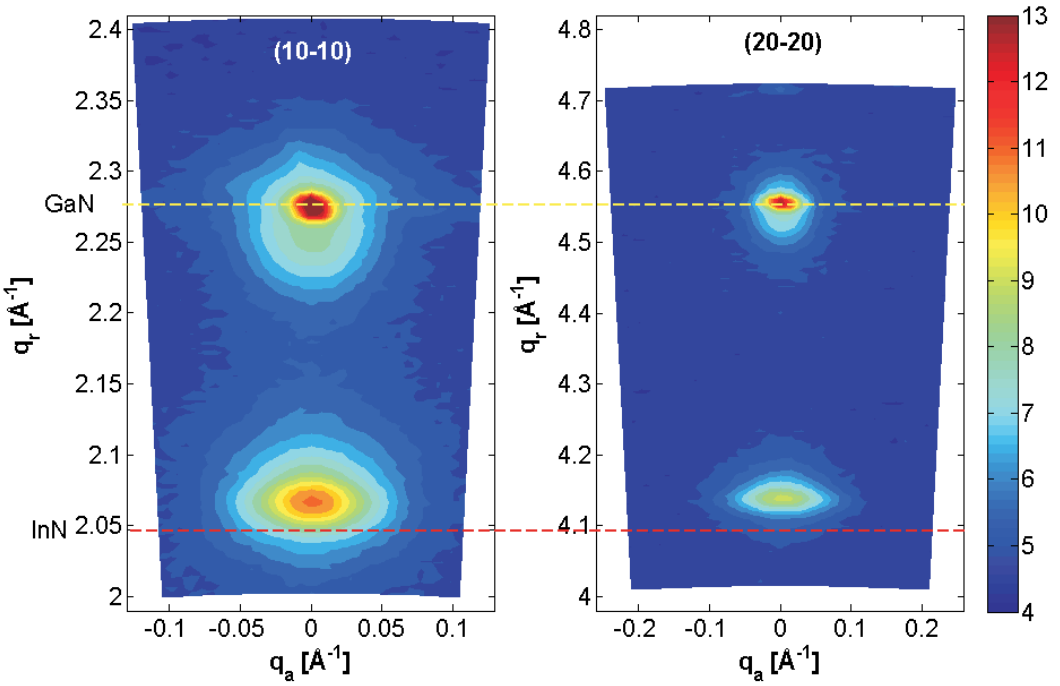

Figure 7.24 GID reciprocal space maps on the sample FT1 in the vicinity of (a) $(10\bar{1}0)$ and (b) $(20\bar{2}0)$. The lines mark the positions of GaN and InN Bragg positions.

both reflections follow the same scale.

Figure 7.24 shows reciprocal space maps on the sample FT1 of (a) $(10\bar{1}0)$ and (b) $(20\bar{2}0)$ reciprocal lattice points. The positions of the GaN and InN Bragg reflections are marked by dashed lines. One can observe a strong GaN buffer layer peak, a broad distribution of InGaN(1) close to GaN with the intensity maximum at the lower position than GaN and the separate peak InGaN(2) close to the InN with the broad intensity distribution and elliptical shape. The peak positions, peak widths and the calculated values are given in the table of the GID results in the figure 7.30.

In contrast to what has been observed for FT1, reciprocal space maps on the sample FT2 (fig. 7.25) exhibit absence of the separate InGaN(1) peak. There is a broad intensity distribution around the GaN buffer peak. InGaN(2) peak has the elliptical shape, but of less eccentricity.

The reciprocal space maps on the samples with the overgrown InGaN quantum dots (fig. 7.26, 7.27, 7.28), generally show much broader intensity distribution of the InGaN(1) peak, in comparison to the RSMs of the samples with freestanding quantum dots. The position of the InGaN(2) peak is shifted to the higher values as was observed on the line radial scans in the previous section. When the RSMs on just overgrown samples are compared, they clearly show a different shape of the InGaN(1) peak. It is elongated in the case of InGaN as an overgrowing material, C1T1 (fig. 7.26), C1T2 (fig. 7.27), but for the GaN used for overgrowing, C2T2 (fig. 7.28) it is more spherical

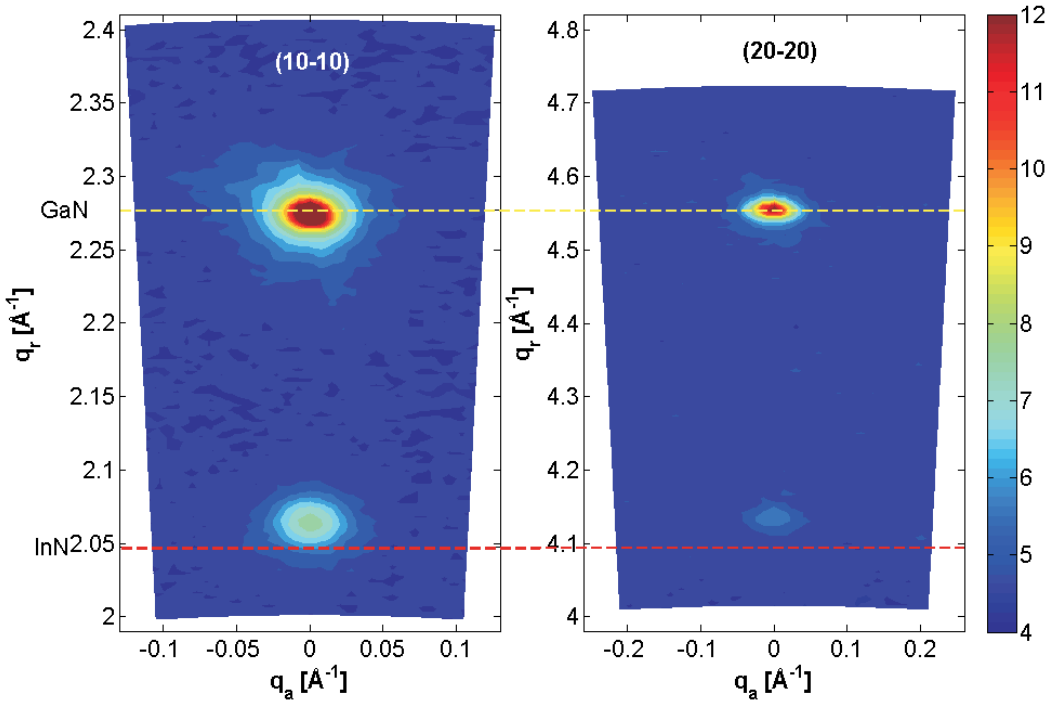

Figure 7.25 GID reciprocal space maps on the sample FT2 in the vicinity of (a) $(10\bar{1}0)$ and (b) $(20\bar{2}0)$. The lines mark the positions of GaN and InN Bragg positions.

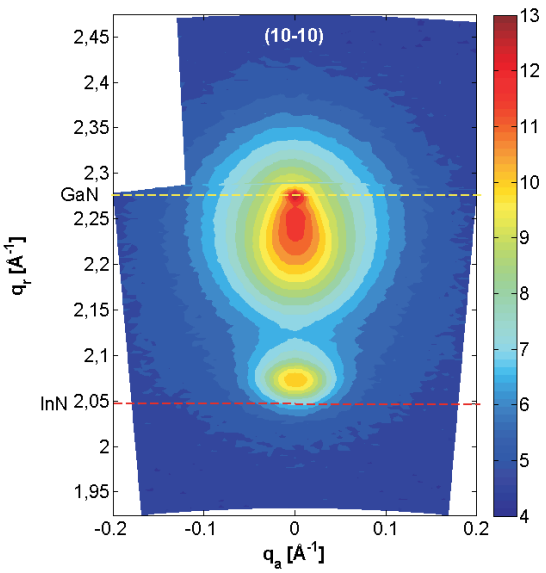

Figure 7.26 GID reciprocal space maps on the sample C1T1 in the vicinity of $(10\bar{1}0)$. The lines mark the positions of GaN and InN Bragg positions.

with the center close to the GaN.

7.3.5 Evaluation of GID results

The first column is the 2θ angle (with θ being a Bragg angle) of the measured peaks given in the blocks: GaN, InGaN(1), InGaN(2) for different samples. The position of the peaks in the reciprocal space is given by the scattering vector calculated from the Bragg angle as in eq. 3.24. The interplanar distance of diffraction planes is calculated by $d = \frac{2\pi}{q}$. A corresponding lateral lattice parameter is determined recalling the expression for hexagonal structure, eq. 3.37.

The widths of the peaks in both radial and angular directions, Δq_r and Δq_a, respectively, were determined by fitting the measured data to a Gaussian function.

The size of coherently scattering domains in radial and angular direction are calculated as follows, the size in the radial direction is determined as:

$$t_\mathrm{r} = \frac{2\pi}{\Delta q_\mathrm{r}} \tag{7.1}$$

and in angular direction as

$$t_\mathrm{a} = \frac{2\pi}{\Delta q_\mathrm{a}}. \tag{7.2}$$

The misorientation of the coherently scattering domains, $\langle \Delta\phi \rangle$, is calculated from:

$$\tan \langle \Delta\phi \rangle = \frac{\Delta q_\mathrm{a}}{q_\mathrm{r}}. \tag{7.3}$$

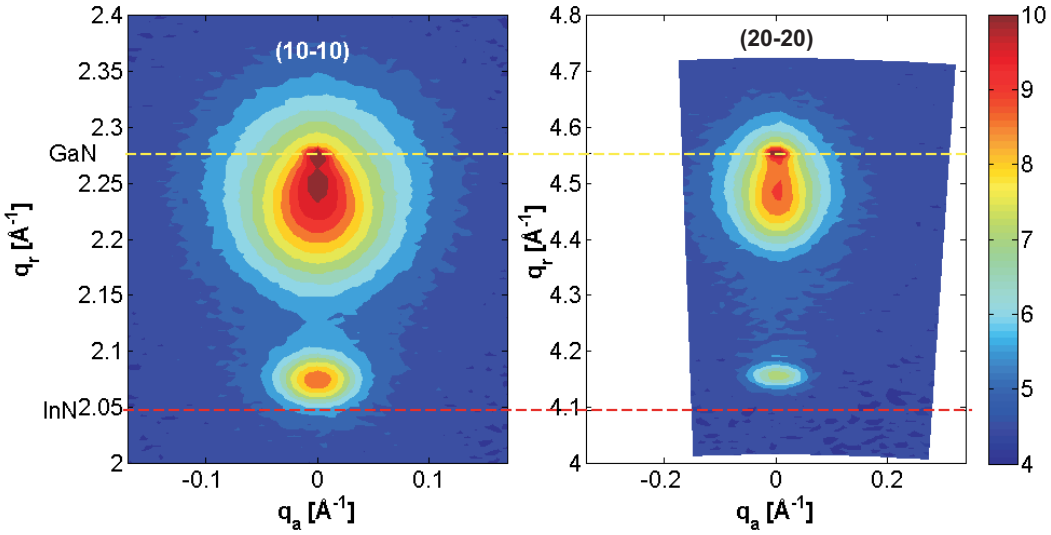

Figure 7.27 GID reciprocal space maps on the sample C1T2 in the vicinity of (a) $(10\bar{1}0)$ and (b) $(20\bar{2}0)$. The lines mark the positions of GaN and InN Bragg positions.

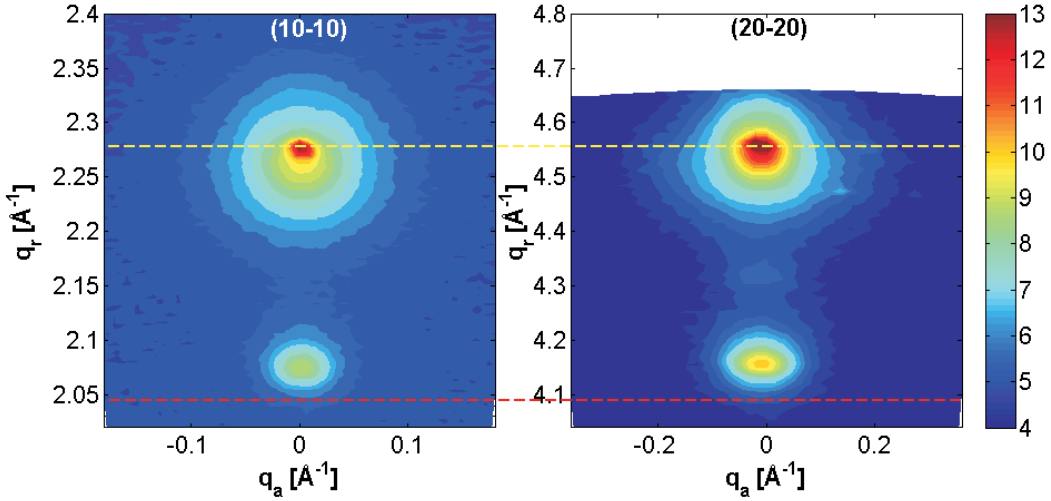

Figure 7.28 GID reciprocal space maps on the sample C2T2 in the vicinity of (a) $(10\bar{1}0)$ and (b) $(20\bar{2}0)$. The lines mark the positions of GaN and InN Bragg positions.

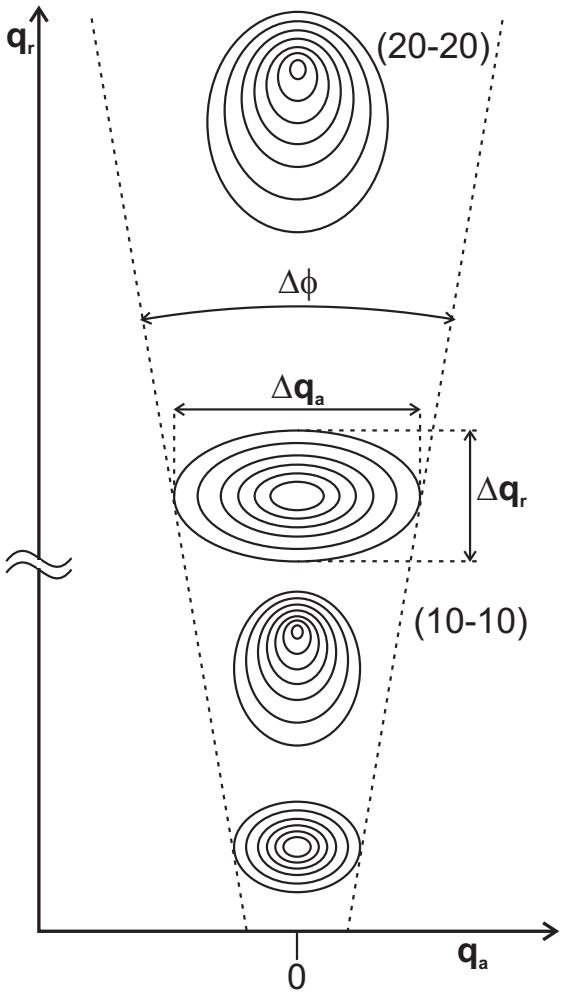

Figure 7.29 Reciprocal space maps evaluation.

The systematical errors of the results are given in the last row of the table.

In order to evaluate GID results let us consider how different effects influence the peak width in both angular and radial direction. The width of angular scan is a sum of contributions from mostly the misorientation and the lateral size of coherently scattering domains inside the islands. Figure 7.31 show the widths (FWHM) of the angular scans normalized by absolute value of the scattering vector plotted in the function of the peak position. Data from the samples grown at temperature T1 is marked by open symbols, while solid symbols are attributed to the sample grown at T2. Comparing the peak widths of two different orders provides the information of dominating effect on the peak width broadening. If the angular width Δq_{a} is the same in both, lower and higher order of diffraction, than the size effect is prevailing. In another case, an angular peak width grows with the order of diffraction forming the same angle $\Delta\phi$ viewed from the origin of the reciprocal space (see fig. 7.29). That indicates the misorientation of the coherently scattering domains being a dominating

	2θ(°)	q(Å-1)	d(Å)	n	a(Å)	Δqr(Å-1)	Δqa(Å-1)	tr(Å)	ta(Å)	Δϕ=Δq/q	Δϕ (°)
GaN											
FT2	33,76	2,281	2,755	1	3,181	0,007	0,01	1049	766	0,0044	0,25
FT2	70,94	4,558	1,378	2	3,183	0,009	0,02	815	383	0,0044	0,25
FT1	33,7	2,277	2,760	1	3,186	0,007	0,0084	1094	912	0,0037	0,21
FT1	70,896	4,556	1,379	2	3,185	0,007	0,017	1094	451	0,0037	0,21
C1T2	33,76	2,281	2,755	1	3,181	0,007	0,013	1094	589	0,0057	0,33
C1T2	70,94	4,558	1,378	2	3,183	0,010	0,026	766	295	0,0057	0,33
C2T2	33,77	2,281	2,754	1	3,180	0,008	0,01	958	766	0,0044	0,25
C2T2	70,948	4,559	1,378	2	3,183	0,009	0,02	851	383	0,0044	0,25
C1T1	33,79	2,283	2,752	1	3,178	0,007	0,011	1094	696	0,0048	0,28
C1T1	70,96	4,559	1,378	2	3,183	0,009	0,021	815	365	0,0046	0,26
InGaN1											
FT2	33,72	2,278	2,758	1	3,185	0,031	0,031	247	247	0,0136	0,78
FT2	70,8967	4,556	1,379	2	3,185	0,029	0,032	261	239	0,0070	0,40
FT1	33,49	2,263	2,776	1	3,206	0,054	0,048	142	160	0,0212	1,22
FT1	70,73	4,546	1,382	2	3,192	0,056	0,048	137	160	0,0106	0,60
C1T2	33,44	2,260	2,780	1	3,210	0,032	0,032	239	239	0,0142	0,81
C1T2	70,75	4,547	1,382	2	3,191	0,025	0,064	313	120	0,0141	0,81
C2T2	33,63	2,272	2,765	1	3,193	0,025	0,043	306	178	0,0189	1,08
C2T2	70,77	4,549	1,381	2	3,190	0,033	0,092	235	83	0,0202	1,16
C1T1	33,44	2,260	2,780	1	3,210	0,032	0,031	239	247	0,0137	0,79
C1T1	70,76	4,548	1,382	2	3,190	0,051	0,062	150	124	0,0136	0,78
InGaN2											
FT2	30,6	2,073	3,031	1	3,500	0,019	0,053	403	145	0,0256	1,46
FT2	63,63	4,141	1,517	2	3,504	0,022	0,042	354	182	0,0101	0,58
FT1	30,56	2,070	3,035	1	3,505	0,018	0,0327	426	234	0,0158	0,91
FT1	63,64	4,142	1,517	2	3,504	0,021	0,059	365	130	0,0142	0,82
C1T2	30,76	2,083	3,016	1	3,483	0,023	0,033	333	232	0,0158	0,91
C1T2	63,98	4,161	1,510	2	3,487	0,032	0,059	239	130	0,0142	0,81
C2T2	30,75	2,083	3,017	1	3,484	0,022	0,0285	355	269	0,0137	0,78
C2T2	63,945	4,159	1,511	2	3,489	0,032	0,052	239	147	0,0125	0,72
C1T1	30,73	2,081	3,019	1	3,486	0,022	0,033	348	232	0,0159	0,91
C1T1	63,9	4,157	1,512	2	3,491	0,027	0,057	284	134	0,0137	0,79
InGaNbroad											
C1T2	33,26	2,248	2,795	1	3,227	0,066	0,032	116	239	0,0142	0,82
C1T2	69,88	4,499	1,397	2	3,225	0,098	0,064	78	120	0,0142	0,82
C2T2	33,606	2,271	2,767	1	3,195	0,068	0,043	113	178	0,0189	1,08
C2T2	70,729	4,546	1,382	2	3,192	0,099	0,092	77	83	0,0202	1,16
C1T1	33,2	2,244	2,800	1	3,233	0,066	0,031	116	247	0,0138	0,79
C1T1	69,31	4,467	1,407	2	3,249	0,095	0,062	81	124	0,0139	0,80
error	±0,063	±0,004	±0,005		±0,006	±0,005	±0,005	±75	±45	±0,0026	±0,15

Figure 7.30 Results of the GID measurements on InGaN samples.

effect. If the points on the graph in the fig. 7.31 belonging to the same sample can be connected by a line which is horizontal within the frame of an error bar, than the misorientation is the main effect. If this is not the case, than the size effect in the direction orthogonal to the radial path takes place.

To conclude more clearly, figure 7.32 (a) shows the ratio of the angular peak widths measured at $(20\bar{2}0)$ and $(10\bar{1}0)$. Open symbols refer to InGaN(1) peak and solid ones to InGaN(2). The values of the ratio being one and two are specially marked by solid lines with the corridor of uncertainty (dashed lines). If the ratio is equal two, than the complete broadening is due to the misorientation. On the other hand, if the ratio is equal one, the angular peak width stays the same for both lower and higher order of diffraction, than the size effect is dominant. Similarly, the ratio of the radial peak widths of $(20\bar{2}0)$ and $(10\bar{1}0)$ is plotted in the figure 7.32 (b). Here again we have a special physical meaning of the ratio being equal to one or two. The ratio equal to one corresponds to the domination of the size effect in the radial direction, while the ratio having the value of two means that the strain effect is prevailing.

Nearly all peaks, with the exception of peak InGaN(1) for the samples capped with InGaN, could be fitted with a Gaussian. Due to their asymmetry, the FWHM of these two peaks was manually determined. The widths of some peaks could not be determined reliably, therefore these results were not shown. As it was shown in the fig. 7.32 (a), the misorientation effect is dominant for the InGaN(2) measured on all of the samples. This is also valid for the InGaN(1) of the samples overgrown with InGaN. Therefore, almost complete responsibility for the broadening of InGaN(1) peak is on the misorientation. Looking to the InGaN(2) peak, there is a small contribution of the size effect beside main of misorientation, but this contribution is estimated to be not significant. The values of a mean misorientation are between $(0.75 \pm 0.15)^\circ$ and $(1.15 \pm 0.15)^\circ$. This is much higher in comparison to other heteroepitaxially grown semiconductor materials with the misorientation being typically in the range of 0.1°.

Figure 7.32 (b) shows that in the radial direction $[10\bar{1}0]$, the broadening of the GID peaks is mainly driven by a size distribution of coherently scattered domains, except for the InGaN(1) peaks belonging to the InGaN capping which ratio is close to 2 and therefore the broadening is driven by the strain. For the InGaN(2) peak, the ratio of the radial scan widths is systematically higher for the capped samples indicating the presence of strain.

In the radial scans measured in the GID configuration the strain and the size effect are overlapped. The evaluation of the reciprocal space maps gives a qualitative information of dominant effect which measure could be determined only if other effects can be neglected. The peak positions in the GID radial scans can not answer on the composition, e.g. indium content, because the peak positions are strongly influenced by the strain inside the material. Also, we do not know whether there is the interdiffusion of indium happening during the growth and overgrowth of InGaN quantum dots. Therefore, the reciprocal space mapping in asymmetrical X-ray diffraction (AXRD) has been performed on all of the samples. In AXRD geometry, characterization is sensitive simultaneously to both out-of-plane and in-plane lattice parameter as well

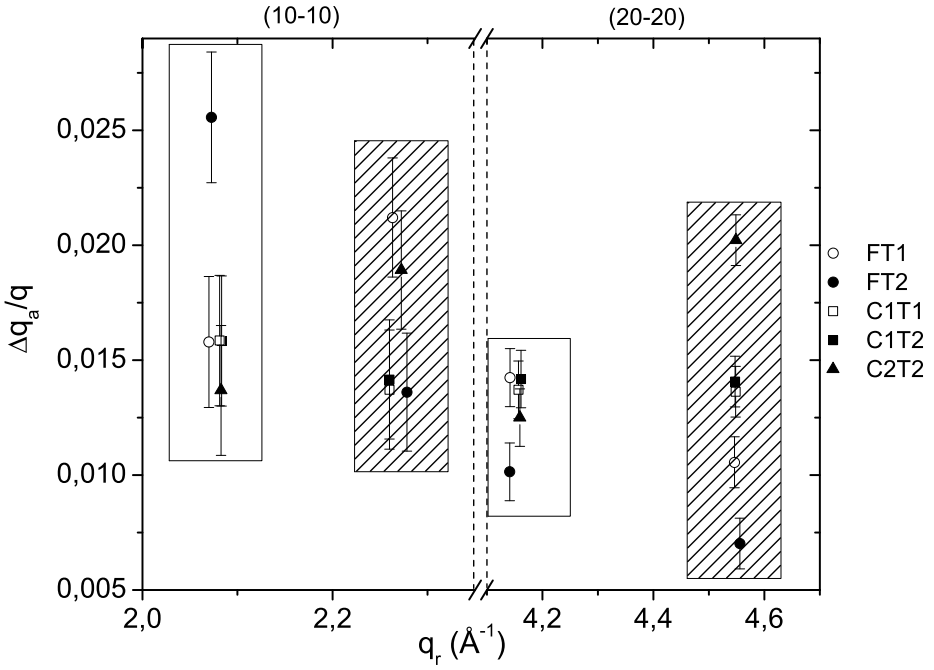

Figure 7.31 The widths of the angular scans normalized by q plotted versus the peak position. The values are calculated from the Gaussian fits. InGaN(1) peaks are in a patterned rectangles and InGaN(2) peaks in the opened. Open symbols belong to the growth temperature T1 and solid to T2.

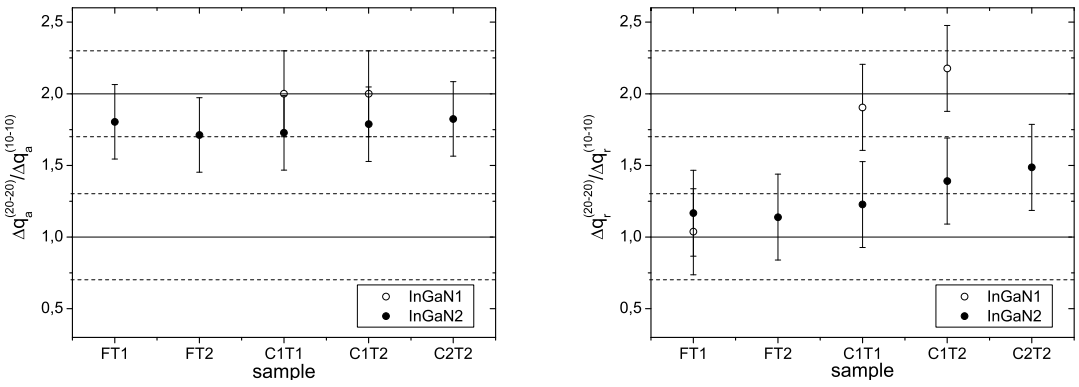

(a) (b)

Figure 7.32 (a) The ratio of the widths of rocking curves measured on $(20\bar{2}0)$ and $(10\bar{1}0)$. The value of one means that the size effects is prevailing, while two corresponds to the case of the misorientation of the coherently scattering domains being completely dominant. (b) The ratio of the widths of radial scans measured on $(20\bar{2}0)$ and $(10\bar{1}0)$. In this case "1" means size effect dominant and "2" means that strain plays a major role.

as to decoupling of the strain and the composition of InGaN islands.

7.4 Asymmetrical X-ray Diffraction on InGaN QDs

The reciprocal space maps in grazing incidence diffraction revealed two InGaN signals indicating the phase separation in the material. Since measuring in GID geometry is sensitive only to the one lattice parameter (in-plane), the composition and the strain in the material is overlapped. The reciprocal space mapping in asymmetrical X-ray diffraction (AXRD) is a method able to distinguish between indium content and the degree of relaxation. Therefore, AXRD reciprocal space maps were performed on all samples in the vicinity of $(10\bar{1}5)$ reflection. Information from AXRD together with two reflections measured in GID, as shown in the figure 7.33, should give a complete picture of the InGaN islands structure.

The AXRD experiment was performed at ANKA, SCD beam line using the synchrotron radiation energy of 10 keV. The experimental setup of six-circle diffractometer with "Mythen 1K" position sensitive detector (PSD) was used. The angular resolution of detector was predefined by channel size 50 μm $\times$ 8 mm (full size of the detector is 64 mm that corresponded to 1280 pixels) and distance between the center of diffractometer and the detector of 700 mm. It was estimated to be about 0.004 degrees per pixel. In the coplanar asymmetrical geometry, "Mythen 1K" detector was placed in the same plane with incoming and outgoing beams. To increase the signal from InGaN islands, it was necessary to enlarge the area of integration of outgoing beams in non-coplanar directions. Therefore PSD was used without slits. The channel width was 8mm and the region of integration in the in-plane direction was 0.65°. The Bragg angle of the reflection $(10\bar{1}5)$ for the energy of 10 keV is $\theta_{\mathrm{B}} = 39.746°$ and the angle between hkil plane and the sample surface $\Delta\phi = 20.5727°$. Therefore, the incidence angle was $\alpha_{\mathrm{i}} = \theta_{\mathrm{B}} - \Delta\phi = 19.1733°$ and the detector was placed at angle $\delta = 2\theta_{\mathrm{B}} = 79.492°$. The angular distance between the main peak of GaN buffer and the signal of InGaN(2) was around 6.5° and the angular acceptance of the "Mythen 1K" detector is 5.22°. Hence, the reciprocal space maps could not be measured with only one scan to have all wanted features captured. Therefore, reciprocal space maps of $(10\bar{1}5)$ were measured in three intersected scans. Each reciprocal space map is normalized to the monitor counts and plotted on a same scale for better comparison.

Figure 7.34 shows the relationship between the reciprocal space maps of $(10\bar{1}5)$ measured by AXRD and of $(10\bar{1}0)$ measured by GID. Diffraction peaks of the same feature are connected with dashed lines and labeled with the same name. The lateral positions of the $(10\bar{1}5)$ peaks correspond well to the radial positions of $(10\bar{1}0)$ peaks measured in-plane. All AXRD reciprocal space maps have two main intensity streaks. One of the streaks, which goes through the GaN peak perpendicularly to the q_x direction, is actually the surface streak from the sample surface well known in the literature as crystal truncation rod (CTR) [81]. Second streak, also going through the GaN Bragg peak, but not perpendicularly to the q_x than inclined by about 60° to

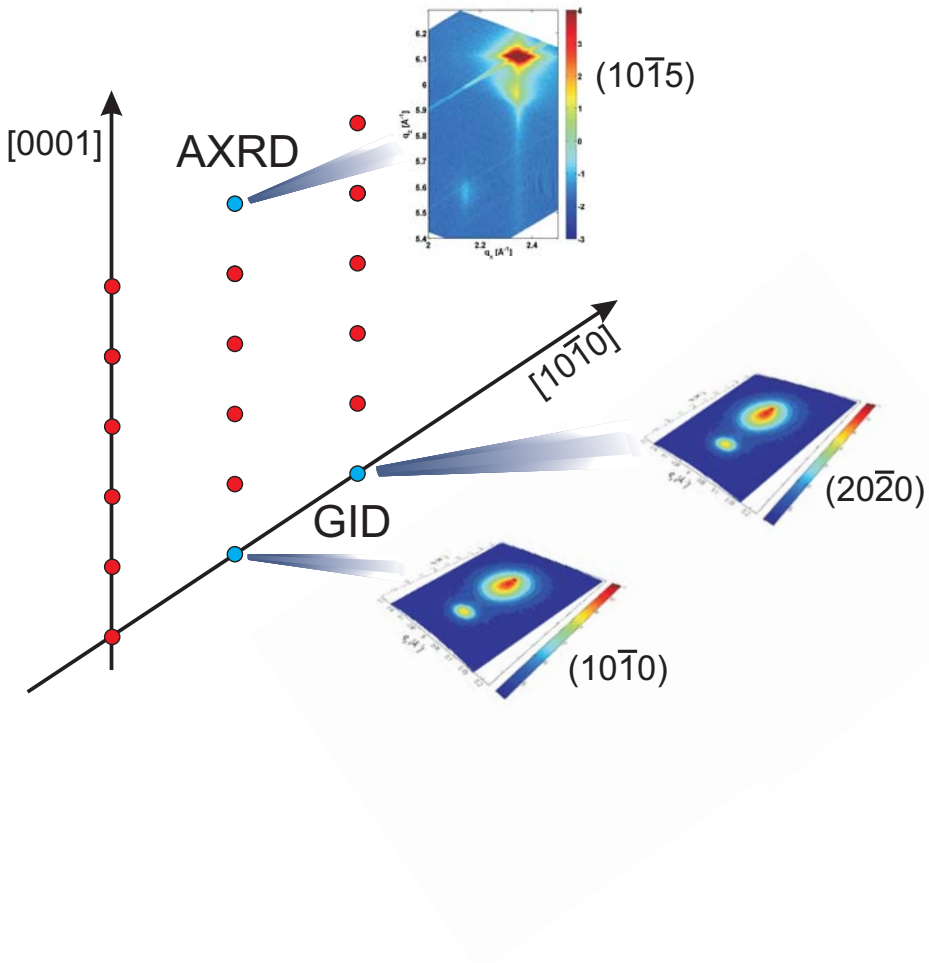

Figure 7.33 The reflections in the reciprocal space which have been measured using AXRD (10$\bar{1}$5) and GID (10$\bar{1}$0), (20$\bar{2}$0).

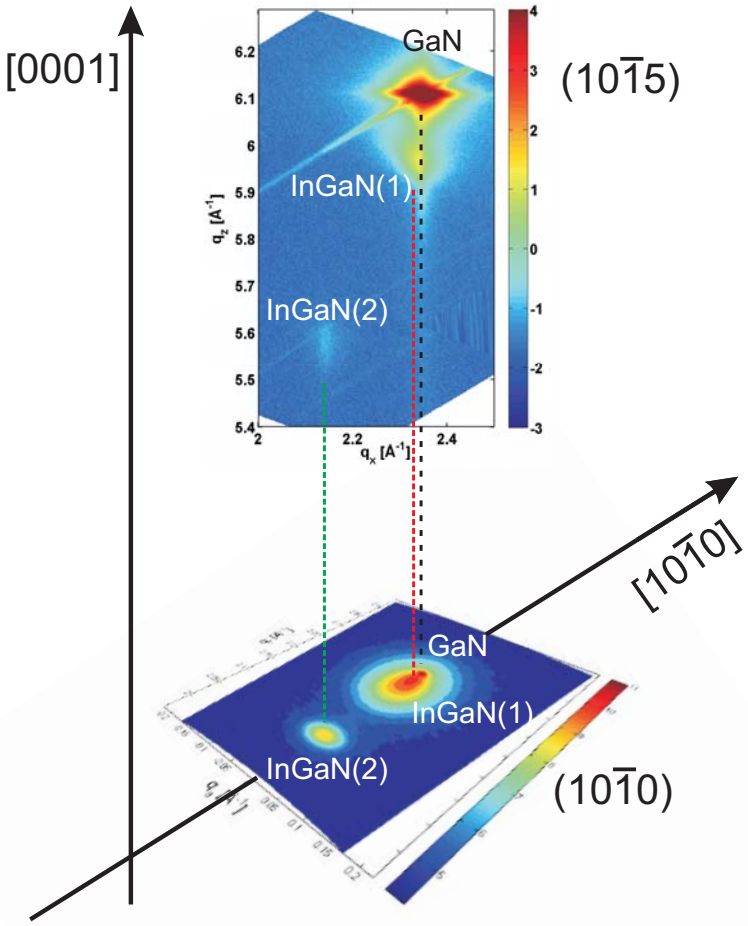

Figure 7.34 Relationship between the reciprocal space maps measured by AXRD and GID. The labeling of the diffraction peaks are kept the same: GaN, InGaN(1) and InGaN(2).

the CTR, is most likely due to the air scattering. Some minor streaks weakly visible around the GaN peak are due to the imperfection of optical elements in the beam line.

The results of the reciprocal space maps of $(10\bar{1}5)$ measured by asymmetrical XRD are shown in the figures as follows. Figure 7.35 shows the reciprocal space maps of $(10\bar{1}5)$ measured on the samples with freestanding InGaN islands grown at temperature T1 (fig. 7.35 (a)) and at temperature T2 (fig 7.35 (b)). Characteristic for both samples is that GaN and InGaN(2) are well visible, but there is no evidence of the scattering signal named InGaN(1) close to GaN which was visible in the GID geometry for the sample FT1. The reason for this could be in the fact that measurements with so high incidence angle of $\alpha_\mathrm{i} = 19.1733°$ make the most of contribution to the scattering intensity from deep crystalline structure of the GaN buffer layer and much less from the surface nano-objects. Therefore, possible InGaN(1) peak could be too weak to be resolved under the bright GaN spot. The InGaN(2) peak is visible for both FT1 and FT2 samples. It has elliptical shape elongated in the q_z direction. The width of InGaN(2) peak in this direction perpendicular to the sample surface is $\Delta q_z = 0.06$ Å^{-1}, what gives a dimension in real space of $D = \frac{2\pi}{\Delta q_z} = 10.5$ nm. D corresponds well to the height of the type B InGaN islands measured by AFM. This gives a rise to conclude that InGaN(2) diffraction peak can be attributed to the big InGaN islands confirming the hypothesis made in the GID study.

The reciprocal space maps of $(10\bar{1}5)$ measured on the samples with InGaN islands overgrown with InGaN are shown in the figure 7.36 (a) grown at temperature T1 and (b) grown at temperature T2. On both, the GaN Bragg peak from the buffer layer, InGaN(1) and InGaN(2) are visible. The InGaN(1) peak has a broad intensity distribution along the relaxation line what indicates different strain states in the formation of the InGaN capping. For the overgrown samples, the InGaN(2) has different positions in comparison to the RSMs measured on the samples with freestanding quantum dots, same as it was observed by GID radial scans (shift to the GaN Bragg position).

Figure 7.37 shows the reciprocal space map of $(10\bar{1}5)$ measured on the sample with InGaN islands overgrown with pure GaN. Again, GaN Bragg peak and InGaN(2) are well visible. Similarly to other overgrown samples, the shift of InGaN(2) peak has been observed. The main difference is in InGaN(1) peak which is for C2T2 much more narrow in contrast to C1T1 and C1T2. Secondly, the lateral (q_x) position of this peak is just as for pure GaN. Moreover, around this peak one can clearly observe the oscillations in the q_z direction along the crystal truncation rod. The period of oscillations corresponds to the thickness of about 10 nm and can be attributed to the GaN capping. The oscillations tell about well defined abrupt interface between the GaN capping and InGaN quantum dots.

As an example of the strain and composition study, the AXRD reciprocal space map is shown in the figure 7.38. The line connecting the pure GaN and the pure InN Bragg peaks which can be extrapolated to the origin of the reciprocal space is indicating the indium content inside the islands. The position of the peak sitting on

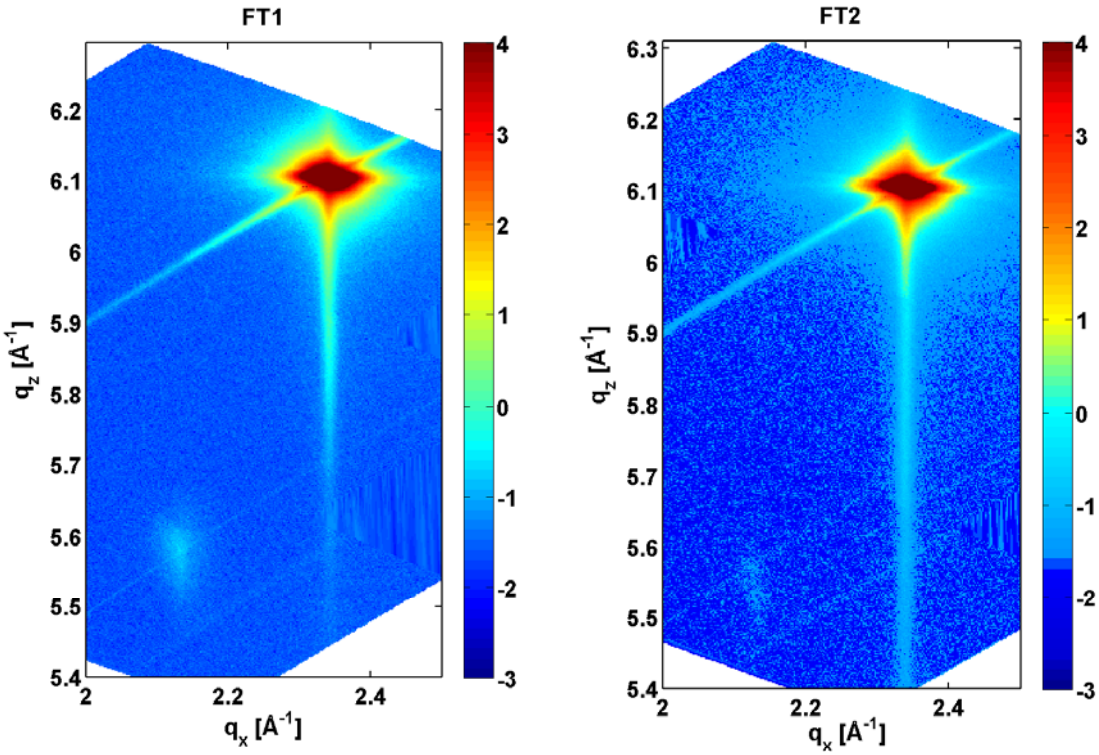

(a) (b)

Figure 7.35 Reciprocal space maps of the $(10\bar{1}5)$ reflection measured on the freestanding InGaN quantum dots samples, (a) FT1 and (b) FT2.

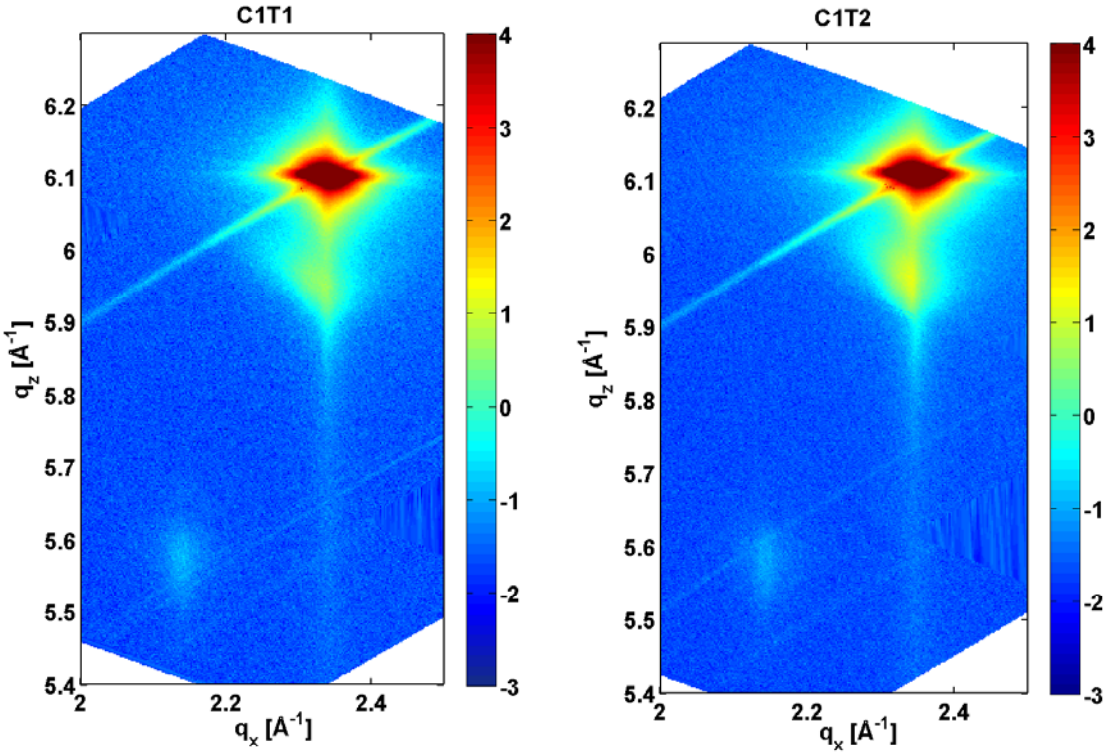

(a) (b)

Figure 7.36 Reciprocal space maps of the $(10\bar{1}5)$ reflection measured on the InGaN quantum dots samples overgrown with InGaN, (a) C1T1 and (b) C1T2.

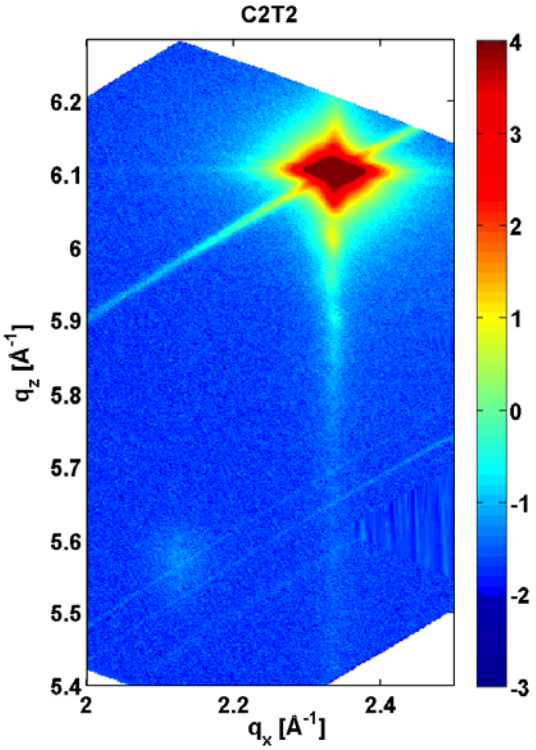

Figure 7.37 Reciprocal space maps of the $(10\bar{1}5)$ reflection on the InGaN quantum dots sample overgrown with GaN, C2T2.

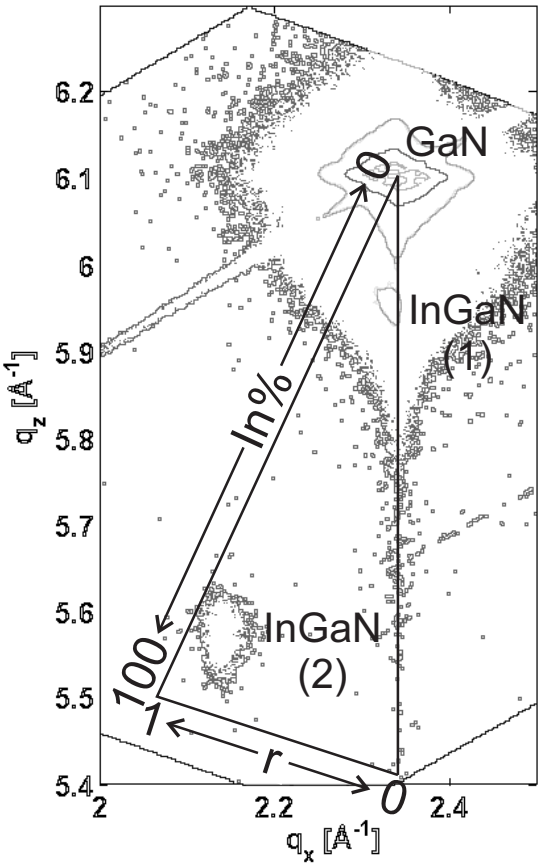

Figure 7.38 Strain and composition of InGaN QDs revealed from reciprocal space maps $(10\bar{1}5)$.

this line gives the percent content x in $In_xGa_{1-x}N$. The degree of relaxation r can be between 0 and 1. If the peak is exactly laterally matched to the GaN (on the crystal truncation rod) then InGaN is fully strained with degree of relaxation being zero. If the InGaN peak is laying on the line connecting the Bragg peaks of pure GaN and InN and the origin of the reciprocal space then it is completely relaxed with degree of relaxation equal to one. All other possibilities are in between extreme solutions and need to be calculated by method explained in the section 2.5.1.

The AXRD results of strain and composition in InGaN islands are given in the table 7.3. The In content x and the degree of relaxation r are given for two different peaks InGaN(1) and InGaN(2).

For the peak InGaN(1), values are given just for the samples with quantum dots overgrown with InGaN (C1T1 and C1T2), because for the freestanding dots samples there is no signal resolved and for the sample with dots overgrown with pure GaN there is no indium in the capping layer. The indium content x in $In_xGa_{1-x}N$ capping layer is determined to be 12 ± 6 % for the sample C1T1 and 9 ± 2 % for the sample C1T2. For both of these samples it was found that they are partially strained with

	InGaN(1)		InGaN(2)	
sample	x(In content) [%]	r (rel. deg.) [%]	x(In content) [%]	r (rel. deg.) [%]
FT1	no signal	no signal	90±6	99±5
FT2	no signal	no signal	90±6	97±5
C1T1	12±6	10±10	87±6	96±5
C1T2	9±2	10±10	87±6	97±5
C2T2	pure GaN	pure GaN	89±6	98±5

Table 7.3 The AXRD results on the InGaN quantum dots samples showing the In content x and the degree of relaxation r given for two different peaks InGaN(1) and InGaN(2).

the dominant relaxation of $r = 10 \pm 10\%$, but the smeared-out peak shape in direction of the relaxation line shows that there are even higher degrees of relaxation present. From the growth conditions it was expected to have about 10% of indium in InGaN capping layers.

The InGaN(2) peak is visible for all of the samples. For the samples with free-standing islands, the indium content is equal to $x = 90 \pm 6\%$, for both FT1 and FT2. It was previously discussed that this peak can be attributed to the InGaN islands of type B. These islands are indium rich in comparison to what has been reported in the literature so far. A bit smaller indium concentration in the type B InGaN islands when overgrown indicates that there is a weak interdiffusion between islands and capping material and that more for the capping with InGaN ($87 \pm 6\%$) than for the capping with pure GaN ($89 \pm 6\%$). For all of the samples, the type B InGaN islands are almost fully relaxed.

To summarize, the lateral components of the diffraction peaks measured by AXRD correspond well to the radial positions measured in GID study on InGaN quantum dots. Comparing the AXRD results with the results of the AFM study, a clear attributing of the peaks to different objects on the sample surface was found: the hight of the type B islands revealed from the width of InGaN(2) peak intensity distribution in q_z direction and InGaN(1) broad intensity distribution belonging to the InGaN capping layer which has non-uniform strain. The AXRD study of freestanding and

overgrown InGaN islands has shown that type B islands are indium rich (90%) and almost fully relaxed, while InGaN capping layers are of low indium concentration (10%) and partially strained ($r = 90\%$). The AXRD indicates the interdiffusion of indium between type B islands and InGaN capping. The overgrowing with pure GaN produces better defined interface between capping and islands.

7.5 Discussion on the Study of InGaN Quantum Dots

The combination of all measurements done on the sample series of freestanding and overgrown InGaN quantum dots: GID and AXRD in the reciprocal space together with AFM in the real space now should be connected to the photoluminescence (PL) measurements measured on same samples to link the structure and morphology of InGaN islands to the emission of the future photonic semiconductor devices.

A clear attributing of the features measured on the samples to the structure of the surface objects is as follows. The growth of InGaN quantum dots by the novel segregation method results in two types of InGaN islands: type A with the typical height of about 1.5-2 nm, with a high density and type B with the height of about 8 nm with the relatively low density. The GID measurements confirm the phase separation in freestanding quantum dots. The indium content in type A is low and unfortunately was not possible to be resolved by AXRD, same as the relaxation degree. From the GID maps, the concentration cannot be determined due to the superposition of strain and concentration effects. The freestanding type B islands have the indium concentration of 90% and they are almost fully relaxed. The overgrowing of InGaN quantum dots do not embed them by surrounding, even opposite, the capping layer continues to grow more on top following the surface morphology of the freestanding islands. In the case of InGaN capping layer with about 10% indium, partially strained to the GaN, there is an interdiffusion happening between the dots and the layer evidenced in the loss of indium in the type B islands when overgrown. Overgrowing with pure GaN produces well defined sharp interface between the islands and capping.

It was observed by AFM that generally, InGaN islands are lower when grown at higher temperature, although it is in a contradiction with the literature. However, a growth rate and other growth parameters as temperature, partial pressure and molar fraction are of very high importance for the growth of InGaN quantum dots. The islands height might be a result of the competition between deposition rate and decomposition rate which increases with temperature [146]. The nucleation of InGaN quantum dots is governed by the surface migration of In adatoms, rather than Ga or both [158]. In adatoms are expected to have a considerably larger migration length on the GaN surface, leading to a much higher nucleation rate and hence governing the formation of InGaN quantum dots. But, it was shown, for pure InN, that the growth rate decreases above 540°C exponentially [166]. In segregation growth method, the

growth rate is reasonably low as above the growth rate 0.5μm/h there is no phase separation in InGaN but homogeneous and single phase alloy [167]. On the other hand, the growth rate is not too low that the system can reach the thermodynamic equilibrium what can be concluded from the Gaussian shape of the islands, already discussed in sec. 7.2.9.

The InGaN islands were grown with intentional indium molar fraction of 0.82 (gas phase). Nearly the same composition should be expected for solids at temperature below 700°C [70]. According to the phase diagram for the strained InGaN shown in fig. 2.13, the expected indium content due to a spinodal decomposition are as follows. For the growth at 600°C, In-rich phase would have more than 86%In and In-poor phase below 16%In, while for the growth at 650°C the values are slightly different, more than 83% for In-rich and below 20% for In-poor phase. The results of indium content in InGaN islands revealed from AXRD study correspond to the theoretical prediction. The results of AFM, GID and AXRD confirmed that both phases coexist even after the capping. The X-ray scattering methods gave an average composition and the strain distribution. The composition is, however, not expected to be homogeneous, since TEM studies have shown for InGaN grown on GaN that segregation takes a place leading to the composition fluctuations [70, 168, 169]. Nevertheless, it was confirmed that InGaN inclusions are formed in a GaN matrix producing the resonant photoluminescence [170].

Figure 7.39 shows the results of photoluminescence measurements measured at room temperature on all of the samples. On all of the plots one can see a yellow band emission around 2.2 eV and the near-band-edge emission at 3.4 eV. The peak belonging to the InGaN quantum dots should be at 2.6 eV. Photoluminescence (PL) study has a proof of the quantum efficiency for the sample with freestanding InGaN quantum dots grown at the lower temperature FT1 and the strong emission signal for the sample with InGaN quantum dots overgrown with pure GaN C2T2. The InGaN islands of type A should be responsible for the PL emission, because no signal from InGaN(2) (type B islands) is expected due to very high indium content which signal (in infrared) cannot be measured in this range. The sample FT1 with quantum efficiency is the one with evidenced phase separation and the InGaN islands of type A are not completely strained to the GaN buffer. On the other hand, the sample C2T2 with InGaN islands overgrown with pure GaN has type A InGaN islands kept by GaN from both sides and most likely without any diffusion of indium from islands. A sharp interface observed by oscillations in AXRD measured on C2T2 indicates that morphology of InGaN quantum dots stays undisturbed. This could be the reason for such a strong PL emission. Seems that for better performances the electron contrast must be strong.

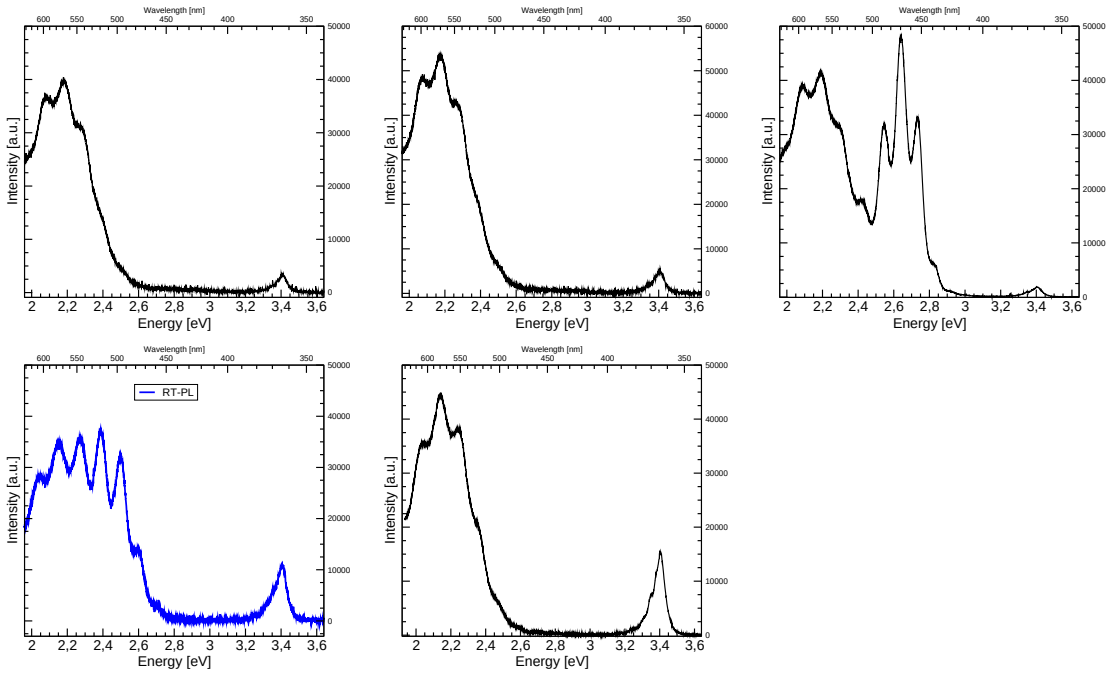

Figure 7.39 The photoluminescence spectra measured on the InGaN quantum dots samples. Upper row: overgrown QDs samples (C1T1-left, C1T2-middle, C2T2-right). Bottom row: freestanding QDs samples (FT1-left, FT2-middle). Only FT1 and C2T2 show the emission from quantum dots. (Courtesy of Ch. Tessarek, Uni-Bremen)

Chapter 8

Conclusions

The nitride-based semiconductor materials have been characterized by use of synchrotron radiation, particularly with various X-ray scattering methods. The thesis is focused on two main topics: the study of thin GaN films with different dislocation densities and the evolution of InGaN quantum dots during capping. Therefore, the results will be summarized in two separate sections as follows.

8.1 Thin GaN Films with Different Dislocation Densities

In order to establish a model system for the study of threading dislocation density and their correlation, the series of thin GaN films with different dislocation densities were characterized. The dislocation density was changed by tuning of the in-situ grown SiN_x interlayer deposition time.

Comparing the widths of the angular and the radial scans measured on different samples in coplanar geometry, indicates that change of the SiN_x interlayer deposition time does not affect the diffraction response of GaN film in the [0001] crystallographic direction. The high crystalline quality of the GaN films is verified. It is observed by study of AlN/GaN interface that the coherence is broken between the nucleation layer and the film in the samples with SiN_x interlayer. The grazing incidence diffraction were performed to characterize the in-plane properties of epitaxially grown thin GaN films with different dislocation densities. It was shown that there is no preferential orientation in thin GaN film confirming perfect in-plane hexagonal symmetry. The radial Bragg peak position stay the same being independent of azimuthal angle and of SiN_x deposition time as well.

The X-ray reflectivity measured on the samples has shown that the thin film surface becomes smoother with more SiN_x deposited. A detailed study of the change of electron density at and close to the surface results in the fit of the reflectivity curves to a model assuming the thin oxide layer on the top of GaN film. The r.m.s. surface roughness of the thin GaN film decreases with increasing SiN_x deposition time and,

therefore, with decreasing of the threading dislocation density. The nominal values of the surface roughness vary from 0.4 nm to 0.8 nm. It was shown that the thickness of the oxide stays almost the same independently on the SiN_x deposition time varying between 0.61 nm and 0.83 nm. The r.m.s. roughness of the oxide layer is found to be between 0.15 nm and 0.3 nm with the tendency to decrease with increasing of the SiN_x deposition time.

The tilts of the layers (GaN film and AlN nucleation layer) follow the crystallographic in-plane orientation of the sapphire substrate miscut, along the GaN[11$\bar{2}$0]. The values are increasing from the bottom to the top, $\delta_{Al_2O_3} < \delta_{AlN} < \delta_{GaN}$. The observed values have been found to be independent of the SiN_x deposition time. The miscut of the substrate and the tilts of the layers have been discussed with the model of better compensating the lattice mismatch looking to the in-plane epitaxial relationship and to the stepped surface morphology of the sapphire substrate. It was found that the miscut optimum value of 0.3° corresponds to the inclination angle formed by step height of monoatomic layer distance of nominally $\frac{1}{6}c_{Al_2O_3}$ and the step width of about 40 nm. It might be that the compensation of the inclination by miscut provides a better partial relaxation of the epitaxially grown material at the step edges.

It was shown that it is possible to tune the dislocation density of the thin GaN film without significantly changing its average crystalline quality. Therefore, the here studied sample type is a perfect model system for studying the correlation of dislocations by a new approach of kinetic Monte-Carlo simulations of the diffuse scattering caused by dislocations. The reciprocal space maps were performed to study diffuse X-ray scattering from dislocations. The diffuse scattering was fitted by the Monte Carlo simulation and a new method for determination of the threading dislocation density non-destructively is developed by our collaborators from Charles University in Prague. The results achieved a good agreement with etch pit density measured on the sample series. By combining of the numerical simulation of diffuse scattering in GID and coplanar geometry it was confirmed that a new method is able to provide the information of threading dislocation density for each type, edge and screw, separately.

As an outlook in further improvement of the growth of thin GaN films towards reduction of dislocation density it would be good to develop a better controlled multistep *in-situ* deposition of the SiN_x interlayer. The X-ray characterization method could be extended to other classes of defects in GaN epitaxial layers.

8.2 Evolution of InGaN Quantum Dots During Capping

The growth of InGaN quantum dots by Stranski-Krastanow method leads to a dissolution of dots due to capping. A series of the freestanding and overgrown InGaN quantum dots are grown at different temperatures and capped with different materials. The islands were grown by segregation method due to a spinodal decomposition

followed by transition 2D→3D without the wetting layer. The samples were measured by GID, AXRD and AFM (the PL was used as a reference).

The two types of InGaN islands are observed: type A of high density with the typical height of 1.5-2 nm, diameter of 40 nm and with circular base, and type B of low density with height of 8 nm, diameter of 80-100nm and with elliptical base. Study of the islands shape with respect to the growth conditions and thermodynamic equilibrium confirmed N-reach atmosphere and that thermodynamic equilibrium is not reached.

First time ever there is an evidence of the phase separation in the InGaN quantum dots revealed from GID measurements. The phase separation in the InGaN QDs material due to a spinodal decomposition is confirmed and studied for the partially strained system. The both types of islands can be explained with expected phase separation from the phase diagram.

The AFM measured on the overgrown InGaN QDs shows the surface morphology which exhibits stabile capping of quantum dots and not the smooth surface as was expected. The morphology stays as of the freestanding samples and both types of the islands are still visible. The overgrowing of InGaN quantum dots do not embed them, even opposite, the capping layer continues to grow more on top of the islands than between them.

Reciprocal space maps in GID geometry have shown that for both freestanding and capped InGaN QDs the misorientation of the coherently scattering domains plays a major role. The broadening of the GID radial peaks is mainly driven by a size distribution of coherently scattered domains. For the freestanding islands this is almost absolutely, but for the overgrown islands the ratio is systematically higher indicating the presence of strain.

For the first time there is an answer on the real structure (composition and relaxation degree) of the InGaN QDs grown by decomposition method. The indium content x in $In_xGa_{1-x}N$ capping layer is determined to be 12 ± 6 % for the sample C1T1 and 9 ± 2 % for the sample C1T2, while for both of these samples it was found that they are partially strained with the dominant degree of relaxation of $r = 10 \pm 10\%$ with a broad strain state distribution. From the growth conditions it was expected to have about 10% of indium in InGaN capping layers. The indium content in type A is low. Their indium content and relaxation degree were unfortunately not possible to be determined by AXRD due to their weak scattering signal below a bright GaN peak for freestanding and due overlap with the capping signal for overgrown islands. For the samples with freestanding islands, the indium content in type B InGaN islands is equal to $x = 90 \pm 6\%$, for both FT1 and FT2. These islands are indium rich in comparison to what has been reported in the literature so far. A bit smaller indium concentration in the type B InGaN islands when overgrown indicates that there is a weak interdiffusion between islands and capping material and that more for the capping with InGaN ($87 \pm 6\%$) than for the capping with pure GaN ($89 \pm 6\%$). For all of the samples, the type B InGaN islands are almost fully relaxed.

For the QDs overgrown with InGaN, the interface can not be seen and a broad

AXRD intensity feature in the relaxation line indicates non-uniform strain distribution. For the QDs overgrown with GaN, the sharp interface capping/islands can be seen from the layer thickness oscillations. This sample, C2T2, shows a high PL signal indicating that electron contrast must be strong with the well defined phase shift. Beside this, just the sample with the freestanding InGaN quantum dots grown at lower temperature FT1 exhibits a PL signal confirming the presence of quantum dots.

For the InGaN islands, lower growth temperature gives better results. The pure GaN capping seems to be advanced over the InGaN. However, there is a need of further improvement of both the InGaN quantum dots growth and the capping process with more thick GaN required for the photonic device technology. The in-situ X-ray study would be necessary for deeper understanding of the growth process and its relation to the grown structure.

Chapter 9

Outlook

9.1 Future Perspectives: an *in-situ* X-ray Study During Growth Process

The knowledge and the experience gained during the work on the thesis should be extended to other various sample systems of nitride-based semiconductors. With this aim, the experiments on the several different material types have been already performed using the synchrotron radiation. Particularly, the diffuse scattering from the stacking faults was studied by measuring the GID reciprocal space maps on the series of non-polar a-GaN thin films grown on the r-sapphire. Then, the high quality InGaN quantum wells (illustrated in the fig. 9.1 (a)) with different indium contents grown on different substrates were investigated. Finally, the characterization of the InGaN/GaN nanopillars (fig. 9.1 (b)) grown coaxially on the ZnO rods has been performed to study their structural properties. The results of these recent studies have not been completely evaluated, therefore a detailed data analysis is still in the process.

The work in this PhD thesis can be considered as a preparation of the future *in-situ* X-ray study of nitride-based semiconductor devices by use of synchrotron radiation. An unique MOVPE-lab at ANKA connected with the NANO beam line is under construction in the frame of the Helmholtz Association Virtual Institute PINCH Photonics. For the purpose of the *in-situ* X-ray scattering characterization during the epitaxial growth, a special *in-situ* chamber has been designed and it is currently under construction. Figure 9.2 shows a space view of the MOVPE reactor design. It will be suitable to be mounted in a center of rotation of the diffractometer at NANO1 experimental hutch that X-ray characterization can be performed while the sample is under the growth process. This approach should give the answers to the fundamental relationship between the epitaxial growth process of group(III)-nitrides and their structure.

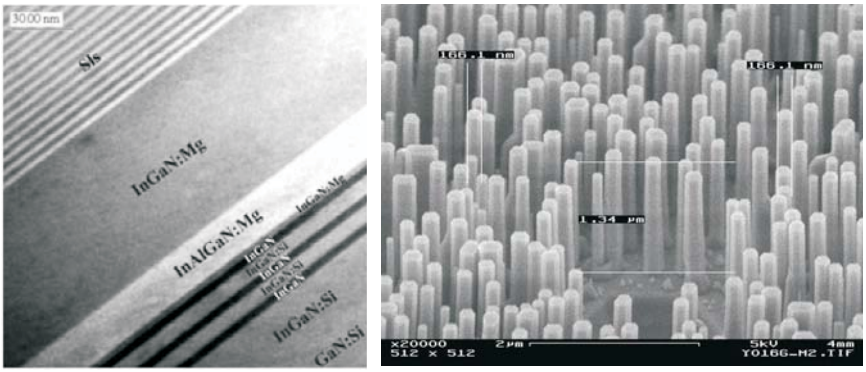

(a) (b)

Figure 9.1 Some of the sample material systems which have been measured by X-ray scattering experiments by use of synchrotron radiation in order to continue research on the topic: (a) InGaN quantum wells multilayer (courtesy of M. Leszczyński) and (b) InGaN/GaN nanopillars (courtesy of F. Scholz).

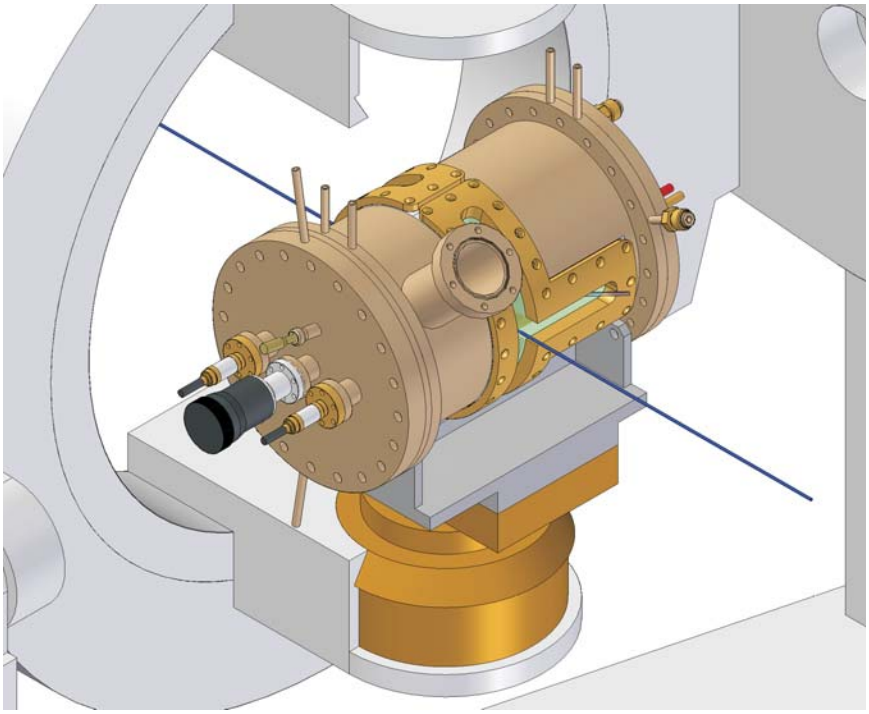

Figure 9.2 The MOVPE reactor for the *in-situ* X-ray scattering experiments during the epitaxial growth [171]. Development, design and construction are made in the collaboration in the frame of Helmholtz Virtual Institute PINCH Photonics.

Bibliography

[1] S. Nakamura, S. Pearton, and G. Fasol, *The Blue Laser Diode*, 2nd ed. (Springer, Berlin/Heidelberg/New York/Barcelona/Hong Kong/London/Milan/Paris/Singapore/Tokyo, 2000), pp. 1–13.

[2] B. University of California-MSE, "Weber research group presentation," http://www.mse.berkeley.edu/groups/weber/research/ganLED.html (Accessed September 21, 2010).

[3] J. Wu, W. Walukiewicz, K. M. Yu, J. W. I. Ager, E. E. Haller, H. Lu, W. J. Schaff, Y. Saito, and Y. Nanishi, "Unusual properties of the fundamental band gap of InN," Appl. Phys. Lett. **80,** 3967–3969 (2002).

[4] I. o. O. University of Ulm, "Lecture Notes in Optoelectronics, Scholz F.," http://www-opto.e-technik.uni-ulm.de/lehre/cs/ (Accessed September 21, 2010).

[5] I. Akasaki, K. Hiramatsu, and H. Amano, Memoirs of the Faculty of Engineering, Nagoya University **43,** 147 (1991).

[6] M. A. Moram and M. E. Vickers, "X-ray diffraction of III-nitrides," Rep. Prog. Phys. **72,** 036502 (2009).

[7] S. Chichibu, T. Azuhata, T. Sota, and N. S., "Spontaneous emission of localized excitons in InGaN single and multiquantum well structures," Appl. Phys. Lett. 69 (1996).

[8] V. Liuolia, S. Marcinkevičius, Y.-D. Lin, H. Ohta, S. P. DenBaars, and S. Nakamura, "Dynamics of polarized photoluminescence in m-plane InGaN/GaN quantum wells," J. Appl. Phys. **108,** 023101 (2010).

[9] A. Chakraborty, K. C. Kim, F. Wu, J. S. Speck, S. P. DenBaars, and U. K. Mishra, "Defect reduction in nonpolar a-plane GaN films using *in situ* SiN_x nanomask," Appl. Phys. Lett. **89,** 041903 (2006).

[10] F. Wu, A. Tyagi, E. C. Young, A. E. Romanov, K. Fujito, S. P. DenBaars, S. Nakamura, and J. S. Speck, "Misfit dislocation formation at heterointerfaces

in (Al,In)GaN heteroepitaxial layers grown on semipolar free-standing GaN substrates," J. Appl. Phys. **109,** 033505 (2011).

[11] G. B. Stringfellow, *Organometallic Vapor-Phase Epitaxy*, 1st ed. (Academic Press, 1989), pp. 3–10.

[12] P. Gibart, "Metal organic vapour phase epitaxy of GaN and lateral overgrowth," Rep. Prog. Phys. **67,** 667–715 (2004).

[13] I. Grzegory, K. S., M. Leszczyński, P. P., S. T., and S. Porowski, in *High-Pressure Crystallization of GaN, part of the book 'Nitride Semiconductors'*, 1st ed., P. Ruterana, M. Albrecht, and J. Neugebauer, eds., (Wiley-VCH Verlag GmbH & Co. KGaA, Weinheim, 2003), pp. 3–43.

[14] R. Parikh and R. Adomaitis, "An overview of gallium nitride growth chemistry and its effect on reactor design: Application to a planetary radial-flow CVD system," J. Cryst. Growth **286,** 259–278 (2006).

[15] R. Pawlowski, C. Theodoropoulos, A. Salinger, T. Mountziaris, H. Moffat, J. Shadid, and E. Thrush, "Fundamental models of the metalorganic vapor-phase epitaxy of gallium nitride and their use in reactor design," J. Cryst. Growth **221,** 622–628 (2000).

[16] L. Teles, J. Furthmüller, L. Scolfaro, J. Leite, and F. Bechstedt, "First-priciples calculations of the thermodynamic and structural properties of strained $In_xGa_{1-x}N$ and $Al_xGa_{1-x}N$ alloys," Phys. Rev. B **62,** 2475–2485 (2000).

[17] H.-T. Lam and J. Vohs, "Surface reactions of trimethylgallium on MOVPE-grown GaN (0001)," Surf. Sci. **426,** 199–211 (1999).

[18] H. Morkoç, *Handbook of Nitride Semiconductors and Devices*, 1st ed. (Wiley-VCH Verlag GmbH & Co. KGaA, Weinheim, 2008), Vol. 1, pp. 373–377.

[19] D. Lu, D. Florescu, D. Lee, V. Merai, J. Ramer, A. Parekh, and E. Armour, "Sapphire substrate misorientation effects on GaN nucleation layer properties," J. Cryst. Growth **272,** 353–359 (2004).

[20] M. di Forte-Poisson, F. Huet, A. Romann, M. Tordjmann, D. Lancefield, E. Pereira, J. Di Persio, and B. Pecz, "Relationship between physical properties and gas purification in GaN grown by metalorganic vapor phase epitaxy," J.Cryst. Growth **195,** 314–318 (1998).

[21] P. Grudowski, A. Holmes, C. Eiting, and R. Dupuis, "The effect of substrate misorientation on the photoluminescence properties of GaN grown on sapphire by metalorganic chemical vapor deposition," Appl. Phys. Lett. **69,** 3626–3628 (1996).

[22] T. Suski *et al.*, "Substrate misorientation induced strong increase in the hole concentration in Mg doped GaN grown by metalorganic vapor phase epitaxy," Appl. Phys. Lett. **93,** 172117 (2008).

[23] P. Brückner, F. Habel, and F. Scholz, "HVPE growth of high quality GaN layers," Phys. Status Solidi C **3,** 1471–1474 (2006).

[24] P. Perlin *et al.*, "Nitride-based quantum structures and devices on modified GaN substrates," Phys. Status Solidi A **206,** 1130–1134 (2009).

[25] P. Perlin *et al.*, "Fabrication and properties of GaN-based lasers," J. Cryst. Growth **310,** 3979–3982 (2008).

[26] J. Hertkorn, P. Bruückner, S. Thapa, T. Wunderer, F. Scholz, M. Feneberg, K. Thonke, R. Sauer, M. Beer, and J. Zweck, "Optimization of nucleation and buffer layer growth for improved GaN quality," J. Cryst. Growth **308,** 30–36 (2007).

[27] S. Lee, H. Choe, T. Oh, J. Jean, B. Shin, Y. Sohn, and C. Kim, "Surface-morphology evolution and strain relaxation during heteroepitaxial growth of GaN films without low-temperature nucleation layers," Appl. Phys. Lett. 90 (2007).

[28] S. Lee, T. Oh, B. Shin, J. Jean, H. Choe, and C. Kim, "Effect of NH_3 Pretreatment of the Surface Morphologies of GaN Films Grown on Miscut Sapphire Substrates by Using Hydride Vapor Phase Epitaxy," J. Korean Phys. Soc. **50,** 785–788 (2007).

[29] Y. Xing, J. Han, J. Deng, J. Li, C. Xu, and G. Shen, "Investigation of GaN leyer grown on different low misoriented sapphire by MOCVD," Appl. Surf. Sci. **255,** 6121–6124 (2009).

[30] H. Amano, N. Sawaki, I. Akasaki, and Y. Toyoda, "Metalorganic vapor phase epitaxial growth of a high quality GaN film using an AlN buffer layer," Appl. Phys. Lett. 48 (1986).

[31] I. Akasaki, H. Amano, Y. Koide, K. Hiramatsu, and N. Sawaki, "Effects of AlN buffer layer on crystallographic structure and on electrical and optical properties of GaN and $Ga_{1-x}Al_xN$ $(0 < x \leq 0.4)$ films grown on sapphire substrate by MOVPE," J.Cryst. Growth **98,** 209–219 (1989).

[32] S. Nakamura, "GaN Growth Using GaN Buffer Layer," Jap. J. Appl. Phys. **30,** L1705–L1707 (1991).

[33] S. Keller, B. Keller, Y.-F. Wu, D. Heying, B. Kapolnek, J. Speck, U. Mishra, and S. DenBaars, "Influence of sapphire nitridation on properties of gallium

nitride grown by metalorganic chemical vapor deposition," Appl. Phys. Lett. 68 (1996).

[34] S. Fuke, H. Teshigawara, K. Kuwahara, Y. Takano, T. Ito, M. Yanagihara, and K. Ohtsuka, "Influence of initial nitridation and buffer layer deposition on the morphology of a (0001) GaN layer grown on sapphire substrates," J. Appl. Phys. 83 (1998).

[35] V. Lebedev, "Strain relaxation in highly mismatched hexagonal heterosystems," J. Appl. Phys. **108,** 013515 (2010).

[36] U. of Ulm, "Lecture Notes in Optoelectronics, Scholz F.," http://www-opto.e-technik.uni-ulm.de/lehre/cs/DOS-DIM.jpg (Accessed September 21, 2010).

[37] P. Ruterana and G. Nouet, "Atomic Structure of Extended Defects in Wurtzite GaN Epitaxial Layers," Phys. Status Solidi B **227,** 177–228 (2001).

[38] G. Dimitrakopulos, P. Komninou, J. Kioseoglou, T. Kehagias, E. Sarigiannidou, A. Georgakilas, G. Nouet, and T. Karakostas, "Structural transition of inversion domain boundaries through interactions with stacking faults in epitaxial GaN," Phys. Rev. B **64,** 245325 (2001).

[39] G. Dimitrakopulos, P. Komninou, and R. Pond, "Topological Analysis of Defects in Epitaxial Nitride Films and Interfaces," Phys. Status Solidi B **227,** 45–92 (2001).

[40] V. Lebedev, V. Cimalla, J. Pezoldt, M. Himmerlich, S. Krischok, J. Schaefer, O. Ambacher, F. Morales, J. Lozano, and D. González, "Effect of dislocations on electrical and electron transport properties of InN thin films. I. Strain relief and formation of a dislocation network," J. Appl. Phys. **100,** 094902 (2006).

[41] S. Rosner, E. Carr, M. Ludowise, G. Girlami, and H. Erikson, Appl. Phys. Lett. **70,** 420 (1997).

[42] N. Pauc, M. R. Phillips, V. Aimez, and D. Drouin, "Carrier recombination near threading dislocations in GaN epilayers by low voltage cathodoluminescence," Appl. Phys. Lett. **89,** 161905 (2006).

[43] J. Elsner, R. Jones, P. Sitch, V. Porezag, M. Elstner, T. Frauenheim, M. Heggie, S. Öberg, and P. Briddon, "Theory of Threading Edge and Screw Dislocations in GaN," Phys. Rev. Lett. **79,** 3672–3675 (1997).

[44] V. Ratnikov, R. Kyutt, T. Shubina, T. Paskova, and B. Monemar, "Determination of microdistortion components and their applications to structural characterization of HVPE GaN epitaxial layers," J. Phys. D: Appl. Phys. **34,** A30–A34 (2001).

[45] Y. B. Kwon, J. H. Je, P. Ruterana, and G. Nouet, "On the origin of *a*-type threading dislocations in GaN layers," J. Vac. Sci. Technol. A **23,** 1588–1591 (2005).

[46] U. o. Alberta, "EAS courses, University of Alberta," .

[47] S. Awschalom Group, University of California, "Spin Coherence in GaN," http://awsch-web.physics.ucsb.edu/research/spintronics/gan/index.php (Accessed December 24, 2010).

[48] Image-Metrology, "Quality Assurance and Dislocation Analysis of GaN Wafers Based on SEM Images," http://www.imagemet.com/index.php?id=22&main=products&sub=applications (Accessed December 24, 2010).

[49] P. J. Hansen *et al.*, "Scanning capacitance microscopy imaging of threading dislocations in GaN films grown on (0001) sapphire by metalorganic chemical vapor deposition," Appl. Phys. Lett. **72,** 2247–2249 (1998).

[50] B. Heying, X. Wu, B. Keller, S. DenBaars, and J. Speck, "Role of threading dislocations structure on the x-ray diffraction peak widths in epitaxial GaN films," Appl. Phys. Lett. **68,** 643–645 (1996).

[51] V. Holý, J. Kuběna, I. Ohlídal, and K. Ploog, "The Diffuse X-ray Scattering in Real Periodical Superlattices," Superlattice. Microst. **12,** 25–35 (1992).

[52] V. M. Kaganer, O. Brandt, A. Trampert, and K. H. Ploog, "X-ray diffraction peak profiles from threading dislocations in GaN epitaxial films," Phys. Rev. B **72,** 045423 (2005).

[53] M. J. Kappers, R. Datta, R. A. Oliver, F. D. G. Rayment, M. E. Vickers, and C. J. Humphreys, "Threading dislocation reduction in (0001) GaN thin films using SiN_x interlayers," J. Cryst. Growth **300,** 70–74 (2007).

[54] L. Teles, J. Furthmüller, L. Scolfaro, J. Leite, and F. Bechstedt, "Influence of composition fluctuations and strain on gap bowing in $In_xGa_{1-x}N$," Phys. Rev. B **63,** 085204 (2001).

[55] F. Bechstedt, J. Furthmüller, M. Ferhat, L. Teles, L. Scolfaro, J. Leite, V. Davydov, O. Ambacher, and R. Goldhahn, "Energy gap and optical properties of $In_xGa_{1-x}N$," Phys. Status Solidi A **195,** 628–633 (2003).

[56] K. O'Donnell, R. Martin, and P. Middleton, "Origin of Luminescence from InGaN Diodes," Phys. Rev. Lett. **82,** 237–240 (1999).

[57] K. O'Donnell, J. Mosselmans, R. Martin, S. Pereira, and M. White, "Structural analysis of InGaN epilayers," J. Phys.: Condens. Matter **13,** 6977–6991 (2001).

[58] K. O'Donnell, S. Pereira, R. Martin, P. Edwards, M. Tobin, and J. Mosselmans, "Wishful physics - some common misconceptions about InGaN," Phys. Status Solidi A **195,** 532–536 (2003).

[59] A. Pretorius, T. Yamaguchi, C. Kübel, R. Kröger, D. Hommel, and A. Rosenauer, "Strustural investigation of growth and dissolution of $In_xGa_{1-x}N$ nanoislands grown by molecular beam epitaxy," J. Cryst. Growth **310,** 748–756 (2008).

[60] M. Schuster, P. O. Gervais, B. Jobst, W. Hösler, R. Averbeck, H. Riechert, A. Iberl, and R. Stömmer, "Determination of the chemical composition of distorted InGaN/GaN heterostructures from x-ray diffraction data," J. Phys. D: Appl. Phys. **32,** A56–A60 (1999).

[61] S. P. Łepkowski and I. Gorczyca, "*Ab initio* study of elastic constants in $In_xGa_{1-x}N$ and $In_xAl_{1-x}N$ wurtzite alloys," Phys. Rev. B **83,** 203201 (2011).

[62] S. Pereira, M. Correia, E. Pereira, K. O'Donnell, E. Alves, A. Sequeira, N. Franco, I. Watson, and C. Deatcher, "Strain and composition distribution in wurtzite InGaN/GaN layers extracted from x-ray reciprocal space mapping," Appl. Phys. Lett. **80,** 3913–3915 (2002).

[63] L. Vegard, "Die Konstitution der Mischkristalle und die Raumfüllung der Atome," Z. Phys. **5,** 17–26 (1921).

[64] T. Matsuoka, N. Yoshimoto, T. Sasaki, and A. Katsui, "Wide-Gap Semiconductor InGaN and InGaAIN Grown by MOVPE," J. Electron. Mater. **21,** 157–163 (1992).

[65] K. Osamura, S. Naka, and Y. Murakami, "Preparation and optical properties of $Ga_{1-x}In_xN$ thin films," J. Appl. Phys. **46,** 3432–3437 (1975).

[66] R. Singh, D. Doppalapudi, T. Moustakas, and L. Romano, "Phase separation in InGaN thick films and formation of InGaN/GaN double heterostructures in the entire alloy composition," Appl. Phys. Lett. **70,** 1089–1091 (1997).

[67] N. El-Masry, E. Piner, S. Liu, and S. Bedair, "Phase separation in InGaN grown by metalorganic chemical vapor deposition," Appl. Phys. Lett. **72,** 40–42 (1998).

[68] I. Ho and G. Stringfellow, "Solid phase immiscibility in GaInN," Appl. Phys. Lett. **69,** 2701–2703 (1996).

[69] S. Karpov, N. Podolskaya, I. Zhmakin, and A. Zhmakin, "Statistical model of ternary group-III nitrides," Phys. Rev. B **70,** 235203 (2004).

[70] C. Tessarek, S. Figge, T. Aschenbrenner, S. Bley, A. Rosenauer, M. Seyfried, J. Kalden, K. Sebald, J. Gutowski, and D. Hommel, "Strong phase separation of strained $In_xGa_{1-x}N$ layers due to spinodal and binodal decomposition: Formation of stable quantum dots," Phys. Rev. B **83,** 115316 (2011).

[71] S. Pereira, M. Correia, E. Pereira, K. O'Donnell, E. Alves, A. Sequeira, and N. Franco, "Interpretation of double x-ray diffraction peaks from InGaN layers," Appl. Phys. Lett. **79,** 1432–1434 (2001).

[72] S. Pereira, "On the interpretation of structural and light emitting properties of InGaN/GaN epitaxial layers grown above and below the critical layer thickness," Thin Solid Films **515,** 164–169 (2006).

[73] V. Chamard, T. H. Metzger, M. Sztucki, V. Holý, M. Tolan, E. Bellet-Amalric, C. Adelmann, B. Daudin, and H. Mariette, "On the driving forces for the vertical alignment in nitride quantum dot multilayers," Europhys. Lett. **63,** 268–274 (2003).

[74] R. A. Oliver, M. J. Kappers, C. J. Humphreys, and G. A. D. Briggs, "Growth modes in heteroepitaxy of InGaN on GaN," J. Appl. Phys. **97,** 013707 (2005).

[75] R. Dingle, K. Shaklee, R. Leheny, and R. Zetterstrom, "Stimulated Emission and Laser Action in Gallium Nitride," Appl. Phys. Lett. **19,** 5–7 (1971).

[76] R. Dingle, W. Wiegmann, and C. Henry, "Quantum States of Confined Carriers in Very Thin $Al_xGa_{1-x}As$-GaAs-$Al_xGa_{1-x}As$ Heterostructures," Phys. Rev. Lett. **33,** 827–830 (1974).

[77] R. Dietz, F. Merritt, R. Dingle, D. Hone, B. Silbernagel, and P. Richards, "Exchange Narrowing in One-Dimensional Systems," Phys. Rev. Lett. **26,** 1186–1188 (1971).

[78] A. Yoffe, "Low-dimensional systems: quantum size effects and electronic properties of semiconductor microcrystallites (zero-dimensional systems) and some quasi-two-dimensional systems," Adv. Phys. **42,** 173–266 (1993).

[79] C. Delerue, M. Lannoo, and G. Allan, "Tight Binding for Complex Semiconductor Systems," Phys. Status Solidi (b) **227,** 115–149 (2001).

[80] *Semiconductor Nanostructures*, 1st ed., D. Bimberg, ed., (Springer-Verlag, Berlin/Heildelberg, 2008).

[81] J. Als-Nielsen and D. McMorrow, *Elements of Modern X-ray Physics*, 1st ed. (John Wiley & Sons, Ltd, New York/Chichester/Weinheim/Brisbane/Singapore/Toronto, 2001).

[82] Prof. Dr. Tilo Baumbach (Modern X-ray Physics, Lecture notes, Karlsruhe Institute of Technology).

[83] H. Wondratschek, *Matrices, Mappings and Crystallographic Symmetry* (International Union of Crystallography, Chester, 2002), No. 22.

[84] Klaus D. Eichhorn (Short Introduction to Crystallography, Lecture notes, Karlsruhe Institute of Technology).

[85] Vaclav Holý (private communication).

[86] U. Pietsch, V. Holý, and T. Baumbach, *High Resolution X-Ray Scattering: From Thin Films and Nanostructures*, 2nd ed. (Springer Verlag, Berlin, 2004).

[87] B. E. Warren, *X-ray diffraction* (Dover Publications, Inc., New York, 1990).

[88] V. Holý, J. Kuběna, E. Abramof, K. Lischka, A. Pesek, and E. Koppensteiner, "X-ray double and triple crystal diffractometry of mosaic structure in heteroepitaxial layers," J. Appl. Phys. **74,** 1736–1743 (1993).

[89] V. Holý, K. Wolf, M. Kastner, H. Stanzl, and W. Gebhardt, "X-ray Triple-Crystal Diffractometry of Defects in Epitaxic Layers," J. Appl. Cryst. **27,** 551–557 (1994).

[90] T. Baumbach, *X-ray Scattering by Periodic Nanostructures*, *Habilitation thesis* (University of Potsdam, Potsdam, 2000).

[91] E. Koppensteiner, P. Hamberger, G. Bauer, V. Holý, and E. Kasper, "Analysis of strain and mosaicity in a short-period Si_9Ge_6 superlattice by x-ray diffraction," Appl. Phys. Lett. **64,** 172–174 (1994).

[92] V. Holý, J. Kuběna, and K. Ploog, "X-Ray Analysis of Structural Defects in a Semiconductor Superlattice," Phys. Status Solidi B **162,** 347–361 (1990).

[93] S. A. Stepanov, E. A. Kondrashkina, M. Schmidbauer, R. Köhler, J.-U. Pfeiffer, T. Jach, and A. Y. Souvorov, "Diffuse scattering from interface roughness in grazing-incidence x-ray diffraction," Phys. Rev. B **54,** 8150–8162 (1996).

[94] R. Chierchia, T. Böttcher, S. Figge, M. Diesselberg, H. Heinke, and D. Hommel, "Mosaicity of GaN Epitaxial Layers: Simulation and Experiment," Phys. Status Solidi B **228,** 403–406 (2001).

[95] R. Chierchia, T. Böttcher, H. Heinke, S. Einfeldt, S. Figge, and D. Hommel, "Microstructure of heteroepitaxial GaN revealed by x-ray diffraction," J. Appl. Phys. **93,** 8918–8925 (2003).

[96] G. Binnig, C. F. Quate, and C. Gerber, "Atomic Force Microscope," Phys. Rev. Lett. **56,** 930–933 (1986).

[97] T. Metzger *et al.*, "Defect structure of epitaxial GaN films determined by transmission electron microscopy and triple-axis X-ray diffractometry," Philos. Mag. A **77,** 1013–1025 (1998).

[98] G. T. Baumbach, S. Tixier, U. Pietsch, and V. Holý, "Grazing-incidence diffraction from multilayers," Phys. Rev. B **51,** 16848–16859 (1995).

[99] M. Birkholz, *X-ray scattering from soft matter* (Springer-Verlag, Berlin/Heildelberg, 2004).

[100] H. Dosch, "Evanescent absorption in kinematic surface Bragg diffraction," Phys. Rev. B **35,** 2137–2143 (1987).

[101] A. L. Golovin and R. M. Imamov, "Obtaining Quantitative Information on Amorphous Layer Thickness on Crystal Surface Using X-Ray Diffraction under Specular Reflection Conditions," Phys. Status Solidi A **80,** K63–K65 (1983).

[102] G. H. Vineyard, "Grazing-incidence diffraction and the distorted-wave approximation for the study of surfaces," Phys. Rev. B **26,** 4146–4159 (1982).

[103] ANKA Instrumentation Book (2010, ANKA, Karlsruhe Institute of Technology).

[104] H. You, "Angle calculations for a "4S+2D" six-circle diffractometer," J. Appl. Cryst. **32,** 614–623 (1999).

[105] T. F. E. Wikipedia, "Atomic Force Microscopy," http://en.wikipedia.org/wiki/Atomic_force_microscope (Accessed March 22, 2011).

[106] G. Binnig, H. Rohrer, C. Gerber, and E. Weibel, "Surface Studies by Scanning Tunneling Microscopy," Phys. Rev. Lett. **49,** 57–61 (1982).

[107] G. Binnig and H. Rohrer, "Scanning tunneling microscopy," Helv. Phys. Acta **55,** 726–735 (1982).

[108] G. Binnig and H. Rohrer, "Scanning Tunneling Microscopy," Surf. Sci. **126,** 236–244 (1983).

[109] G. Binnig, C. Quate, and C. Gerber, "Atomic Force Microscope," Phys. Rev. Lett. **56,** 930–933 (1986).

[110] S. N. Magonov and M.-H. Whangbo, *Surface Analysis with STM and AFM*, 1st ed. (VCH, Weinheim/New York/Basel/Cambridge/Tokyo, 1996), pp. 12–39.

[111] *LS AFM User's Guide and Service Manual*, 2nd ed. (Omicron Nanotechnology, Taunusstein, Germany, 2004).

[112] G. Omicron, "Large Sample SPM, Omicron, Instrument Concept," http://www.omicron.de/en/products/large-sample-spm/instrument-concept (Accessed September 22, 2011).

[113] S. NanoWorld, "Contact Mode AFM Probes, Type: CONTR," http://www.nanoworld.com/print/A-02.html (Accessed March 2, 2011).

[114] I. Horcas, R. Fernández, J. M. Gómez-Rodríguez, J. Colchero, J. Gómez-Herrero, and A. M. Baro, "WSXM: A software for scanning probe microscopy and a tool for nanotechnology," Rev. Sci. Instrum. **78,** 013705 (2007).

[115] M. Barchuk, V. Holý, B. Miljević, B. Krause, T. Baumbach, J. Hertkorn, and F. Scholz, "X-ray diffuse scattering from threading dislocations in epitaxial GaN layers," J. Appl. Phys. **108,** 043521 (2010).

[116] M. Barchuk, V. Holý, B. Miljević, B. Krause, and T. Baumbach, "Grazing-incidence x-ray diffraction from GaN epitaxial layers with threading dislocations," Appl. Phys. Lett. **98,** 021912 (2011).

[117] G. Aixtron, "Horizontal reactors, Type: AIX 200/4 RF-S," http://www.aixtron.com/index.php?id=154 (Accessed September 15, 2011).

[118] M. A. di Forte-Poisson, F. Huet, A. Romann, M. Tordjman, D. Lancefield, E. Pereira, J. Di Persio, and B. Pecz, "Relationship between physical properties and gas purification in GaN grown by metalorganic vapor phase epitaxy," J. Cryst. Growth **195,** 314–318 (1998).

[119] J. Hertkorn, F. Lipski, P. Brückner, T. Wunderer, S. B. Thapa, F. Scholz, A. Chuvilin, U. Kaiser, M. Beer, and J. Zweck, "Process optimization for the effective reduction of threading dislocations in MOVPE grown GaN using in situ deposited SiN_x masks," J. Cryst. Growth **310,** 48674870 (2008).

[120] J. Hertkorn, *Verbesserung der lateralen Stromführung in Hocheffiziente Halbleiterlichtquellen*, *Ph.D. thesis*, 1st ed. (Cuvillier Verlag, Göttingen, Univ. Ulm, 2009).

[121] G. Bruker AXS, "Leptos - XRD software, Bruker AXS," http://www.bruker-axs.com/leptos.html (Accessed September 22, 2011).

[122] K. Prabhakaran, T. G. Andersson, and K. Nozawa, "Nature of native oxide on GaN surface and its reaction with Al," Appl. Phys. Lett. **69,** 3212–3214 (1996).

[123] S. D. Wolter, B. P. Luther, D. L. Waltemyer, C. Önneby, S. E. Mohney, and R. J. Molnar, "X-ray photoelectron spectroscopy and x-ray diffraction study of the thermal oxide on gallium nitride," Appl. Phys. Lett. **70,** 2156–2158 (1997).

[124] C. Schulz, T. Schmidt, J. I. Flege, N. Berner, C. Tessarek, D. Hommel, and J. Falta, "Oxide removal from GaN(0001) surfaces," Phys. Status Solidi C **6,** S305–S308 (2009).

[125] N. J. Watkins, G. W. Wicks, and Y. Gao, "Oxidation study of GaN using x-ray photoemission spectroscopy," Appl. Phys. Lett. **75,** 2602–2604 (1999).

[126] L. Liu and J. H. Edgar, "Substrates for gallium nitride epitaxy," Mater. Sci. Eng. **R37,** 61–127 (2002).

[127] F. R. C. X. J. Ning, P. Pirouz, J. W. Yang, and M. A. Khan, "Growth defects in GaN films on sapphire: The probable origin of threading dislocations," J. Mater. Res. **11,** 580–592 (1996).

[128] W. E. Lee and K. P. D. Lagerlof, "Structural and Electron Diffraction Data for Sapphire (α-Al_2O_3," J. Electron Microscopy Technique **2,** 247–258 (1985).

[129] *Thermophysical Properties of Matter: Thermal expansion - nonmetallic solids*, Y. S. Touloukian, ed., (IFI/Plenum, New York/Washington, 1977), Vol. 13.

[130] M. Leszczynski, T. Suski, H. Teisseyre, P. Perlin, I. Grzegory, J. Jun, S. Porowski, and T. D. Moustakas, "Thermal expansion of gallium nitride," J. Appl. Phys. **76,** 4909–4911 (1994).

[131] Y. Shiratsuchi, M. Yamamoto, and Y. Kamada, "Surface Structure of Self-Organized Sapphire (0001) Substrates with Various Inclined Angles," Jpn. J. Appl. Phys. **41,** 5719–5725 (2002).

[132] F. Cuccureddu, S. Murphy, I. V. Shvets, M. Porcu, H. W. Zandbergen, N. S. Sidorov, and S. I. Bozhko, "Surface morphology of c-plane sapphire (α-alumina) produced by high temperature anneal," Surf. Sci. **604,** 1294–1299 (2010).

[133] F. Dwikusuma, D. Saulys, and T. F. Kuech, "Study on Sapphire Surface Preparation for III-Nitride Heteroepitaxial Growth by Chemical Treatments," J. Electrochem. Soc. **149,** G603–G608 (2002).

[134] J.-H. Kim, S. C. Choi, J. Y. Choi, K. S. Kim, G. M. Yang, C.-H. Hong, K. Y. Lim, and H. J. Lee, "Effects of Initial Thermal Cleaning Treatment of a Sapphire Substrate Surface on the GaN Epilayer," Jpn. J. Appl. Phys. **38,** 2721–2724 (1999).

[135] V. Ratnikov, R. Kyutt, T. Shubina, T. Paskova, E. Valcheva, and B. Monemar, "Bragg and Laue x-ray diffraction study of dislocations in thick hydride vapor phase epitaxy GaN films," J. Appl. Phys. **88,** 6252–6259 (2000).

[136] V. M. Kaganer, O. Brandt, H. Riechert, and K. K. Sabelfeld, "X-ray diffraction of epitaxial films with arbitrarily correlated dislocations: Monte Carlo calculation and experiment," Phys. Rev. B **80,** 033306 (2009).

[137] V. Holý, T. Baumbach, D. Lübbert, L. Helfen, M. Ellyan, P. Mikulík, S. Keller, S. P. DenBaars, and J. Speck, "Diffuse x-ray scattering from statistically inhomogeneous distributions of threading dislocations beyond the ergodic hypothesis," Phys. Rev. B **77,** 094102 (2008).

[138] S. Daniš, V. Holý, Z. Zhong, G. Bauer, and O. Ambacher, "High-resolution diffuse x-ray scattering from threading dislocations in heteroepitaxial layers," Appl. Phys. Lett. **85,** 3065–3067 (2004).

[139] M. A. Krivoglaz, *X-Ray and Neutron Diffraction in Nonideal Crystals* (Springer-Verlag, Berlin, 1996).

[140] A. Pretorius, T. Yamaguchi, C. Kübel, R. Kröger, D. Hommel, and A. Rosenauer, "TEM analyses of wurtzite InGaN islands grown by MOVPE and MBE," Phys. Status Solidi C **3,** 16791682 (2006).

[141] T. Yamaguchi, K. Sebald, H. Lohmeyer, S. Gangopadhyay, J. Falta, J. Gutowski, S. Figge, and D. Hommel, "A novel approach for the growth of InGaN quantum dots," Phys. Status Solidi C **3,** 3955–3958 (2006).

[142] C. Tessarek, T. Yamaguchi, S. Figge, and D. Hommel, "Improved capping layer growth towards stability of InGaN quantum dots," Phys. Status Solidi C **6,** S561–S564 (2009).

[143] T. Yamaguchi, J. Dennemarck, C. Tessarek, K. Sebald, S. Gangopadhyay, J. Falta, J. Gutowski, S. Figge, and D. Hommel, "Two-step growth of InGaN quantum dots and application to light emitters," Phys. Status Solidi C **4,** 2407–2410 (2007).

[144] Y. Arakawa, "Progress in Growth and Physics of Nitride-Based Quantum Dots," Phys. Status Solidi A **188,** 37–45 (2001).

[145] S. Gangopadhyay, T. Schmidt, S. Einfeldt, T. Yamaguchi, D. Hommel, and J. Falta, "Growth and morphology of MOVPE grown InGaN/GaN islands," Phys. Status Solidi C **3,** 1557–1560 (2006).

[146] S. Gangopadhyay, T. Schmidt, S. Einfeldt, T. Yamaguchi, D. Hommel, and J. Falta, "Formation and morphology of InGaN nanoislands on GaN(0001)," J. Vac. Sci. Technol. B **25,** 791–795 (2007).

[147] H. Hirayama, S. Tanaka, P. Ramvall, and Y. Aoyagi, "Intense photoluminescence from self-assembling InGaN quantum dots artificially fabricated on AlGaN surfaces," Appl. Phys. Lett. **72,** 1736–1738 (1998).

[148] K. Tachibana, S. T., and A. Y., "Nanometer-scale InGaN self-assembled quantum dots grown by metalorganic chemical vapor deposition," Appl. Phys. Lett. **74,** 383–385 (1999).

[149] Y. G. Cao, M. H. Xie, Y. Liu, Y. F. Ng, H. S. Wu, and S. Y. Tong, "InN island shape and its dependence on growth condition of molecular-beam epitaxy," Appl. Phys. Lett. **83,** 5157–5159 (2003).

[150] O. Briot, B. Maleyre, and S. Ruffenach, "Indium nitride quantum dots grown by metalorganic vapor phase epitaxy," Appl. Phys. Lett. **83,** 2919–2921 (2003).

[151] D.-H. Kang, D.-W. Kim, L. S.-H., L. S.-J., K. J.-S., S. Kannappan, Y.-K. Lee, and C.-R. Lee, "Fabrication and Characterization of $In_xGa_{1-x}N$ Quantum Dots Using Nitridation of Nano-alloyed Droplet Growth Technique," Jpn. J. Appl. Phys. **47,** 3053–3055 (2008).

[152] H. J. Kim *et al.*, "Growth of In-rich InGaN/GaN quantum dots by metalorganic chemical vapor deposition," J. Cryst. Growth **269,** 95–99 (2004).

[153] H. J. Kim *et al.*, "Growth behavior and optical properties of In-rich InGaN quantum dots by metal-organic chemical vapor deposition," Phys. Status Solidi C **4,** 112–115 (2007).

[154] D. Simeonov, E. Feltin, J.-F. Carlin, R. Butté, M. Ilegems, and N. Grandjean, "Stranski-Krastanov GaN/AlN quantum dots grown by metal organic vapor phase epitaxy," J. Appl. Phys. **99,** 083509 (2006).

[155] H. Wang, D. S. Jiang, J. J. Zhu, D. G. Zhao, Z. S. Liu, Y. T. Wang, S. M. Zhang, and H. Yang, "Kinetically controlled InN nucleation on GaN templates by metalorganic chemical vapour deposition," J. Phys. D: Appl. Phys. **42,** 145410 (2009).

[156] Q. Wang, T. Wang, J. Bai, A. G. Cullis, P. J. Parbrook, and F. Ranalli, "Growth and optical investigation of self-assembled InGaN quantum dots on a GaN surface using a high temperature AlN buffer," J. Appl. Phys. **103,** 123522 (2008).

[157] R. A. Oliver, M. J. Kappers, C. J. Humphreys, and G. A. D. Briggs, "The influence of ammonia on the growth mode in InGaN/GaN heteroepitaxy," J. Cryst. Growth **272,** 393–399 (2004).

[158] W.-C. Tsai, H. Lin, W.-C. Ke, W.-H. Chang, W.-C. Chou, W.-K. Chen, and M.-C. Lee, "Structural and optical properties of In-rich InGaN nanodots grown by metallo-organic chemical vapor deposition," Nanotechnology **18,** 405305 (2007).

[159] V. Jindal and F. Shahedipour-Sandvik, "Theoretical prediction of GaN nanostructure equilibrium and nonequilibrium shapes," J. Appl. Phys. **106,** 083115 (2009).

[160] D. Du, D. J. Srolovitz, M. E. Coltrin, and C. C. Mitchell, "Systematic Prediction of Kinetically Limited Crystal Growth Morphologies," Phys. Rev. Lett. **95,** 155503 (2005).

[161] J. Neugebauer, "Ab initio Analysis of Surface Structure and Adatom Kinetics of Group-III Nitrides," Phys. Status Solidi B **227,** 93–114 (2001).

[162] Q. Wang, T. Wang, P. J. Parbrook, J. Bai, and A. G. Cullis, "The influence of a capping layer on optical properties of self-assembled InGaN quantum dots," J. Appl. Phys. **101,** 113520 (2007).

[163] J. E. Northrup, L. T. Romano, and J. Neugebauer, "Surface energetics, pit formation, and chemical ordering in InGaN alloys," Appl. Phys. Lett. **74,** 2319–2321 (1999).

[164] A. L. Golovin, R. M. Imamov, and E. A. Kondrashkina, "Potentialities of New X-Ray Diffraction Methods in Structural Studies of Ion-Implanted Silicon Layers," Phys. Status Solidi A **88,** 505–514 (1985).

[165] H. Rhan and U. Pietsch, "Grazing incidence diffraction of X-rays in semiconductor heterostructures: application of the integral mode," Z. Phys. B Con. Mat. **80,** 347–352 (1990).

[166] C. Meissner, S. Ploch, M. Leyer, M. Pristovsek, and M. Kneissl, "Indium nitride quantum dot growth modes in metalorganic vapour phase epitaxy," J. Cryst. Growth **310,** 4959–4962 (2008).

[167] B. N. Pantha, J. Li, J. Y. Lin, and H. X. Jiang, "Evolution of phase separation in In-rich InGaN alloys," Appl. Phys. Lett. **96,** 232105 (2010).

[168] D. Gerthsen, B. Neubauer, A. Rosenauer, T. Stephan, H. Kalt, O. Schön, and M. Heuken, "InGaN composition and growth rate during the early stages of metalorganic chemical vapor deposition," Appl. Phys. Lett. **79,** 2552–2554 (2001).

[169] D. Gerthsen, E. Hahn, B. Neubauer, V. Potin, A. Rosenauer, and M. Schowalter, "Indium distribution in epitaxially grown InGaN layers analyzed by transmission electron microscopy," Phys. Status Solidi C **0,** 1668–1683 (2003).

[170] I. L. Krestnikov *et al.*, "Quantum dot origin of luminescence in InGaN-GaN structures," Phys. Rev. B **66,** 155310 (2002).

[171] Leszczyński, M. et al. (private communication, VI PINCH Photonics).

[172] T. Chakraborty, *Quantum Dots: A survey of the properties of artificial atoms*, 1st ed. (Elsevier Science B.V., Amsterdam, 1999), pp. 1–17.

[173] Y. Arakawa and H. Sakaki, "Multidimensional quantum well laser and temperature dependence of its threshold current," Appl. Phys. Lett. **40,** 939–941 (1982).

[174] Y. Wang and N. Herron, "Nanometer-Sized Semiconductor Clusters: Materials Synthesis, Quantum Size Effects, and Photophysical Properties," J. Phys. Chem. **95,** 525–532 (1991).

[175] U. Woggon and S. Gaponenko, "Excitons in Quantum Dots," Phys. Status Solidi (b) **189,** 285–343 (1995).

[176] Y. Kayanuma, "Wannier exciton in microcrystals," Solid State Comm. **59,** 405–408 (1986).

Appendix A

List of Acronyms

AFM atomic force microscopy
ANKA Angströmquelle Karlsruhe
AXRD asymmetrical X-ray diffraction
AXS anomalous X-ray scattering
CCD charge coupled device
CDI coherent diffraction imaging
CL cathodoluminscence
CTR crystal truncation rod
DCM double crystal monochromator
DWBA distorted wave Born approximation
ELO epitaxial layer overgrowth
EPD etch pit density
ESRF European Synchrotron Radiation Facility
FFT fast Fourier transform
FWHM full width at the half maximum
GID grazing incidence diffraction
GISAXS grazing incidence small angle X-ray scattering
HRTEM high resolution transmission electron microscopy
HRXRD high resolution X-ray diffraction
HVPE hydride vapour phase epitaxy
ID insertion device
LD laser diode
LED light emitting diode
LT low temperature
MBE molecular beam epitaxy
MM multilayer monochromator
MOCVD metal-organic chemical vapour deposition
MOVPE metal-organic vapour phase epitaxy
OMVPE organometallic vapour-phase epitaxy
PL photoluminescence

PSD position sensitive detector
PSIC PSI-circle geometry modes
QD quantum dot
QW quantum well
RSM reciprocal space map
SAXS small angle X-ray scattering
SCD single crystal diffraction
SEM scanning electron microscopy
SK Stranski-Krastanow
SPM scanning probe microscopy
SXRD symmetrical X-ray diffraction
TEA triethylaluminium
TEG triethylgallium
TEI triethylindium
TEM transmission electron microscopy
TER total external reflection
TMA trimethylaluminium
TMG trimethylgallium
TMI trimethylindium
UHV ultra high vacuum
XRD X-ray diffraction
XRR X-ray reflectivity

Appendix B

Quantum effects in low-dimensional systems

Theoretically considered, space confinement or reduction of free motion in certain directions in low-dimensional systems can be described as follows. In the bulk material we have a three-dimensional (3D) gas of quasi-free electrons which have a free motion in all three directions with corresponding energy [172]:

$$E = \frac{\hbar^2}{2m^*}({k_x}^2 + {k_y}^2 + {k_z}^2) \tag{B.1}$$

where m^* is an effective mass of electrons and k_x, k_y, k_z are the wavevectors in all three directions. Therefore, the energy spectrum of electrons in 3D system is continuous and the density of states (DOS) follows $D_s(E) \propto E^{\frac{1}{2}}$ (fig. 2.7). In the case of the two-dimensional (2D) systems the motion of the electrons is free in xy-plane, but in the z-direction is quantized into discrete electric subbands:

$$E = \frac{\hbar^2}{2m^*}({k_x}^2 + {k_y}^2) + {E_z}^k \tag{B.2}$$

(k is an integer) showing step-function modification of the energy spectrum from the bulk (fig. 2.7 2D). In the one-dimensional (1D) system, electrons have a free motion only in one dimension due to additional lateral confinement in respect to the 2D system:

$$E = \frac{\hbar^2}{2m^*}{k_x}^2 + {E_y}^j + {E_z}^k \tag{B.3}$$

(j is an integer) where DOS is highly peaked (fig. 2.7 1D) at all relevant energies. When the motion of electron is confined in all three directions, we have zero-dimensional system (0D) where the energy spectrum is discrete and the DOS is a series of δ-function peaks (fig. 2.7 0D):

$$E = {E_x}^i + {E_y}^j + {E_z}^k \tag{B.4}$$

with i is an integer. Dimensions of the quantum dot are about De Broglie wavelength expressed as:

$$\lambda_{deBroglie} = \frac{2\pi\hbar}{\sqrt{3m^* k_B T}} \tag{B.5}$$

where the product of Boltzmann constant k_B and the temperature T represent thermal energy of the system. Emission spectra for n-dimensional electron system assuming the spherical symmetry in the electron-hole recombination are defined by [173]:

$$N_n = \frac{2}{(2\pi)^n L^{3-n}} \int_{E=const.} d^n k = \frac{2}{(2\pi)^n L^{3-n}} \frac{1}{\left(\frac{n}{2}\right)!} \left(\frac{2\pi m^*}{\hbar^2}\right)^{\frac{n}{2}} E^{(\frac{n}{2})} \tag{B.6}$$

where L^3 is the volume of n-dimensional sphere. Corresponding density of states is as follows:

$$D_n(E) = \frac{dN_n}{dE} = \frac{2}{(2\pi)^n L^{3-n}} \frac{1}{\left(\frac{n}{2}-1\right)!} \left(\frac{2\pi m^*}{\hbar^2}\right)^{\frac{n}{2}} E^{(\frac{n}{2}-1)}. \tag{B.7}$$

Density of electronic states depending on the energy changes with the space confinement as motion of the electrons are restricted:

$$D_{3D}(E) = \frac{2}{(2\pi)^2} \left(\frac{2m^*}{\hbar^2}\right)^{\frac{3}{2}} \sqrt{E} \quad \text{Bulk} \tag{B.8}$$

$$D_{2D}(E) = \frac{m^*}{\pi\hbar^2 L_z} \sum_l \theta(E - E_l) \quad \text{Quantum Well} \tag{B.9}$$

$$D_{1D}(E) = \frac{\sqrt{2m^*}}{\pi\hbar L_z L_y} \sum_{l,m} \frac{1}{\sqrt{E - E_{l,m}}} \quad \text{Quantum Wire} \tag{B.10}$$

$$D_{0D}(E) = \frac{2}{L_z L_y L_x} \sum_{l,m,n} \delta(E - E_{l,m,n}) \quad \text{Quantum Dot} \tag{B.11}$$

Previous equation shows that energy spectra of the quantum dots is represent by atomic-lines-like delta-functions.

Let us see how the exciton energies behave in different n-dimensional systems. In a bulk semiconductor, the electron and hole are bound together by a screened Coulomb interaction to form an exciton. The Bohr radius of the exciton is given by [174]:

$$a_0 = \frac{\hbar^2 \epsilon}{e^2} \left(\frac{1}{m_e^*} + \frac{1}{m_h^*}\right) \tag{B.12}$$

If the radius of the spherical quantum dot r_{QD} is much bigger than exciton Bohr radius $r_{QD} \gg a_0$, then the energy of the electron-hole pair recombination is equal to [175]:

$$E_{eh} = E_g^0 + E_{Ry} \left[\frac{\mu}{M} \left(\frac{\pi a_0}{r_{QD}}\right)^2 - 1\right] \tag{B.13}$$

where $\frac{1}{\mu} = \frac{1}{m_e^*} + \frac{1}{m_h^*}$, μ is reduced electron-hole mass, M is an exciton mass and E_g^0 is a bulk band-gap. E_{Ry} is the effective Rydberg energy, $e^4/\left(2\epsilon^2\hbar^2\mu^{-1}\right)$ [174]. In the opposite limit, when $r_{QD} \ll a_0$, the exciton energy is described by:

$$E_{eh} = E_g^0 + E_{Ry}\left(\frac{\pi a_0}{r_{QD}}\right)^2. \tag{B.14}$$

In the case that quantum dot radius is of the same order as exciton Bohr radius $r_{QD} \approx a_0$, energy is given by [174, 176]:

$$E_{eh} = \frac{\hbar^2\pi^2}{2\mu r_{QD}^2} - \frac{1.786e^2}{\epsilon r_{QD}} - 0.248E_{Ry}. \tag{B.15}$$

The first term in the previous equation represents the "particle in a box" quantum localization energy, the second term represents the Coulomb energy and the third term is a result of the spatial correlation effect [174].

More detailed description of the electrical and optical properties of quantum dots will not be considered here and can be found elsewhere [80].

Index